Measurement of wind on the surface of Mars

A thesis submitted for the degree of Doctor
of Philosophy at the University of Oxford

September 2003

Colin F. Wilson

Linacre College

Abstract

The Martian atmosphere is of great scientific interest, both because of its similarity to Earth's atmosphere, and because of its relevance to exploration of Mars. Although satellite instruments have provided a wealth of atmospheric data, they have provided little information about the atmospheric boundary layer. Conditions in the lowest few metres of the Martian atmosphere are perhaps the most directly interesting to humans, as this is the portion of our own atmosphere with which we have the most contact.

In this thesis is described the design, calibration and operations planning for a new wind sensor for use on Mars. This sensor is lighter and smaller than previous Mars wind sensors. At the time of writing, the wind sensor is on its way to Mars as part of the science payload of Beagle 2, a small exobiology lander due to arrive in December 2003.

The Beagle 2 wind sensor (B2WS) is a hot-film anemometer. Three platinum films are equally spaced around the surface of a vertical cylinder. A known current is dissipated in each film, heating the film 40-80°C above the ambient gas temperature. The film temperature is obtained by measuring its resistance. An effective heat transfer coefficient is then calculated for each film. A novel scheme has been developed which allows calculation of a wind vector from the differences between these heat transfer coefficients, rather than from their average. This makes the measured wind vector less prone to common-mode errors such as uncertainties in air temperature or sky temperature.

The sensor was calibrated in a low density wind tunnel, optimised to provide stable winds of air or carbon dioxide at Martian pressures (5 – 10 mbar) and speeds (0.5 – 30 m/s). The flow field in the test section was calculated using analytical and finite element modelling techniques, and validated experimentally using a pitot probe. This facility's stability and accuracy represent a significant improvement over previous calibration facilities.

An analytical model of heat flow in the sensor has been developed in order to permit correction for conditions which may be encountered on Mars, but were not tested for in the wind tunnel. The wind sensor's performance in a real Martian atmosphere is simulated using wind and temperature data from a previous Mars lander.

The position of the wind sensor position at the end of Beagle 2's motorised arm allows several new possibilities for wind measurement on Mars that were unavailable in previous missions. The height of the wind and air temperature sensors can be adjusted to any height between 20 and 95 cm above the ground. The temperature sensor can be scanned horizontally and vertically above the lander to study convective updrafts above the heated lander. Planned operations sequences on Mars are discussed.

Table of Contents

Acknowledgements

This project would never have come together without contributions from many people.

Simon Calcutt, my supervisor, supported the project from the very beginning, and trusted me somehow to be getting on with the project despite long months away at the wind tunnel.

Fred Taylor helped in the early stages of the project to make connections with the Beagle 2 team.

This project never would have occurred without the enthusiastic support of Professor Terry Jones, who loaned me a wind tunnel for two years, and with whom the concept of the Beagle 2 wind sensor was worked out.

Martin Oldfield of Engineering Science had the original idea of the data interpretation technique, and helped with the circuit design.

All the wind sensors were built by the tireless Trevor Godfrey.

Jon Temple provided invaluable support all the way along, has supplied me with endless computers, and assembled the B2WS flight electronics.

Nick O’Donnell has always been ready to help with any mechanical design queries.

Bob Watkins and Dan Peters provided invaluable help with the cryostat operation.

Thanks to John Zarnecki for inviting me onto the Beagle 2 project, and to Derek Pullan and Mark Sims for useful comments along the way – and to Martin Towner, Tim Ringrose & Manish Patel, with whom most of the ESS details were thrashed out.

The NetLander ATMIS science teams have also provided useful comments.

All the workshop staff at Atmospheric Physics and in Osney have been very helpful.

Most of all, though, the fellow DPhil students both in AOPP and in Osney have provided invaluable support through the years. Neil Bowles, Paul Parrish, and Jaime Reed in particular. Thanks to Chiara for binding this thesis!

Filakia, Koukouli, for putting up with me and Trevor and Penelope for three years….

Finally, I am grateful for the patience of Liz, and the support of my parents, without which none of this would have been possible.

Chapter 1 - Introduction to Mars and its atmosphere

1.1 Why study the atmospheric circulation of Mars?

Mars has long fascinated humans. Thousands of years ago humans had already noticed its red-brown colour and odd trajectory across the sky, different from any star. Now in the space age that we know much more of Mars, our interest grows only more keen. Though the long-cherished hope of finding human-like life on Mars has been ruled out, the atmosphere of Mars is in many ways the most Earth-like in our solar system. Earth-like features of the Martian climate include its day length, largely transparent atmosphere, and yearly cycle of seasons. On the other hand, the Martian atmosphere differs from ours in its low pressure and temperature, in its atmospheric composition (mainly CO_2 with only minute concentrations of atmospheric water), and in the crucial role played by atmospheric dust. This atmosphere, which is so like our own in some ways but crucially different in others, offers us an intriguing tool with which to develop our understanding of atmospheric dynamics.

Our interest in the Martian atmosphere is more than merely scientific. It is also an essential prerequisite for any missions, manned or unmanned, bound for the surface of Mars. Martian meteorologists must be able to tell mission planners what conditions (temperatures, dust levels, winds etc) to expect at a landing site. Though a global understanding of the Martian climate is essential to predict conditions at a given landing site at a given time, the most direct data for this purpose are those from a surface meteorological station.

1.2 Mars and its orbit

In Table 1.1 are listed some crucial parameters of Mars and its orbit.

Parameter	Mars	Earth	Units
Planetary radius (Equatorial)	3394	6378	km
Mean planetary density	3945	5517	kg m^{-3}
Length of solar day (1 *sol*)	88775	86400	seconds
Length of solar year	687	365	Earth days
Planet-sun distance	1.38-1.67	0.98-1.02	(AU)
Orbital eccentricity	0.093	0.017	
Axial inclination	25 °	23.5 °	
Bolometric albedo	0.25	0.29	
Surface gravity	3.72	9.81	m s^{-1}
Surface pressure	5-8	1013	mbar
Mean molecular weight (atmospheric)	43.4	29.0	g mol^{-1}
Specific heat capacity (constant *p*)	860	1000	J K^{-1} kg^{-1}
Speed of sound	229	321	m s^{-1}
Mean scale height	10.8	7.5	km
Mean lapse rate (lower atmos.)	~2.5	6.5	K km^{-1}
Visible atmospheric optical depth	0.1-10	0.2-100	

Table 1.1 – Planetary parameters for Mars and Earth. After [Zurek *et al.*, 1992].

The rotational period of Mars is almost identical to that of the Earth, and its atmosphere is largely transparent at visible wavelengths, also like our own. Because of these two factors, the global circulation of Mars is remarkably similar to that on our own planet, more so than any other body in our solar system. Most of the incoming solar radiation is absorbed at the planet's surface. Heat is then transferred to the atmosphere both by convective overturning at low levels (as in our troposphere), and by thermal infrared radiation (as in our stratosphere).

Mars' climate is subject to Earth-like seasons, due to its almost identical axial tilt. Unlike the Earth, however, which has an almost circular orbit, the orbit of Mars is significantly elliptical. Thus its seasons are asymmetrical: Mars is closest to the sun (at perihelion) during its Northern hemisphere's winter. Therefore the Northern hemisphere's winter is warmer and shorter than that in the Southern Hemisphere. The passing of the seasons is measured using the *areocentric longitude* (L_s). 0° represents the northern spring equinox, 90° the northern summer solstice, and so on. The relationship between L_s and time is nonlinear due to the ellipticity of the Martian orbit. Much of Mars' atmospheric behaviour varies greatly over the Martian year. Hence L_s is a critical parameter for mission design.

The surface pressure on Mars is only 6.1 mbar on average, varying with both altitude and season. As a consequence, the atmosphere has a very low thermal inertia. The Martian surface also lacks oceans, which act as very powerful thermal sinks on Earth. This low thermal inertia, both of the atmosphere and of the planetary surface, results in a large diurnal temperature fluctuation (typically ~ 60 K). Furthermore, this low thermal inertia has several important consequences for the atmospheric circulation, as will be discussed below.

1.3 Atmospheric composition

The Martian atmosphere is primarily composed of carbon dioxide (CO_2), with small amounts of nitrogen and other gases (see Table 1.2). Since Mars is further from the Sun than the Earth, it receives less solar energy. Furthermore, greenhouse warming is less than on Earth, due to Mars' thin atmosphere. For these two reasons, surface temperatures are generally colder on Mars than on Earth. However, the atmospheric temperature cannot sink lower than the freezing point of carbon dioxide, which is about 145-150 K at the surface, at which carbon dioxide starts precipitating out of the atmosphere. Much of the atmospheric carbon dioxide can precipitate out of the atmosphere in the winter polar regions, forming seasonal polar ice caps. This leads to an annual pressure oscillation of roughly ±10% of the yearly average [Catling, 1995]. These polar ice caps have attracted a great deal of scientific study, a review of which can be found elsewhere [Clifford *et al.*, 2000].

Gas	Molecular Abundance
Carbon dioxide (CO_2)	95.32 %
Nitrogen (N_2)	2.7 %
Argon (^{40}Ar)	1.6 %
Oxygen (O_2)	0.13 %
Carbon monoxide (CO)	0.07 %
Water vapour (H_2O)	0.03 %

Table 1.2 – Major gases in the Martian lower atmosphere. Note that the proportion of water vapour is highly variable with location and season. After [Owen, 1992].

The Martian atmosphere today holds very little water, comprising only 0.03% by volume of the atmosphere. This is because of the low temperatures and pressures on Mars, at which the saturation levels in the atmosphere are very low. Liquid water is not stable at the low pressures of the Martian atmosphere; upon cooling, water vapour condenses directly into ice. Many observations of frozen water ice clouds have been recorded [Kahn, 1984]. The north polar ice cap contains large amounts of frozen water [Farmer *et al*., 1976]. Recent evidence suggests that vast quantities of frozen water ice are mixed into the Martian regolith, forming up to 50% by weight of the soil [Boynton *et al*., 2002]. Another paper suggests that gullies are currently being carved by liquid water flows originating from seasonally melting snow packs which contain water ice [Christensen, 2003]. Current observations of the Martian surface are providing large amounts of new data at the present time, so this is a rapidly evolving field.

The past climate of Mars is hotly debated. Possibly the most popular theory is that Mars once had a much wetter, warmer climate. This theory comes about mainly in reaction to a host of Martian geographic features which bear a striking similarity to water-carved features on earth: for example deep canyons, eroded ‘shorelines’ [e.g. Smith *et al*., 1997], and ‘muddy flows’ in impact craters [e.g. Strom *et al*., 1992]. Further support comes from analyses of meteorites from Mars which show high levels of water-altered minerals [Kargel & Strom, 1996]. If liquid water were present in large quantities in the past, the atmospheric pressure must have been much higher, which would have sustained a stronger greenhouse effect, warming the atmosphere sufficiently to allow liquid water to exist freely. However, many of these geographic features could have been caused by other mechanisms, such as wind erosion or pyroclastic flows. Opponents of the ‘wet Mars’ theory further point out that a warmer, wetter Mars would have led to the formation of vast quantities of carbonates, of which only small quantities have been found [Bandfield *et al*., 2003].

Understanding the water cycle on Mars, both in the present and in the past, is often cited as the single most important theme of Martian research, as epitomised by NASA’s slogan ‘Follow the Water’. The atmospheric science contribution to this goal is to understand the water cycle on Mars; to quantify surface-atmosphere exchanges and atmospheric transport of water.

1.4 Atmospheric dust

The atmospheric component which most greatly influences atmospheric variability is suspended dust. Dust is always present to some extent in the Martian atmosphere, though its distribution in time and space is highly variable. The optical depth of the Martian atmosphere at visible wavelengths can vary due to atmospheric dust from 0.5 to 5 during global storms [Zurek & Martin, 1993].

The large variability in the atmospheric dust concentrations implies extensive surface-atmosphere exchange of dust. In the absence of any wind, atmospheric dust would slowly settle to the surface. Meanwhile, dust is lifted into the atmosphere by near-surface winds. Dust in the atmosphere absorbs solar radiation and radiates heat at night, and thus significantly changes the forcing of atmospheric dynamics. This can lead to extremely strong winds, which in turn cause more dust lifting; this positive feedback can lead to planet-wide dust storms. The two photos of Mars shown in Figure 1.1 were taken two weeks apart; in the intervening time a dust storm spread to encompass the whole atmosphere. One of the main goals of near-surface wind studies is improve understanding of dust-lifting processes, so that the occurrence of such global storms can be better understood.

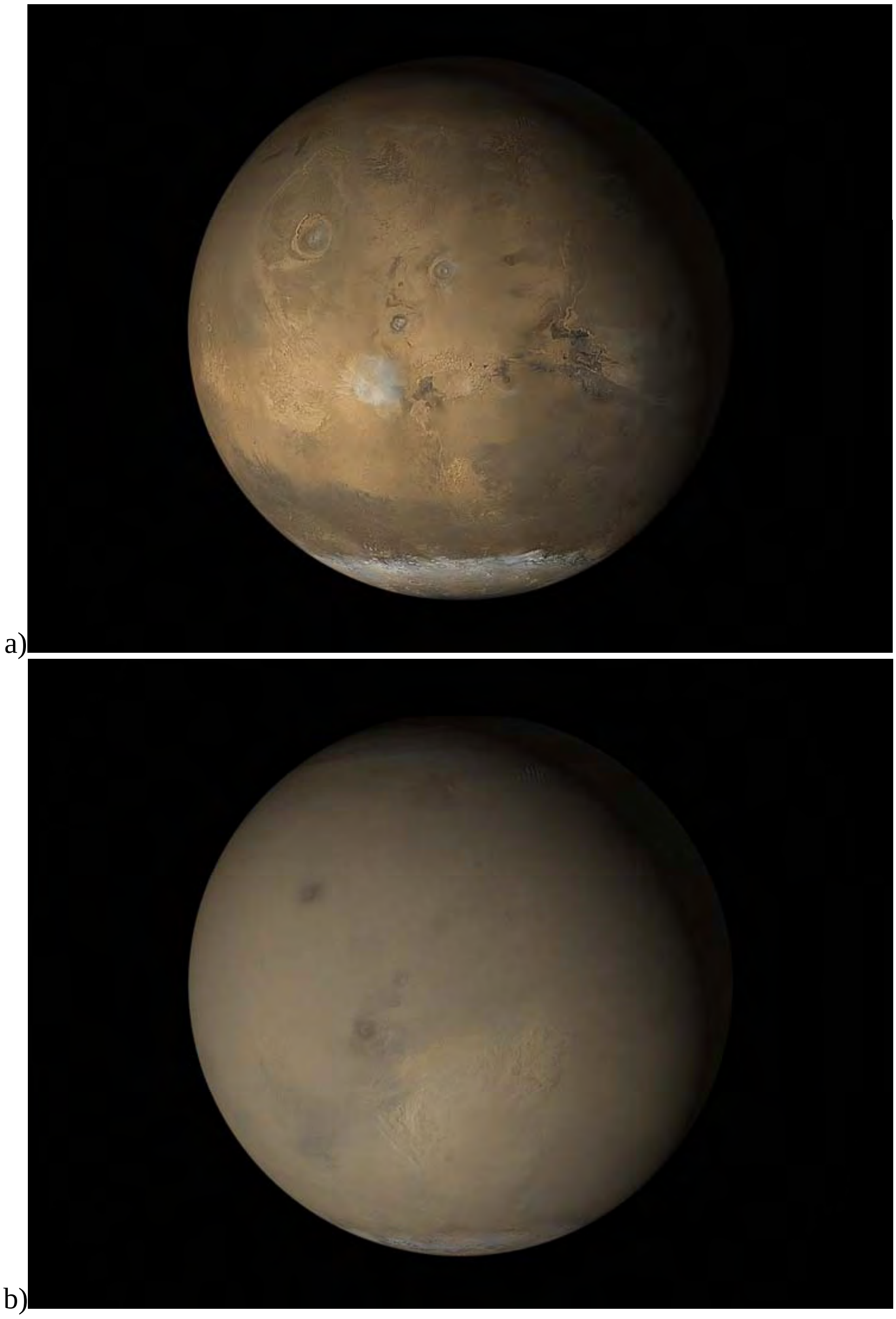

Figure 1.1 – A global dust storm on Mars, observed using the Mars Orbital Camera aboard the Mars Global Surveyor spacecraft: a) is taken on the 10th June 2001, b) is taken on the 31st July 2001. NASA/JPL/Malin Space Science Systems http://www.msss.com

Atmospheric dust is typically very fine, typically < 2 μm in diameter (larger particles settle out of the atmosphere more quickly). When these particles are lying on the surface, the shear stress exerted on them by typical wind speeds is not enough to break the adhesion forces between particles on the surface. Larger diameter ‘sand’ particles (> 20 μm) are more easily lofted by near surface winds – a process called *saltation* – although they do not stay airborne for long. When these sand particles fall back to the surface their kinetic energy can liberate dust particles which can then be lifted up by the wind. Wind tunnel tests suggest that little saltation occurs until wind speeds measured 1 m above the surface exceed ~ 25 m/s [Greeley, 1980; Greeley & Iversen, 1985]. This is higher than most wind speeds observed by Mars landers, so it is difficult to explain how there comes to be so much dust in the Martian atmosphere.

Another possible dust-lifting mechanism is convective vortices. When a convective vortex travels over a dusty surface, it may pick up dust and become visible, in which case it is known as a dust devil. These are often observed in deserts on Earth, where they may be ~1-150 metres in diameter. On Mars, they are larger, sometimes as large as 1 km in diameter. Models of terrestrial convective vortices scaled to Martian conditions predict that such evens can give rise to wind speeds of up to 60 m s^{-1} [Renno *et al.*, 2000]. They have been seen in satellite pictures [Thomas & Gierasch, 1985], as shown in Figure 1.2; from lander meteorological data [Ryan & Lucich, 1983; Schofield *et al.*, 1997], and even in a photograph from a lander [Metzger *et al.*, 1999] – these different data sources are discussed in turn below. From these data, we know that dust devils are commonplace in many regions of Mars; two studies of lander meteorological data show occurrences of 0.5 to 2 convective vortices per day [Ringrose *et al.*, 2003; Murphy & Nelli, 2002]. Experiments on Earth have found that the amount of dust lofted in these events is greater simply than what would be expected given the near-surface horizontal winds associated with a dust devil; this is interpreted as being due to the simultaneous pressure drop in the core of the dust devil [Greeley *et al.*, 2003].

It is unclear at present which of these two dust-lifting methods (Near-surface wind stress, or dust devils) is the more important one on Mars. Surface wind measurements taken with a high temporal resolution (~1 Hz) would help to characterize both of these dust-lifting mechanisms.

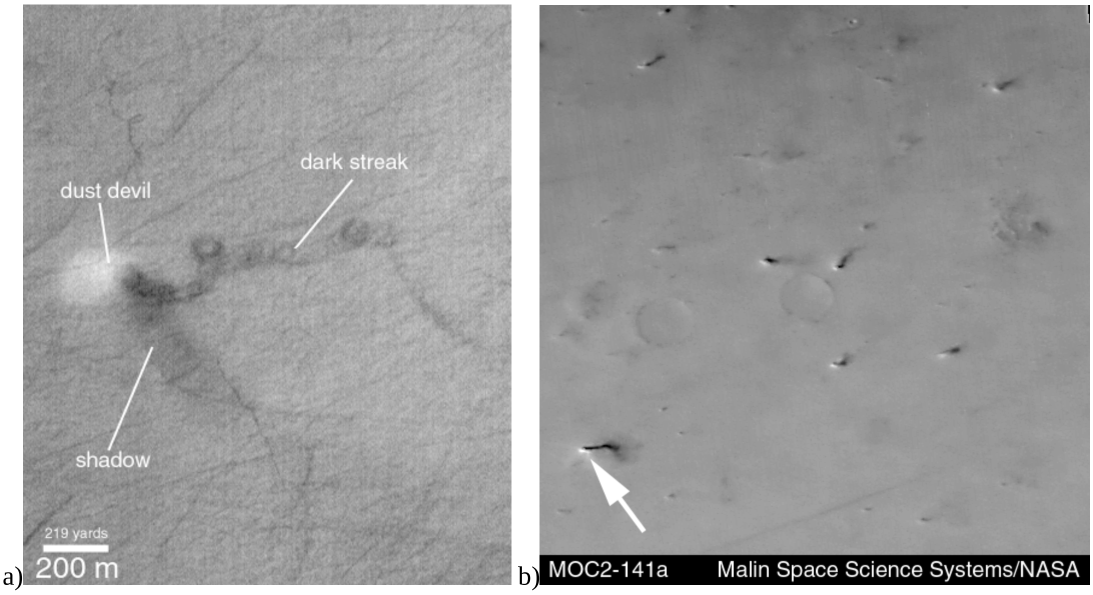

Figure 1.2 – Dust devils seen from orbit. MGS photos of a) a single dust devil, b) several dust devils on a single photo. For scale, the photo on the right is 88 km across. Photos are from NASA/JPL/Malin Space Science Systems/NASA http://www.msss.com/

1.5 Atmospheric dynamics

In this section, the main features of the Martian global circulation are summarised. This discussion will be subdivided into three sections: Large-scale dynamics (global in scale), mesoscale phenomena (inherently local in scale, occurring over distances of a few kilometres to hundreds of kilometres), and finally planetary boundary layer (PBL) dynamics.

1.5.1 Large-scale dynamics

On Mars, as on Earth, the general atmospheric circulation is primarily driven by differential solar heating. At equinox, when the sun is directly above the equator, air rises above the equator and then moves away from the equator towards the poles. It is replaced by cooler air drawn towards the equator near the surface. This is similar to the Hadley cell circulation on Earth. When the sun moves away from the equator a single cross-equatorial convective cell is established (note that this is unlike the Earth). Warm air rises in the ‘summer’ hemisphere and sinks in the ‘winter’ hemisphere, creating in the low latitudes a global meridional near-surface wind flowing from the winter to the summer hemisphere.

Another seasonal circulation pattern arises due to the freezing and sublimation cycle of carbon dioxide at the polar caps. As mentioned above, up to 25% of the atmosphere can precipitate out of the atmosphere in winter at the winter polar cap. This leads to a meridional flow to and from the polar cap in the winter and summer respectively. This meridional flow, when integrated zonally and vertically, can be as great as $0.5\ \mathrm{m\ s^{-1}}$ [Zurek *et al.*, 1992].

Atmospheric tides are global oscillations of the atmosphere, primarily due to thermal forcing through solar insolation. The strongest components of the tides are diurnal and semi-diurnal (twice daily), with some higher-frequency components acting as well. These lead to a diurnal pressure variation of 5 to 10% which are easily seen in the surface pressure records of Martian landers [Leovy & Zurek, 1979; Schofield *et al.*, 1997]. The semi-diurnal tide has a measurable effect on near-surface wind vectors; the diurnal component, though also significant is less easy to discern because of the dominance of ‘mesoscale’ dynamics. The influence of tides – notably the semi-diurnal component – is evident also in surface wind observations; however, such influences are often masked by local phenomena, as will be described below [Leovy & Zurek, 1979].

1.5.2 Mesoscale dynamics

The mean winds observed at any point on the surface are due not only to global-scale dynamics as described above, but also to local circulations referred to as *mesoscale* phenomena. These must be well understood, therefore, before attempting to draw conclusions about global circulation from surface measurements.

The term ‘mesoscale’ refers to distance scales ranging from a few kilometres to a few hundred of kilometres. Mesoscale phenomena include both terrain-induced mesoscale circulations and synoptically induced (free atmosphere) circulations. The former are far more influential near the planetary surface, so it is these that will be reviewed here. *Terrain-induced* circulations can be further classified as *mechanically* and *thermally* induced. Mechanically induced circulations include lee waves and wake phenomena. These are primarily forced by topography, and depend strongly on the general circulation (i.e. atmospheric circulation above the boundary layer). Therefore these mechanically induced phenomena can be predicted to some extent using a high-resolution global circulation model which includes detailed measurements of topography (for larger scale features), or analytically if detailed local topography is known.

On the other hand, thermally induced systems are essentially mesoscale convective cells driven by thermal contrast between adjacent surface regions. This thermal contrast may be due to variations in surface characteristics, including ice coverage, albedo, thermal inertia, or surface elevation. A familiar example on Earth is the sea/land breeze phenomenon, which is driven by the difference in thermal inertia between sea and land. Slope winds occur when adjacent regions of the surface, at different elevations, are heated equally. The air above the higher region is thus warmer than the free atmosphere at that height. Therefore, convection patterns form, leading to up-slope winds during the day and down-slope winds at night. On Mars, thermally-induced winds can be very strong due to the high diurnal temperature range and low thermal inertia of the atmosphere.

Mesoscale circulation on Mars has been modelled for situations including slope winds [Savijärvi & Siili, 1993], albedo and thermal inertia induced circulation [Siili, 1996], winds to be expected at polar cap edges [Siili *et al.*, 1999], and wind patterns expected at Viking Lander sites [Hess *et al.*, 1977; Haberle *et al.*, 1993].

1.5.3 Planetary Boundary Layer (PBL) dynamics

The term *planetary boundary layer* (PBL) refers to the lowest layer of the atmosphere, in which the surface of the planet directly exerts a significant effect on atmospheric dynamics. In this layer one finds large vertical gradients of temperature and wind speed, which lead to strong thermal and mechanical turbulence respectively. In the daytime, air temperature decreases strongly with height, as the surface absorbs solar radiation faster than the atmosphere. At night, an inversion (temperature decreasing with height) develops. Temperature gradients in the PBL are generally much greater on Mars than on Earth, because the thin Martian atmosphere has a low thermal inertia and is inefficient at transporting heat away from the surface. Temperature gradients of 10 K m^{-1} are typical at mid-day in the lowest metre of the atmosphere [Schofield *et al.*, 1997].

The fluxes in the PBL of heat, momentum and dust drive the circulation of the atmosphere. There is particular interest in processes which govern the movement of dust and sand particles. However, we currently have very little empirical data about this layer. Our understanding of Earth’s PBL has developed through hundreds of ground-based experiments, involving measurements of temperature, pressure and wind at many locations simultaneously. In contrast, on Mars one has only data from occasional landers to work with, for satellite observations do not provide sufficient resolution in the PBL to analyse its structure.

The vertical structure of the PBL is illustrated schematically in Figure 1.2. The left-hand panel shows temperature $T(z)$, the right hand panel show the same data expressed as *potential temperature*, $\Theta(z) = T(z)\left(p_{surface} / p(z)\right)$. Potential temperature is useful as a temperature scale because it shows convective stability: a negative $d\Theta/dz$ signifies that the atmosphere is convectively unstable, whereas a positive $d\Theta/dz$ indicates stable stratification.

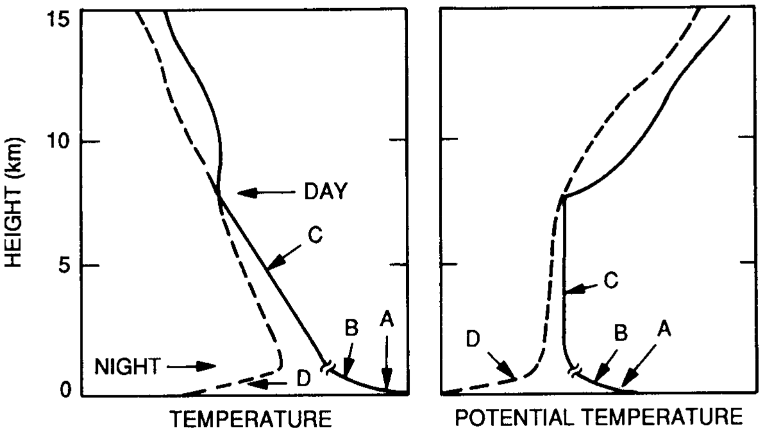

Figure 1.3 – Schematic representation of the planetary boundary layer (PBL) on Mars. The variations of temperature and potential temperature are sketched for a relatively clear atmosphere. Solid lines represent mid-afternoon conditions, when the PBL is likely to attain its maximum depth; dashed lines indicate night-time conditions. Horizontal arrows indicate the PBL top for the day and night profiles. Regions A: molecular conduction layer; B: unstable surface layer; C: convective layer of PBL; D: (night-time) radiatively produced surface inversion. The disconnection indicates that the heights of A and B are greatly exaggerated. Figure and caption reproduced from [Zurek, 1992].

The PBL can be considered to consist of three separate regions. Immediately next to the surface is the *molecular conduction layer,* also called the *laminar sub-layer*. Here, wind speeds are very close to zero, due to friction with the ground. Due to these low speeds, flow in this layer is laminar. Transport of heat and volatiles through this layer occur by thermal conduction and molecular diffusion respectively. On Mars, this layer is roughly 1 cm thick [Zurek, 1992]. This is about 100 times greater than on Earth, due to the much longer path length of gas molecules in the Martian atmosphere.

Above this is the *turbulent* or *unstable surface layer*. This can vary in thickness from metres to hundreds of metres. Strong vertical gradients of potential temperature are found in this region, due to the large temperature difference between the ground and the atmosphere. In the daytime, the temperature decreases strongly with height, leading to strong convective turbulence. At night-time the ground cools radiatively and becomes colder than the atmosphere, leading to a temperature inversion in this layer. This layer can be a few metres in height at night-time, or in regions of low surface roughness, or can grow to a few hundred metres thickness in the daytime [Zurek 1992].

Above the surface boundary layer is a thicker layer, called the *convective* or *well-mixed layer*. In this layer, convective mixing is fully developed, which keeps the potential temperature gradient $d\Theta/dz$ near zero. This region grows in height as the atmosphere is heated from below, from a few tens of metres in the morning to several kilometres by late afternoon. The length scale of convective cells here can approach the thickness of the layer, so Coriolis forces can become important. Modelling results suggest that the total height of the Martian PBL varies from ~0.1 km in the early morning to > 5 km on a clear summer afternoon.

Clearly, the most relevant of these layers for *in situ* meteorological measurements from a lander is the unstable surface layer. The structure of this layer is now examined in more detail.

In this portion of the PBL, vertical profiles of wind speed $u(z)$ and temperature $\Theta(z)$ can be scaled using the Monin-Obukhov equations:

$$\frac{U(z)}{u_*} = \frac{1}{0.4}\left[\ln\frac{z}{z_0} - \Psi_m\left(\frac{z}{L}\right)\right]$$

$$\frac{\Theta(z)-\Theta_0}{\Theta_*} = \frac{1}{0.4}\left[\ln\frac{z}{z_0} - \Psi\left(\frac{z}{L}\right)\right]$$

In this equation, z_o is the surface roughness height and $\Theta_o = \Theta(z_o)$. The velocity scale is provided by the u_* ($u_* = \sqrt{\tau/\rho}$ where τ is the shear stress acting at the surface), and the equivalent temperature scale is provided by $\Theta_* = u_*^2\Theta_o / kLg$. Finally, L represents the Monin-Obukhov length, which is inversely proportional to convective heat flux from the surface to the atmosphere [see e.g. Arya, 1988]. The stability functions ψ and ψ_m are used to correct for buoyancy effects in stably or unstably stratified conditions; they are empirical functions of z/L determined from field measurements of the surface boundary layer on Earth. Note that in neutral conditions, $\psi = \psi_m = 0$, in which case the equations show that the wind and temperature vary logarithmically with height.

There are a number of methods of determining the heat and momentum fluxes in the PBL. A good overview is provided in Arya [1988]. The most common technique involves simultaneous measurement of wind and temperature at at least three heights. This allows plotting of wind and temperature profiles and thus calculation of all the coefficients in the equations above, including L and therefore the heat flux. However, if simultaneous measurements at different heights are not available, other methods may be used. Sutton *et al.* (1978) derived these values by using wind and temperature measurements at only one height combined with an assumed surface temperature.

The PBL scaling laws also affect the turbulence spectra, i.e. the frequency distribution of wind speed and temperature fluctuations. Turbulence models developed for Earth conditions, scaled to Martian conditions, can successfully reproduce turbulence spectra observed on Mars, in both stable and unstable conditions [Tillman, Landberg, & Larsen, 1994]. However, this work was only done for a few data segments; it would be useful to take further measurements at high temporal frequency (~1 Hz or better) in order to improve further our understanding of turbulence spectra on Mars.

1.6 Data sources for Mars global circulation

1.6.1 Mars Global Circulation Models (MGCMs)

It may seem unusual to put this heading before ‘real’ data sources such as satellite and lander observations. However, much of the detail of our current understanding of Martian atmospheric dynamics is based on results from MGCMs, validated with experimental data. This dominance of modelling data over experimental data has two causes.

Firstly, the dynamics of the Martian atmosphere are quite similar to the dynamics of the Earth’s atmosphere, simplified by the omission of oceans and atmospheric water, but with the added complication of atmospheric dust. This means that the highly developed science of terrestrial general circulation modelling can be readily applied to modelling the circulation of Mars [Forget et al., 1999, Haberle et al., 1999].

Secondly, as will be shown, data on the Martian atmosphere are obtained only rarely, and are often not of sufficiently high resolution to confirm directly the existence of specific atmospheric phenomena.

For example, atmospheric wave behaviour is most easily observed either by considering temporal variation of atmospheric parameters at a single point, or by considering spatial variation of parameters at a single time. Such data can be directly obtained from MGCMs, but not directly from spacecraft observations.

To ensure that the output of MGCMs represents actual conditions on Mars, observational data must be assimilated into the models. It has been shown that data assimilation from a single polar orbiting satellite may be used to reconstruct the thermal state of the atmosphere and indirectly the velocity field, to a reasonable degree of accuracy; and that the quality of such analyses are substantially enhanced by simultaneous surface pressure measurement at even a small number of sites [Lewis et al., 1996;]. This provides an important justification for the measurement of pressure at surface stations on Mars [Haberle & Catling, 1996]. Surface wind data are harder to assimilate into MGCMs than pressure data, because much of surface wind behaviour is governed by local phenomena which are not well modelled in MGCMs. However, high-resolution MGCMs have proved capable of reproducing mesoscale circulations, and thus have recreated observed near-surface winds with some success [e.g. Tyler *et al.*, 2002].

1.6.2 Remote sensing data

Remote sensing data for study of the Martian atmosphere consist mostly of data from Mars satellites rather than Earth-based observations. Earth-based data can provide a useful record during times in which no spacecraft data are available. For example, microwave techniques have been used to monitor inter-annual variation of temperature [Clancy *et al.*, 1990]. Martin & Zurek (1993) have collated a record of dust storms dating back to 1877. However, Earth-based observations provide very poor spatial resolution (returned data are typically averages over the planetary disc), and thus cannot be used to deduce atmospheric circulation.

Global circulation can be inferred if the global temperature field, i.e. temperature as a function of longitude, latitude, altitude, and time, is known. From these data it is then possible to calculate pressure and wind fields by using the thermal wind equations assuming hydrostatic and geostrophic balance (see for example [Salby, 1996]). Atmospheric temperature data can be obtained from a radiometer or spectrometer observing in the thermal infrared. Most Mars orbiters to date have carried such an instrument (a list of Mars missions is included in Table 1.3). Most atmospheric data obtained to date come from three IR sounders: the Mariner 9 Infrared Interferometer Spectrometer (IRIS), the Viking Orbiter Infrared Thermal Mappers (IRTM), and the Mars Global Surveyor Thermal Emission Spectrometer (TES). The IRIS measurements provided temperature profiles up to ~ 45 km altitude, with an accuracy of roughly one scale height (~ 10 km). However, the spatial coverage of IRIS data is erratic due to hardware problems; global coverage was only obtained during a short period during the Northern Hemisphere winter. The IRTM was designed primarily to observe the Martian surface rather than the atmosphere. However, it produced horizontal maps of vertically integrated atmospheric temperature, defined by a weighting function corresponding broadly to the 20 to 35 km altitude range. The IRTM data are of good spatial coverage, and cover a period of several years. The TES, currently in orbit around Mars, is like the IRTM a nadir-viewing instrument designed primarily for surface-observing purposes. The TES returns temperature profiles up to ~40 km, again with vertical resolution no better than one scale height. The global coverage of these data lends itself well to data assimilation into MGCMs [e.g. Houben, 2000]. Better vertical resolution, and temperature data at higher altitudes,

Name	country	Type[†]	Success	Launch / Arrival	Remarks
[unnamed]	USSR	F	×	10.10.60	Launch failure
[unnamed]	USSR	F	×	14.10.60	Launch failure
[unnamed]	USSR	F	×	24.10.62	Failed to leave Earth orbit
Mars 1	USSR	F	×	1.11.62 / 19.6.63	Contact lost in cruise
[unnamed]	USSR	F	×	4.11.62	Failed to leave Earth orbit
Mariner 3	USA	F	×	5.11.64	Solar orbit far from Mars
Mariner 4	USA	F	✓	28.11.64 / 15.7.65	First successful flyby, sent 21 photos
Zond 2	USSR	F	×	30.11.64/15.7.65	No data due to radio failure
Mariner 6	USA	F	✓	24.2.69/30.7.69	Returned 75 photos
Mariner 7	USA	F	✓	27.3.69/4.8.65	Returned 126 photos
[unnamed]	USSR	O	×	27.3.69	Launch failure
[unnamed]	USSR	O	×	14.4.69	Launch failure
Mariner 8	USA	F	×	8.5.71	Launch failure
Kosmos 419	USSR	O/L	×	14.4.71	Failed to leave Earth orbit
Mars 2	USSR	O/L	Partial	19.5.71 / 27.11.71	Lander crashed; some data from orbiter
Mars 3	USSR	O/L	Partial	28.5.71 / 2.12.71	Lander failed after 20 s; some useful data
Mariner 9	USA	O	✓	30.5.71 / 14.11.71	Orbited; ceased operations 27.10.72
Mars 4	USSR	O	×	21.7.73 / 3.74	Missed Mars
Mars 5	USSR	O	Partial	25.7.73 / 2.2.74	Contact lost after 20 orbits
Mars 6	USSR	F/L	Partial	5.8.73 / 3.74	Returned some atmos. data during descent
Mars 7	USSR	F/L	×	9.8.73 / 3.74	Lander missed Mars
Viking 1	USA	O/L	✓	20.8.75 / 19.6.76	Orbiter ceased 8.80; lander ceased 11.82
Viking 2	USA	O/L	✓	9.9.75 / 7.8.76	Orbiter ceased 7.78; lander ceased 12.79
Phobos 1	USSR	O	×	7.7.88	Contact lost in cruise
Phobos 2	USSR	O	Partial	12.7.88 / 29.1.89	Orbited; contact lost 27.3.89 before landing
Mars Observer	USA	O	×	25.9.92 / 24.8.93	Large satellite, lost 3 days before arrival
Mars Global Surveyor	USA	O	✓	11.7.96 / 9.12.97	Currently observing Mars
Mars 96	USSR	O/L	×	11.16.96	Orbiter & landers; Launch failure
Mars Pathfinder	USA	L	✓	12.4.96 / 7.4.97	Rover & base station, lasted 83 sols
Nozomi (Planet B)	Japan	O	(×)	7.4.98 / 9.12.03	Fatally crippled by arrival at Mars in Dec 2003
Mars Climate Orbiter	USA	O	×	11.12.98 / 23.9.99	Would have mapped atmospheric temperature
Mars Polar Lander	USA	L	×	3.1.99 / 3.12.99	Would have examined polar regions
Mars Odyssey ‘01	USA	O	✓	7.4.01 / 24.10.01	Detected high H content (H_2O ice?) in regolith
Mars Express	Europe	O	(✓)	2.6.03 / 25.12.03	European Space Agency’s first Mars mission
Beagle 2	UK	L	(×)	2.6.03 / 25.12.03	Astrobiology lander of Mars Express
Mars Exploration Rovers A and B	USA USA	L L	(✓) (✓)	10.6.03 / 4.1.04 7.7.03 / 25.1.04	Two identical six-wheeled rovers, focussing on mineralogy.
Mars Recon. Orbiter	USA	O		2005	Payload includes atmospheric IR radiometer
Phoenix lander	USA	L		2007	Payload includes atmospheric LIDAR.

[†] F = flyby, O = Orbiter, L = lander

(✓) signifies success/failure since initial thesis submission

Table 1.3 – Spacecraft missions to Mars. The greatest amount of data has been obtained from Viking missions, which returned data and 50000+ pictures over a mission lifetime of more than six years; and from Mars Global Surveyor and Mars Odyssey ‘01, which are both currently in orbit.

will be obtained from Mars Climate Sounder, which is a dedicated atmospheric infrared limb-sounding radiometer due for launch in 2005 on NASA's Mars Reconnaissance Orbiter.

Thousands of temperature profiles have been obtained by radio occultation [see e.g. Hinson *et al.*, 1999; Lindal *et al.*, 1979]. The vertical resolution of these profiles, ~1 km, is much better than that achievable using other remote sensing techniques, but they are only obtained at most twice per orbit, and are irregular in their spatial coverage.

Occasional measurements of wind speed have been made by observing drift of cloud features, both using satellite pictures [e.g. Kahn, 1983] and using Earth-based telescopes [e.g. Mischna *et al.*, 1998]. Wind directions over longer periods of time have been deduced by observation of Aeolian surface features such as dunes, streaks, and the topography of polar caps [e.g. Thomas *et al.*; 1984; Greeley *et al.*, 1992].

Global dust distribution can be usefully measured from orbiter data, either using visual images such as those in Figure 1.1 or in more quantitative detail using infrared spectrometers. Images such as those shown in Figure 1.2 can be used to estimate the frequency of occurrence of dust devils and of dust devil tracks [Balme *et al.*, 2002], both of which can be used to estimate the amount of dust lifted by such events.

1.6.3 Mars Landers

Mars landers can provide atmospheric information both during their descent phase – atmospheric profiles of temperature, pressure, and wind – and once on the surface. Only the surface phase measurements will be discussed here. These records help our understanding of Martian meteorology in several ways. Firstly, the data can be used to study global and mesoscale phenomena, as well as PBL dynamics. Secondly, the data can be assimilated into MGCMs, or can be used as a test of MGCM predictions. Thirdly, the record itself provides useful support for the planning of future missions. Past lander missions will now be described, and scientific results concerning near-surface winds are summarised.

1.6.3.1 Mars landers: Viking

The two Viking Landers (VL-1 and VL-2) were the first man-made craft ever to return data successfully from the Martian surface. A photo of a Viking lander is shown in Figure 1.4. They were generously funded, which had several beneficial results. Firstly, their scientific instruments had been exhaustively researched and calibrated (compare the calibration procedure used for Viking anemometers with that used for later missions, described in Section 2.4.3 below). Secondly, the landers were robust and hardy enough to survive for several Mars years, providing a useful long-term record of surface conditions in all Martian seasons. VL-1 returned meteorological data for 3.3 Mars years, VL-2 for 1.7 Mars years (5.6 and 3.2 Earth years respectively). This may be compared with the mission lifetimes of today's landers: 83 sols for Mars Pathfinder, 90 sols proposed for Mars Polar Lander, 180 sols proposed for the Beagle2 lander (1 sol = 1 Martian day = 1.026 Earth days). (In fairness, modern missions have not had Viking's advantage of using a radioactive source for their heat and power needs. Instead, they have to rely on solar panels, which provide less energy and get obscured over time by dust).

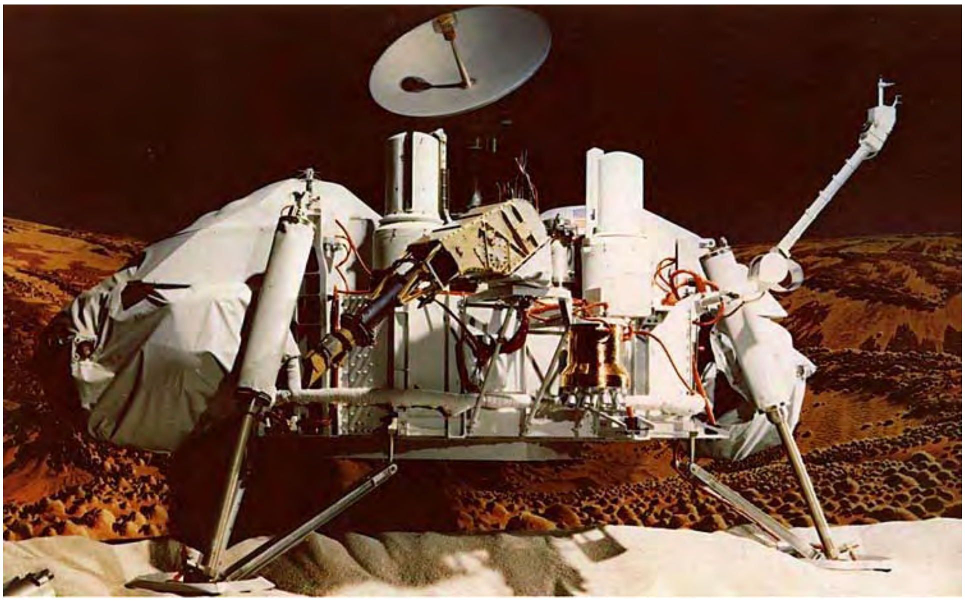

Figure 1.4 – Replica of a Viking Lander. The wind and air temperature sensors can be seen on the end of the boom at right. Photo from NASA’s Planetary Data system http://pds.jpl.nasa.gov

The Viking Meteorological Instrument System (VMIS) included pressure, temperature, and wind speed and direction sensors [Chamberlain *et al*., 1976]. The temperature and wind sensors were made at the end of a boom, 1.6 m above the ground (as can be seen in Figure 1.4). The extensive data set returned by Viking is the basis of much of the current scientific understanding of the lower Martian atmosphere as outlined above.

The atmospheric pressure readings alone provide a wealth of information about the global circulation. Shown in Figure 1.5, the annual record shows a 10% seasonal variation in atmospheric pressure as a result of sublimation and evaporation of CO_2 in the polar regions. The vertical offset between the results from the two landers is due to a difference in altitude between the two. The standard deviation per sol (shown in the top panel of the figure) is largely due to the diurnal and semi-diurnal tides. Unusually high standard deviations were associated with the onset of dust storms. The reader is referred to [Tillman, 1988] for a further discussion of the Viking Lander pressure record.

The wind data at both VL-1 and VL-2 exhibit a diurnal cycle which is largely due to slope winds – this has been recreated through mesoscale modelling [Haberle *et al*. 1993]. A strong semi-diurnal thermal tide was also observed. These diurnal trends can be removed from the data by using a running average over a 24-hour period, allowing study of longer-term meteorological oscillations. An example of such data, reproduced in Figure 1.6, shows regular oscillations with a period of 3-6 days, interpreted as travelling baroclinic waves [Ryan *et al*., 1978]. In another case, Tillman *et al*. (1979) report possible evidence of a frontal system passing over VL-2. Averaging on even longer time scales, Ryan (1985) showed that the prevailing wind direction observed at the VL sites generally agreed with early MGCM predictions.

Temperature and wind data were obtained at sampling rates of up to 1 Hz. These high rate data have been used, as mentioned earlier, to calculate PBL turbulence spectra [Tillman, Landberg & Larsen, 1994]. Viking lander meteorological data provided the first evidence of convective vortices on Mars [Ryan & Lucich, 1983]. Convective vortices appear to have occurred at a rate of roughly 0.6 per sol at

Viking Lander 2 – however, this is based only on the first 60 days of the mission [Ringrose *et al.*, 2003]. The same study also confirmed that dust devils on Mars tend to be larger than on Earth, with diameters ranging from 20 to 400 m.

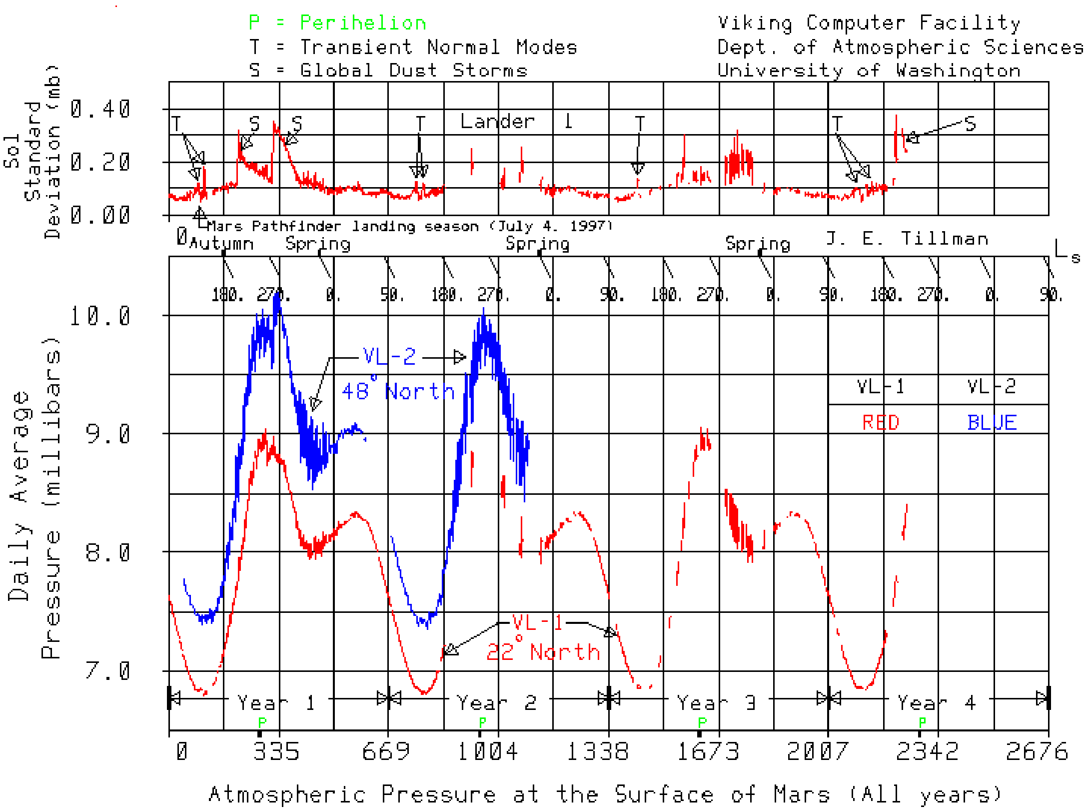

Figure 1.5 – The atmospheric pressure record from the Viking landers. From [Tillman, 1988].

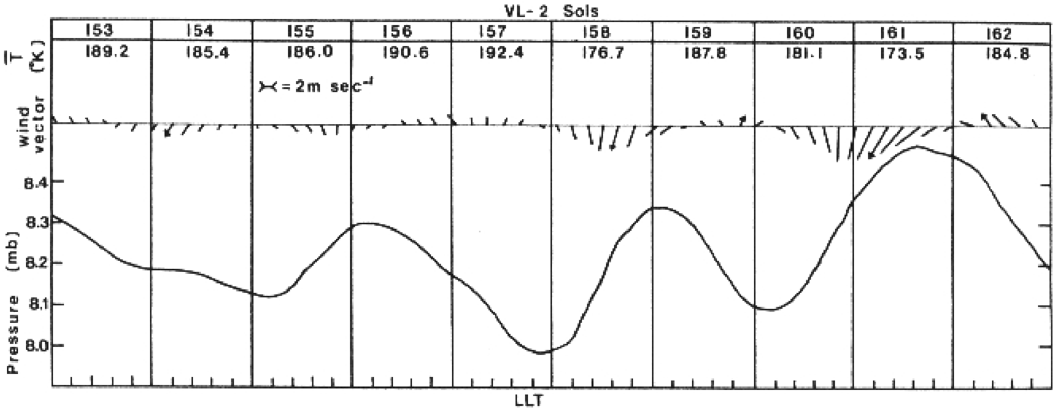

Figure 1.6 – Sample wind and pressure, and temperature data from Viking Lander-2 showing regular oscillations thought to be baroclinic waves. Diurnal and semi-diurnal variations have been removed (using a running average of data spanning 24 hours). From [Ryan *et al.*, 1977].

1.6.3.2 Mars landers: Pathfinder

Mars Pathfinder was an American lander which reached Mars in 1997. It consisted of a small six-wheeled rover and a base station which provided power and telecommunications. The base station also carried a suite of meteorological sensors measuring wind, temperature and pressure [Seiff *et al.*, 1997]. One great addition to Pathfinder's meteorological package (compared with VMIS) was the inclusion of temperature sensors at different heights: at 0.25 m, 0.5 m, and 1.0 m above the lander base. This allowed direct measurements of the often extreme temperature gradients present in the lowest layers of the atmosphere (the temperature difference between the top and bottom sensors was typically ~ 8 K at midday). Air temperature measurements for a single day from Mars Pathfinder are shown in Figure 1.7.

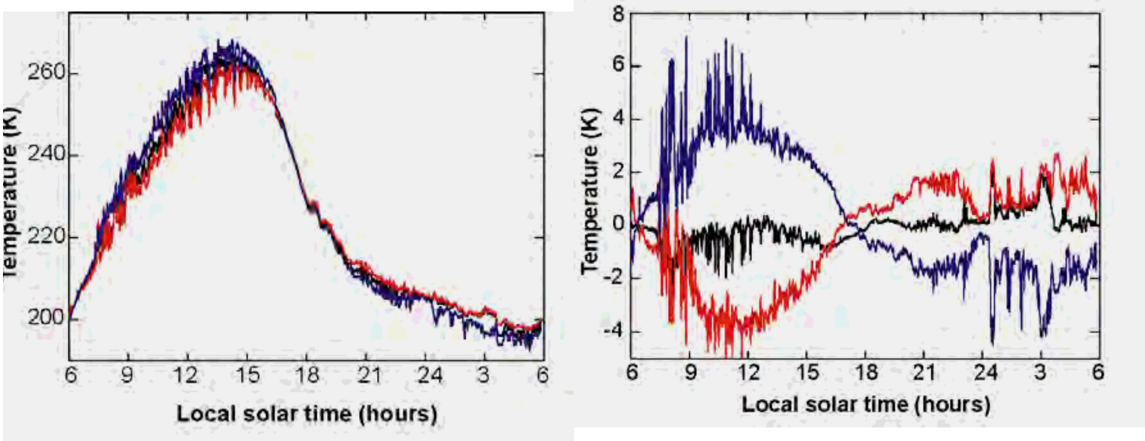

Fig. 1.7 – The diurnal variation of atmospheric temperature measured by the top (red), middle (black), and bottom (blue) thermocouples on the Mars Pathfinder Lander. These thermocouples are respectively 100, 50, and 25 cm above the plane of the lander solar panels. Temperatures are sampled continuously at 4-second intervals throughout this period, but the plots use 30-point (2-min) running means for clarity (the smoothing reduces the amplitude and frequency of the fluctuations that are present in the raw data). The right plot shows the same data, plotted as deviations from the mean of all three thermocouples. Figure copied from [Schofield *et al.*, 1997].

It is worth commenting on this figure, since it contains a wealth of information about the near-surface environment of Mars. It can be seen that the diurnal temperature range is 60 K, much greater than on Earth; this is due to the much lower thermal inertia on Mars. Secondly, the large vertical temperature gradients (up to – 10 K/m at noon) can be seen here. Temperature decreases strongly with height during the day, and increases strongly with height in the night-time. The temperature difference between top and bottom thermocouples is typically ~ 8 K, or more if the raw (un-smoothed) data are examined. Closer examination of the data reveals large temperature fluctuations, with typical magnitudes of 10 K, on timescales of ~ 10 seconds. These short-term fluctuations were sometimes as great as 20 K; this may be partly due to the influence of the heated lander. These rapid variations of temperature have an important influence on wind measurements.

Wind speed data from Pathfinder have not yet been published at time of writing, six years after the end of Pathfinder's mission. The problems with the wind sensor and its calibration will be discussed in following chapters. The lack of published wind speed data has hampered comparison with mesoscale and global circulation models. Such models have however been able to reproduce wind direction and pressure observations from Pathfinder to some extent [Haberle *et al.*, 1999; Lewis 1998]. The

Pathfinder wind data, like that from the Viking landers, are dominated by a large diurnal variation due to boundary layer and mesoscale effects.

Mars Pathfinder returned many suspected observation of dust devils, at a rate of roughly one per sol, though the incompleteness of the data record implies a higher occurrence rate of roughly 2 per sol [Murphy & Nelli, 2002]. The clearest sign of the passage of dust devils was found to be a precipitous drop in air pressure associated with the core, along with a rapid swing in wind direction; an example of this is shown in Figure 1.8 [Schofield *et al.* 1997]. A dust devil was also observed in a photo taken with the Imager for Mars Pathfinder (IMP) camera [Metzger *et al.*, 1999].

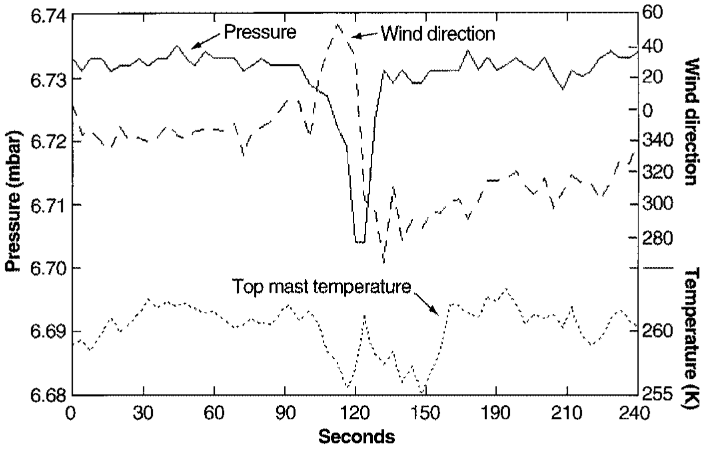

Figure 1.8 – Pressure, wind direction and temperature data from Mars Pathfinder associated with the passage over the sensors of a small convective vortex, or dust devil. The measurements were taken at 4-second intervals. This figure is reproduced from [Schofield *et al.*, 1997].

A limited determination of vertical wind speed profile was obtained using Pathfinder's windsock experiment. Three aluminium 'windsocks' were mounted at heights of 0.25 m, 0.5 m, and 1 m above the lander base. By observing these windsocks using the Imager for Mars Pathfinder (IMP) camera, a very small number of near-surface wind profiles were taken. These wind profiles were used to calculate the aerodynamic roughness (z_0) and the wind friction speed (u_*), both of which are key parameters for PBL scaling laws. However, the data obtained using this method were very limited in number, due both the limited observing time available with the IMP, and to the method's inability to detect wind speeds of less than 7 m s^{-1} [Sullivan *et al.*, 2000].

1.6.3.3 Mars landers: Mars Polar Lander (MPL)

Mars Polar Lander was a NASA-funded mission due to land in the south polar region in late 1999. Unfortunately it was lost during atmospheric entry. Its meteorology package was similar to those described above, with two novel features. Firstly, atmospheric humidity was to be measured using a tuneable diode laser spectrometer. Secondly, temperature and wind measurements were to be made both on a primary mast above the lander, and on a secondary mast deployed downwards from the lander body. This would have allowed more extensive determination of temperature and wind profiles. It should be noted that the primary wind sensor used on the MPL is proposed for re-use on NetLander. This sensor is a combined hot-wire anemometer and thermal wake sensor, and is described in more detail in Section 2.2 below.

1.6.3.4 Mars landers: Beagle 2

The Beagle 2 lander, launched in June 2003, is a small (landed mass ~35 kg) single lander station. The main stated aim of the lander is 'to search for life, or for environments conducive to life’ [Sims *et al.*, 1999]. The payload includes an Environmental Sensors Suite (ESS), which will measure air temperature at two heights, atmospheric pressure, wind speed and direction, saltated grain momentum, UV flux (diffuse and direct at five wavelengths), the total accumulated radiation dose and investigate the nature of the oxidizing environment [Towner *et al.*, 2003]. Wind and temperature sensors are mounted on the end of a jointed, motorised arm, ~ 0.9 m in length, allowing them to be positioned at several locations around the lander body. The design of a wind sensor for this lander represents the major portion of this thesis, and is described in chapters 4 to 7 below.

1.6.3.5 Mars landers: Mars Exploration Rovers

There are two identical Mars Exploration Rovers, MER-A and MER-B. They will land in January 2004, within a month after Beagle 2 lands. The MER Rovers have a smaller science payload than Beagle 2, but a higher data downlink rate thanks to their onboard high-gain antennae. The science payload includes spectrometers and a microscope to examine the rocks, but no dedicated meteorology package. This is presumably because the mobile rovers were not considered a good meteorology platform (unlike Pathfinder, the MER mission will not have a ‘base station’ where a static meteorological mast could be erected, because all communications and power systems are onboard the rover). The payload does include a thermal emission spectrometer (mini-TES) which will periodically be used to take spectra of the sky. This should yield for the first time temperature profiles of the lower atmosphere [Smith *et al.*, 1996], as well as information about dust and water concentrations. However, there seems to be no wind sensor included in the science payload.

1.6.3.6 Mars landers: NetLander

The proposed Mars NetLander project consists of four surface stations carrying identical scientific instruments for seismology and meteorology. Components of the meteorology package include: pressure sensors, temperature sensors at three different levels, and a humidity sensor that is much lower in mass than the MPL sensor [Harri *et al.*, 1995]. The wind sensor proposed for this mission is a hot-wire anemometer / thermal wake sensor whose design is based on that used for MPL, described below in Section 2.4.1 [Crisp, 1998]. At the time of writing, the NetLander mission has been cancelled. However, the wind tunnel described in Chapter 3 was originally intended for testing and calibration of NetLander wind sensors.

A specific aim of the NetLander mission is network science, i.e. the analysis of measurements taken simultaneously at different locations. It has been shown that such a network of surface pressure measurement provides useful insight into global atmospheric waves [Haberle & Catling, 1996]. A similar analysis of wind data is considerably more difficult, because much of wind behaviour is associated with local rather than global circulation.

1.6.3.7 Mars landers: Phoenix lander

At time of writing (2003), NASA has announced funding for a Mars lander in 2007. Called Phoenix, it is to land at high latitudes (roughly 70°N) and will recapture many of the science goals which were to be addressed by Mars Polar Lander and by another cancelled lander in 2001. It includes a digging arm which will dig a trench up to 1 m deep. Its meteorology package will include a LIDAR instrument, which will probe the Martian atmosphere up to an altitude of 20 km. The LIDAR should be able to measure PBL depth, and return information about dust devils, clouds, and fog in the lower atmosphere. The meteorology package also includes a pressure sensor and thermocouples for temperature measurement; thermocouples are probably included at several points along the arm to allow temperature profiles to be obtained. If the mass budget allows, the meteorology package may also measure humidity and wind. It appears that a wind sensor has not yet been chosen for the Phoenix lander: some reports indicate a preference for an ultrasonic anemometer[*], while others indicate a Laser Doppler anemometer[†]. This indecision reflects the current lack of a completely satisfactory wind sensing instrument, which is one of the main motivations for the research in this thesis. Different wind sensing technologies are discussed in detail in the next chapter.

1.7 Wind characterisation to aid mission design

Finally, it should be noted here that near-surface winds are of interest not only to Mars climatologists but also to mission design engineers. After the loss of the Mars Polar Lander Mission in 1999, NASA has become increasingly concerned about uncertainty in atmospheric conditions on Mars for mission safety reasons. For example, the landing site selection of the MER rovers has been greatly constrained by predicted local wind conditions. Winds affect landing strategy in several ways.

Most current landers (such as Pathfinder and Beagle 2) use an entry, descent and landing system (EDLS) based on parachutes and airbags. This is a passive landing system, in that it does not have the capability to correct actively for deviations from nominal trajectory. The lander’s trajectory is therefore modified by winds at all altitudes, leading to an uncertainty of up to 200 km in the landing site. A better knowledge of winds at all altitudes would help reduce the size of this ellipse.

A second constraint which became clear only during extensive testing for the MER rovers is that the airbag landing system is reliably safe only if near-surface wind speeds are under 20 m/s. Mesoscale modelling of several proposed sites revealed unacceptably high winds. For example, proposed landing sites at Melas Chasma and Eos Chasma were ruled out not only because of the roughness of the terrain but also because they were predicted to have very strong canyon winds, i.e. thermal terrain induced flow.

Finally, the EDLS has to cope with vertical winds associated with convection in the PBL. This is especially critical for active landing systems, such as that used on the MER Rovers, which actively control rockets in an attempt to bring the lander to a controlled soft-landing. The lander in this case is very sensitive to vertical winds, whether caused by mechanical turbulence or by convection. We have to date no measurements of vertical wind speeds from Mars, vertical wind speeds have to be estimated using analytical models of PBL turbulence.

---

[*] Private communications with Nilton Renno, U. of Michigan; and Richard Dissly, Ball Aerospace, USA.

[†] Quoted on a Phoenix project webpage: http://phoenix.lpl.arizona.edu/mars_environmental_compatibility.htm

Chapter 2 - Anemometry techniques

In this chapter I present a brief review of anemometry techniques, with a focus on their suitability for use on Mars. The order in which these are discussed reflects roughly how often they are used on Earth. Dynamic pressure devices are reviewed first, followed by a detailed discussion on thermal anemometers focussing especially on past Mars anemometers and their strengths and weaknesses. Finally I will discuss developments in ultrasonic, laser Doppler, and ionic anemometry relevant to use on Mars.

For an introduction to wind measurement techniques with applicability to use on Mars landers see [Henry & Greene, 1974].

2.1 Dynamic pressure devices

Most anemometers used on earth rely on the dynamic pressure of moving air. Such devices include windsocks and turbines as well as the ubiquitous rotating-cup anemometers (shown in Figure 2.1). Alternatively, dynamic pressure is often measured directly using a differential pressure sensor connected to a pitot tube. The dynamic pressure exerted by a moving fluid is given by $p_{dyn} = ½\,\rho u^2$, where ρ and u represent respectively the density and velocity of the fluid. It can immediately be seen that the dynamic pressure associated with Martian winds will be two orders of magnitude smaller than on earth due to the low Martian pressure. In Martian conditions (CO_2 at p = 7 mbar and T = 250 K), wind speeds of 1 to 36 m/s will give rise to dynamic pressures of only 10^{-2} to 10^{1} Pa.

To give an indication of the difficulty of sensing a force this small, the wind-induced force on a sensing area of 1 cm^2 would be equivalent to the weight of only 10^{-4} to 10^{-1} grams for the wind speeds of 1 to 36 m/s. It is difficult to build a dynamic pressure device which will be sensitive to Martian winds, while still being small enough for spaceflight and robust enough to withstand the mechanical loads of launch and landing.

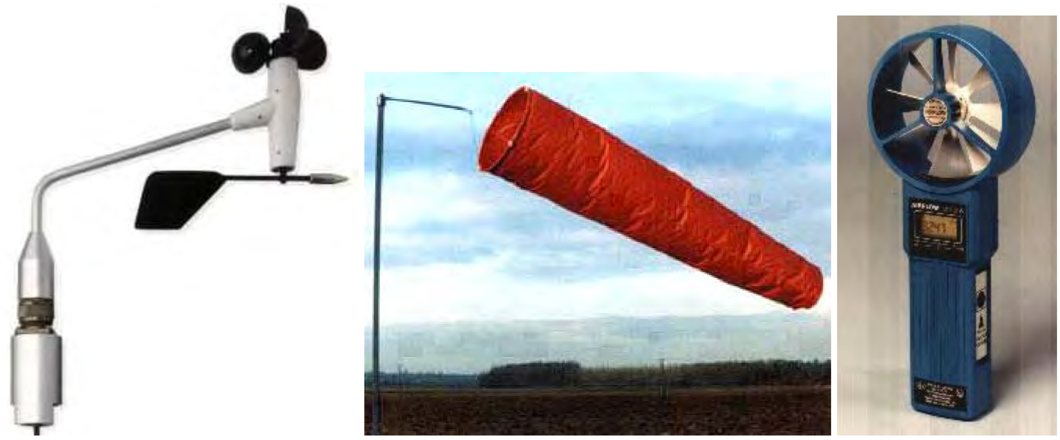

Figure 2.1 – Several types of anemometers used on Earth which rely on the dynamic pressure exerted by wind. From left to right: a cup-and vane anemometer, a windsock, and a rotating vane anemometer. Pictures left-right are from Schiltknecht Messtechnik (Switzerland); The Flight Store (UK); and Airflow Technical Products (UK).

The possibility of using a dynamic pressure device for Beagle 2 was considered. Ideally one would like to use a compact off-the-shelf silicon differential pressure sensor. However, the most sensitive commercially available such device[*] has a maximum range of only 0-100 Pa, with an accuracy of < 0.5 Pa. This is clearly not sensitive enough for Martian anemometry.

The most sensitive commercial differential pressure sensor available at time of writing[†] has a range of 0-20 Pa, with a nominal resolution of 10^{-3} Pa. As discussed in the next chapter, this will be used to calibrate a wind tunnel used for wind sensor calibration on Earth. The Earth version is a large assembly, weighing 0.5 kg and consisting of many discrete components on a circuit board measuring 120 x 80 mm. It might be possible to make a space-ready sensor based around this sensor's diaphragm (~30 mm diameter), but this would take a lot of development work. For example, it might prove very difficult to make this sensor retain its calibration through the vibration loads of launch, and the shock of landing. Another problem with the use of such a sensor would be how to mount it to provide a good wind measurement and yet remain protected from Martian dust. Adding to the mass implications of using such a sensor, one must also remember that a single sensor would provide only one component of wind direction, so two would be required in order to provide a two-dimensional wind vector.

Three small aluminium 'windsocks' were included on the Mars Pathfinder lander meteorological boom. The windsock experiment is shown in Figure 2.2. The windsocks were mounted at different heights (0.53 m, 0.82 m, and 1.12 m above ground) in order to return information about the near-surface wind profile [Sullivan *et al*, 2000]. However, this experiment returned only a few wind readings (data have been published for a total of 30 individual wind measurements out of the whole mission). This was mainly because the windsocks only moved measurably when wind speeds exceeded ~7 m/s. It should also be noted that the data return was low because each reading of the windsocks required a picture from the lander's camera, requiring significant data downlink bandwidth.

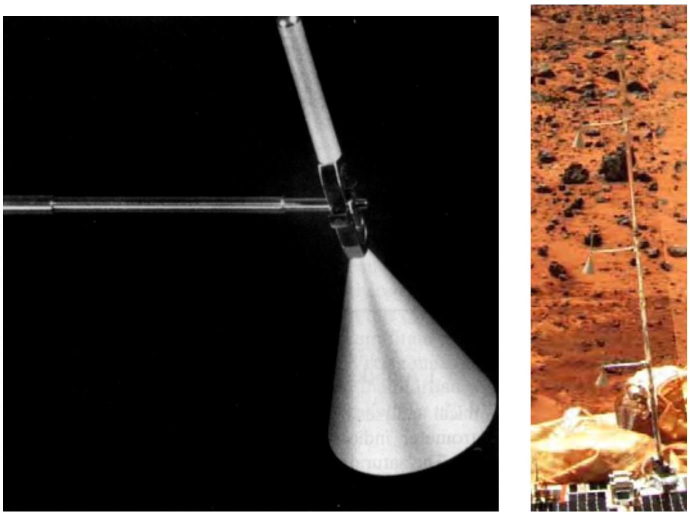

Figure 2.2 – The Mars windsock experiment on Mars Pathfinder; a) a single windsock, b) the windsock mast on Mars. From the NASA Planetary Data System (http://pds.jpl.nasa.gov).

---

[*] SensorTechnics 144LP01D-PCB. http://www.sensortechnics.com/download/144lp-004.pdf

[†] Furness Controls FCO332. http://www.furness-controls.com/datasheets/fco332.pdf

2.2 Thermal anemometry

Hot-wire anemometry is a well-established technique for measurement of flow speed [e.g. Bruun 1995, Lekakis 1996]. A thin wire is positioned in a free flowing fluid (in this case, the atmosphere). It is heated by dissipating electrical energy in it (Joule heating). This excess heat is then lost to the surrounding air, by a combination of convection (to the surrounding air), conduction (to the support of the hot wire), and radiation (to the visible surroundings). The temperature of the wire is determined by measuring the resistance of the wire. The ambient temperature is measured independently by a separate temperature sensor. Using these two pieces of information, one can calculate the heat transfer coefficient. The convective heat transfer, h_{conv}, is sensitively dependent on the wind speed, u. An empirical formulation often used is $h \sim u^n$, where the best fit to empirical data is often found by setting $n = 0.5$ (King's law). However, there is no one analytical solution for this relationship, largely because of the non-linear effect of flow separation on the downstream side of the wire.

Hot-wire anemometers are typically either run in a constant-power mode, in which the heating power is kept constant, or in a constant temperature mode, in which the power is continuously varied to maintain a constant wire temperature. This is usually done using the simple circuit shown in Figure 2.3, in which a feedback circuit is used to ensure that the hot wire maintains a constant resistance, which corresponds to a constant temperature. The constant-temperature mode is the one usually used on Earth, mainly because it allows an extremely fast response time, although this advantage is somewhat diminished in a non-isothermal environment such as the Martian daytime atmosphere. The CTA mode was used for the Viking, Mars Polar Lander and NetLander anemometers for its high frequency response and because it reduces power consumption in low wind conditions, while still providing measurable signal at high wind speeds [Crisp, 1998]. The *overheat*, i.e. the temperature difference between the wire and ambient, must be quite large (typically ~100 K) in order to minimise uncertainties due to the rapid fluctuations in air temperature of 10-20 K often encountered near the Martian surface [Schofield *et al*. 1997].

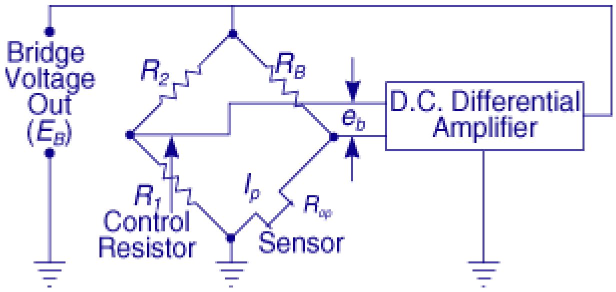

Figure 2.3 – Constant Temperature Anemometer (CTA) circuit traditionally used for hot wire anemometry. Picture from Dantec measurement and Technology, http://www.dantecmt.com

Note that a simple hot-wire anemometer gives wind *speed* information, but no wind *direction* information. In order to measure wind direction, the technique used in previous missions (notably the Viking Landers and Mars Polar Lander) has been a thermal wake technique. A central hot wire or hot cylinder is placed in a vertical orientation. This central element is then surrounded by an array of temperature-sensing devices, typically thin-wire thermocouples. The sensors downwind of the central heated element register a higher temperature than those mounted upwind of the central element, allowing determination of wind direction.

The wind sensor proposed for use on Mars NetLander is shown schematically in Figure 2.4. In the centre of the sensor is a hot wire element, which actually consists of two wires for redundancy, twisted together for strength. Surrounding the central wire at a radius of 5 mm are twelve equally spaced thermocouple arrays. The multiple thermocouples in each array provide redundancy. Thus the central wire acts as a normal hot-wire anemometer, with an estimated accuracy of 'better than ±10%' for wind speed measurement. The eight temperature sensors provide a measurement of wind direction to an accuracy of 'better than ±15°' [Crisp, 2002].

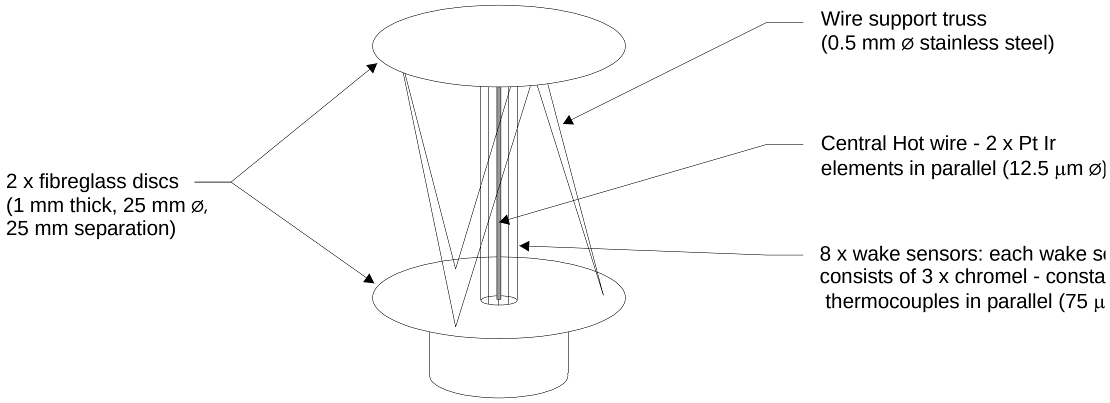

Figure 2.4 – Hot-wire anemometer / wake sensor as proposed for use on NetLander. Based on description given in [Crisp, 1998].

Advantages of hot-wire anemometry on Mars include the sensor's simplicity, low mass, low power requirements, compactness and lack of moving parts [Henry & Greene, 1974]. Not to be overlooked is the technique's proven flight record in past Mars missions. However, the disadvantages are numerous. Firstly, the calibration is of critical importance – one cannot form a purely analytical solution for sensor response. Secondly, the sensor calibration can drift with time as the resistance of the wire either increases (due to erosion by windblown dust) or decreases (due to accretion of electrically conductive dust). Thirdly, a sensor such as the MPL/NetLander is difficult to construct, involving dozens of extremely thin wires and many separate electrical connections. A fourth disadvantage of thermal anemometry is that a variation in ambient temperature can produce the same signal as a variation in wind speed; therefore the accuracy of the wind speed measurement is crucially dependent on the accuracy of the temperature sensor. Though it is fairly straightforward to measure air temperature accurately in stable conditions, it becomes more difficult in rapidly varying temperatures in a low-pressure environment, as is the case on Mars. If the desired sampling frequency is, for example, 1 Hz, both the wind and air temperature sensors should ideally have a response time of less than 1 second. If this is not possible, they should at least be exactly matched to have an identical response time.

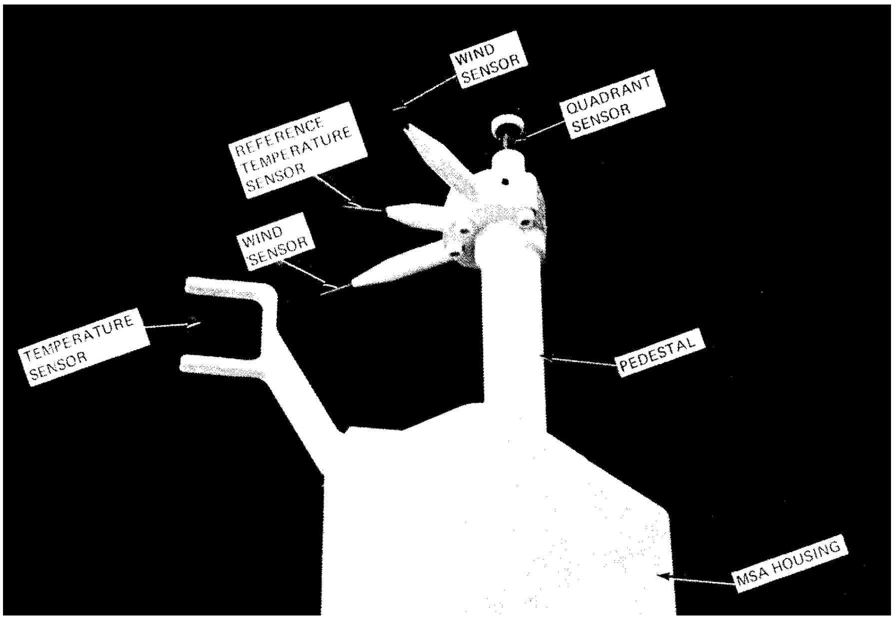

Figure 2.5 – Wind sensor assembly as used on Viking Landers 1 & 2. The wind speed measurement comes from two cylindrical hot films oriented at right angles to another. A reference air temperature measurement is made using an identical hot film located between the two hot films. A quadrant sensor at the top of the assembly provides wind direction. Finally, a separate air temperature measurement is made using a thin wire thermocouple. From [Chamberlain *et al.*, 1976].

This second approach was used for the Viking Lander wind speed sensor. The sensing element of both the wind and air temperature sensors was a platinum film coating on the outside of a quartz cylinder, 0.5 mm diameter x 15 mm long (the film itself was 10 mm long). Two of the wind sensors were used, at right angles to each other, each measuring orthogonal horizontal components of the wind speed[*]. A third identical film located between the two hot films was used as a reference air temperature sensor for the hot films. The films were operated in constant temperature overheat mode, so were always 100°C above the temperature measured by the third film. To determine the *sign* of each wind vector, i.e. the wind *direction*, there was additionally a thermal wake sensor as described above, called a quadrant sensor. Finally, a parallel array of thin wire thermocouples was included to provide an air temperature measurement with a fast response time. The complete assembly is shown in Figure 2.5 [Chamberlain *et al.*, 1976].

In addition to the Viking wind speed and direction sensors, there has been one other thermal wind sensor which has returned data from Mars: the wind sensor for Pathfinder, shown in Figure 2.6. This consisted of an unheated cylinder, 27 mm in diameter, surrounded by six hot wire anemometers. Each hot wire element was only 3 mm from the surface of the cylinder. The wind *speed* was determined

---

[*] Each cylindrical hot film measured the component of wind speed which was perpendicular to the axis of the cylinder. Each sensor was therefore sensitive to vertical winds as well. Because vertical winds are usually smaller than horizontal winds, it was assumed that the vertical wind was negligibly small in all cases. This is not the case during convective vortex events, at which time vertical winds can introduce an error in the deduced horizontal wind speeds; this error has been estimated to be up to 18% [Ringrose *et al.*, 2003].

from the average of all the wire temperatures; *differences* between wire temperatures were then used to find the wind direction [Seiff *et al.*, 1997].

A plot of the overheat ($T_{film} - T_{air}$) of a single hot element as a function of wind speed and direction is shown in Figure 2.7. It can be seen that the maximum cooling occurs not when the hot element faces directly upstream, but rather when it faces at about 50° to the upstream direction. This is because the local flow velocity past the wire is fastest at this point, whereas flow is slower at the upstream face of the cylinder. This 'double-peaked' dependence on wind speed is characteristic for the convective heat transfer coefficient from an isolated heated element on the face of a cylinder, and will be seen again later in this thesis.

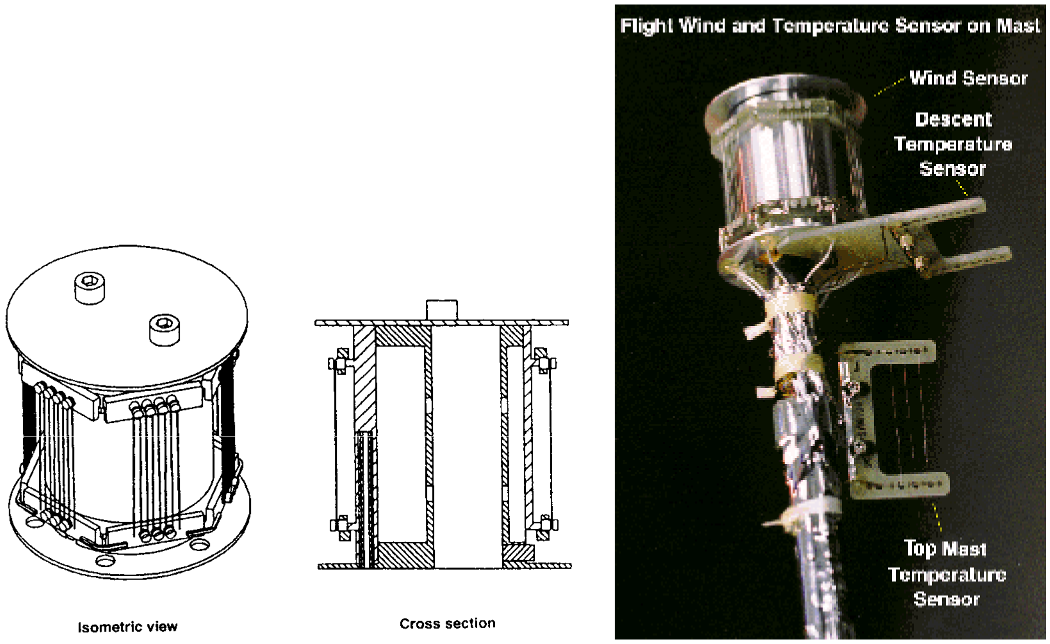

Figure 2.6 – These pictures show the Mars Pathfinder wind sensor. A central cylinder is surrounded by six arrays of hot wires. The wind speed is determined from the average overheat of all the wires. The two left figures are from [Seiff *et al* 1997], the photo at right is from the NASA Planetary Data System (http://pds.jpl.nasa.gov).

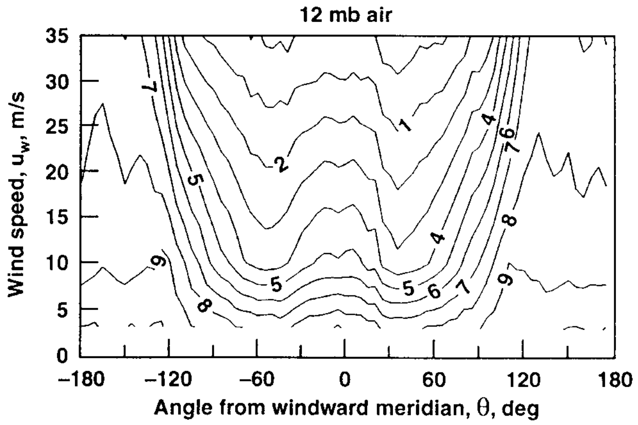

Figure 2.7 – Calibration chart for the Pathfinder wind sensor. This plot shows contours of constant overheat ($T_{wire} - T_{air}$) for a single hot element as a function of wind speed and direction. Figure from [Seiff *et al.*, 1997].

Wind speed data have not yet been published for Pathfinder (at time of writing, 5 years after the end of the mission). This is due to a few different causes. Firstly, as can be seen in Figure 2.7, a very low temperature overheat (i.e. $T_{wire} - T_{air}$) was used, of only 1-10 ˚C (depending on wind speed). This is not larger than the fluctuations in air temperature at midday on Mars. This low overheat requires that T_{wire} and T_{air} be known very accurately in order to extract useful wind data. However, the hot wires were very close to the large cylinder. Therefore, the wires were sometimes inside the thermal boundary layer surrounding the cylinder, sometimes outside (typically the upstream wires might be outside the thermal boundary layer while the downstream wires were inside it). This led to an uncertainty in the local temperature at each hot wire of up to several degrees. A larger overheat, such as the 100 K overheat used on Viking, would have greatly reduced the impact of this uncertainty.

The Pathfinder wind sensor also suffered from inadequate calibration. The facilities used to calibrate this wind sensor are discussed in the next chapter. For the present discussion it suffices to say that they suffered from turbulent fluctuations in both speed and temperature, and were only available to the Pathfinder wind sensor team for very limited periods of time. Evidence for the first of these assertions can be seen in the fluctuations in the data of Figure 2.7, which were obtained during the wind sensor calibration.

Many variants of thermal anemometry have been developed for use on Earth. Hot films may be used instead of hot wires, to provide a more robust sensor. One particular hot film sensor will be mentioned here, for it shall prove relevant to the Beagle 2 wind sensor design. Manufactured by Dantec Measurement & Technology of Denmark, the ‘triple-split fibre’ probe was designed to measure a two-dimensional air flow vector. It consists of three U-shaped films deposited on the surface of a 400 µm diameter quartz fibre, as shown in Figure 2.8. Each film is separately driven in constant-temperature overheat mode. As for Pathfinder, wind speed can be calculated from the average power required by the three films, while wind direction is obtained from the differences in heat transfer coefficients between the films [Jørgensen, 1982]. The entire probe is coated with a quartz coating, 0.5 µm in thickness, for extra durability. At only 0.4 mm diameter x 4 mm long, this sensor head represents an impressively compact and robust solution for measurement of a two-dimensional wind vector.

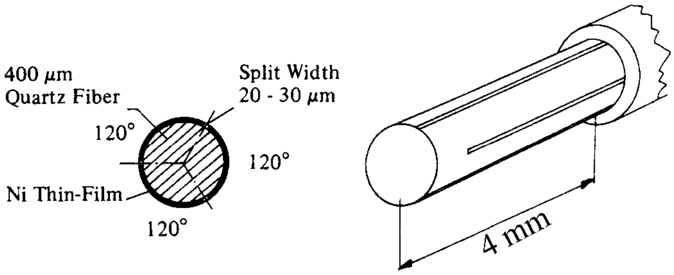

Figure 2.8 – Triple-split fibre probe for hot-film anemometry, manufactured commercially by Dantec Measurement & Control. Figure from [Jørgensen, 1980]

Further miniaturisation of thermal anemometry is possible using micro-machined silicon structures, reviewed in [Nguyen, 1997]. Such sensors seem attractive for space purposes due to their very small mass and energy requirements. Furthermore, they typically have a very fast response time due to their small size. However, a complication arises because these sensors will not be measuring the true free stream velocity, but rather the boundary layer behaviour above the film. As was seen above for the Pathfinder sensor, this leaves an uncertainty in the *local* temperature and gas behaviour next to the hot film, and in the relation of the *local* gas properties to the *free-stream* properties. This is more of a problem in the low-density Martian atmosphere, where the thermal boundary layer grows much more rapidly than on Earth. The scale of these micro-electronic sensors is similar to the mean free path length in the Martian atmosphere (~ 6 μm), so the fluid can no longer be treated as a continuum. The mass, power and response time advantages of such micro-thermal sensors are attractive enough to justify evaluation testing in low-density flows.

2.3 Ultrasonic anemometry

Various ultrasonic techniques are used for anemometry on earth. The technique used most often is simple time-of flight sensing. A pulse is sent from one ultrasonic transceiver to a second one, and then another one is sent in the reverse direction; the time of flight in each case is recorded. The difference between these two measurements gives the component of wind velocity in the direction of the transceiver pair, while the average of the two gives the speed of sound, which is dependent primarily on temperature[*]. Thus an ultrasonic sensor returns *simultaneous* and *independent* measurements of wind speed and temperature. Two or three orthogonal pairs of transceivers permit determination of a 2-D or 3-D wind vector.

The independence of the wind and temperature measurements gained from an ultrasonic anemometer is particularly attractive on Mars, given the large and rapid temperature fluctuations in the PBL. The time-of-flight measurement principle of the anemometer is in principle very robust and immune to drift; if the position of the transceivers and the operating frequency are well known, the wind speed can be calculated independently of gas temperature and composition. This is in stark contrast to thermal anemometers, for which the calibration need always be empirically determined for each new sensor constructed. Another strength of ultrasonic anemometry is its ability to operate at high measurement frequency (up to 100 Hz). However, ultrasonic anemometry is difficult on Mars because of its rarefied atmosphere. To get a sufficiently great sound signal in the low density air requires a large amount of power, which has in the past hindered attempts to build an ultrasonic Martian anemometer.

The anemometer originally proposed for use on the Beagle2 mission, developed commercially for use on Earth by the UK-based company FT Technologies Ltd [Kapartis & Strachan, 1999] in collaboration with the Space Sciences Department of the University of Kent at Canterbury (UKC), has reduced

---

[*] The speed of sound $v_s = \sqrt{\frac{\gamma RT}{m}}$. where *m, R, T,* and *γ* represent respectively the molar mass, temperature and specific heat ratio of the gas, and *R* is the universal gas constant 8.31 J mol^{-1} K^{-1}. Ultrasonic anemometers thus return a measurement of $\gamma T/m$. On Earth, an additional uncertainty is introduced by varying humidity, which can significantly affect the average molar mass. On Mars, however, this is not a problem due to the extremely low concentrations of water.

power consumption using an ingenious new approach. As this is a promising Mars wind sensor technology, it is described here in detail.

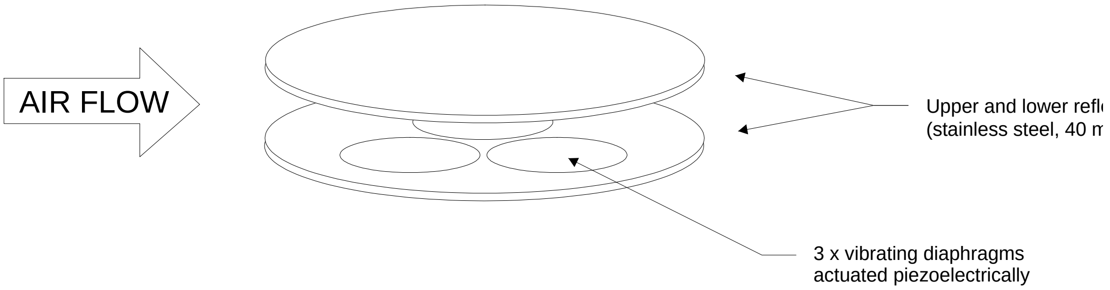

Figure 2.9 – Ultrasonic Resonance Anemometer (URA) as proposed for use on Beagle 2. After [Kapartis & Strachan,1999].

The FT Tech wind sensor, shown in Figure 2.9, consists of two horizontal circular plates separated by a few millimetres. Wind is free to pass through the space formed between these plates from any direction. In the bottom plate are located three vibrating diaphragms that are each driven using their own piezoelectric element. The diaphragms are located in an equilateral triangle as can be seen in Figure 2.9. The diaphragms are electrically excited one at a time, in turn. This excites a complex wave pattern between the two plates, which behaves ‘like a superposition of a vertical quasi-standing wave and a horizontal two-dimensional radial travelling wave’ [Kapartis & Strachan, 1999]. The frequency at which the device operates is constantly adjusted to maintain resonance. In so doing, the anemometer returns a measurement of the speed of sound, and thus of air temperature. Meanwhile, the time-of-flight measurement between each diaphragm pair allows calculation of a one-dimensional wind vector. By combining measurements from different diaphragm pairs a two-dimensional wind vector is obtained. Operation at the cavity’s resonant frequency, and use of fairly large diaphragms, allows for significant reductions in operating power compared with conventional ultrasonic anemometers.

The proposed sensor had an impressive specification, with a mass of 35 g and using 250 mW of power. In testing, the off-the-shelf Earth version of the sensor apparently continued to operate at pressures down to ~15 mbar; below this pressure the electronics started picking up a structural resonance rather than an acoustic signal transmitted through the air. A feasibility study eventually showed that with some modification the sensor had been demonstrated to work at 4 mbar. However, the development of this device for the Beagle 2 lander was cancelled at this stage due to funding difficulties.

Given the advantages outlined above, as well as the preliminary development work which has been done, this sensor may be viable for future missions. A feasibility study of this sensor is suggested as a promising area for future research.

One particular issue which needs further study is the accuracy of the air temperature measurement made with this instrument. In the rarefied Martian atmosphere, the thermal boundary layer near the surfaces of the device would grow very quickly. Therefore the air temperature measurement might reflect the temperature of the sensor rather than that of the ‘free stream’ air flow. If this proved to present a problem, however, thin-wire thermocouples could be used to provide a reference air temperature measurement.

It should be noted that careful measurement of acoustic propagation and attenuation can also be used to evaluate gas parameters such as viscosity, thermal conductivity, specific heat ratio and water vapour content. An acoustic sensor based on this principle is proposed in [Farrelly *et al.* (2001)] for use on Mars. Though it yields no information on local winds, the information from such a sensor would add to our knowledge of the near-surface atmospheric properties and thus would complement data from wind sensors.

2.4 Ion drift anemometry

The principle of ion drift anemometry is to ionize a small amount of gas, and then to measure its drift due to local wind. On earth, ionization of gas is often achieved by applying voltages of several kV to achieve coronal discharge (see e.g. [Barat 1982]). This has mass implications, as the high voltage power supplies required may be prohibitively heavy for inclusion on Mars spacecraft. Evlanov *et al.* (2001) reduce the voltage required for discharge to ~ 500 V by using a weak β-emitting anode. Their anemometer, developed for the ill-fated Russian Mars-96 mission, is shown in Figure 2.10. Electrons are accelerated from the anode (1) to the cathode (2). Some of these ions escape through a small hole in the centre of the cathode into the central chamber. This ion beam passing through the chamber is then deflected sideways by wind before being sensed by electrodes in the bottom surface of the chamber (6). For scale, the cylindrical central chamber (II) has a height of $l = 2$ cm and diameter $2R_0 = 4$ cm. The complete device, including power supplies, weighs 0.1 kg, and requires only 200 mW of power from the spacecraft. Their sensor appears to exhibit good performance in Martian conditions, although the one paper describing their work readily available in the West [Evlanov *et al.*, 2001] does not include much performance data.

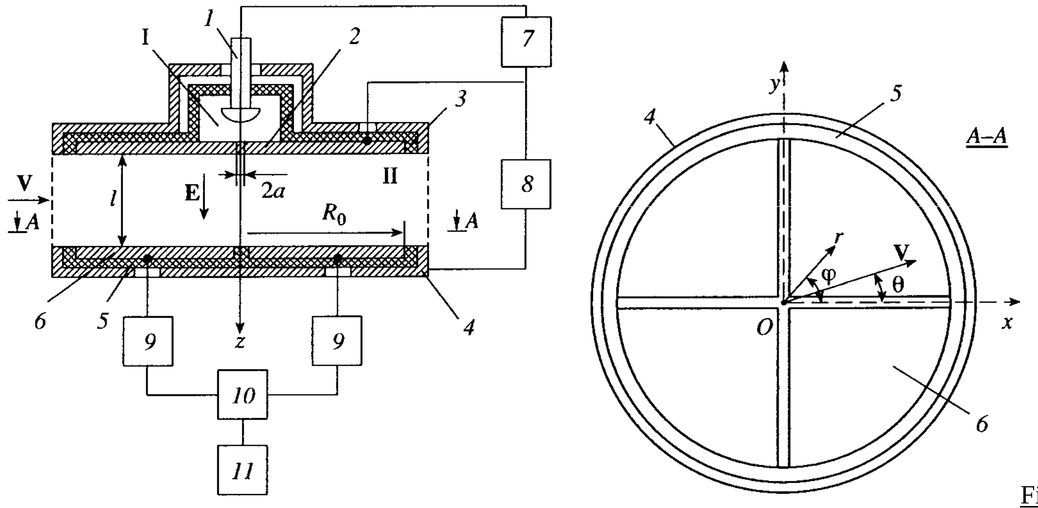

Fi

Figure 2.10 – Ion drift anemometer designed for Mars-96 mission; section view on left, plan view on right. For scale, the cylindrical central chamber (II) has a height of $l = 2$ cm and diameter $2R_0 = 4$ cm. See text for description. Diagrams reproduced from [Evlanov *et al*, 2001].

This ionic anemometer was flown on the Mars-96 mission, so represents the only flight-ready non-thermal anemometer for Mars. Development of an ionic anemometer was however considered impractical for the present PhD work due both to its use of a radioactive anode and to the intricacy of the design.

2.5 Laser Doppler anemometry

Both the ionic and the ultrasonic sensors described above have the same geometry in that the wind is forced to pass through a cylindrical space between two circular plates. This can be problematic on Mars, as the thermal boundary layer next to any surface grows very rapidly due to the large mean free path length between collisions. Therefore there is some uncertainty as to what the gas temperature of the gas at the centre of the wind sensor is. The solution to this problem is to conduct measurements away from any surfaces.

Laser Doppler Anemometry (LDA) is a non-intrusive method of accurately measuring particle velocity in a small probe volume located at a distance from the optical elements. Commercially available LDA instruments have been successfully used for particle sizing as well as the measurement of fluid flows in wind tunnels and water tunnels. The most common technique is *backscatter* LDA, in which the receiving optics are co-located with the transmitting optics; this is evidently advantageous for use on Mars.

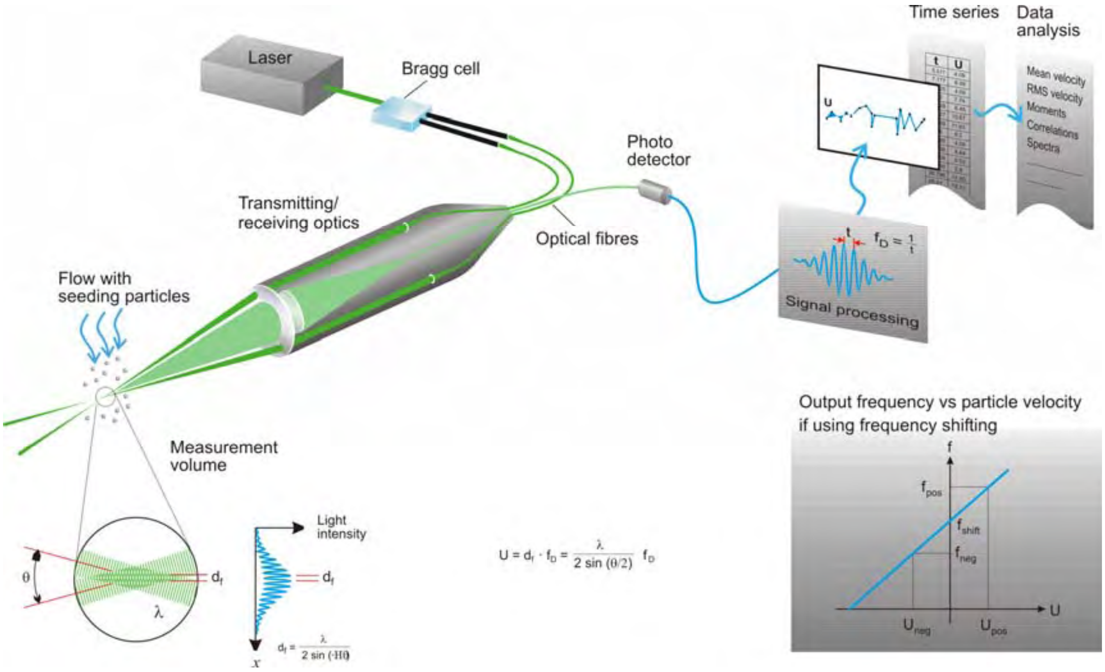

Figure 2.11 – Sketch illustrating the principle of backscatter Laser Doppler Anemometry (LDA). This diagram is copied from material provided by Dantec Measurement and Technology, http://www.dantecmt.com

Figure 2.11 illustrates the principle of backscatter Laser Doppler Anemometry. Intersecting coherent light waves form a standing wave at the probe position causing an interference fringe pattern. The light scattered from a particle passing through this volume is sensed by a photo-detector. If the particle is moving through the volume, the backscattered light fluctuates in brightness as the particle moves through the interference fringes (let us call this the *x*-direction). The frequency of this fluctuation sensed at the photodetector is linearly proportional to the speed of the particle. As a result of the linearity of the measurement, the instrument does not require on-site calibration and is relatively insensitive to changes in atmospheric pressure, air temperature, or dust loading.

The technique as described in the last paragraph is not direction-sensitive; a particle travelling backwards causes the same signal as one travelling forwards. This can be circumvented by introducing a phase shift into one of the intersecting laser beams, using a rotating grating or a Bragg cell*. This causes the interference pattern in the probe volume to move constantly in the x-direction. As a result, it is possible to distinguish between a particle moving in the negative and positive x directions, as illustrated by the graph in lower right-hand corner of Figure 2.11. However, using this phase shift technique requires adding extra optical components, and requires either a signal generator for the Bragg cell (typically running at ~10^2 kHz) or a rapidly rotating grating – these complications might be difficult to implement for a sensor on Mars.

A second beam can be added to provide a measurement of particle size. This would be scientifically very useful on Mars as it would provide more information about the size distribution of suspended dust particles.

A miniature LDA system has been designed with Mars missions in mind [Modaress *et al.*, 2002]. Its detector head, including the laser diode light source, a rotating grating to provide frequency shifting, and receiver optics, measures only 25 mm diameter x 50 mm long, yet achieves a stated 0.3% accuracy. This physical size is still quite large for a Mars mission, especially since three of these would have to be included in order to measure three components of wind velocity, and a sophisticated signal processing electronics package would be required as well. The same research group has been developing a much smaller ‘micro-LDA’ system, which aims to incorporate a laser diode and all the optical elements on a single chip [Modaress *et al.*, 2002]. This would enable, in principle, all the optical elements to be contained within a square mm or so. This compact sensor does not allow directional sensing, so a full implementation of this for meteorology would require a separate method of determining the sign of the different components of wind direction, perhaps a hot-wire device like the quadrant sensor on the Viking landers or perhaps a micro-machined silicon version of this.

The miniaturisation potential of LDA sensors combined with their high accuracy, absolute calibration and temperature independence make LDA a clear favourite for wind measurement on Mars in the long term. However, considerable development work is yet required to develop a LDA system mature enough for inclusion on a Mars lander.

2.6 Conclusions

Many techniques can be used to measure wind speed and direction. Anemometers measuring the dynamic pressure exerted by the wind, such as most anemometers used on Earth, are very difficult to adapt for use on Mars because the Martian atmosphere is two orders of magnitude less dense than that of the Earth. Past Mars missions have used hot-wire or hot-film anemometers because of their

---

[*] In a Bragg cell, the laser beam is passed through a piezoelectric crystal which is being stimulated at a frequency f_s. The beam is then split into two components, with frequencies f and $f + f_s$.

simplicity of construction and low mass. However, thermal anemometry has the inescapable disadvantage that it is very sensitive to variations in air temperature, which is especially critical on Mars. Also, the accuracy of thermal anemometers is limited by the accuracy of their calibration, because their calibration must be entirely empirical.

Ultrasonic, ion drift, and laser Doppler anemometers are immune to the sensitive dependence on air temperature which plagues thermal anemometry. Ultrasonic anemometry needs only a little more development before it is ready for use on Mars missions. In the long term, though, laser Doppler anemometry shows the most potential because it may allow extreme miniaturisation, because it allows a ‘remote’ measurement which better represents free stream velocity, and because it has a robust, stable, temperature independent calibration. The ion drift anemometer, though developed to a flight-ready form in Russia, is mechanically very intricate, requires a high voltage power supply and requires a radioactive anode. In the meantime, then, thermal anemometry remains the most viable option for current Mars missions.

Chapter 3 - Mars Environment Wind Tunnel

A wind tunnel facility was designed and constructed in order to test and calibrate different anemometers under Martian conditions. In this chapter I first review previous and current Mars wind tunnels, noting their advantages and disadvantages for the purpose of wind sensor testing and calibration. In the light of this background, the design of the present facility is presented. The design of different subsystems of the wind tunnel is then explained in detail, and validated with experimental data.

3.1 Background: other Mars wind tunnels

3.1.1 Rotating arm

A rotating arm is perhaps the oldest form of wind testing facility, and is still used today thanks to its simplicity and low cost. A rotating arm facility is not, strictly speaking, a wind tunnel; it relies on moving the test piece (in this case a wind sensor) through the fluid medium, rather than moving the medium past the test piece. The test piece is affixed to an arm, which is then rotated such that the test piece moves through the medium with a known velocity. An example is shown schematically in Figure 3.1a. The arm assembly is enclosed within a chamber containing gas with the desired composition, pressure, and temperature. The main drawback to this technique stems from the assumption that the gas is at rest. The rotating arm acts as a paddle in the chamber, causing a circular flow in the direction of movement of the paddle (leading to a systematic error in air speed) as well as turbulent eddies in the chamber (leading to fluctuations in the true air speed past the sensor). Both of these sources of error increase with increasing rotation speed. The maximum speed obtainable with a rotating arm facility is also limited by mechanical concerns, especially the vibrations caused by rapid rotation rates (≥ 1 revolution per second). The current Mars wind sensor test facility at NASA’s Jet Propulsion Laboratory (JPL) uses a rotating arm with a length of 1 m, rotating in a 3 m diameter chamber. Speeds obtainable in this facility are limited, for aerodynamic and mechanical reasons, to a maximum of 10 m/s, at which speed the arm is rotating at ~1.5 revolutions per second. [D. Crisp, personal communication, June 2002].

On the other hand, an advantage of this facility is good control over gas composition, pressure and temperature. This is achieved because the facility is located within a sealed test chamber within which the gas properties can be well-controlled.

3.1.2 Re-circulating wind tunnels

These are wind tunnels in which the test gas is re-circulated through the test section multiple times. As for a rotating arm facility described above, an advantage of this approach is that the wind tunnel can be located entirely within a sealed vacuum chamber, which can be filled with test gas at the appropriate pressure, temperature, and composition. Within this chamber, a fan is then used to create a wind, usually by drawing air through a closed test section, as shown in Figure 3.1b.

This approach is adopted in two current Mars simulation facilities. At the University of Aarhus, the Danish Mars project operates a compact wind tunnel with a test section ~ 1.2 m long x ~ 0.3 m

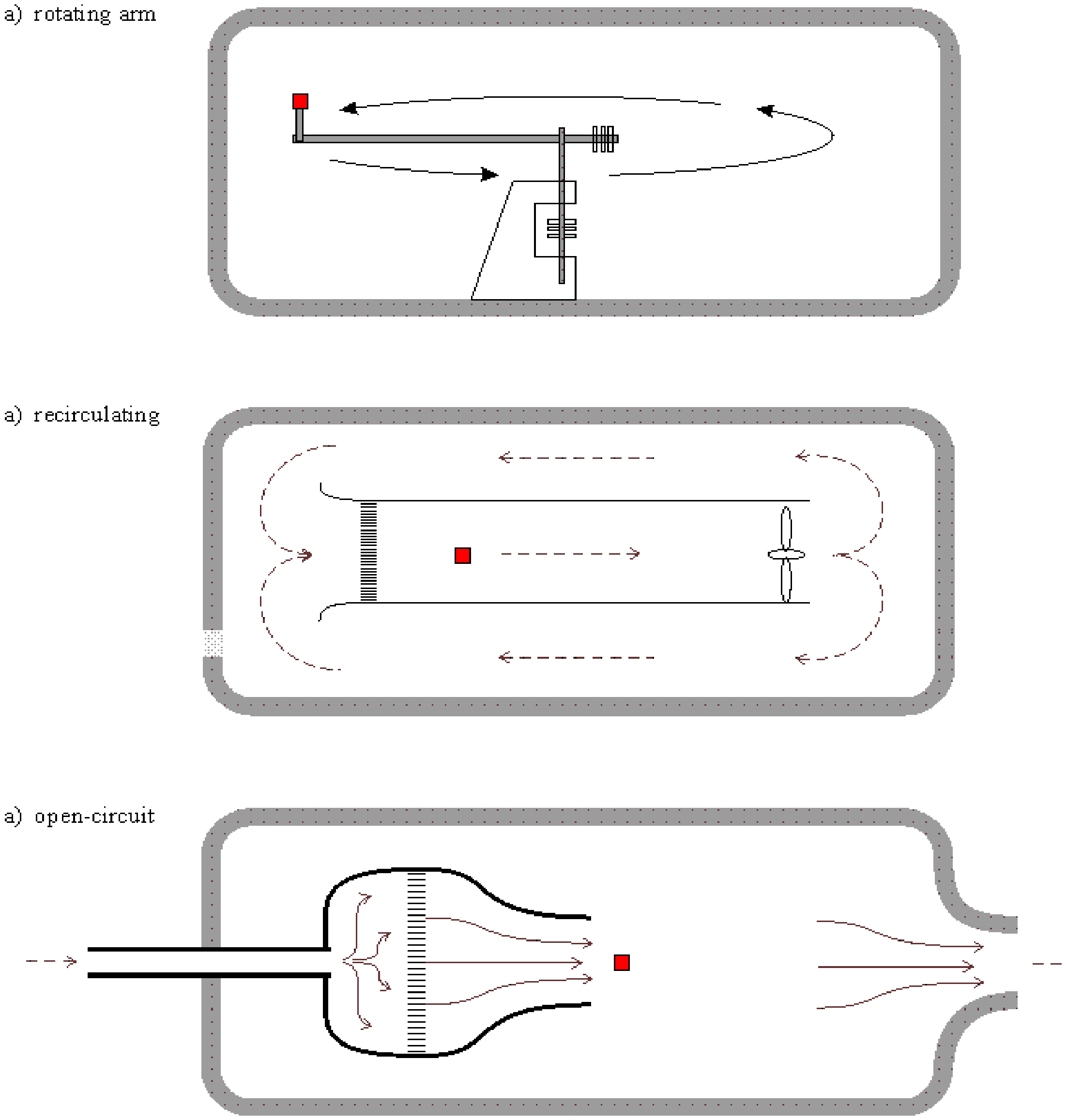

Figure 3.1 – Three basic types of low density wind testing facility. In each diagram the red square indicates the position of the wind sensor (or test piece), the thick grey lines represent the walls of a vacuum chamber, and arrows represent airflow.

diameter. This elegant facility, used mainly for studies related to suspended Martian dust, permits control of temperature and gas composition. The wind speed and turbulence properties in this wind tunnel have been well characterised using a laser Doppler anemometer. However, it is operated only at low speeds (< 7 m/s), due to increased turbulence at higher speeds [Merrison *et al.*, 2002].

The MARS Wind Tunnel (MARSWIT), at NASA Ames Research Centre, has a test section 13 m long x 1.3 m high x 1.3 m wide. This wind tunnel is used to study dust transport in the turbulent boundary layer. Attempts have been made to calibrate wind sensors in this tunnel, but have been hampered because of large fluctuations in wind speed at any point locally in the test section [D. Crisp, personal communication, November 2000]. These are inevitable in a large diameter facility because of the high Reynolds number of the flow.

In the rarefied Martian atmosphere, any wind tunnel with a diameter of order 1 m is likely to exhibit flow in the transition region between laminar and turbulent flow, because it will have a Reynolds number in excess of 10^4 for speeds above 10 m/s (equations and a fuller discussion will be given in Section 3.3 below). In addition, the boundary layer at the wind tunnel walls grows very quickly due to the long mean free path length of the gas molecules (~5 μm). Therefore, a large wind tunnel with a large length-to-width ratio will always suffer from large-eddy turbulence, especially at higher speeds. Though this may be useful for boundary-layer turbulence studies (a particular focus of research at MARSWIT), it is unhelpful for wind sensor calibration, in which one requires the flow to be locally well-known and steady at the wind sensor itself.

3.1.3 Open-circuit wind tunnels

A disadvantage of all the re-circulating wind tunnels is that it is difficult to introduce sudden changes in either wind speed or temperature. One solution to this problem is to feed the test section with an external gas supply rather than re-circulate the air already in the chamber. The external gas supply is introduced to the chamber through a contoured nozzle, which is used to ensure a well-known steady flow field at the test section. This is shown in Figure 3.1c. The chamber pressure is maintained at the required low pressures by continually evacuating the chamber using a vacuum pump. A temporary facility of this kind was used successfully for the calibration of Viking wind sensors [Henry & Green, 1974]. This was housed in a large vacuum chamber at NASA's Langley Research Centre. The sensor was placed immediately downstream of a nozzle aerodynamically contoured to produce a uniform flow field. A small (15 cm) test section was chosen, large enough to fully contain the sensor but small enough to minimise some of the turbulence problems encountered in the wind tunnels above. This same principle has been used as the basis for a new wind tunnel at Oxford, purpose-built for the testing and calibration of anemometers for Mars.

It is worth noting here another dedicated Mars wind tunnel facility which exists at the time of writing: the Mars Atmospheric Simulation Chamber (MASC) at the University of Washington. The design of this facility is notable in that it is an open-circuit wind tunnel design very similar both to the Viking wind tunnel described above and to the Oxford facility described in this thesis. Moreover, it is quite advanced in that it allows fully automatic control of flow rates, temperature, pressure and humidity. However, it is too small for wind sensor testing, with a test section diameter of only 38 mm.

Note that one feature of the Martian atmosphere which cannot be simulated in an open-circuit wind tunnel of this design is suspended dust or sand particles. Such particles would damage the vacuum pumping system, unless an elaborate screening system is included. It is worth noting that suspended dust *can* be included in both the re-circulating tunnels mentioned above (MARSWIT and the Aarhus facility), because the chamber is sealed. Though 'dustiness' is a feature desirable in any Mars wind environment simulation facility, it is sacrificed in open-circuit wind tunnels in order to provide more sensitive control over temperature and flow speed.

3.2 Wind tunnel design

An open-circuit wind tunnel has been created, called the Mars Environment Wind Tunnel and shown in Figures 3.2 and 3.3. The present wind tunnel is an adaptation of a previously existing facility, the Low Density Wind Tunnel (LDWT), at the Southwell Laboratory of Oxford University's Department of Engineering Science. The LDWT already operated as an open-circuit wind tunnel of the type described above, so it was possible to use without modification the large vacuum chamber itself and its powerful vacuum pumping system. The flow conditions required for this work (cool subsonic gas at a few millibars) are very different from those of the original LDWT (heated hypersonic gas at a few microbars), so several new sub-systems had to be implemented. The design of the different subsystems of the wind tunnel is described below.

In principle, the wind tunnel has been designed to eventually allow operation at the full range of Martian temperatures (160 – 300 K). Though a gas cooling system was designed and partially implemented, it was never completed due to the pressing needs of the Beagle 2 wind sensor development schedule. However, the wind tunnel allows fine control of operating pressure, and can be run either with CO_2 or with air, so that the effects of air density can be studied. The cooling system design is presented in Appendix A.

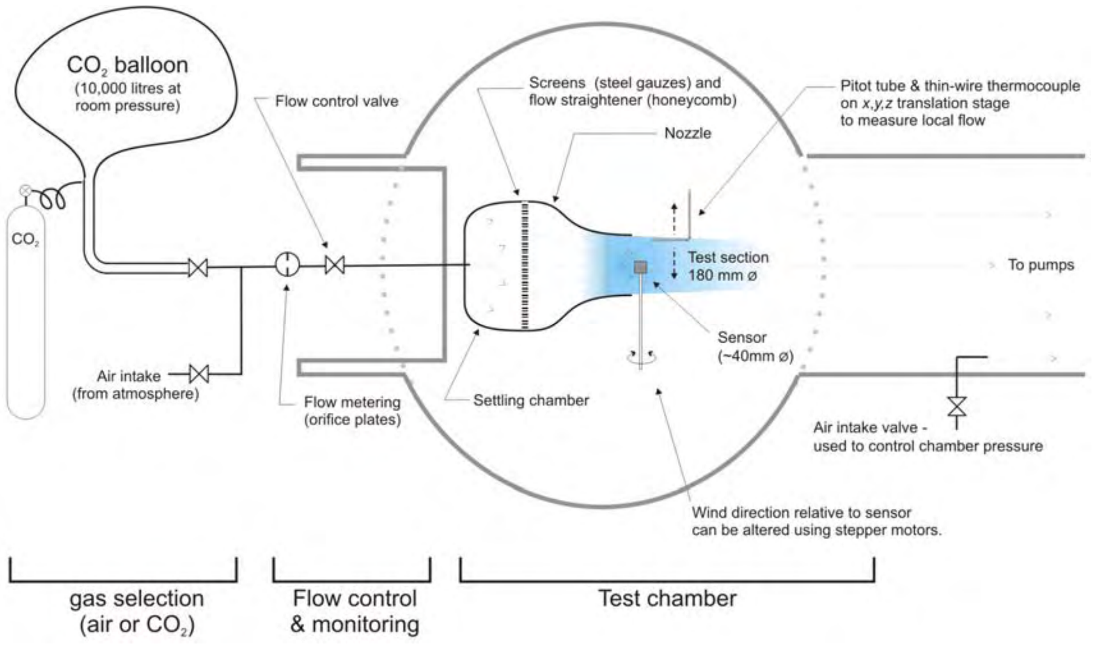

Figure 3.2 – Schematic layout of wind tunnel.

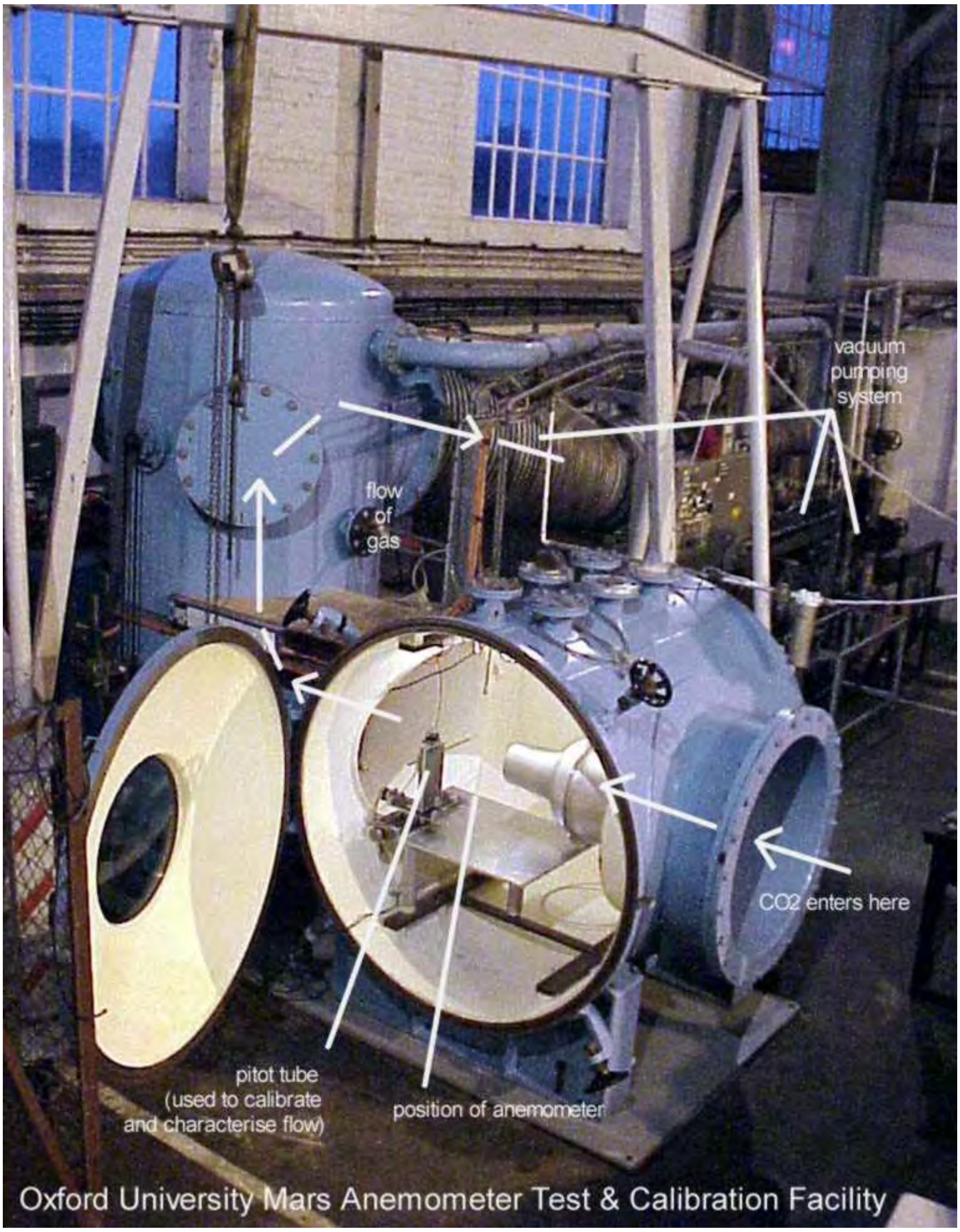

Figure 3.3 – Photograph of wind tunnel.

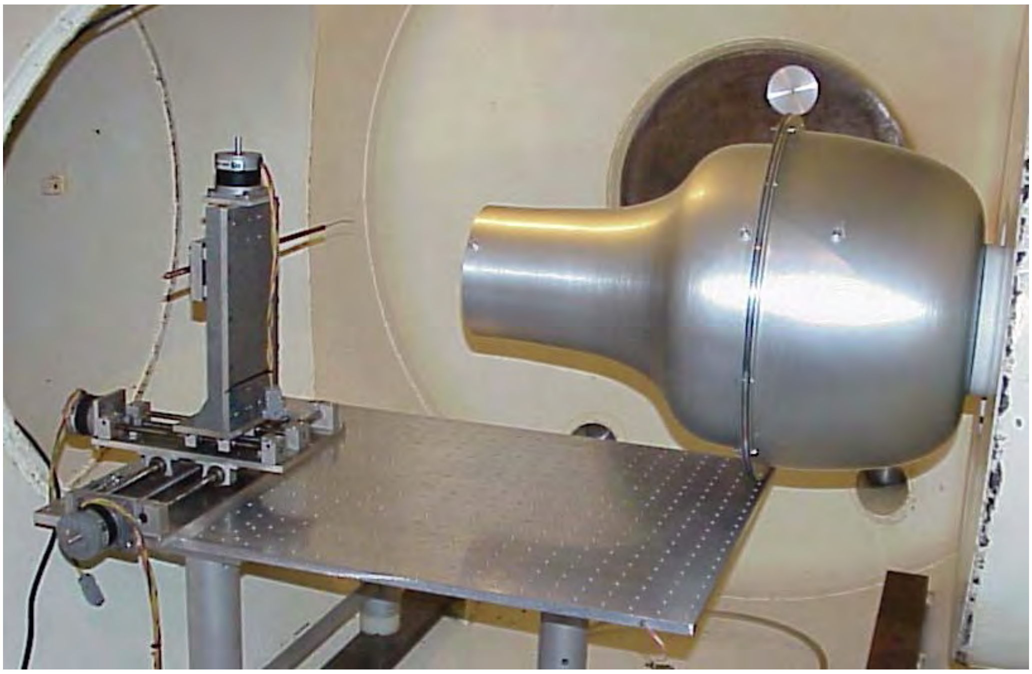

a)

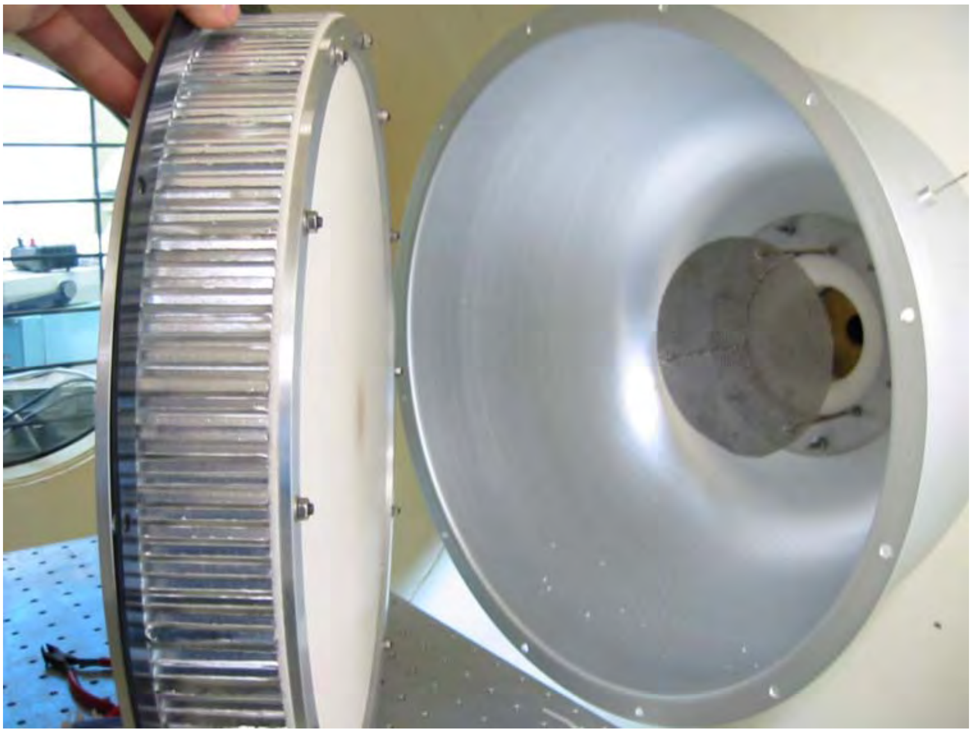

b)

Figure 3.4 – Details of the wind tunnel. The top photo shows the test section of the wind tunnel, showing the nozzle and the translation stage used to move the pitot tube through the flow field. The lower photo shows construction details of the baffle inside the nozzle. Air enters from the right, is slowed by a perforated metal baffle. At left it passes thorough a porous sintered plastic disc (white), then through an aluminium honeycomb, then finally through a wire mesh (not visible). This photo was taken during disassembly of the wind tunnel.

3.3 Nozzle design

The first task in any wind tunnel design is to find the Reynolds number of the flow – this characterises the level of turbulence to be expected in the flow. The Reynolds number is given by $Re = uD\rho/\mu$, where u is flow velocity, D is a length (in this case the diameter of the wind tunnel test section)[*], and ρ and μ represent respectively the density and dynamic viscosity of the fluid. The Reynolds number is a dimensionless expression of velocity; in aerodynamic design it is common to use the Reynolds number instead of velocity because much of the aerodynamic behaviour of a system scales with Reynolds number. It will be shown below that the boundary layer thickness and thus the velocity profile in the wind tunnel scales with Reynolds number. In subsequent chapters, the wind sensor performance will be expressed in terms of Reynolds number. In the present work this is particularly useful, due to the many variations of pressure, temperature, and gas composition encountered.

The wind tunnel design is complicated by the wide range of test conditions to be simulated: flow velocities range from 0.5 to 30 m/s, and gas densities range from air at room temperature (0.008 kg/m^3) to cold CO_2 (0.03 kg/m^3). One more parameter is needed to calculate the Reynolds number in the wind tunnel: the diameter of the test section. The optimum diameter was obtained by dividing the maximum possible pumping speed, conservatively estimated at ~ 0.84 m^3 s^{-1} [Edwards, 1963], by the maximum flow speed needed (30 m/s). This gives a test section area of ~ 0.03 m^2, corresponding to a test section of diameter D = 0.18 m. Thus we can calculate that the Reynolds numbers of the flow will range from 80 to 6000. At lower Reynolds numbers the flow will clearly be laminar; however, a well-designed nozzle is required in the range $10^3 < Re_D < 10^4$ to ensure uniform and laminar flow in the test section.

When gas enters the vacuum chamber, it is travelling at high velocity in a small-bore pipe, and is very turbulent. It first enters a settling chamber, where the gas can come to thermal equilibrium at near-Martian pressure. The gas then passes through a porous sintered plastic plate; this ensures an even distribution of airflow across the width of the wind tunnel. Parallel flow is ensured by passing the flow through a honeycomb flow straightener (5 mm cell width x 50 mm length), and then any residual vortices are broken into smaller cells by a final wire mesh with 1 mm spacing. At this point the diameter of the flow is still 400 mm, greater than the 180 mm test section diameter. This larger diameter ensures that the flow is still slow when the flow passes through the flow straightener and mesh, which ensures that turbulent eddies can be quickly dissipated, resulting in laminar flow even at the highest test speeds. Finally, a contracting nozzle is used to reduce the flow diameter from 400 mm to 180 mm, accelerating the flow smoothly by a factor of ~5. The test section, i.e. the location in the wind tunnel where the wind sensor is placed, is simply at the outlet of the nozzle. A nozzle with a circular section was used in preference to a rectangular one because it has does not have corners,

---

[*] In this chapter the diameter of the test section, D = 180 mm, is used; in this case the Reynolds number is denoted as Re_D . In subsequent chapters I will only use the wind sensor diameter, d = 10 mm, to calculate Reynolds number, in which case the Reynolds number is simply denoted as Re.

which can introduce inhomogeneity into the flow. The test section of the wind tunnel is shown in Figure 3.4.

The shape of the nozzle itself was based on established nozzle design principles; the rate of change of the nozzle's cross section is rapid at first, then less so as the fluid is accelerated [see e.g. Barlow, 1999]. Several likely shapes for the nozzle were drawn based on previous wind tunnels, and then the best of these shapes was chosen after modelling with a Computational Fluid Dynamics (CFD) Finite Element Modelling (FEM) package*. The mesh used for the calculation, shown in Figure 3.5, was two-dimensional and axisymmetric, with a higher density of nodes in the boundary layer. The mesh used had 40 x 40 nodes; it was found that higher node densities did not significantly change the results (mesh densities of up to 120 x 60 elements were tried). A uniform inlet velocity was specified as a boundary condition. The output parameter of most interest is the velocity profile at the test section, i.e. at the exit of the nozzle.

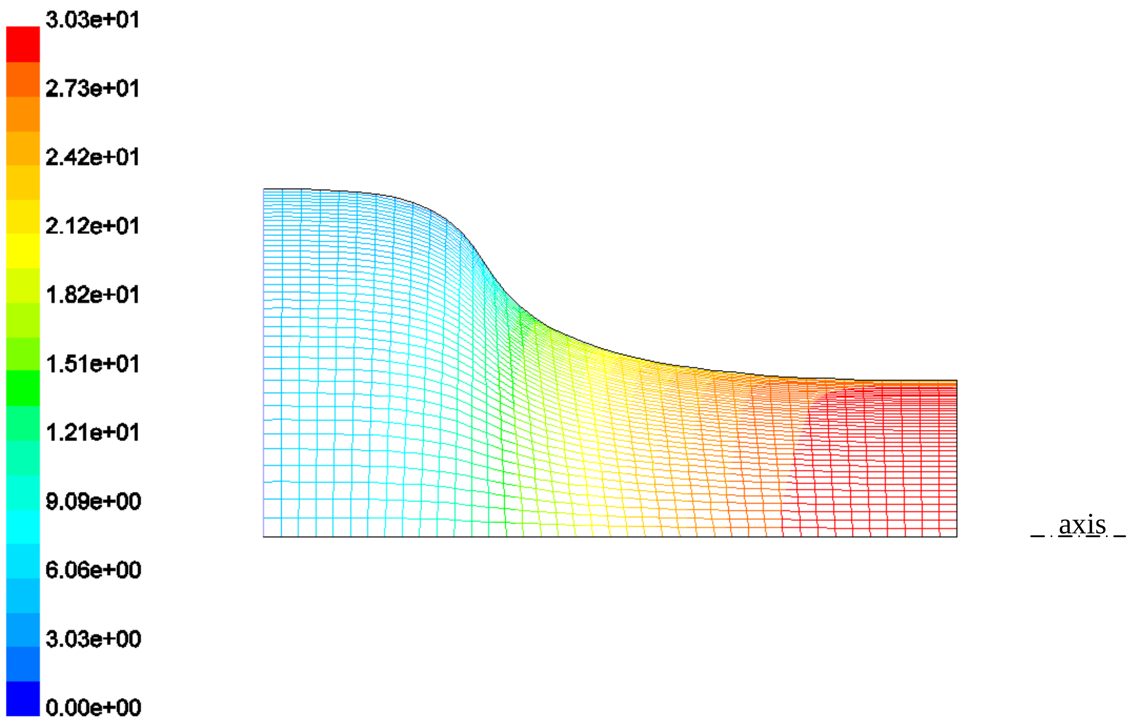

Figure 3.5 – The final mesh used for CFD calculations of flow in the nozzle is two-dimensional and axisymmetric. Colours represent flow speed (in m/s): it can be seen that flow accelerates smoothly from the inlet (at left) to the test section (at right).

---

* Fluent version 5.5, published by Fluent Inc. http://www.fluent.com

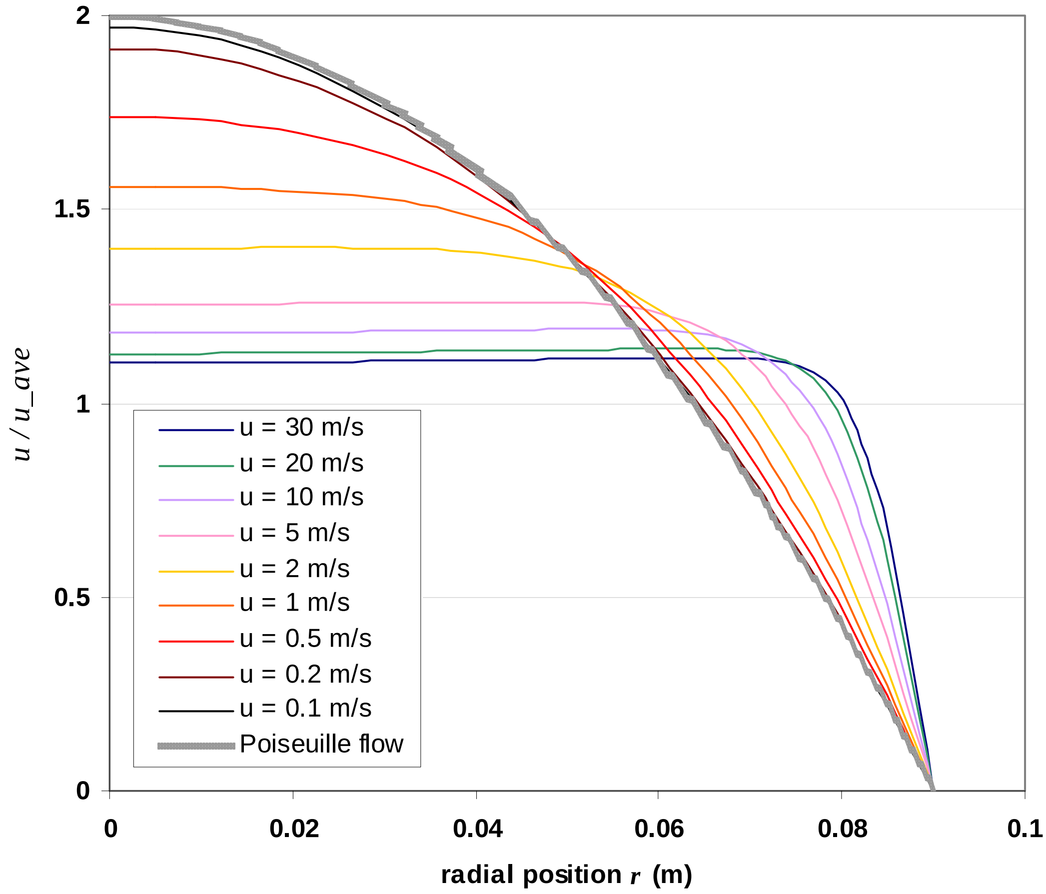

Figure 3.6 – FEM calculations of flow profile. At all velocities above 2 m/s the velocity variation in the central section (defined as r < 2.25 mm) of the wind tunnel is < 1 %. At low velocities the solution approaches the quadratic profile of Poiseuille flow (fully-developed laminar pipe flow). Velocity is expressed as a proportion of u_{ave} ($u_{ave} = \int_0^R u(r)2\pi r dr$). Velocities indicated are for air at p = 10 mbar and T = 300 K.

Calculated flow profiles are shown in Figure 3.6 for various flow speeds ranging from 0.1 m/s to 30 m/s. flow speed is presented as a proportion of u_{ave}, where u_{ave} is the averaged flow speed in the section ($u_{ave} = \int_0^R u(r)2\pi r dr$). These calculations assumed that the test gas was air at p = 10 mbar and T = 300 K. It can be seen that the flow velocity is quite uniform in the centre of the test section, especially at high speeds. At all speeds above 1 m/s, the variation in velocity across the central 45 mm of the test section is under 1%; at all speeds above 3.5 m/s, the variation in velocity across the central 45 mm of the test section is under 0.5%.

In order to validate and to better understand the FEM results, the velocity profile was also studied analytically by calculating boundary layer development. The boundary layer at the wall of the wind tunnel is expected to be laminar in all flow conditions. If the Reynolds number is calculated using the length of the wall (x ~ 0.45 m), it stays well below 3×10^5 – commonly accepted as a guideline value for the onset of turbulence in this case – for all test conditions. The displacement thickness of the boundary layer was calculated using the Thwaites method for boundary layer development in accelerating flow [see e.g. Young, 1989]. This states that the boundary layer momentum thickness θ is given by

$$\theta^2 = 0.45\nu u^{-6}\int_0^x \left[u(x)\right]^5 dx\,,$$

where $u(x)$ is the free stream flow velocity as a function of x, the distance along the wall, and ν is the dynamic viscosity of the fluid ($\nu = \mu/\rho$). The value of the integral on the right is proportional to u^5. Therefore the boundary layer thickness scales as $\theta^2 \sim \nu/u$, i.e. $\theta \sim Re^{-1/2}$. Therefore the profile calculated for any given flow conditions should be the same as that for any other flow conditions with the same Reynolds number.

Given the displacement thickness and the free stream flow velocity, the expected velocity profile in the boundary layer can be obtained using a numerical solution to the Blasius equation [see for example Fay and Sonwalkar 1991, chap 6]. Calculated velocity profiles are in good agreement with FEM results at $u > 3$ m/s; examples will be shown later in this chapter.

At very low velocities ($Re_D \leq 300$, corresponding roughly to $u \leq 2$ m/s), the displacement thickness becomes significant in comparison to the radius of the wind tunnel, so the approach becomes invalid (because there is no longer a central region of undisturbed air in which to obtain a *free stream* velocity). Another analytical solution is useful to bear in mind: that of fully developed laminar pipe flow, also called Poiseuille flow. In this case, the velocity profile is given by

$$u(r) = \left(-\frac{dp}{dx}\right)\frac{R^2 - r^2}{4\mu}\,,$$

where R is the radius of the pipe. If this is integrated with respect to dr over all r within the pipe, one can obtain the averaged flow velocity in the pipe $u_{ave} = (-dp/dx)\, R^2/8\mu = u_{centre}/2$. The FEM results presented in Figure 3.6 show that at the test section exhibits such a profile at extremely low velocities. Though such low velocities ($u \sim 0.1$ m/s) are not within the nominal range of the wind tunnel, the fact that the FEM can match this analytical result is taken as partial validation of the FEM.

In Figure 3.7, the analytical and FEM results are summarised. The central flow speed enhancement u_{centre}/u_{ave} is expressed in terms of Reynolds number Re_D. The equivalent flow velocity u_{ave} for air at 10 mbar, 300 K is plotted at the top of the figure for convenience. In addition to FEM results and analytical solutions for Poiseuille flow (low speeds) and Thwaites equation (high speeds), the figure includes experimental points, which will be discussed below.

This nozzle, then, is designed for flow speeds ranging from ~ 0.5 to 30 m/s. If only low flow speeds ($u < 6$ m/s) were of interest, the nozzle could be removed entirely. At such low flow speeds, flow will be laminar with or without the aerodynamic nozzle. This would also allow a large test section (400 mm in diameter), and would remove the problem of the growing boundary layer which causes uncertainty in the exact flow speed at the test piece. A similar approach (a porous plug without a contoured nozzle) was used for low speed flow in the temporary Viking wind sensor test facility at NASA’s Langley Research Centre [Henry & Greene, 1974].

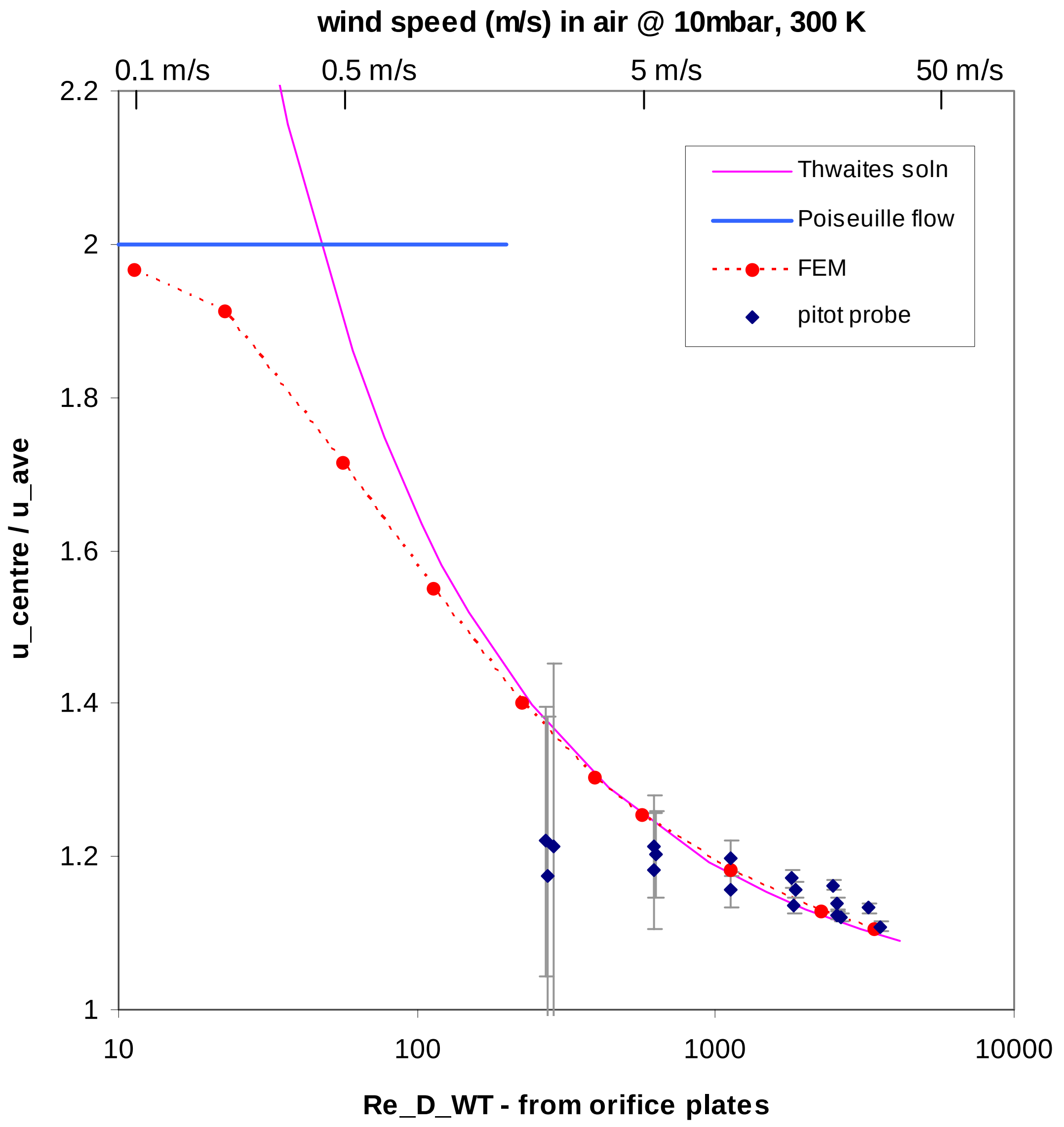

Figure 3.7 – Enhancement of flow velocity in the centre of the test section, expressed as u_{centre}/u_{ave} . FEM results show the transition between the analytical approximations of Thwaites boundary layer development at high speeds and Poiseuille flow at extremely low speeds. The plot also shows experimental data obtained with the pitot probe (see Section 3.7 for discussion). The Reynolds number on the x-axis is calculated using the diameter of the nozzle, D = 180 mm.

The wind tunnel can also be modified to be used at higher velocities. Wind speeds of up to 60 m/s can be achieved by using a 120 mm diameter nozzle instead of the 180 mm diameter nozzle described above. Such a nozzle has been built, and would probably be used for NetLander wind sensor testing, to complement low-speed calibrations performed at JPL’s rotating arm facility. However, all tests described in the present thesis were performed with the 180 mm nozzle.

3.4 Temperature measurement

At first, air temperature measurements were obtained using platinum resistance thermometers (PRTs). A small sensing current is used to measure the resistance of a platinum wire element, which varies with temperature. Predictably, however, it was found that this sensing current heated the sensors at low pressures, typically by about 1 K. Therefore this system was replaced by thermocouples, which are not compromised by self-heating. The thermocouples were read using AD595 chips*, which were located inside the wind tunnel. Several thermocouples were made up, with wires as fine as 0.008 mm to enable sensitivity to rapid temperature fluctuations. The absolute temperature accuracy of this measurement is only ± 1 K, limited both by the accuracy of the internal cold junction compensation in the AD595 chip and by the input resolution of the ADC being used to read its output.

3.5 Gas flow and pressure control

The wind tunnel can be run using either air, drawn in from the lab, or carbon dioxide. A large (~10 m^3) balloon, filled with CO_2 at room pressure, is used as the source reservoir. This system is used rather than using CO_2 directly from gas cylinders for two reasons. The main reason is that, at the high flow rates used in the wind tunnel, CO_2 would freeze up the regulators in the flow path. This possibility is commonly avoided by heating the CO_2 immediately before it passes through the regulators, but this leaves one with warm gas, the temperature of which would be dependent on the flow rate being used.

A single valve, immediately upstream of the pressure chamber, is used to set the mass flow rate. All gas upstream of this valve is at, or near, atmospheric pressure. Downstream of this valve, the gas is at or near Martian pressure (~6 mbar). Using an ordinary rubber weir-type vacuum valve for this purpose, it was found that the mass flow rate could be set to a resolution of ~0.1% of the maximum flow rate (i.e. roughly 0.03 m/s), which is more than adequate.

Once the mass flow through the wind tunnel is set, the chamber pressure must be stabilised. The chamber pressure is controlled by using a vent valve positioned immediately upstream of the pumps such that it admits air from the atmosphere. This valve is always partially open to provide a variable load for the pumps, essentially setting the pumping speed from the chamber. Opening this valve increases the chamber pressure, and closing it decreases the chamber pressure. For all tests described in this thesis, this valve was actuated by hand. This worked quite well; it was possible to keep the test pressure stable to within 0.02 mbar during tests (i.e. about 0.3% of absolute chamber pressure). It would be possible to replace this manual control by a PID-controlled motorised valve; however, this would require ~£1000 - £2000 which were not available for this experiment. Computerisation of pressure and flow controls is recommended if the system is to be used for funded calibration programs in the future, as manual control requires full-time operator attention.

3.6 Mass flow rate monitoring.

The mass flow rate of the gas flow entering the wind tunnel is constantly monitored by measuring the pressure drop across an orifice plate, which is proportional to the square of the flow rate. The flow rates in the wind tunnel vary from ~ 0.1 to 10 g/s, so the differential pressure sensors must be capable of accurately reading pressures varying over 4 orders of magnitude, clearly a difficult task. Therefore

---

[*] Analog Devices, Inc AD595C. http://www.analogdevices.com

two orifice plates are used to cover the full range, respectively 6 mm and 14 mm in diameter. The larger orifice is used for higher flow rates (mass flow > 3 g/s). The smaller orifice plate is monitored using two differential pressure sensors, with ranges of 0-10 mbar and 0-100 mbar respectively. This allows sensitivity across the whole range of flow rates.

The differential pressure sensors were calibrated using an inclined-tube mercury manometer, leading to an absolute accuracy of 0.02 mbar in the range 0-10 mbar, and 0.1 mbar in the range 10-50 mbar, i.e. about 1 - 2% over most of the flow range (see Figure 3.8). The flow rate is determined using BS1024, Sections 1:1, 1:2, 1:4. According to the BS, the absolute accuracy of this method of flow rate determination is 1% to 2%. The absolute accuracy of the mass flow determination in the wind tunnel is thus estimated at 2 to 3 %. The resolution of the system is better than this, though – the repeatability of the differential pressure sensors is 0.25% of their full-scale range (limited at present by the resolution of the ADC used to record their output). Thus the precision to which flow conditions can be repeated is better than 1% of flow speed, for all flow speeds above ~1 m/s.

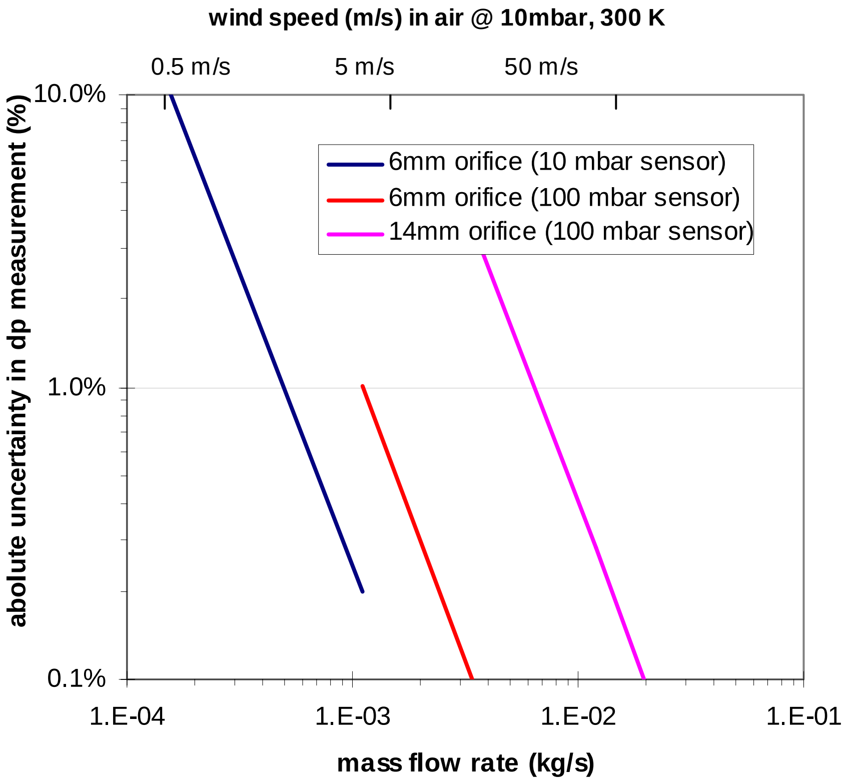

Figure 3.8 – Absolute accuracy of differential pressure measurement at the orifice plates for the different *dp* sensors. For all *u* > 1 m/s, the absolute uncertainty in *dp* is ~2% or less. This contributes ±1% uncertainty to the determination of mass flow rate in the wind tunnel.

Note that the orifice plates allow determination of the *total* mass flow rate into the wind tunnel; if one divides this by the fluid density and by the cross-sectional area of the wind tunnel one can calculate the *average* velocity in the wind tunnel, u_{ave}. The local flow velocity at any point in the test section is then deduced from the modelling results presented in Figures 3.6 and 3.7. However, an experimental confirmation of the local flow velocity in the centre of the wind tunnel is desirable. This proved very useful, as will be seen below.

3.7 Local flow speed measurements

Local wind speed in the wind tunnel can be measured using a pitot/static tube mounted on a three-dimensional translation stage to enable it to be moved through most of the test section (shown in Figure 3.4). This incorporates both static tappings (which face perpendicular to the flow direction, thus measuring the absolute ambient pressure), and a pitot probe (facing into the flow). The difference between the static and the pitot pressure is the dynamic pressure, equal to $p_{dyn} = ½\rho u^2$. This is extremely low in the Martian atmosphere, due to a combination of low density and low wind speeds, being less than 10 Pa for all wind speeds below 30 m/s. The most sensitive differential pressure sensor readily available commercially was obtained, which has a full-scale sensitivity of 20 Pa[*]. The stated accuracy of the calibration is 0.03 Pa; therefore, an accuracy of 10% or above could only be obtained for readings above 0.3 Pa. This corresponds to wind speeds of 6 m/s and above, for CO_2 at 7 mbar and 250 K.

It was found however that the dynamic pressure measurement was very sensitive to fluctuations in chamber pressure. Though fluctuations in chamber pressure were typically of order 1 Pa, i.e. only 0.1% - 0.2% of the absolute chamber pressure, this is important in comparison to the dynamic pressure to be measured (0.3 - 10 Pa). It was difficult to obtain exactly the same trapped volume in tubing on either side of the differential pressure sensor, leading to discrepancies in the response time of the positive and negative sides of the differential pressure transmitter. As a result, a drop in the chamber pressure of only 0.2 Pa/s would cause a rise in measured differential pressure of as much as 0.2 Pa. Therefore, it proved impossible to obtain a measurement of velocity fluctuations with respect to time. However, time-averaging of several measurements was used to greatly reduce this problem. This allowed local velocity measurements for comparison with velocity profiles calculated by analytical and FEM techniques.

Very quickly, however, it became clear that velocities measured using the pitot probe were all 20% - 40% greater than those expected on the basis of mass flow measurements. Though the spatial dependence was as expected analytically, the magnitudes were too high, as shown in Figure 3.9a). It was eventually discovered that there had been a leak in an O-ring seal immediately adjacent to the Baratron measuring chamber pressure, p_{test}. As a result, measurements of p_{test} had been erroneously high, by ~ 1 - 2 mbar. This problem was exacerbated by poor design: the pressure sensing head was connected to the side of the test section – the location at which the pressure measurement was sought – using a long, small diameter tube. As a result, gas flow from the leaking O-ring caused a significant pressure gradient in the small-bore tube, despite the very small gas flow in question (which must be «1 mg/s[†]). Velocity calculated from using the pitot tube is given by $u_{pitot} = \sqrt{2 p_{dynamic} / \rho_{test}}$. In contrast, the orifice plates measure mass flow rate; therefore, the calculated flow speed is proportional to the

---

[*] Furness Controls FCO-332. http://www.furness-controls.co.uk

[†] This calculation of the maximum possible mass flow rate assumes sonic flow through a 1mm diameter orifice at ~ 3 mbar (which was the lowest p_{test} measured). Mass flow = $\rho A v_{sound}$ = (0.004 kg m^{-3}) (0.001 m · π/4)^2·(340 m s^{-1}) ~ 1 mg s^{-1}.

mass flow rate divided by ρ_{test}. Because an erroneously high value was being used for ρ_{test}, flow velocities calculated using the pitot tube ($\delta u_{pitot}/u_{pitot} \sim (\delta p_{test}/p_{test})^{-1/2}$) were anomalously high when compared with those calculated from the orifice plate data ($\delta u_{orifice}/u_{orifice} \sim (\delta p_{test}/p_{test})^{-1}$).

Unfortunately, this fault was only discovered after Beagle 2 wind sensor (B2WS) calibration tests had been completed. Due to the accelerated schedule of the B2WS development, the B2WS tests were conducted before wind tunnel characterisation had been completed, in fact before the pitot system was implemented at all! A correction to p_{test} therefore had to be applied retroactively to all previously taken data. It was assumed that p_{test} had been uniformly overestimated by 1.7 mbar during all measurements at Mars pressures. The magnitude of this correction was chosen to optimise the agreement between mass flow measurements (from the orifice plates) and local flow velocity measurements (from the pitot probe).

Though clearly simplistic, it was decided that a more complicated correction scheme was not justified because 1) the magnitude of the leak was not known, and may have varied with time, and 2) the sensitivity of the calculated flow velocity to the assumed chamber pressure is relatively small. The effect of the correction is shown in Figures 3.9a) and 3.9b), which respectively show results before and after this correction was applied.

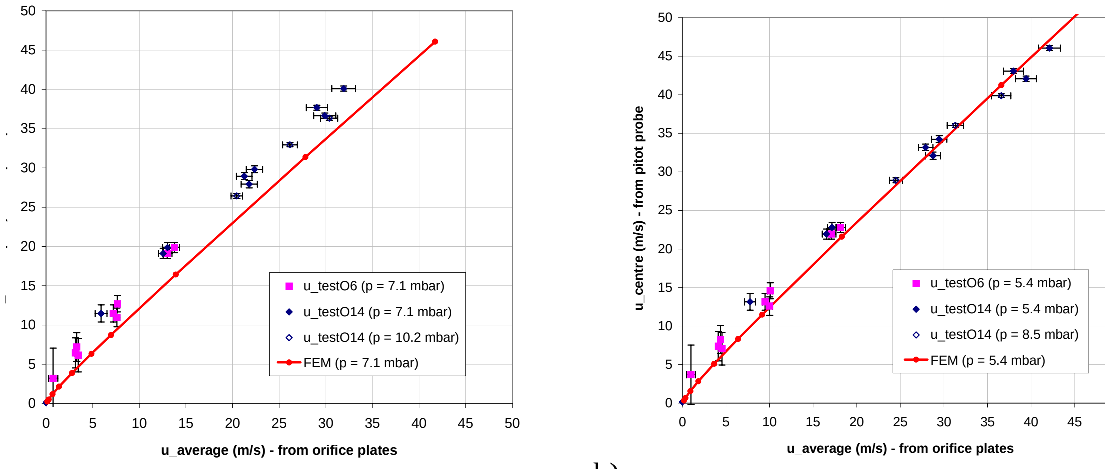

b)

Figure 3.9 – Measurements of local flow velocity in the centre of the test section. a) shows results before correction for chamber pressure was implemented; b) shows results after correction. Mass flow measurements are obtained from the pressure drop across (pink) 6 mm orifice plate, and (blue) 14 mm orifice plate.

Though this uncertainty in p_{test} is obviously undesirable – especially for a calibration facility! – it has had a surprisingly small impact on the B2WS calibration. This is because, as will be seen, the sensor performance scales with *Reynolds number* rather than with *velocity*. Reynolds number is proportional to $u\rho$ and therefore to mass flow rate, which is measured directly by the orifice plates.

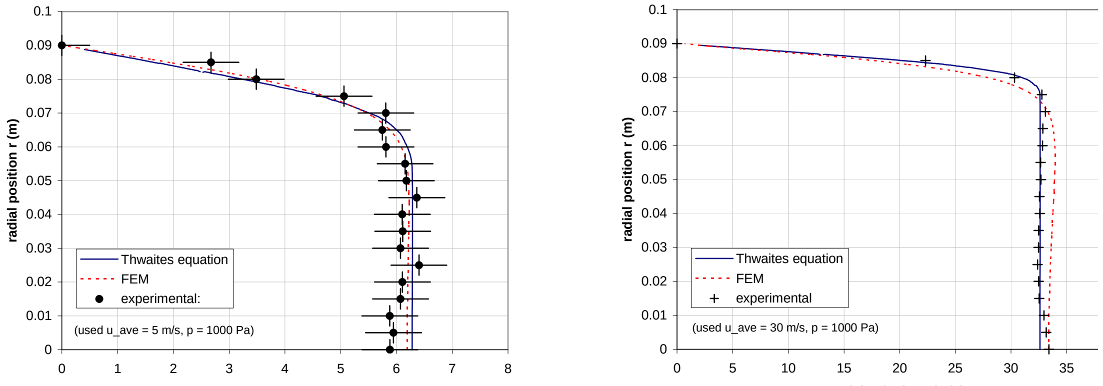

b)

Figure 3.10 – Velocity profiles in the wind tunnel. Analytical and FEM results are presented, as are experimental measurements obtained using the pitot probe.

Two further flow profiles obtained using the pitot probe are shown in Figure 3.10. Analytical and FEM results are included as well as experimental results; it can be seen that all three are in good agreement. The flow enhancement in the centre of the test section at high speed of about 1 m/s, seen in Figure 3.10b, is not seen in the FEM results. This is a real, repeatedly observed effect, and is almost certainly due to an inadequate baffle design. When disassembling the wind tunnel, it was found that there was a slightly dirty patch in the centre of the porous plastic plate in the nozzle (visible in Figure 3.4b). This suggests that the air entering the wind tunnel at sonic speed is not sufficiently slowed by the perforated plate included for this purpose, depositing suspended dust particles from the lab air in the centre of the porous plate. If the wind tunnel is reassembled in future the baffle can easily be replaced with a less porous one. That this flow enhancement at high speeds was detected at all can be viewed as a validation of the accuracy of the flow characterization.

A two-dimensional scan across the test section is shown in Figure 3.11. It can be seen that the velocity is uniform to ~ 3% over the whole test section. This non-uniformity is attributed mainly to the sensitivity to chamber pressure fluctuations as discussed above (due to the number of data points taken in this scan, it was not possible to time-average many readings for each data point). Thus it is suspected that the real velocity non-uniformity across the central area of the test section is less than 3%, quite possibly less than 1% as predicted by the FEM results.

In any case, a uniformity of 3% would still be better than what has been achieved in previous Mars wind sensor calibration facilities. Measurement of dynamic pressure will always be difficult given the extremely low dynamic pressure associated with low-density, low-speed flow. However, it may be possible to improve performance of the pitot measurements through further experimentation with different sensors and sensor configurations.

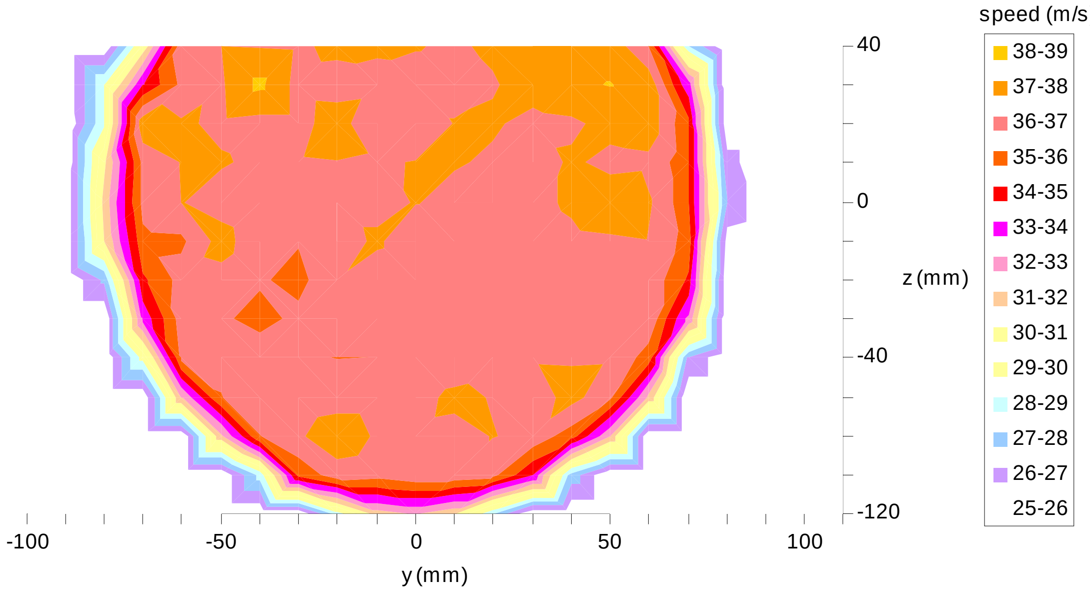

Figure 3.11 – 2D flow profile at test section, obtained using the pitot probe. The test gas was air at p_{test} = 5.5 mbar, u_{ave} = 28.1 m/s.

3.8 Temporal stability

A shortcoming of many previous wind tunnels has been temporal fluctuation in wind speed (see Section 3.1). The present wind tunnel design should produce a very stable flow due to its nozzle design which ensures laminar flow even at high speeds. As discussed above, it was not possible to test this directly using the pitot probe system. However, it was tested briefly using a constant temperature anemometer (see description in Section 2.2), which has a good high-frequency sensitivity. No fluctuations at any frequency were observed in the output of this anemometer, either using an oscilloscope or a high-frequency ADC. Based on the gain settings used in this test, it can be concluded that any temporal fluctuations must be less than ~1%. The flow in the nozzle, then, is aerodynamically very stable.

At high flow speeds, the flow rate at the orifice plates is observed to fluctuate by ~ 0.3%, perhaps due to turbulence at the flow control valve (this valve emits a 'whistle' which fluctuates slightly in pitch at high flow rates). This fluctuation is only large enough to be detectable at $u > 20$ m/s; at this speed the fluctuations are only ~± 0.06 m/s, i.e. ~± 0.3%. This is a very small fluctuation, and represents a significant improvement on previous wind tunnel simulations.

3.9 Wind direction variation

The position of the sensor can be changed to simulate different wind directions. For Beagle 2 wind sensor testing, sensors were mounted on a Perspex rod, 10 cm in length, which was mounted directly on the axis of a stepper motor (see Figure 3.12). The stepper motor's axis was vertical, allowing direct computer control of horizontal wind direction with an accuracy of 1.8° (the step angle of the motor). The choice of stepper motor was not ideal in that it was a high power version which dissipated 500 mW of heat even at rest, an appreciable amount compared with the ~100 mW heat dissipation typical in Beagle 2 and Viking hot film sensors. This caused two problems: Firstly, it caused the Perspex rod to heat up in low wind conditions, causing a temperature increase of up to 2°C at the base of the sensor (this temperature rise, measured using thermocouples, only occurred when the wind speed was zero). Secondly, it caused a thermal updraft, increasing air temperatures above the sensor. This second problem was circumvented by upending the motor/sensor system so that the motor was above the sensor (such that the axis of rotation was again vertical). Though not ideal, this solution proved adequate in the short term. If repeated in future, an obvious first step would be to use a much smaller stepper motor which does not dissipate so much heat. Also, a relay could be put on the stepper motor supply lines to cut off power to the stepper motor when it is not in use.

The effect of sensor tilt, i.e. non-horizontal winds, was not simulated during this DPhil research. This would be a useful area for future work. Such studies would require only minimal new equipment; a new adapter to mount the wind sensor on a stepper motor with a horizontal axis would easily fit on the large work surface in the wind tunnel (visible in Figure 3.4a).

Figure 3.12 – Stepper motor and mount, used to rotate the sensor about a vertical axis (thus changing wind direction). The wind sensor is mounted on the top of the Perspex rod (shown here is an early Beagle 2 wind sensor prototype).

3.10 Conclusions

A wind tunnel optimised for testing of sensors in Martian pressures and wind speeds has been designed and implemented. Detailed analytical and finite element modelling techniques have been used to characterise its flow characteristics. By measuring mass flow rate using a set of orifice plates on the gas inlet, the Reynolds number of the flow in the test section can be determined with an absolute accuracy of 2 to 3%. Experimental confirmation of flow profile predictions are possible only for speeds of above ~ 5 m/s, and these show very good agreement with modelling predictions. Due to poor design there was a persisting uncertainty in measurement of chamber pressure; though this has led to a large uncertainty in the *real* flow speed, the mass flow rate and thus the Reynolds number of the flow are well known.

In any case, the absolute accuracy of ±3%, and the stability of the flow to within ±0.2%, compares favourably with that achieved in previous Mars wind sensor calibration facilities. Further experimentation with differential pressure sensors in conjunction with the pitot probe may serve to improve the performance and usefulness of the pitot probe as a flow characterisation tool. There are many possibilities for future improvement, many of which have been singled out in the text. In particular, there is a pressing need to develop a cooling system to allow the full range of Martian temperatures to be simulated; a design is suggested in Appendix A.

Chapter 4 - Beagle 2 wind sensor: Design / Manufacture

The wind tunnel described in the last chapter was designed for the calibration of wind sensors for two missions: Beagle 2 (UK, 2003) and NetLander (France, 2007 – now cancelled). However, the ultrasonic wind sensor originally proposed for Beagle 2 was cancelled in May 2001 due to lack of funds. Hence the opportunity arose to design a new Beagle 2 Wind Sensor (B2WS), a work which is the subject of the remainder of this thesis.

In this chapter I first introduce the Beagle 2 mission and the constraints it imposes on the wind sensor design, as well as performance goals for the wind sensor. In Section 4.2 I will describe the construction of the wind sensor head, as well as a brief rationale for the design decisions made. In Section 4.3 I will present the electronics design. This chapter is largely free of experimental data. Rather than provide experimental data for each of the prototype sensors, this chapter is intended to describe the development of the final Flight Model sensor and electronics designs. Given this background, the performance of the Flight Model design will then be analysed in detail, first through wind tunnel test data in Chapter 5, then analytically in Chapter 6.

4.1 Introduction: context / requirements

4.1.1 Mars Express and the Beagle 2 lander

Beagle 2 is the lander component of the European Space Agency’s Mars Express satellite, which was launched successfully in June 2003 [Chicarro *et al.*, 2004]. Beagle 2 relies on Mars Express for all its power and communications during cruise phase, and for its telecommunications relay once on the surface. The payload of Mars Express includes a High Resolution Stereo Camera (HRSC), an infrared spectrometer with a range of 1.2 – 45 µm (PFS), and another spectrometer with ranges of 118 – 320 nm and 1 – 1.7 µm (SPICAM). The first of these will provide topographical context for the Beagle 2 landing site, and the two spectrometers will help us characterise the global and regional context for meteorological measurements made with the Beagle 2 lander.

The Beagle 2 lander is due to land in the Isidis Planitia region of Mars (265.0°W, 11.6°N) on the 25 December 2003. Its principal objective is “the detection of extinct and/or extant life, or at least to establish if the conditions at the landing site were ever suitable for life to have evolved in the planet’s history.” [Pullan *et al*, 2004]. It is the smallest lander yet sent to Mars, with a mass of only 33 kg on the surface (The total *probe* mass at atmospheric entry is 69 kg including heatshield, parachutes and airbags). Despite this low total mass, it carries almost 9 kg of science instrumentation. The largest in the payload of Beagle 2 is a sophisticated Gas Analysis Package (GAP) consisting of a mass spectrometer and pyrolysis / steeped combustion package, designed for identification of analysis of carbon-containing organic compounds as well as measurement of isotopic ratios. A motorised, jointed arm, ~ 0.9 m in length, allows delivery of soil and rock samples to the GAP. Mineralogical analysis can be performed using X-ray and Mössbauer spectrometers mounted on the end of the arm. The Beagle 2 wind sensor is part of an Environmental Sensors Suite (ESS), which will also measure air temperature at two heights, atmospheric pressure, saltated grain momentum, UV flux (diffuse and direct at five wavelengths), the total accumulated radiation dose and investigate the nature of the oxidizing environment [Towner et al., 2003]. The wind and temperature sensors are mounted on the end of the arm, allowing them to be positioned at several locations around the lander body up to a height of 0.96 m. A picture of Beagle 2, highlighting the position of the wind sensor, is shown in Figure 4.1.

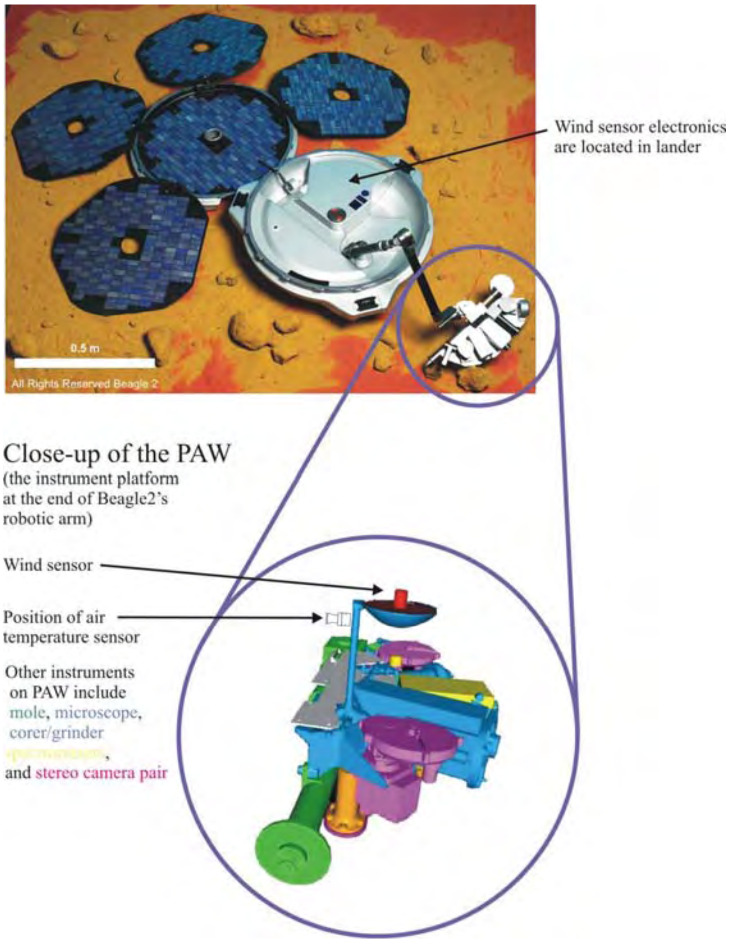

Figure 4.1 – The Beagle 2 Wind Sensor (B2WS) is located at the end of a movable arm. At its highest position (with the arm vertical, wind sensor vertically above it), the wind sensor is 0.96 m above the ground.

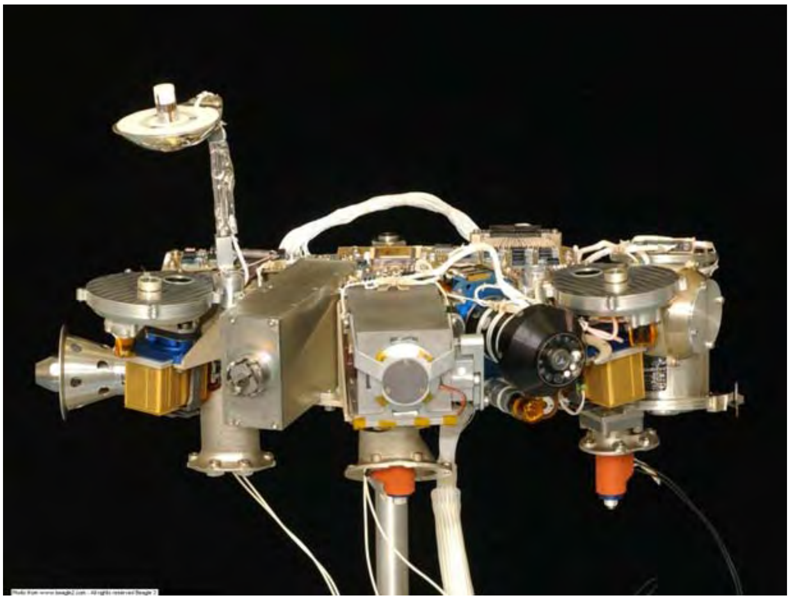

Figure 4.2 – Photograph of the nearly completed Flight Model (FM) Beagle 2 PAW. The wind sensor is clearly visible at top left. The wind air temperature sensor had not been mounted yet when this photo was taken.

4.1.2 Performance goals

Before embarking on the Beagle 2 wind sensor design, it was important to have clear science and performance goals. The science aims for the pressure, temperature and wind sensors are:

- to obtain a long-term record of diurnal and seasonal variations of pressure, temperature, and wind (requires low-frequency measurements at regular intervals, day and night);
- to characterise the planetary boundary layer through high-frequency measurements of temperature and wind speed fluctuations (requires high-frequency measurements at different heights, day and night).
- to observe convective vortices (requires high-frequency measurements in daytime).

The performance targets for the wind sensor in order to achieve those goals, informed by the experience of past sensors as discussed in Chapter 2, is:

- to measure horizontal wind speed in a the range 0.5 – 30 m/s, with an accuracy of ±10%;
- to measure wind direction in the range 0 – 360°, with an accuracy of ±10°;
- to make these measurements with a response time ideally of 1 second.

This specification only prescribes measurement of a two-dimensional wind vector horizontal to the ground. The measurement of vertical wind speeds, if possible, would undoubtedly contribute to the science goals. It was decided that the mounting situation of the B2WS made simultaneous 3-D wind measurements impossible, due to the shielding effect of the wide-angle mirror on which the B2WS is mounted. However, it may be possible to measure vertical wind speed by rotating the PAW by 90° about a horizontal axis using Beagle 2’s robotic arm, such that the axis of the wind sensor is horizontal. The feasibility of such tests will be further considered later in this thesis.

4.1.3 Resources and constraints

The wind sensor design described here was a last-minute replacement for an ultrasonic wind sensor. As a result, the physical constraints, including the physical space available for the sensor, were already defined, with very little negotiation possible. The spacecraft resources – mass, power, space, and data bandwidth – allocated for the B2WS are listed in the following table:

Total Mass	< 25 g including electronics
Volume (sensor head)	18 mm high × 50 mm diameter
Volume (electronics)	Double-sided PCB, 55 mm × 30 mm × 8 mm height
Power	< 250 mW (200 mW nominal)
Data return	3 × DC analogue outputs, 0-5 V
Control signals	No control signals may be sent to the sensor (other than power on/off)
Location	At end of movable arm – see Figures 4.1 and 4.2
Air temperature sensor	Required use of Beagle 2 temperature sensor

A particularly unusual element of these constraints was that the physical envelope for the sensor head was already defined. Based on the shape of the ultrasonic sensor shown in Figure 2.9, it is not an ideal shape for a thermal sensor (c.f. Figures 2.4 and 2.8). The mounting position is wide and flat because the B2WS is mounted on the back of a convex wide angle mirror, which is deployed in front of one of B2's cameras to provide a panoramic view of the surface.

The two greatest constraints for the development, not listed above, were those of time and money. Because of the late start date of this project – only two years before the launch date – the complete wind sensor development design, construction and calibration was to be completed within six months (this was later extended to twelve months). Secondly, no funds from Beagle 2 were available for the wind sensor development.

These last two constraints - money and time - demanded a wind sensor technology which could be manufactured and tested entirely in-house, i.e. at Oxford University. Because of this approach, no costs were incurred from external contractors. Equally importantly, many rapid cycles of prototype design, construction, testing and redesign were achieved; in the seven months of prototype development (June – December 2001) we designed and built no fewer than eleven *different* prototype sensors. Most of these are shown in Figure 4.3, including the final Flight Model (FM) sensor and electronics.

4.1.4 Deliverable models

It is convenient at this stage to mention the 'model philosophy', i.e. the different deliverable models required. The B2WS consists of a sensor head as well as an electronics board. Three identical Flight Model (FM) sensor heads were constructed at the same time, all of which were calibrated using the same procedure. One of these ('FM4') was delivered as the FM to go to Mars, the other two (FM1 and FM2) were designated as flight spares, and used for further performance testing. Because of the very short calibration time available, subsequent performance testing forms a very important part of the understanding of sensor performance. As a result, an important criterion for sensor design was that the FM sensors be very similar to each other. Earlier deliveries included an Accommodation Model (AM) and a qualification model (QM).

Electronics deliveries consisted of one QM and one FM version of the electronics board. A flight spare (FS) and a proto-flight model (PFM) were also built using the same printed circuit board design. The QM and the PFM used slightly different resistor values to the FM and FS. Additionally, a breadboard version of the electronics with non-final resistances, designated the Electronics Ground Support Equipment (EGSE-1a), was used during FM sensor calibration in place of the FM electronics, which had not yet been manufactured.

4.1.5 Beagle 2 Temperature Sensor (B2TS)

The Beagle 2 air temperature sensor was already designed by the time the B2WS development started. Interpretation of data from any thermal wind sensor requires good knowledge of the air temperature, as discussed in Chapter 2; therefore the B2TS is described here in detail. It consists of a negative temperature coefficient (NTC) thermistor element encapsulated in a small glass bead which is roughly 0.3 mm long x 0.2 mm diameter. This is supported on four platinum wires, 30 µm in diameter x ~3.5 mm long, which also provide an electrical interface. The resistance of the thermistor varies from

Figure 4.3 – A gallery of photos of various B2WS protoypes.

roughly 4 kΩ at 0°C to 140 kΩ at –70°C. Onboard Beagle 2, this resistance is measured by putting it in series with a 50 kΩ resistor, making a potential divider.

The original air temperature sensor was mounted on the edge of one of the main solar panels. The solar panels can get quite hot during the day, so a sensor in this mounting position will not provide a very representative temperature for the free atmosphere. For the B2WS, moreover, an air temperature measurement near the wind sensor is needed. Therefore, a second air temperature sensor was added, identical to the first. This sensor is mounted ~5 cm away from the wind sensor, as shown in Figure 4.1 (it was not yet mounted on the PAW when the photo in Figure 4.2 was taken). The temperature of this mounting position is expected to be quite similar to that of the surrounding air [Peskett, 2001], due to its exposed position to airflow and distance from the main heated portion of the lander. All subsequent references to an air temperature sensor in this document will refer to this second sensor, labelled in B2 documentation as the ‘wind air temperature sensor’.

Some rough calculations were performed to estimate the error in temperature measurement. Since the air temperature sensor is not the main subject of this thesis, these calculations are not presented here in full; only the results are given. The maximum power dissipation in the bead is only ~ 30 μW, so self-heating should not be severe – self-heating is estimated to cause an error of only ~ 0.05 K. Sunlight falling directly on the bead may cause a further temperature increase of ~ 0.5 K. Also of concern is conduction from the lander; this would be far greater if it were not for the very small diameter (30μm) of the wires by which the bead is supported. At low wind speeds, conductive coupling of the bead to the lander is expected to be only ~ 1/40 as great as the coupling to the air, in which case $T_{measured} \sim T_{air} + (T_{lander} - T_{air})/40$. Therefore, if $T_{lander} - T_{air} = 10$ K, the temperature error would be only +0.25 K. The response time of the sensor is not known, but simple aerodynamic calculations suggest it may be of the order of ~ 5 seconds.

The calibration of the temperature sensors will be described in Section 5.1 below. It consisted only of a resistance-temperature characterisation of the sensor heads, without flight-like electronics or cables. The accuracy of the temperature measurement, including the calibration error as well as the above uncertainties, is estimated to be ± 1 K [Towner *et al.*, 2003]. Uncertainties regarding the accuracy of the air temperature measurement would favour the design of a wind sensor which is not particularly sensitive to errors in measured air temperature. This has implications for the choice of B2WS data interpretation procedure, as will be discussed below.

4.2 Sensor head design / construction

4.2.1 Choice of thermal anemometry

As discussed in Section 2.2 above, thermal anemometry is the only wind-sensing technique which has been used on Mars before; this is due to its simplicity and low mass. The extremely short development time available for the Beagle 2 wind sensor precluded prolonged development and optimisation of any other technique. Oxford University’s Engineering Department was already proficient at the design and in-house manufacture of a range of thermal sensors, of both hot-film and hot-wire varieties.

A *static* thermal anemometry approach was chosen, meaning that the sensor is in a steady state when turned on (if in a steady wind field). This is in contrast to a time-of-flight sensor or one in which heating is pulsed or cycled on and off. These dynamic solutions require more sophisticated electronics, as well as user input to set various parameters. For the B2WS development we had neither the time to develop a sophisticated electronics package nor the possibility of digital telemetry with which to communicate to the B2WS electronics *in situ*. Without the possibility of sending commands to the wind sensor, many of the advantages afforded by using a dynamic sensor are lost. Therefore, a simple, static anemometry solution was adopted for Beagle 2.

In addition to the sensor performance targets noted above, another one specific to thermal anemometry may be added here. As discussed in Chapter 2, the overheat ($T_{wire} - T_{air}$) should be much greater than the air temperature fluctuations. These fluctuations can be as large as 20 K during the day [Schofield *et al.*, 1997], so a goal of $T_{wire} - T_{air} = 100$ K should be aimed for.

4.2.2 Choice of films rather than wires

Hot-film and hot-wire designs can both be used for wind sensing. The sensing elements in each can be made to have small surface areas and small sensor masses, crucial to achieving low power consumption and a low response time. The fundamental performance difference between them lies in the fact that the hot film is in contact with the substrate supporting it. This complicates the thermal design of hot-film sensors, as one cannot ignore conductive heat transfer between the film and the substrate. However, the substrate provides mechanical support to the hot films, which ensures that the sensor will survive the high mechanical loads (vibration and shock) experienced by the sensor during takeoff and landing. This was a deciding factor in the B2WS design, as the short development time precluded repeated cycles of design/manufacture/vibration testing which would be necessary to qualify a hot-wire design for flight.

4.2.3 Choice of substrate

The first prototype built (B2WS-V4) consisted of 4 platinum films on a glass tube, 3mm in diameter (this is the first picture in Figure 4.3). This prototype demonstrated that the design concept worked, showing that the local heat transfer coefficient exhibited a strong angular dependence. However, the thermal conductivity through the glass tube is fairly large compared with the convective heat transfer to ambient, so the entire surface of the glass tube was at a temperature approaching that of the hot films. As a result, this model required ~100 mW of power in each film alone in still wind conditions, despite only achieving an overheat of $\Delta T = 65$ K. The final B2WS circuit can dissipate only 35 mW per film; therefore this first sensor design would not be able to achieve a sufficiently high overheat. Even if the sensor diameter were reduced to 2 mm – the narrowest which would have been feasible for in-house manufacture – this design would still have required too much power.[*]

---

[*] One feasible solution would have been to use the ‘triple-split fibre’ probe manufactured by Dantec, mentioned in Chapter 2 [Jørgensen, 1982]. This has a diameter of only 400 µm, so would almost certainly have a sufficiently low power consumption to be useable. However, the price of the sensor put it beyond reach of the B2WS development.

As a result of this first prototype's performance, a new technique was adopted for the next prototype. Rather than use a fairly high-conductivity substrate, allowing the entire circumference of the cylindrical substrate to get hot, a substrate with very low thermal conductivity was chosen. This, combined with small, distantly-spaced hot films, was used in a hope that most of the heat energy dissipated in the films would remain in a very small area of the surface, i.e. local to the films themselves, rather than be conducted through the substrate. The degree to which this was achieved will be addressed in Chapter 5.

The glass tube was replaced with a cylinder of Rohacell. Rohacell is a rigid polyimide foam with extremely low thermal conductivity of only $k = 0.03\ \mathrm{W\ m^{-1}\ K^{-1}}$ at 1 atm, and $k = 0.01$ to $0.02\ \mathrm{W\ m^{-1}\ K^{-1}}$ at Martian pressures [Caps & al., 1997]. The variant used for the B2WS has a density of only 51 $\mathrm{kg\ m^{-3}}$. A less dense variant exists, with a density of 31 $\mathrm{kg\ m^{-3}}$, but it proved less robust and not as readily machinable. Rohacell's outgassing properties have been measured by NASA and are found to be acceptably low [NASA EPIMS database]. Due to this combination of properties Rohacell is often used as insulation for space purposes, for example it is used elsewhere in the Beagle 2 lander.

Rohacell is a closed-cell foam. This may cause structural change during pressurization and depressurization. Because Rohacell's pore size is very small (< 100 µm), the structure remains intact thanks to the relatively rigid polyimide skeleton. In the longer term, the internal gas pressure stabilises to that of the external atmosphere through diffusion, though it is not known how fast. Open-cell polyimide foams do exist [see e.g. Caps 1997], but it was impossible to procure a space-qualified version for this experiment.

Does this affect the performance of the Beagle 2 wind sensor? In Section 5.4, data will be presented which show that the calibration of the sensor did not change over a period of four months, despite repeated cycling between 1000 and 5 mbar. Once arrived on Mars, the ambient pressure on Mars will not vary by more than ± 1 mbar, and that at rates far slower than experienced in the lab. However, the rate of gas diffusion through the Rohacell is not known, so the potential effect on the stability of the calibration remains a concern.

4.2.4 Choice of film geometry

The hot films consist of platinum sputtered onto a 50 µm thick Kapton substrate. The film has an inverted "U" shape, as shown in Figure 4.4. At either end, the platinum film widens to form a solder pad onto which electrical connections can be made. Electrical current is passed between these wires, causing ohmic heating in the film. Most of the ohmic heating occurs in the narrow top section of the film, due to its high electrical resistance.

The area and geometry of the film crucially determine sensor performance. A relatively high length-to-width ratio is needed in order to achieve a high film resistance (needed because only a small current may be drawn from the lander). Another advantage of a narrow sensing element is that it allows for better resolution of wind direction. Early prototypes, which had hot films covering almost ~10 $\mathrm{mm^2}$ each, were found to require too much power (only a 35°C overheat would have been attained given the power available). The penultimate prototype, with a hot film area of only ~3 $\mathrm{mm^2}$, exhibited relatively low power consumption; however, only a very small proportion of the heat dissipated in the film was being lost to convectively to wind, leading to a relatively low signal level. Therefore the final FM

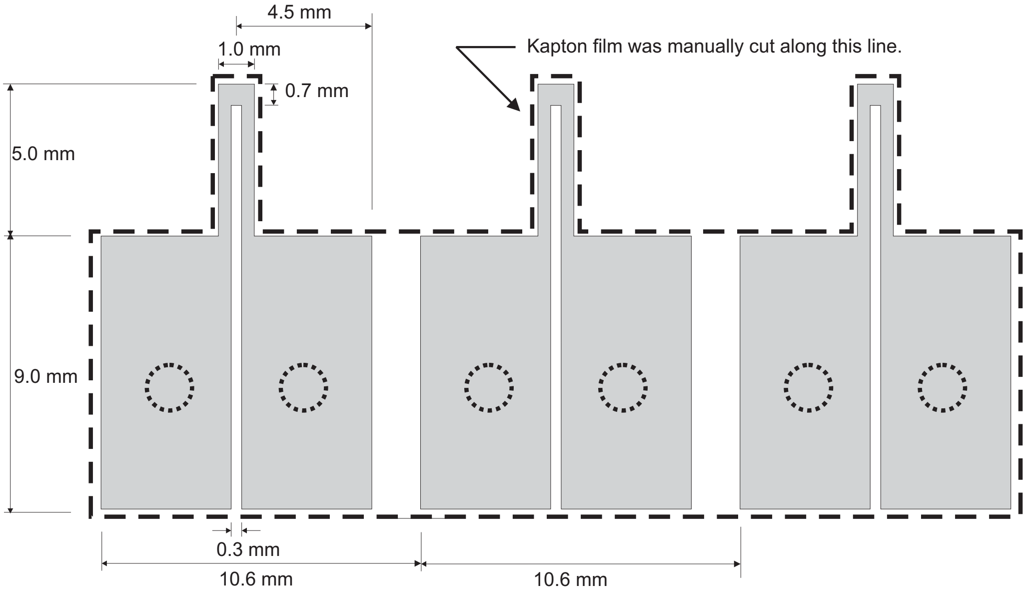

Figure 4.4 – The hot film geometry for the flight model B2WS sensors. The Kapton film was cut manually along the dotted line as shown (with an accuracy of ~ ±0.2 mm) before being bonded to the Rohacell substrate. The round dotted circles indicate the approximate positions of solder connections.

design has an intermediate hot film area of ~5 mm^2. This allows operation at an acceptably high overheat of 40 - 80°C, while maintaining a high signal level.

The shape of the solder pads, i.e. the widened areas at the bottom of the film, is also important. The solder pad acts as a low-thermal-conductivity, air-cooled link between the hot film itself and the rest of the circuit. This minimises heat losses down the wires to the lander. There will obviously be a temperature gradient in the solder pad area of the platinum film: a rough calculation shows that the film temperature decreases by a factor 1/*e* for every 1-2 mm moved down the film, depending on wind speed. In the FM, therefore, ~ 5 mm are left between the solder connection and the hot film itself. If this distance were increased it would lead to more electrical resistance, and thus more heat dissipation, in the solder pad area of the platinum film. It can be shown analytically that the optimal geometry would consist of an exponential increase in the width of the film from the base of the constriction; however the final shape used (as shown in Figure 4.4) provides reasonable performance.

4.2.5 Film manufacture

Early prototype films were made by manually cutting the required shape out of a sheet of Kapton onto which a uniform platinum film had been deposited. The accuracy of this technique was only ~ ± 0.3 mm. Though this was well suited to the production of prototypes, a higher reproducibility was required for the Flight Model sensors. The FM films were therefore made by starting with a copper-coated Kapton sheet, then using photolithography to etch a mask in the copper layer. Platinum was deposited through this mask using a sputtering process. Finally the copper layer was removed using an acid treatment. This leaves a thin layer of platinum, whose shape is determined by the mask. Thus, all films produced have the same shape, to an accuracy of order 1 μm. To ensure that the relative positions of the film are the same in all FM sensors, three films were manufactured on one strip of Kapton, which was then positioned around the Rohacell cylinder as can be seen in Figure 4.3. However, much of the Kapton between the hot films themselves is cut away, as can be seen in Figure

4.3; this is done in order to reduce the sensitivity of the sensor to sunlight (Kapton film has a higher absorptivity than Rohacell at visible frequencies).

The Kapton film is held in place using a thin layer of epoxy adhesive. To ensure that the final shape of the Kapton film was as cylindrical as possible, a purpose-built cylindrical clamp was applied during the curing process.

The thickness of the platinum film is not known. The thickness of the platinum film was selected by varying the deposition time until the finished film had a resistance of 155 Ω ± 5 Ω. This resistance would be expected from a film of platinum ~10 nm thick, based on the resistivity of solid platinum. However, the properties of these thin films vary somewhat from those of bulk platinum. For example, the temperature coefficient of resistivity α ($\alpha =$ proportional change in resistance per degree temperature rise) for the B2WS films was measured to be 2.02×10^{-3} K^{-1} at 25°C, a figure much smaller than the value of 4×10^{-3} K^{-1} typical for bulk platinum at this temperature. The measurement of resistance as a function of temperature will be described in Section 5.1 below.

4.2.6 ‘Annealing’ of films

The stability of the films was investigated at length using the QM wind sensor head, and later with the FM sensors as well. The resistances of all films were found to decrease by ~5% within the first few hours of use (see Figure 4.5). This is attributed to some kind of annealing process. As a result, all FM wind sensor heads were subjected to an acceptance procedure which included 500 on/off cycles (each lasting 1 minute) as well as periods of continuous operation, resulting in a cumulative operation time of ~50 hours at Martian pressures. This cycling was done to ‘anneal’ the sensors before any calibration was started.

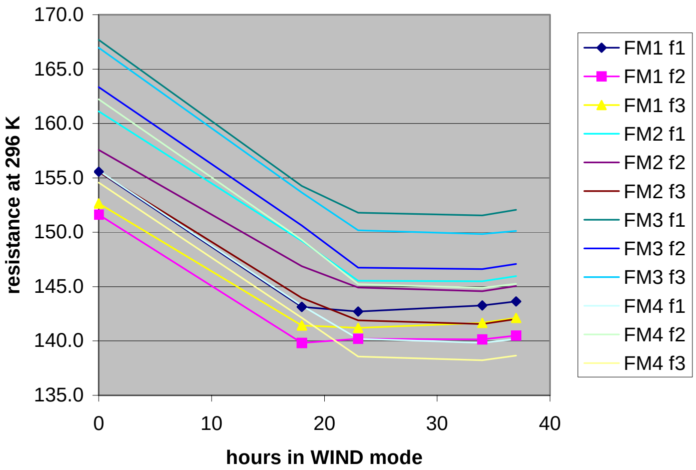

Figure 4.5 – During the first few hours of use, the resistance of all films was found to drop by ~5%. After this initial period, the resistances were stable.

A QM sensor head was subjected to extensive on/off cycling at room pressure surrounded by carbon dioxide ice, such that its temperature varied from ~196 K when off to ~250 K when on. It survived this test with no detectable effect on the film resistance or sensor performance, so no cold cycling (i.e. in dry ice or liquid nitrogen) was specified for FM acceptance testing (pre-calibration). Flight Model sensors were later subjected to temperatures of -70° C for several hours during calibration in a cryostat. This caused no detectable change in the sensor performance.

4.2.7 Electrical interface

The electrical interface of the wind sensor head consist of six wires (two per film), the other end of which is connected to the B2WS electronics board. The electrical interface at the sensor head has to satisfy the following requirements. Firstly, there must be some strain relief to prevent any forces on the wires from being transmitted to the fragile solder joints on the platinum films. Secondly, it must be possible to replace the sensor with a Flight Spare sensor head in case of damage during assembly. Thirdly, it should have a low thermal conductivity, to minimise conductive heat loss from the films.

To satisfy these conditions, the electrical interface is made via six solder pins on a ‘contact board’, which is a small printed circuit board that is bonded to the underside of the wind sensor. From this circuit board, six wires run up through holes in the Rohacell to the films. These wires are stainless steel rather than copper, in order to provide a low thermal conductivity link to the film. This does increase the lead resistance by 0.4 Ω/conductor, but this is negligible compared with the R_{film} ~140 Ω. The contact board is largely sheltered from Martian dust, as it is in the hollow of the Wide Angle Mirror, and protected by the Rohacell base of the wind sensor. Nevertheless, it has been covered in Uralane (a conformal coating) to protect it from any adhered dust. The Uralane coating also seals the through-holes in the Rohacell base to dust and provides strain relief for the steel wires running through them. The contact board is shown in Figure 4.6.

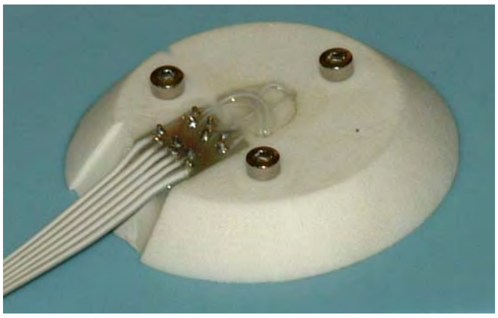

Figure 4.6 – View of the underside of wind sensor. A small PCB bonded to the underside of the wind sensor provides an electrical interface. This provides strain relief and allows replacement of the wind sensor in case of damage during assembly.

4.3 Electronics design

4.3.1 Choice of constant-current or constant-temperature anemometry

The electronics must dissipate a known amount of power in each film, while measuring the film’s temperature, and then transmit the information to Earth. The traditional approach used for hot-wire or hot-film anemometry is the constant temperature anemometry (CTA) circuit shown in Figure 2.3. In this approach, a simple feedback circuit is used to maintain the heated film at a certain resistance. This set resistance corresponds to the desired film temperature. The main advantage of this approach is that it is capable of a very fast response time, although this is somewhat compromised in non-isothermal fluids as in the Martian PBL.

However, an important disadvantage of the simple CTA circuit is that it is unable to respond to a change in the film’s resistance. Specifically, the B2WS films have a resistance of about 140 Ω at 293

K, with a temperature coefficient α ~ 0.0021 K^{-1}. Therefore, for a temperature overheat of 100 K, the set resistance would need to be $R_{set} = R_{ref}\left(1+\alpha\left(T_{set} - T_{ref}\right)\right)$ = 169.4 Ω. The resistance of the film may either decrease over time due to erosion by windblown dust, or increase due to accretion of electrically conductive dust. If the resistance of the films were to increase, the R_{set} of the CTA circuit would only correspond to a mild overheat, if any at all, which would render the film inoperative. If the resistance of the films were to decrease when on Mars, the set resistance would correspond to a much higher temperature, in which case the films might reach unsustainably high temperatures!

The above discussion reveals that it is necessary to have some mechanism for coping with changes in the resistances of the films over the lifetime of the mission. An important step in achieving this is to be able to measure the resistance of the film when it is cool. Even if a classic CTA circuit is modified to allow this measurement, however, it is not trivial to construct the circuit to adjust its resistors in order to correct the operating temperature T_{set}, especially when no control inputs are available from Earth.

Another factor specific to the B2WS development is that it was impossible to have coaxial cables between the sensor head and the electronics; instead the B2WS had to use spare conductors on a ribbon cable common to all PAW instruments. The CTA circuit is a feedback circuit, so any interference picked up in these long conductors might be amplified, making the circuits unstable.

For the above reasons it was decided to use a ‘constant current’ approach circuit, using the circuit shown in Figure 4.7. This circuit dissipates a nearly constant amount of power in each film, and incorporates a second low power mode which allows measurement of the film’s resistance. This circuit incorporates two sensing modes (TEMP and WIND) without the need for a separate control line. On power-up, the electronics start in a low power (TEMP) mode, in which only ~ 1 mW is dissipated in the sensor. After 33 seconds, it switches to a high power mode (WIND) mode, in which ~35 mW are dissipated in the film. The electronics remain in WIND mode until they are next powered off and back on again. This is illustrated in the sample output graph shown in Figure 4.8. The transition between modes at t = 33 s is clearly visible.

At the heart of the circuit is a simple voltage divider. In the low-power ‘TEMP’ mode, the film is placed in series with a 1.5 kΩ resistor. For WIND mode, a timing circuit switches a transistor, adding a 200 ohm resistor in parallel with the 1.5 kΩ resistor, allowing a far higher heater current to pass through the film. The output voltage from this voltage divider is amplified using an op amp. The offset of the op amp is changed between TEMP and WIND modes to deal with their different voltage ranges, using the same switching transistor mentioned above.

It may be noted that only 35 mW of power is dissipated in each film. This may seem a small proportion of the total power available for B2WS (out of 250 mW total power available), so I will briefly suggest how this could be improved in future models. In the CCA circuit, some power needs to be dissipated in the bridge (specifically, in the resistor R_{WIND}). The optimal sensitivity for sensing R_{film} is obtained when $R_{WIND} = R_{film}$. However, a smaller R_{WIND} leads to greater power dissipation in the hot film and thence higher sensitivity to wind; bearing this in mind, the optimal balance is $R_{WIND} = \frac{1}{2} R_{film}$.

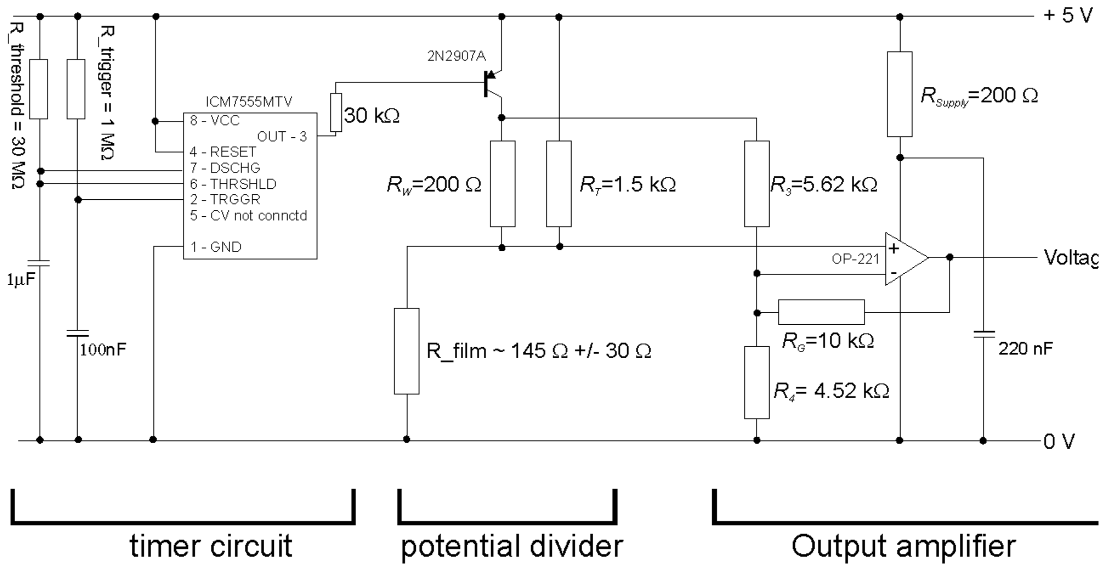

Figure 4.7 – Circuit diagram of a single circuit of the wind sensor electronics. The timer circuit, at the left of the diagram, was shared between all three circuits. A photo of the final FM electronics can be seen in Figure 4.3.

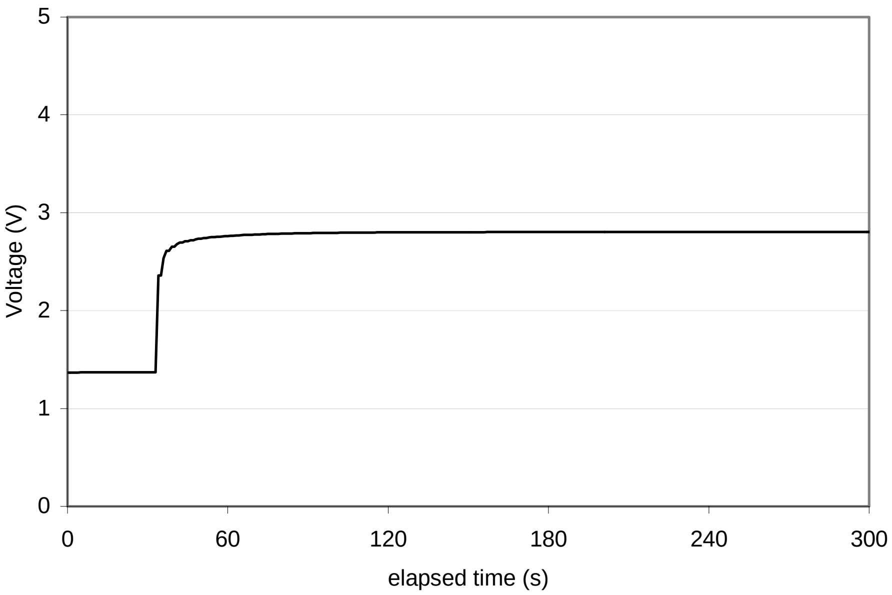

Figure 4.8 – Output voltage on a single channel, as a function of elapsed time after power-up. The transition between TEMP mode and WIND mode can be clearly seen at $t = 33$ s. Following this change one can see that the sensor takes up to 60 s to warm up fully. These data were obtained using FM electronics and an FM sensor head, in air at 12.0 mbar (this is the same density as is expected at the Beagle 2 landing site).

The power supply allows a maximum of 80 mW per circuit (one circuit for each film) at 5V, which leads to an optimal total $R_{WIND} + R_{film} \sim 300\ \Omega$; therefore the optimal value of R_{film} is about 200 Ω. Use of this greater film resistance would result in a higher overheat, 40% greater than that obtained with the B2WS-FM films of ~ 145 Ω. However, this is unachievable given the present film geometry as it would necessitate that the films be even thinner than they currently are, which was deemed not robust enough based on previous experience. If repeating the development, a double-U shaped film might be used instead of a single U; this geometry would easily allow a film resistance of 200 Ω. This would result in a higher q_{film} of perhaps 50 mW, which would allow an operating overheat of $\Delta T = 100$ K on Earth, up to 115 K on Mars.

4.3.2 Electronics output

The output from a single channel as a function of air temperature and wind speed is shown in Figure 4.9. This model assumes that the test gas is CO_2 at $p = 7.9$ mbar and $T = 250$ K, and that the film is facing at 50° to the upwind direction, and is thus experiencing the maximum possible heat transfer. This calculation uses wind tunnel test data which will be presented in Chapter 6. However, it is included here to clarify the function of the electronics. It can be seen that the temperature sensitivity of the film output is ~2.5 mV/K and ~12 mV/K in TEMP and WIND modes respectively. The absolute accuracy of the ADC reading the output voltage is expected to be ~2.5 mV, so this leads to a temperature accuracy of ±1 K and ±0.2 K in TEMP and WIND modes respectively.

Better resolution and accuracy could have been obtained by using a higher gain. However, this was impossible because of two main constraints. Firstly, the op amp used, which was the only flight-rated op amp available on such short notice, was only specified to have an output range of only ~1.1 – 4.0 V over the full temperature range of operation, so output voltages had to be kept within this range. Furthermore, some margin was left to allow full use of the sensor even if the film resistance should increase or decrease by ±10% on Mars. The strategy of using a single op amp for both WIND and TEMP modes resulted in a necessarily limited sensitivity in TEMP mode, but it has also minimised power consumption in the electronics.

This figure also clearly illustrates the fundamental handicap of using thermal wind sensors on Mars, namely the inability of a single sensor to distinguish between a change in air temperature and a change in wind speed. A rise in the output signal of 100 mV, for example, might signal either an air temperature increase of 8°C or a fall in wind speed from 14 m/s to 7 m/s[*]. In the next chapter, the thermal performance of the sensor is analysed, and a technique is proposed for combining data from the three films and the air temperature sensor in order to distinguish between temperature and wind speed fluctuations.

From the voltage outputs, the film resistances are calculated using the equations shown in Figure 4.10. The temperature of each film is then calculated from the film resistance, using $R_{film}(T)$ calibration

---

[*] Note that the sensor response does not vary linearly with wind speed.

curves, whose measurement will be described in Section 5.1. The remainder of the data interpretation procedure will be explained in Chapter 5.

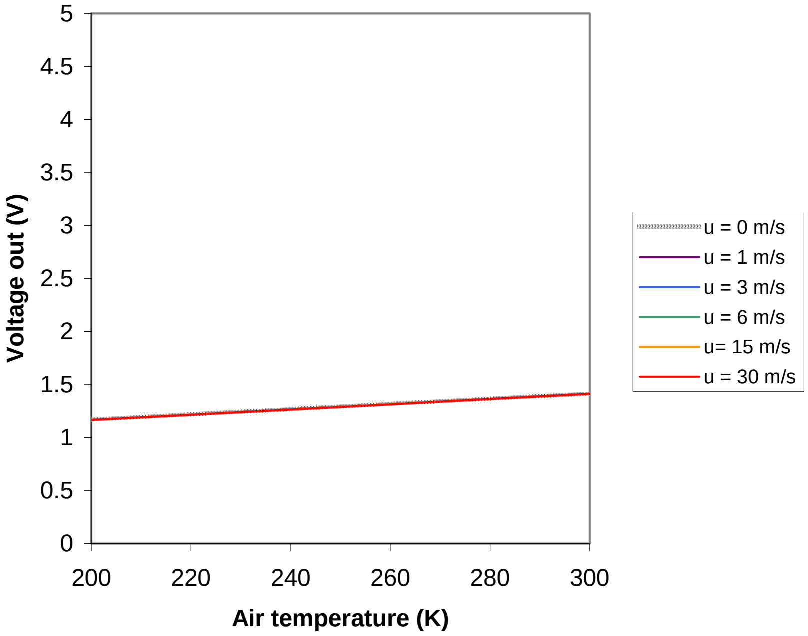

a)

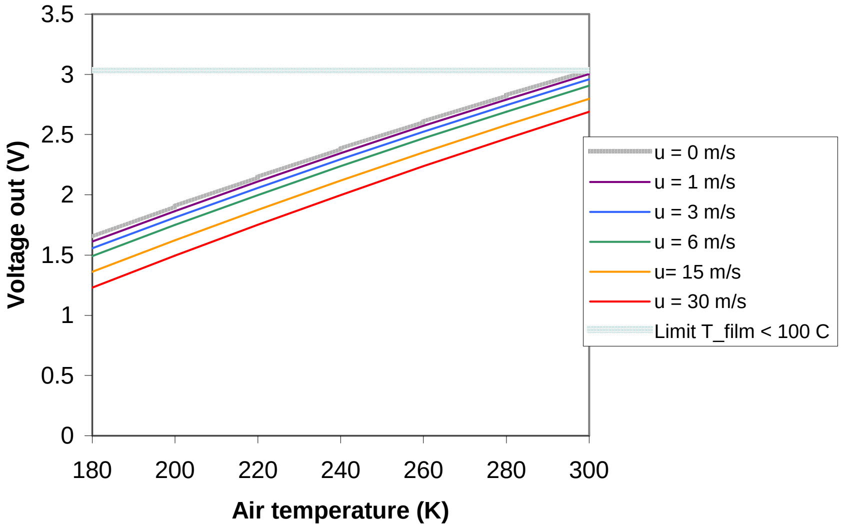

b)

Figure 4.9 – Approximate output voltages from the wind sensor electronics with an FM wind sensor head in different air temperatures and wind speeds, a) in TEMP mode, and b) in WIND mode. Calculations assume a film whose resistance $R = 140\ \Omega$ at $T = 293$ K. These output voltages are for a film experiencing maximum possible heat transfer rates, i.e. facing ~ 50° from the wind direction. The wind speeds shown assume a CO_2 atmosphere at 7 mbar and 250 K.

TEMP MODE:

$$Gain_{TEMP} = 1 + \frac{R_G}{R_4}$$

$$V_b = \frac{V_{out}}{Gain_{TEMP}}$$

$$R_{film} = \frac{R_T}{\frac{V_+}{V_b} - 1} - R_{leads}$$

$$q_{film} = R_{film}\left(\frac{V_b}{R_{film} + R_{leads}}\right)^2$$

WIND MODE:

$$Gain_{WIND} = 1 + R_G\left(\frac{1}{R_3} + \frac{1}{R_4}\right)$$

$$V_b = \frac{V_{out}}{Gain_{WIND}} + \frac{\left(V_+ - \Delta V_{sw}\right)}{Gain_{WIND}}\frac{R_G}{R_3}$$

$$R_{film} = \frac{1}{\left(\frac{1}{R_W} + \frac{1}{R_T}\right)\left(\frac{V_+}{V_b} - 1\right) - \frac{\Delta V_{sw}}{V_b R_W}} - R_{leads}$$

$$q_{film} = R_{film}\left(\frac{V_b}{R_{film} + R_{leads}}\right)^2$$

Symbols:

$R_{W,\,T,\,G,\,3,\,4}$	resistors
R_{leads}	resistance of leads between sensor head and electronics (~ 3 Ω per film).
V_+	Positive supply voltage
ΔV_{sw}	voltage drop across 2N2907A in WIND mode
V_{out}	Output voltage
V_b	‘Bridge’ voltage at positive input of op amp

Figure 4.10 – Equations used to calculate a film resistance from each of the three voltage outputs of the B2WS electronics.

4.3.3 Sensitivity of output to exact resistance values

During initial analysis of the calibration data, an apparent discrepancy of almost 10% was found between the effective gains of the different channels of the EGSE-1 electronics. Eventually, it was discovered that this was due to differences of only 0.5% in the exact value of resistor R_{WIND} in different channels of the EGSE. This resulted in an error of 0.4% in the calculated film resistance, i.e. about 0.6Ω. This, however, represents quite a large error in the calculated film temperature, of about 2.5 K or 4% of the overheat $T_{film} – T_{air}$. This problem was compounded by similar discrepancies in the channels between the exact values of other resistances, which in this case doubled the size of the error. This error was easily corrected by simply measuring the exact resistance values in the EGSE electronics box and then using these exact values to re-process the data. The effect which this uncertainty will have on calculated wind speeds will be discussed later, once the data interpretation procedure has been presented.

Chapter 5 - B2WS: Performance & calibration tests

In this chapter is described the experimental testing of the wind sensor. Before discussing the aerodynamic testing which forms the core of the wind sensor calibration, two other tests are described. Firstly, a calibration was performed of the temperature dependence of resistance, not only of the wind sensor but also of Beagle 2's temperature sensors. Secondly, the wind sensor's dependence on ambient pressure and dissipated power was tested in still-wind conditions. Then, the main calibration sequence for wind speed and direction dependence is described. With this background, the procedure of how to calculate a wind vector from sensor outputs is proposed. A further series of tests investigated the sensor's response to step changes in wind speed.

5.1 Temperature – resistance calibration

Calculation of sensor performance requires knowledge of the temperature of the hot films. This temperature is obtained from the film resistance, as calculated from the sensor output voltages as explained in Figure 4.10. The temperature dependence of the resistance was initially obtained over the temperature range 20 °C < T < 50°C using a water bath. However, for a more accurate determination of $R_{film}(T)$ it was decided to run a more accurate calibration over a larger temperature range, from –70°C to +70°C. Though less than the -100°C to +100°C temperature range which might be experienced by the hot films in use on Mars, this is the greatest temperature range for which a calibration could be arranged in time for flight model delivery.

While performing this calibration for the wind sensor films, it was simultaneously performed for the Beagle 2 temperature sensors. This is useful, as good accuracy in the temperature measurement is needed to obtain good accuracy in the wind measurement.

5.1.1 Apparatus for temperature calibration

The four B2WS FM sensors were mounted in an aluminium block, to ensure that they were all at the same temperature. The block is shown in Figure 5.1. Also mounted in the isothermal block were three flight model Beagle 2 temperature sensors (B2TS), as well as four platinum resistance thermometers used to measure temperature in the wind tunnel. A reference temperature standard measurement was obtained using a Rhodium-Iron reference standard sensor, which had been calibrated to an accuracy of better than ± 5 mK. Although all sensors, including the vulnerable B2WS films, were not directly touching the aluminium block, they were all within 2 mm of the surrounding aluminium walls.

This block, containing the sensors, was placed inside a cryostat. The cryostat consisted of an inner chamber, filled with helium at 1 atm, in which was suspended the isothermal block. Helium was used to ensure good heat transfer both between the block and the temperature-controlled cryostat walls, and between the sensors and the block. This inner chamber was covered in an insulating jacket of multi-layer insulation (MLI) – this is shown in Figure 5.2 – and placed in a vacuum jacket, to minimise radiative heat transfer from the outside. This cryostat had been developed for temperature sensor calibrations to accuracies of ~ 1 mK [Peters, 2004]. For the current calibration, however, only an accuracy of 50 mK was needed, so the inner chamber (containing the isothermal block) was not evacuated during the measurement.

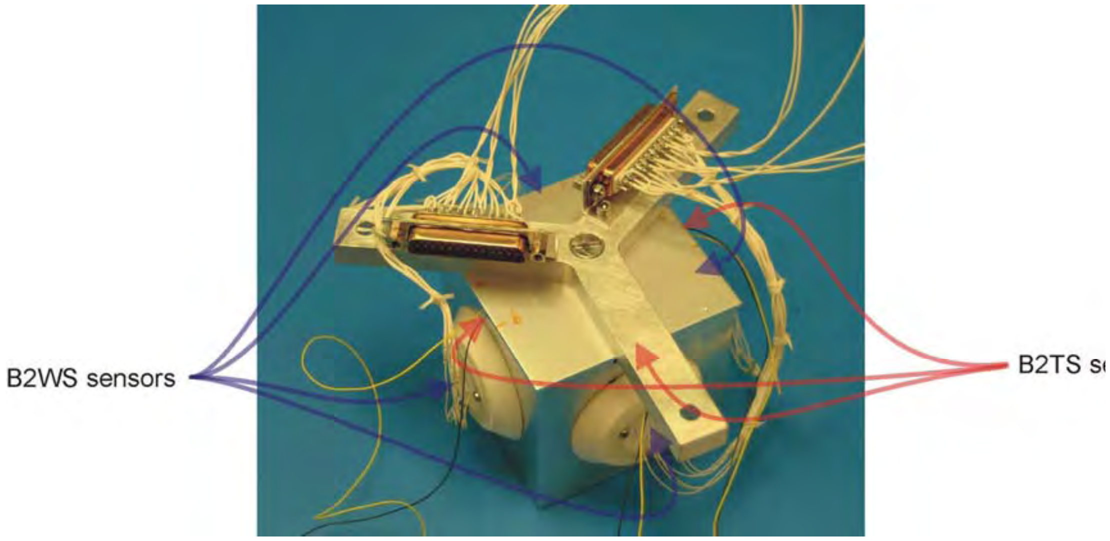

Figure 5.1 – Isothermal block showing FM wind sensors (B2WS) and FM temperature sensors (B2TS) in place for resistance-temperature calibration. The block is upside-down; in the top face (not visible) were four platinum resistance thermometers used in the wind tunnel and a reference RhFe temperature sensor.

Figure 5.2 – Photograph of cryostat. Visible here is a jacket of multi-layer-insulation (MLI) which surrounds a central chamber. The central chamber contains the isothermal block shown above. The walls of the central chamber, under the MLI jacket, are cooled using a closed-cycle refrigerant loop. The whole assembly shown above is insulated using a vacuum jacket, the O-ring seal of which can be seen on the circular base-plate.

Thin conductors (30 awg) were used for all connections between the sensors and equipment outside the cryostat in order to prevent any heat loss though the cryostat walls; four-wire resistance measurements were used in order to counteract the high resistance of the electric pass-throughs.

The B2WS film resistances, and those of the reference sensor, were measured using an AC bridge. Some self-heating of the sensors was observed and corrected for, by measuring the self-heating as a function of power dissipated in the sensor and then extrapolating to zero power consumption. Resistance measurements were taken at 25°C, 10°C, -10°C, -30°C, -50°C, -70°C, followed by -50°C, -30°C, -10°C, 10°C, 30°C, 50°C, 70°C, 50°C, 30°C, and then finished off by taking another measurement at -70°C, and then again at 20 °C. After changing the set temperature, the cryostat was left to reach thermal equilibrium for at least six hours before the next reading. The temperature drift during measurements was typically only 1 mK/ minute, showing that a high level of temperature stability had been reached.

Some self-heating was observed in B2WS, PRT and RhFe sensors. This was corrected for by making 4-wire resistance measurements using different sensing currents, and then extrapolating the results to find what the resistance would be with zero current.

5.1.2 Results

The results for a single film (B2WS-FM1, film 1) are shown in Figure 5.3a. A quadratic fit, i.e. $R = a_1 T^2 + a_2 T + a_3$, was found to provide a good fit to the data, to an accuracy of ± 0.1 Ω over the whole range. This error corresponds to ~ 0.3 K. The difference between the actual resistance and that calculated using this quadratic approximation is shown in Figure 5.3b.

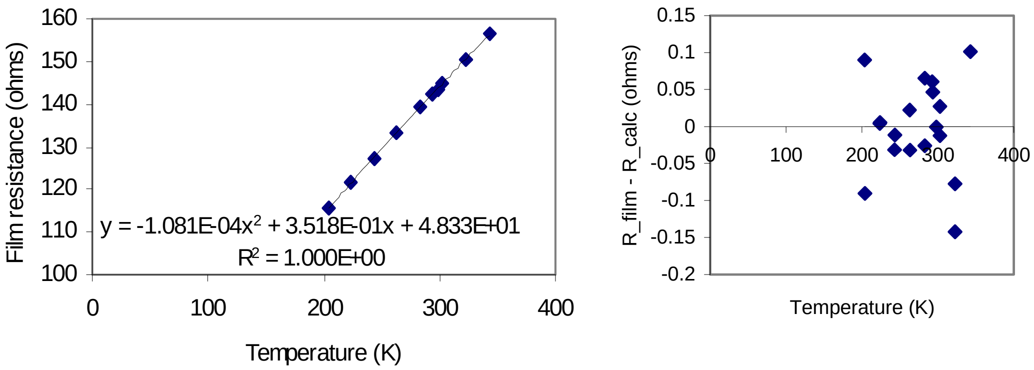

Figure 5.3 – The left panel shows measured film resistance of B2WS-FM1-f1 (film 1 of FM1) as a function of temperature. A quadratic equation was found to fit the dependence well; the right panel shows that this prediction works well to an accuracy of ± 0.1 Ω.

All wind tunnel tests described later in this chapter were performed at or near room temperature. The range of temperatures experienced by the films in these tests was 20ºC - 90ºC. Over the range 20ºC < T_{film} < 70ºC it was found that the $R_{film}(T)$ data were satisfactorily fit by:

$$R(T) = R_{T=293\text{ K}}\left(1+\alpha\left(T-293\text{ K}\right)\right),$$

using α = 0.00209 K^{-1}. This equation described the $R(T)$ data to within ±0.1 Ω over this range. Therefore this simpler dependence was used for all data interpretation described in this chapter. The full quadratic fit will be used to interpret data from Mars.

The resistances of the Beagle 2 temperature sensors were recorded, also in a 4-wire measurement, using a Fluke 88242 precision multimeter. They could not be measured with the AC bridge because of their high resistance (up to 140 kΩ at -70°C). My preliminary analysis of the data suggests an accuracy of ± 0.25 K (this is the level of repeatability observed). Further analysis of the temperature sensor data has been left to the ESS Co-Investigator responsible for the temperature sensors[*].

5.2 Sensor performance in no wind

5.2.1 Dependence on dissipated power

Figure 5.4 shows the overheat $\Delta T = (T_{film} - T_{air})$ for varying amounts of power dissipated in the film, in the range $20\ \text{mW} < q_{film} < 40\ \text{mW}$. To obtain these data, a simple version of the B2WS electronics circuit was used, and different currents were obtained by varying the resistance used for R_W. It can be seen that, to a first approximation, ΔT is proportional to the power dissipated in the film, q_{film}.

Because of this proportionality, the output of each channel will be expressed from now on as a 'conductance' $C_{film} = q_{film} / (T_{film} - T_{air})$. The film temperatures of each of the three films are obtained from the sensor output voltages first by using the equations of Figure 4.10 to calculate the film resistances, then by using the $R(T)$ data presented above. The use of the term 'conductance' for C_{film} may be misleading, because this C_{film} is due to a combination of radiation, convection and conduction; therefore it is not a constant, but will vary with wind speed and direction, and with gas pressure and temperature, and with changing radiative environment such as sunlight shining on the sensor, and indeed with ΔT. This near-proportionality between ΔT and q_{film} is not expected to hold true for the whole range of environmental conditions; however, use of this ratio $C_{film} = q_{film}/\Delta T$ to express the B2WS outputs allows comparison of results from different versions of the B2WS electronics, which used different power dissipations.

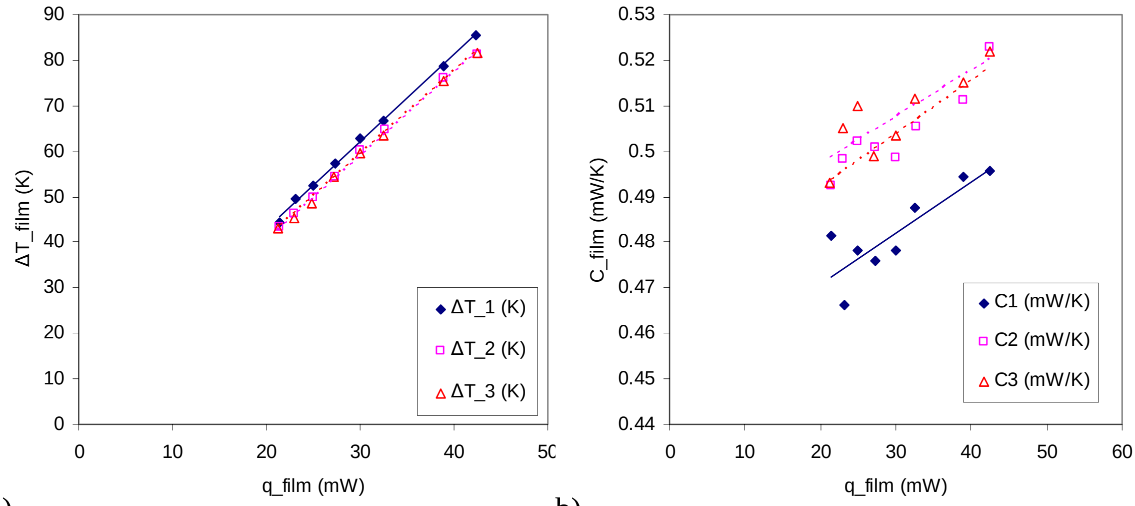

a) b)

Figure 5.4a shows the overheat $\Delta T_{film} = (T_{film} - T_{air})$ achieved as a function of power dissipated in the film, for the three films of sensor FM2 in still air. Figure 5.4b shows the same information, plotted as $C_{film} = q_{film}/\Delta T_{film}$. These measurements were obtained in air at $p = 5.9$ mbar, at $T = 293$ K.

---

[*] Dr. Martin Towner at the Open University

If one plots C_{film} against q_{film} (as in Figure 5.4b), one can see that there is only a slight variation of ~ 1% in C_{film} over the range of 32 mW < q_{film} < 37 mW. This particular range represents the range of power outputs of different prototypes of wind sensor electronics used in B2WS testing. Specifically, the electronics module EGSE-1a – which was used for the bulk of FM wind tunnel calibrations – dissipated 32 mW in each film rather than the 35 mW which the FM electronics module produces. The data shown in this graph suggest that this difference in q_{film} produces only a mild (< 1%) effect on the sensor output in no wind.

The different values of C_{film} for the different films may be due to differences in the thermal contact underneath the different films, or perhaps to blemishes in the films themselves – this latter condition would lead to localised changes in resistance and thus variations in local heating along the film. Though the resistances of the different films varied by a few ohms, it was found looking at the different FM prototypes that variations in C_{film} were not correlated with resistance differences between the films.

5.2.2 Dependence on pressure

Figure 5.5 shows the output of the three films as a function of operating pressure, in air. As above, the sensor output is expressed not as an overheat ($T_{film} – T_{air}$) but as a ratio $C_{film} = q_{film} / (T_{film} – T_{air})$. To obtain these data, the operating pressure of a test chamber containing the FM2 wind sensor was slowly reduced as far as possible; then, air was slowly re-admitted.

Possibly the most important result of this test is that, at Martian pressures, the still-wind sensor performance is only very weakly dependent on ambient pressure. This suggests that free convective heat transfer, which is dependent on pressure, plays a relatively weak role in heat transfer in still wind. In the next chapter, a thermal analysis of the sensor will confirm this analysis, showing that heat transfer from the sensor in still air is largely through radiation and gaseous conduction, neither of which varies with pressure.

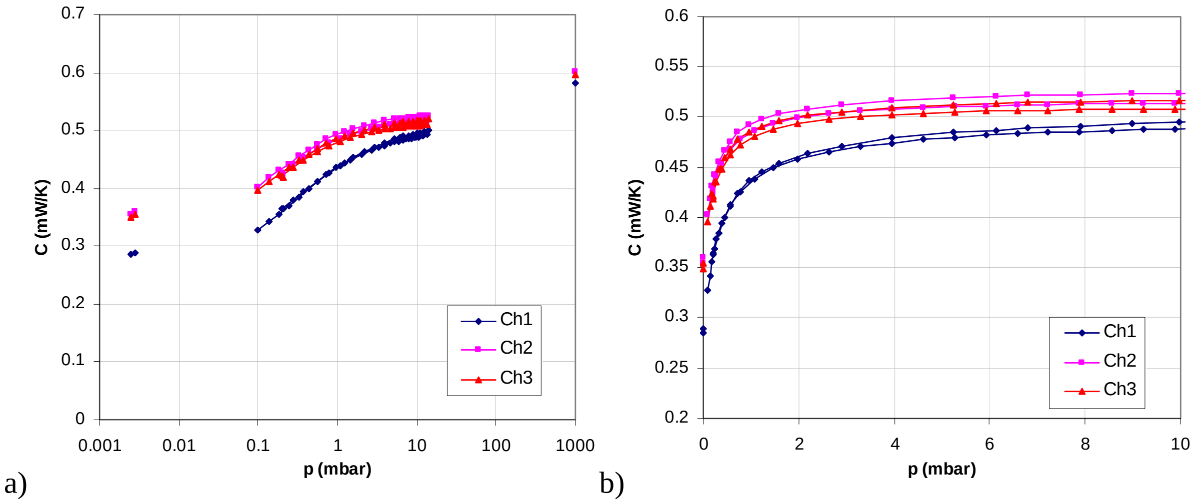

Figure 5.5 – Pressure dependence of the sensor output C_{film}, shown as a function of pressure. Note that the left panel shows a logarithmic pressure scale, while the right panel shows a linear plot of $p < 10$ mbar. Experimental data were obtained in air at $T = 293$ K.

The experimental points are qualitatively in agreement with the analytical prediction, though the latter appears to overestimate the free convection at higher pressures. The analytical model allows us to confirm that at the lowest pressure attained experimentally, $p = 0.0025$ mbar, convective and conductive heat transfer through the gas are negligible. This is a reasonable assumption because the mean free path at this pressure is of the order of a few centimetres, i.e. greater than the diameter of the sensor.

Note the slight hysteresis in the points obtained. This is probably due to adiabatic temperature changes in the air, as it was being depressurised during the first run and repressurised during the next. This effect may have been particularly acute because the rate of change of pressure in this experimental run was relatively rapid, in that only 30 seconds were allowed for the sensor to reach equilibrium after each pressure change. This hysteresis was not observed in experimental runs in the wind tunnel, when longer periods of time were allowed to reach equilibrium. To find out whether adiabatic heating was responsible for the observed hysteresis, a fine-wire thermocouple should have been placed in the test chamber to measure the air temperature – however, this was not done.

5.3 Sensor performance in wind

5.3.1 Wind testing procedure

The main calibration of FM wind sensors was performed in a single week in February 2003. All tests were performed using the same EGSE electronics box (EGSE-1a), which uses the same circuit as the flight electronics but only dissipates 32 mW of power in each film rather than 35 mW. Tests were not performed using an FM electronics board because it was not yet available. A later calibration of the Flight Spare wind sensor head (FM2) was performed using the flight-like protoflight model (PFM) electronics to validate the earlier calibration.

These tests were all performed in air, at room temperature, using the wind tunnel described in Chapter 3. The main calibration sequence was the following:

1- Turn on wind sensor, record TEMP mode output at 0.2 Hz for 30 s.

2- Switch to WIND mode.

3- With film 1 facing upstream (angle = 0º), record output (average voltage over 1 second).

4- Rotate 9º, wait for *t* seconds, record output ($t = 5$ s for main calibration run).

5- Repeat steps 3-4 at 18º, 27º, … , 360º, and then at 360º, 351º, … 9º, 0º.

6- Repeat steps 3-5 at flow speeds of $Re_{ave} \sim 4, 16, 36, 64, 100, 144, 196$. This corresponds to flow velocity in the centre of the test section of $Re = 7, 22, 45, 76, 115, 161, 216$.[*]

---

[*] All Reynolds numbers quoted for B2WS testing are calculated using a characteristic length scale of $D = 1$ cm, the diameter of the wind sensor. Note that this is in contrast to Reynolds numbers quoted in Chapter 3, which were calculated using $D = 18$ cm, the diameter of the wind tunnel's test section.

The test pressure for most tests was a nominal p_{test} = 7 mbar – which, due to the error in pressure measurement explained in Chapter 3, means a real p_{test} of 5.3 mbar. It was only possible to maintain this nominal p_{test} = 7 mbar up to Re_{ave} = 144. For higher wind speeds, a nominal test pressure of p_{test} ~ 10.5 mbar was used. This is based on the premise that sensor performance varies with *Re*, and not with p_{test}. This premise will be validated below.

These flow speeds were chosen because the sensor needs high resolution particularly at low wind speeds.

5.3.2 Basic dependence on angle and wind speed

Figure 5.6 shows the basic output of three films at Re = 116, which is equivalent to 10 m/s on Mars (CO_2, p = 7mbar, T = 250 K). As above, output is expressed as $C_{film} = q_{film}/(T_{film} - T_{air})$. It can be seen that, for a given output from films 1, 2, and 3, there is a single possible value of wind speed and direction.

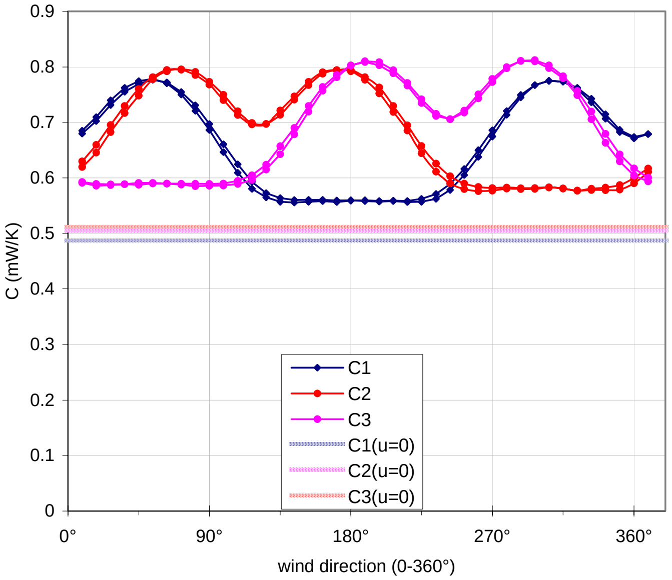

Figure 5.6 – Sensor output C_{film} of the three B2WS film as a function of wind direction, at wind speeds of *Re* = 0 and *Re* = 160. Data obtained during a rotation of the sensor from 9° to 369°, and then back again.

Note also that some hysteresis is evident in this figure, due to the non-zero response time of the sensor to changes in wind direction. These data were obtained using a wait time of t = 5 s; in this case the hysteresis is very small. To eliminate this hysteresis effect from the calibration data, the two data points obtained at each angle were simply averaged to give a single value. The response time of the sensor will be discussed in more detail in connection with full data retrievals below in Section 5.5.

Figure 5.7 shows the output of a single film, as a function of angle, for different wind speeds. Hysteresis has been removed as detailed above. Overlaid on this plot is $C(p = 0)$, i.e. the output without convection or gas conduction, obtained from Figure 5.5. Note that the maximum heat transfer occurs when the film is pointed at ~ 50 to 55 ° to the upwind direction. This figure may be compared with the calibration plot for the Pathfinder wind sensor, shown in Figure 2.7. Though not directly comparable because the axes are different, the double-peaked dependence on wind direction is clearly evident in both plots.

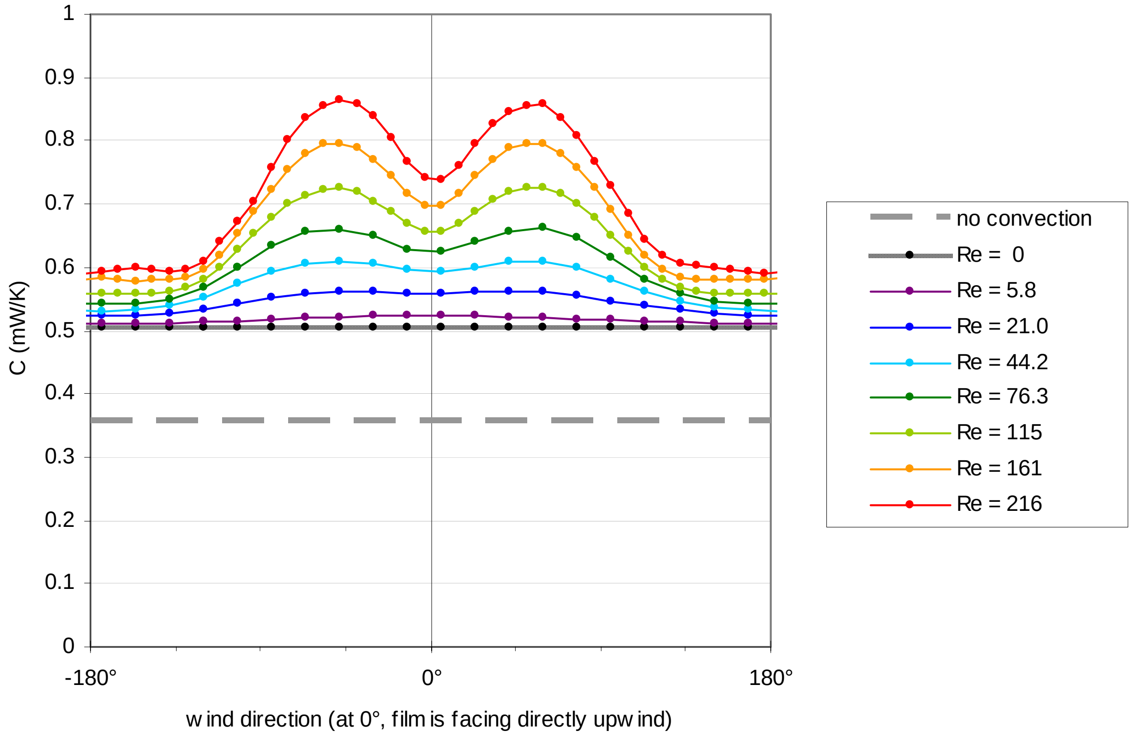

Figure 5.7 – Response of a single B2WS film as a function of wind direction, shown for different wind speeds. Sensor performance is expressed as a ratio $C = q_{film} / \left(T_{film} - T_{ambient} \right)$. The grey dotted line at the bottom of the figure is the value of C_{film} measured at p = 0.002 mbar.

5.3.3 Effect of gas density

Aerodynamic theory says that the effects of different gas density can be eliminated by expressing the wind speed and heat transfer in dimensionless form, as Reynolds and Nusselt numbers respectively. They are defined as

$$Re = \frac{uL\rho}{\mu} \qquad , \qquad Nu = \frac{h_{conv} L}{k}$$

where u represents flow velocity, L is a characteristic length of the system (we shall use the diameter of the sensor, 10 mm, for this quantity), h_{conv} is the heat transfer coefficient associated with convection, and ρ, k and μ represent respectively the fluid’s density, viscosity and conductivity. Though one might normally use $L = 1$ mm (the width of the film) for Nusselt number calculation, I have used $L = 10$ mm (the diameter of the sensor) in the calculation of both Nu and Re for convenience.

A complication arises in that we do not know exactly how much of the heat transfer from the sensor is due to convection. The approach used here is to simply subtract the sensor output when there is no wind – denoted $C_{film}(u{=}0)$ or just $C(u{=}0)$ – from the sensor output in wind. Dividing this by the area of the hot film then gives an effective convective heat transfer coefficient h_{conv}, from which a Nusselt number can then be calculated. The revised equation is therefore:

$$Nu_{film} = \frac{\left[C_{film} - C_{film}(u=0) \right] D_{sensor}}{A_{film} k_{fluid}}$$

The symbol k_{fluid} denotes the thermal conductivity of the fluid. This is a function of temperature, varying roughly as $T^{1.4}$. It is common practice to evaluate k_{fluid} at a 'skin temperature'[*] which is the average of the fluid temperature and the hot surface's temperature. This has *not* yet been done for B2WS, mainly due to the complexity introduced in the data analysis procedure. Determining the appropriate skin temperature is not trivial because, as seen in the analytical calculations which will be presented in next chapter, much of the heat transfer from the B2WS is from the exposed surface of the Rohacell, for which a lower skin temperature would be appropriate than for the film. The viscosity μ used in the calculation of Reynolds number Re, too, has been calculated using the free air temperature rather than a 'skin temperature', for the same reasons. How best to choose an appropriate skin temperature might be a useful topic to explore in future.

A number of tests were performed using carbon dioxide and air at different pressures. Figure 5.8 shows, for several different test gas conditions, sensor output C_{film} as a function of flow speed in m/s. These data are presented again in Figure 5.9, in dimensionless form; the Nusselt number has been calculated as set out above and has been plotted against Reynolds number.

It can be seen that this approach succeeds in reducing data points for different gas conditions onto one dimensionless curve (for each angle).

5.4 Data interpretation procedure

The term 'data interpretation' will be taken to mean the processing of raw spacecraft data – the three output voltages from the wind sensor, as well as data from the temperature and pressure sensors – to arrive at a calculated wind speed and direction. In Chapter 4 it was explained how the film resistances are calculated from the voltage outputs from the B2WS electronics. In this chapter it has been explained that the sensor output can be expressed as a ratio $C_{film} = q_{film}/(T_{film} - T_{air})$, where the film temperatures are obtained from the film resistances using $R(T)$ calibration data. Finally, it has been shown that differences in gas properties can be accounted for by expressing the heat transfer coefficient at the sensor as a Nusselt number $Nu = C_{conv}D/kA$, where it is assumed that the convective heat transfer from the sensor C_{conv} is given by $C_{film} - C_{film}(u=0)$. In this section is explained how the three Nusselt numbers (one for each film) are used to calculate a wind vector. Some flexibility is available here because one has three degrees of freedom (three voltages, or equivalently three Nusselt numbers) to calculate a two-dimensional wind vector.

For the Mars Pathfinder wind sensor, the *average* temperature of all the hot elements was used to calculate a wind speed; then, the remaining information was used to calculate a wind direction. That

---

[*] Sometimes called 'film temperature' – this nomenclature is not used here because film temperature has other connotations in this work.

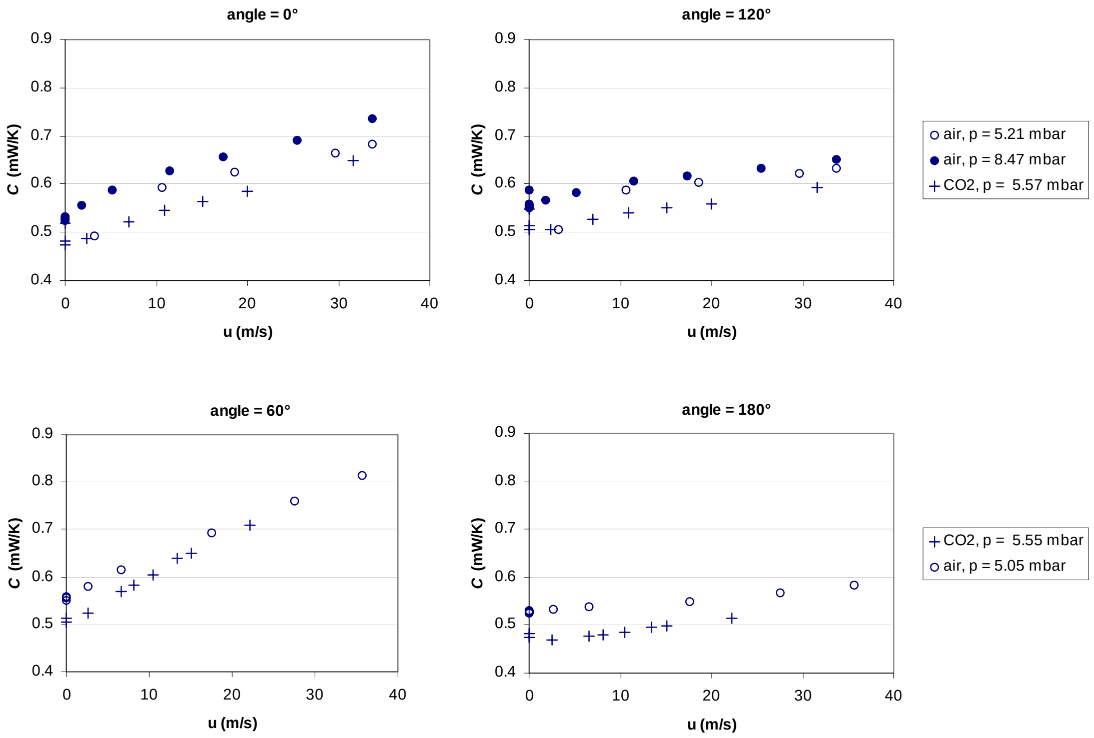

Figure 5.8 – These graphs show response of a hot film to wind speed: sensor output C_{film} is plotted again wind speed *u* (m/s). Data is presented for different wind directions; the angle between the film and th upwind direction is given at the top of each graph.

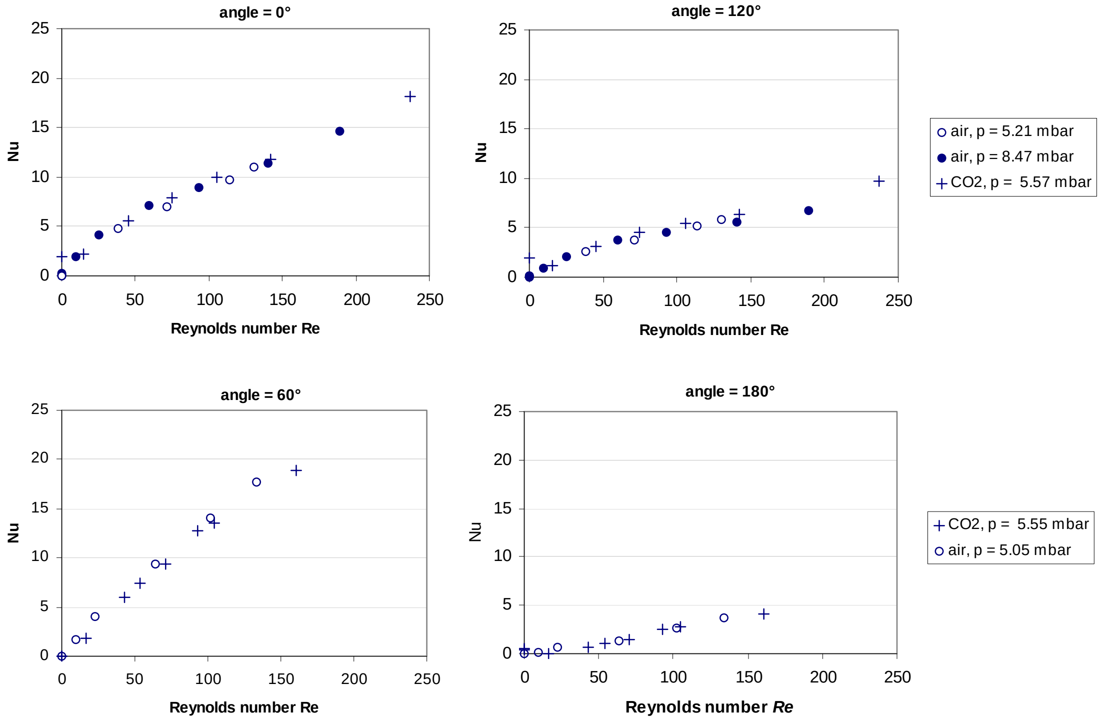

Figure 5.9 – These graphs show the same data as Figure 5.8, but in dimensionless form; sensor response expressed as Nusselt number *Nu* and is plotted against wind speed, expressed as a Reynolds number *Re*.

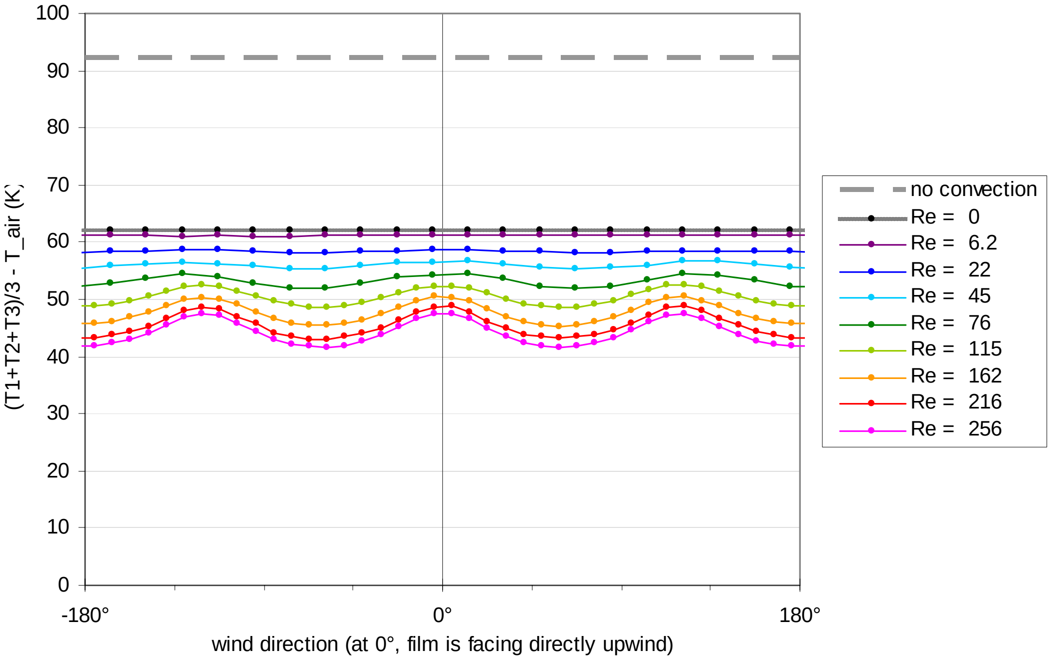

Figure 5.10 – This shows the average overheat of the three films during a calibration run. Derived from same data as is shown in Figure 5.7.

approach would not work directly for B2WS, because the average of the film temperatures is not independent with respect to wind direction, as shown in Figure 5.10. This is because the B2WS has only 3 hot elements compared with the Pathfinder wind sensor's 6 elements.

The approach taken here will be to discard the common-mode variability of the sensors (e.g. $T_1 + T_2 + T_3$), and to obtain wind speed from the *differences* between the Nusselt numbers of the various films, as these differences are due mainly to local convective heat transfer. This approach therefore acts as a filter against changes which affect all films simultaneously, such as changes in air temperature and background temperature. The approach of calculating wind speed from the average temperature of the three films would be more sensitive to such common-mode changes. This statement will be supported by experimental evidence in below.

How, then, to extract a two-dimensional wind vector from three films? The technique used here is inspired by the work of Main *et al.*, (1996), who used a similar technique to measure a two-dimensional transverse wind vector using a four-hole pitot probe. If the azimuthal angles of the film are θ_1, θ_2 and θ_3, we can define three vectors $\underline{Nu}_1$, $\underline{Nu}_2$, and $\underline{Nu}_3$, which are respectively

$$\underline{Nu}_1 = \begin{pmatrix} Nu_1 \cos\theta_1 \\ Nu_1 \sin\theta_1 \end{pmatrix}$$
$$\underline{Nu}_2 = \begin{pmatrix} Nu_2 \cos\theta_2 \\ Nu_2 \sin\theta_2 \end{pmatrix}.$$
$$\underline{Nu}_3 = \begin{pmatrix} Nu_3 \cos\theta_3 \\ Nu_3 \sin\theta_3 \end{pmatrix}$$

We then define a vector $\underline{Nu} = \underline{Nu}_1 + \underline{Nu}_2 + \underline{Nu}_3 = (Nu_x, Nu_y)$, which can then be mapped on to the 2D wind field vector $\underline{Re} = (Re_x, Re_y)$. This process is illustrated in Figure 5.11.

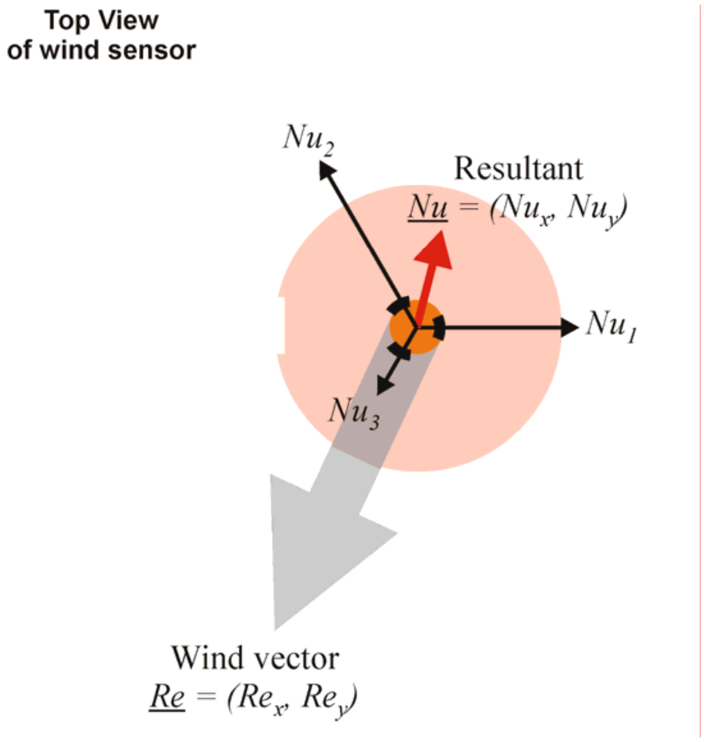

Figure 5.11 – Schematic representation of the data interpretation scheme. The heat transfer coefficient at each film is expressed as a Nusselt number *Nu*. The three *Nu* numbers are combined as described in the text to make a ‘resultant’ Nusselt vector *Nu*. This is then mapped against the non-dimensional wind vector *Re*.

If θ_1 is defined to be 0º, then $\theta_2 = 120°$ and $\theta_3 = 240°$, the above equations can be reduced to:

$$Nu_x = Nu_1 - \frac{1}{2}\left(Nu_2 + Nu_3\right)$$

$$Nu_y = \frac{\sqrt{3}}{2}\left(Nu_2 - Nu_3\right)$$

From the calibration data, we can tabulate the (Re_x, Re_y) values and corresponding (Nu_x, Nu_y) values. The entire set of calibration data for a given sensor can be conveniently displayed as a *calibration map*, which is a plot of (Nu_x, Nu_y) vectors for all the different wind speed vectors tested. This will then be used as a lookup chart which will be used to interpret data returned from Mars. The data interpretation procedure is summarised in Figure 5.12.

One item in this figure has not been discussed yet, and that is the possibility of picking a new $C(u=0)$, as a result of calibration *in situ*, essentially re-zeroing the sensor. This will be discussed later. At first, though, the values of $C(u=0)$ as measured in the lab will be used in the retrieval process, for all environmental conditions.

This may seem very surprising and unjustifiable, because $C(u=0)$ will vary with gas temperature and radiative environment. However, the choice of $C(u=0)$ is less of a potential source of error than it may seem. This is because the data interpretation is sensitive only to *differences* between the C of different

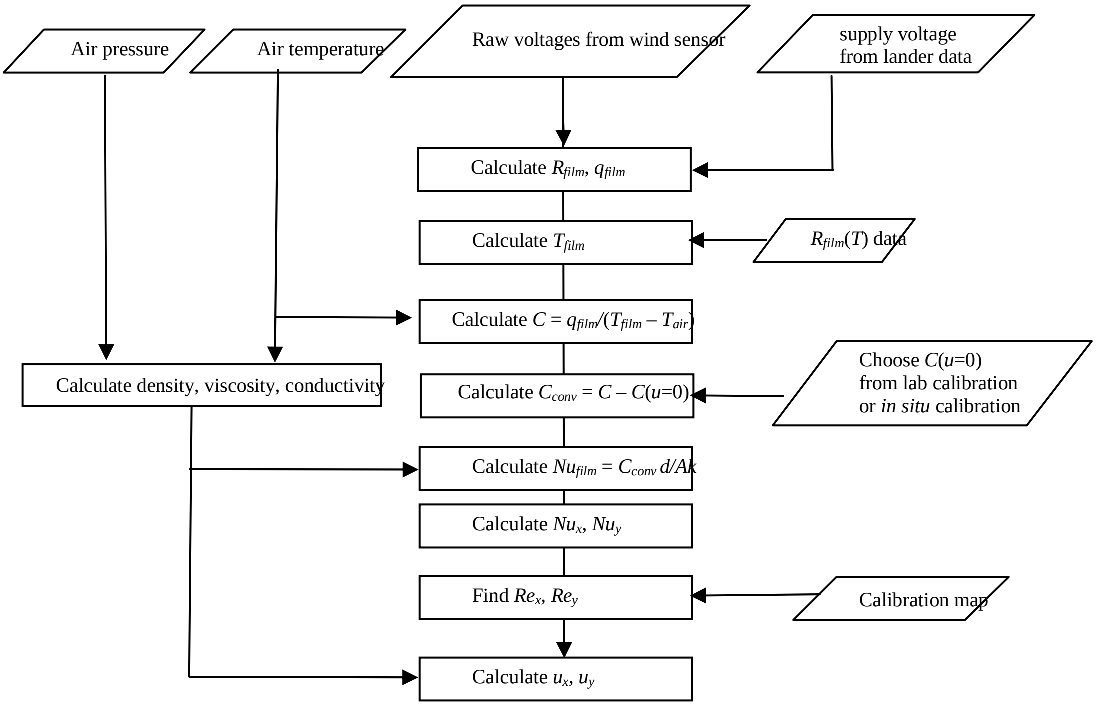

Figure 5.12 – Overview of data interpretation procedure. To create a calibration map, the last two steps are omitted, and measured values (Nu_x, Nu_y) and corresponding wind vectors (Re_x, Re_y) are tabulated.

films, rather than to its common-mode variability. This can be seen by re-expressing the above equations to calculate (Nu_x, Nu_y) in terms of C_1, C_2, and C_3:

$$\begin{aligned} Nu_x &= \frac{D}{kA}\left(C_1 - \frac{1}{2}\left(C_2 + C_3\right)\right) + \delta Nu_x \\ Nu_y &= \frac{\sqrt{3}D}{2kA}\left(C_2 - C_3\right) + \delta Nu_y \end{aligned} ,$$

where (δu_x, δNu_x) represents an 'error vector' given by:

$$\begin{aligned} \delta Nu_x &= \frac{1}{2kA}\left(2C_1\left(u=0\right) - \left[C_2\left(u=0\right) + C_3\left(u=0\right)\right]\right) \\ \delta Nu_y &= \frac{\sqrt{3D}}{2kA}\left[C_2\left(u=0\right) - C_3\left(u=0\right)\right] \end{aligned} .$$

This error vector expresses the error in calculated (Nu_x, Nu_y) due to differences between the films (note that if $C_1 = C_2 = C_3$ then $\delta C_x = \Delta\delta C_y = 0$). The information which has been discarded in the transformation from three variables (C_1, C_2, C_3) to two variables (δu_x, δNu_x) is the common mode variability, e.g. $(C_1 + C_2 + C_3)/3$. The magnitude of the error vector is relatively small. For the flight FM4 sensor the δNu error vector has a magnitude at $p = 7$ mbar in air of only 0.6; this, it will be seen, is equivalent to an error of ~ 1 m/s in wind speed. Failing to properly account for the variation in this vector will cause a small error in this vector, leading to a total error of < 1 m/s. This is small in comparison to other errors, as will be seen.

5.4.1 Calibration maps

The calibration maps for sensors FM1, FM2 and FM4, calculated as described above, are shown in Figures 5.13, 5.14 and 5.15 respectively.

Many details can be observed in these plots. Firstly, it is noted that a higher maximum speed was reached in the FM4 calibration than in the other two runs. This is because the vacuum pumping system can only operate for a limited amount of time at high speeds before overheating. Higher speeds were achieved in the FM4 calibration run than in the FM1 and FM2 runs. Note also that the outermost contour of the FM2 calibration map is out of symmetry with the rest of the calibration map. This is because the vacuum pump failed during this highest-speed run; for this reason it was impossible to remove hysteresis from half the data at this speed, which is why they appear out of place. Because the best and largest set of calibration data was obtained for sensor FM4, this was the one selected as the flight model.

Secondly, it can be seen that the plots exhibit fairly good three-way symmetry, i.e. symmetry when rotated by 120º. This implies that the aerodynamic performance of films is well matched, i.e. that the gain of all three films is equal (to within 3% for all films on all models; to within 1% for FM4). This is as expected, because the physical shape of each of the FM hot films is identical to within a few µm due to the photolithographic production process.[*]

Thirdly, it can be seen that the calibration maps for the three FM sensors are very similar to each other. To enable a better comparison, the three calibration maps are superimposed in Figure 5.16. On most of the plot, the Nusselt vectors match to $|\Delta Nu|/|Nu| < 5\%$. On the right hand side of the figure, there is a larger discrepancy for FM2 figures, with an error in $|\Delta Nu|/|Nu|$ of up to 10%. In any case, these discrepancies between the sensors are not very concerning, given that we have a calibration map for each sensor.

5.4.2 Repeat calibration of Flight Spare sensor

The main calibration maps presented above were all obtained using the EGSE-1a breadboard electronics board. It was unfortunately not possible to calibrate the sensors using the FM electronics board, as the latter had not yet been manufactured at the time of the wind tunnel calibration of the FM sensors. However, a second calibration of the flight spare sensor (FM2) was performed using a proto-flight model (PFM) electronics board. Though physically identical to the FM board, the PFM has slightly different resistances and therefore dissipates 37 mW of power per film – larger than both the FM (35 mW) and the EGSE-1a electronics (32 mW) used for the main calibration run. This second calibration, performed four months after the first, was intended to check that the original calibration was affected neither by the different electronics module used, nor by any drift in sensor properties over a 4-month period.

---

[*] (This was markedly not the case for most earlier prototype wind sensors, which were cut by hand. For these an effective area had to be assigned in order to make the magnitude of their responses equal).

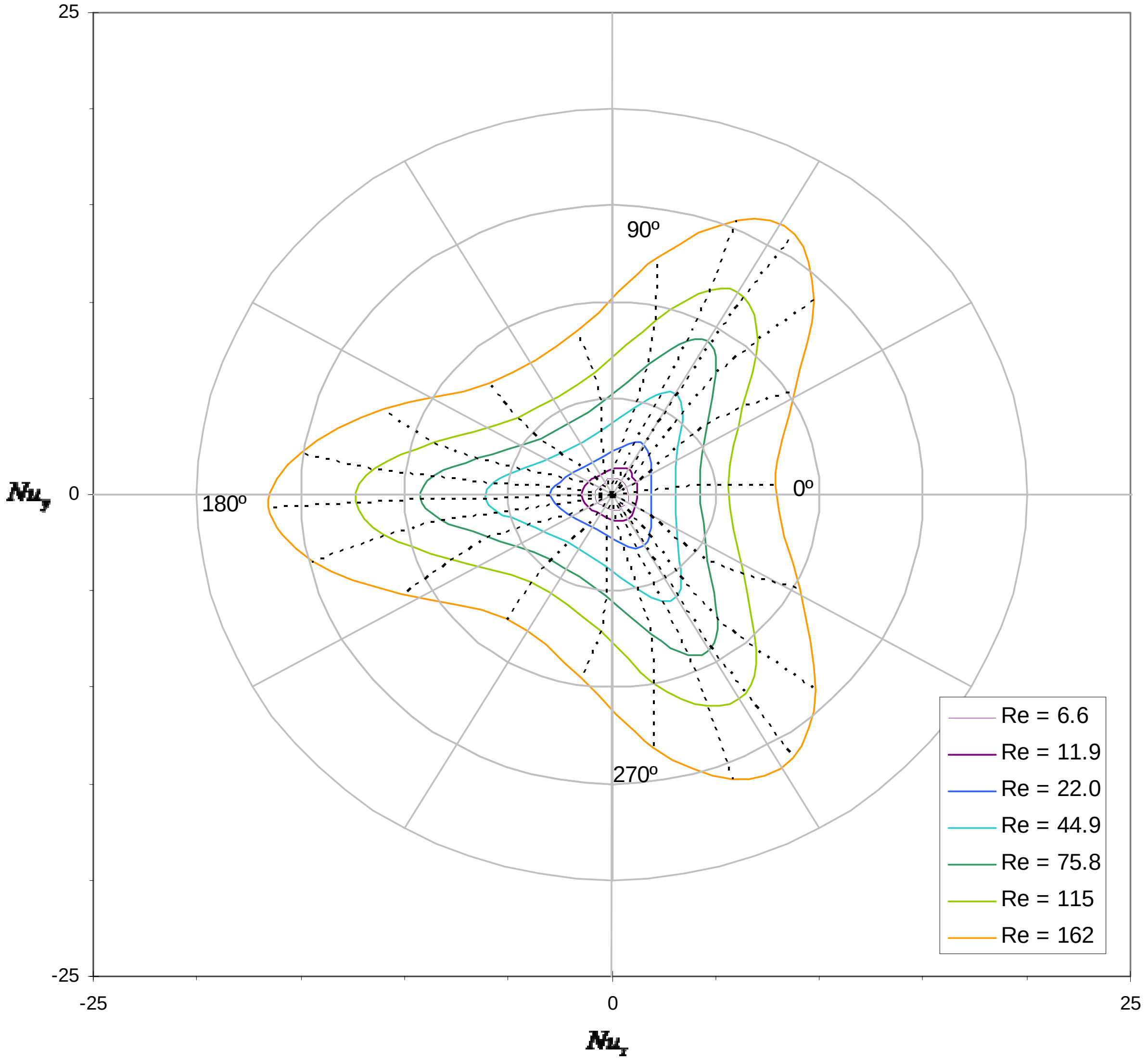

Figure 5.13 – Calibration map of B2WS-FM1 sensor head. See text for details.

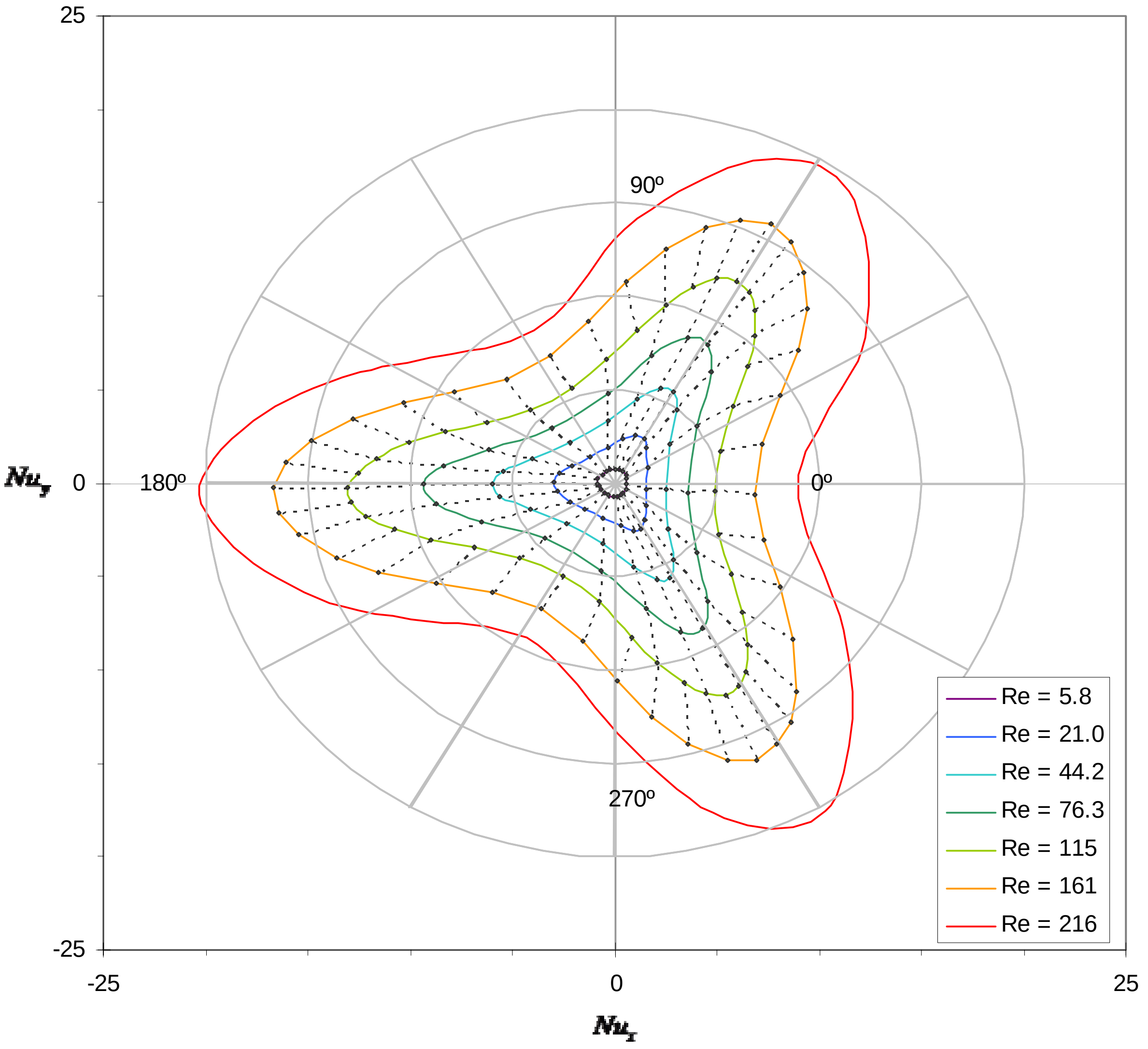

Figure 5.14 – Calibration map of B2WS-FM2 sensor head. Note that some of the contour at Re = 216 was not corrected for hysteresis (rotation was only completed in one direction). For this reason this last contour is not considered accurate, and is not reproduced in subsequent plots.

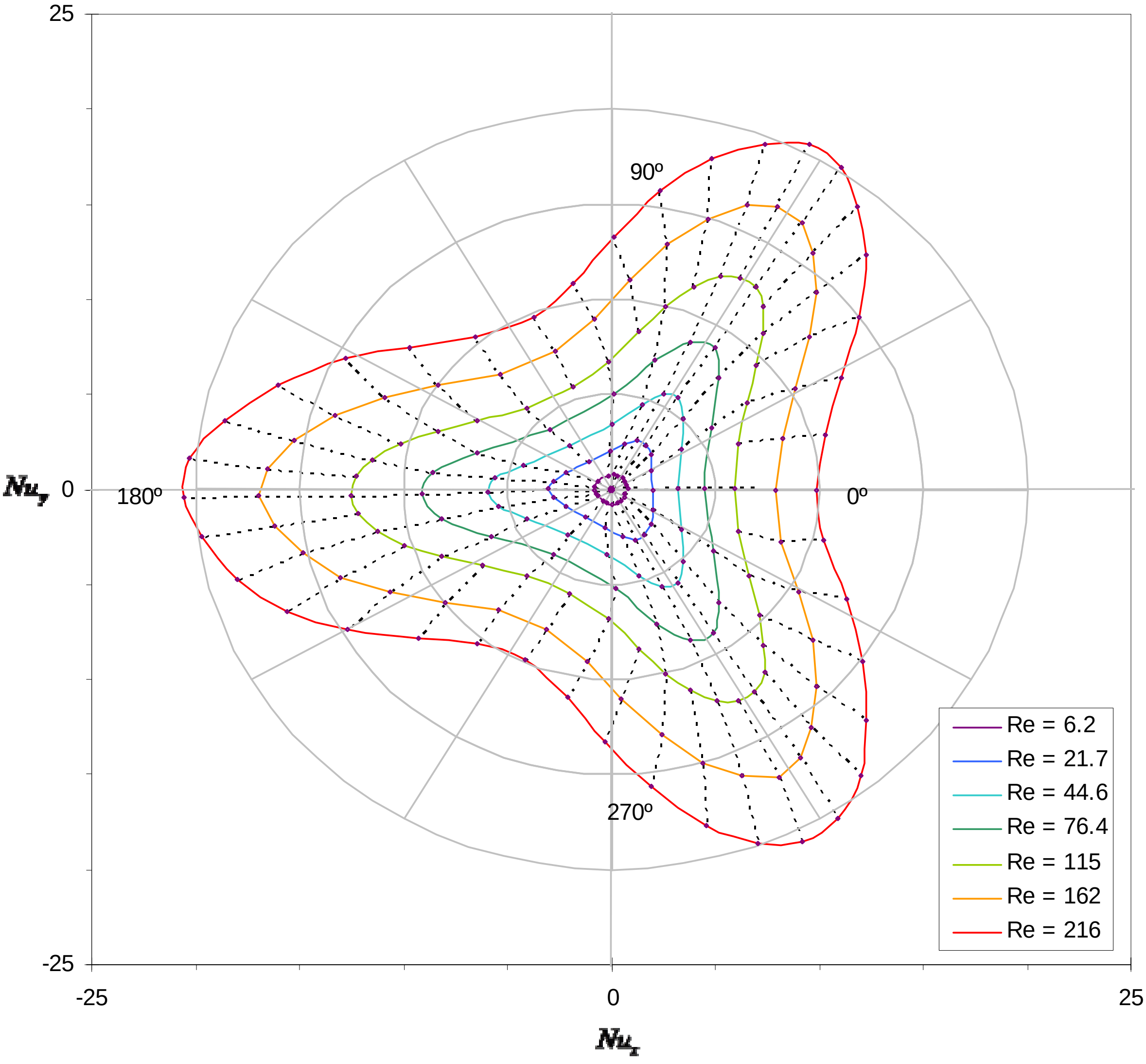

Figure 5.15 – Calibration map of B2WS-FM4 sensor head.

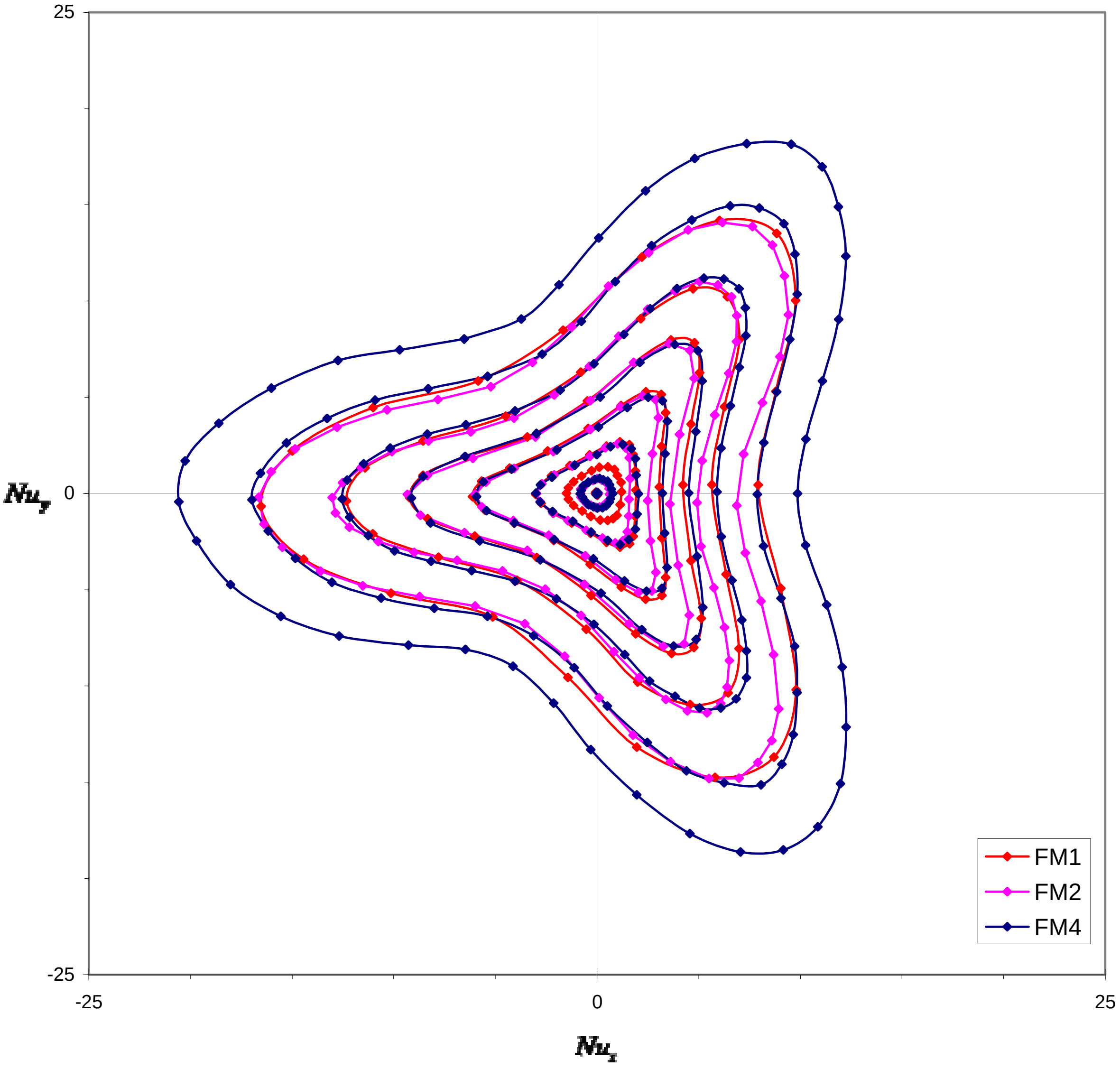

Figure 5.16 – The calibration map data for sensors FM1, FM2, and FM4 have been overlaid to allow intercomparison.

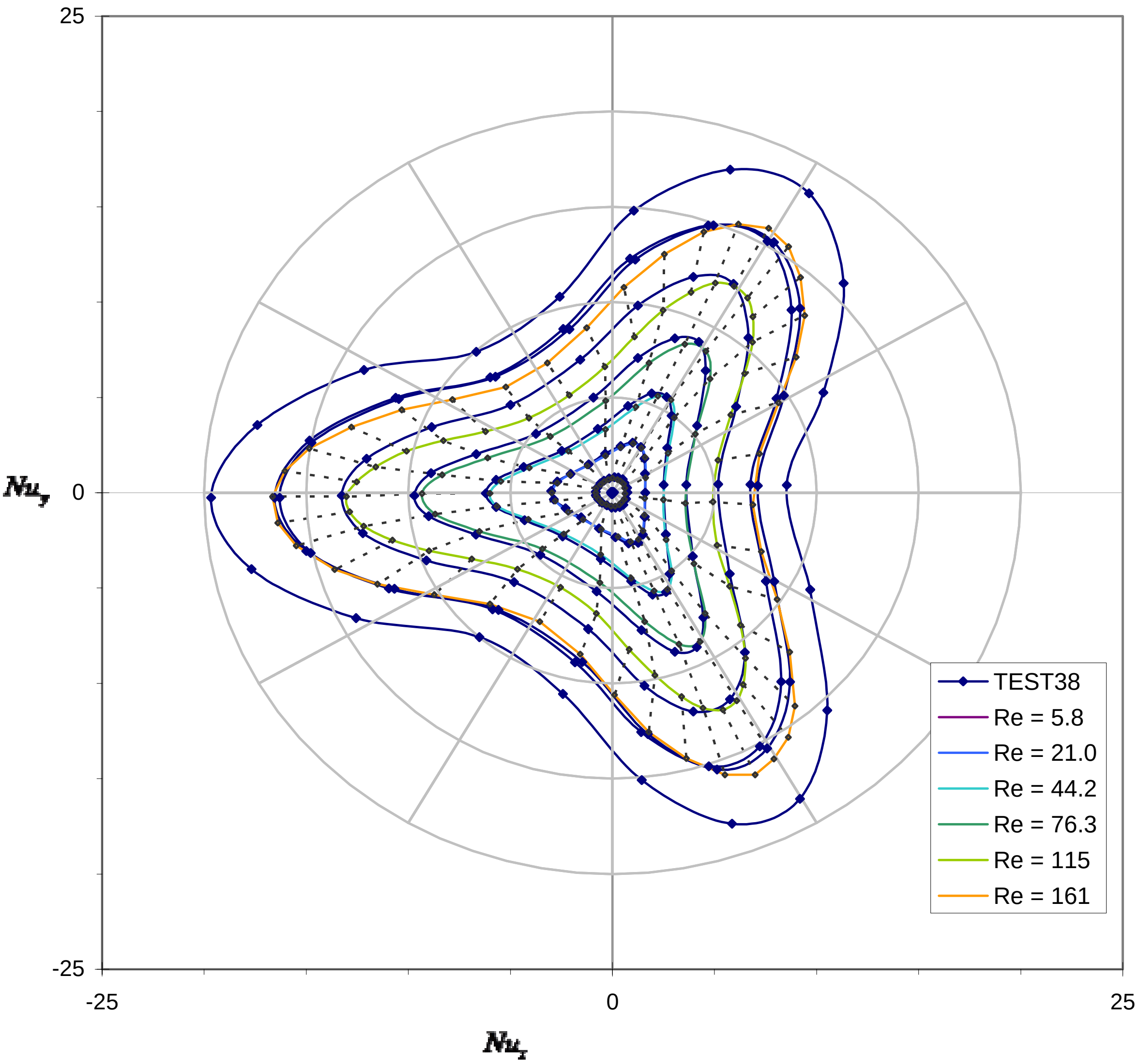

Figure 5.17 – Two calibration maps for FM2 sensor are overlaid; TEST38 data are overlaid on the FM2 calibration map shown in Figure 5.14. The Re contours for the TEST38 calibration map are at Re = 0, 6.3, 21.4, 44.4, 75.5, 116, 158, 157, and 199. See text for details.

The calibration map resulting from this second test (TEST38) is shown in Figure 5.17, superimposed on the original FM2 calibration map (RUN1) which had been presented before. The Reynolds numbers in TEST38 are almost identical to those used in RUN1. The two runs agree fairly well, though some discrepancies of up to $|\Delta \mathrm{Nu}| \sim 1$ can be seen. The agreement in the sensor response (as measured by |Nu|) is good, and suggests that no correction needs to be made for the different power dissipation used in the two calibration runs. This conclusion is consistent with the data of Figure 5.4b, which show that heat transfer from the sensor in still air is only weakly dependent (0.2% change per mW) on power dissipation in this range.

It does seem as if there may be a slight difference in gain between the three films in the two calibrations – particularly in film 2 (dominant in the top left quadrant of the plot). The discrepancy between the two calibrations could be due in part to variation of the exact values of resistors in the PFM electronics. This error, as explained in Section 4.3.3 above, contributes an uncertainty of ~2% in the calculated C_{film} on individual channels.

There is another useful point to note in the TEST38 calibration data shown in Figure 5.17. There are two sets of data presented at Re ~ 158. This is because two rotations were performed at this Reynolds number, at different pressures. The first was at p_{test} = 5.7 mbar, the second was at p_{test} = 8.6 mbar. As can be seen, the two agree very well, to within experimental error. This, as did the data in Figures 5.8 and 5.9, further validates the approach of using Reynolds number to interpret data at different gas densities.

5.4.3 Extrapolation of calibration map to higher Reynolds numbers

Wind gusts of over 30 m/s may occur on Mars. Calibration data were only obtained at speeds of up to $Re = 216$, which corresponds to a wind speed of ~ 18 m/s on Mars (in CO_2 at $T = 250$ K and $p = 7$ mbar). It was not possible to achieve higher Reynolds number in the wind tunnel when using air at room temperature. In the event of a recalibration, speeds of up to $Re = 400$ could be achieved either by using cold carbon dioxide, or by using a 120 mm diameter nozzle in the wind tunnel instead of a 180 mm nozzle.

Though the sensor has not been calibrated at these high speeds, it is useful to extrapolate the calibration map to higher Reynolds numbers. This technique ensures that we will know clearly when a high wind speed is being recorded, even if the magnitude of that wind speed is difficult to validate.

Figure 5.18 shows the magnitude of the *Nu* vector plotted against *Re*, for all wind angles. It is clear that the relationship is not directly proportional, and so might be difficult to appropriately extrapolate to higher *Re*. A better fit was found when $|Nu|$ was plotted against $|Re|$^n, with $n = 0.75$ (see Figure 5.19). For each angle, a simple linear fit $|Nu| = m|Re|^{0.75} + b$ was fitted to the highest three speeds (Re = 115, 162 and 215); this linear fit was then extrapolated higher to obtain a predicted *Nu* vector for Re = 256, 324, 400, 600, 1200, and even 2400.

The extended calibration map is shown in Figure 5.20. It is acknowledged that this technique may misrepresent not only the wind speed but also the wind angle at high speeds – however, it represents a reasonable first guess at the wind speed dependence.

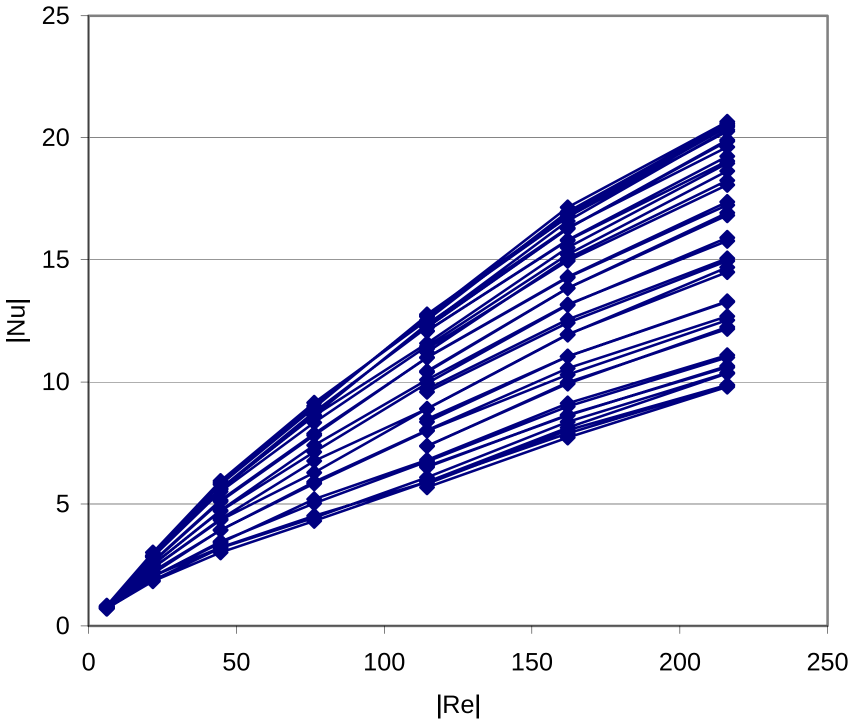

Figure 5.18 – Magnitude of the Nusselt vector |*Nu*|, plotted as a function of the magnitude of Reynolds vector |*Re*|, plotted for all wind angles. This plot is the data from the FM4 calibration map (Figure 5.15).

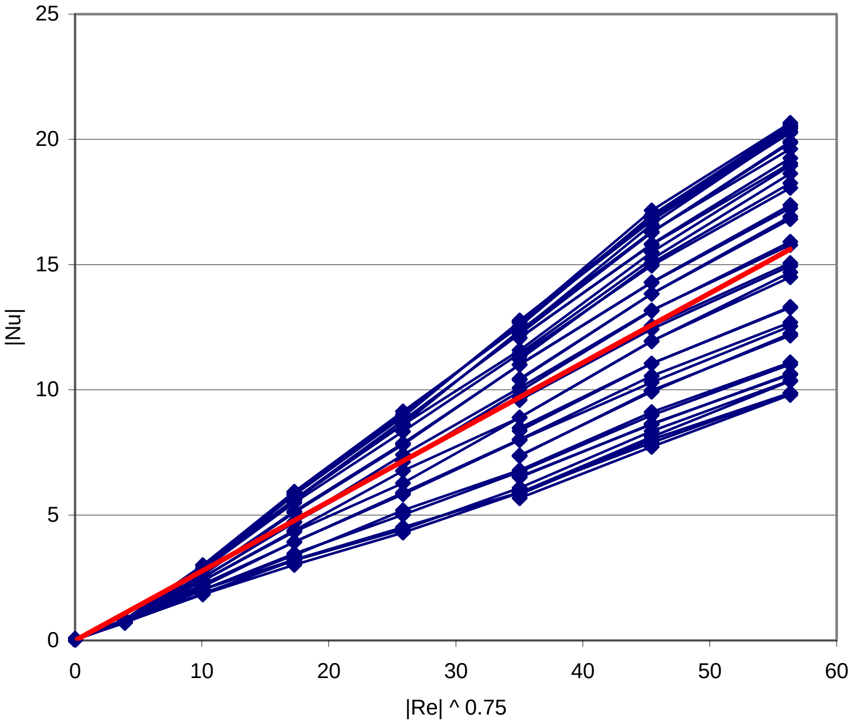

Figure 5.19 – The same data as Figure 5.18, but now |*Nu*| is plotted against $|Re|^{0.75}$.

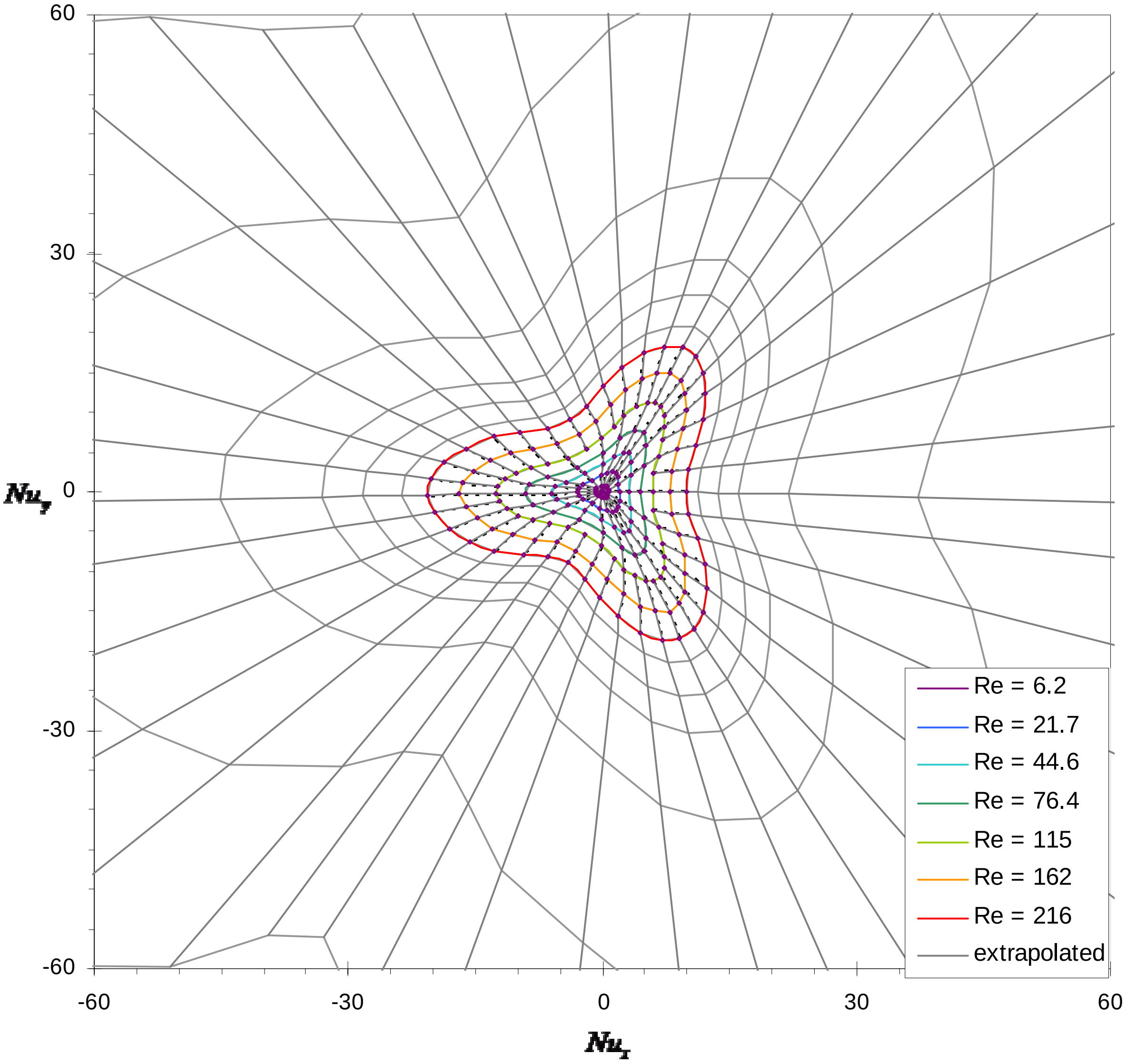

Figure 5.20 – The calibration map for FM4 (see Figure 5.15), extrapolated to higher Reynolds numbers. *Re* contours represent |*Re*| = 256, 324, 400, 600, 1200, and 2400.

5.5 Sensor performance during step changes in wind speed

A series of wind tunnel runs was carried out to test the overall performance of the wind sensor and data interpretation procedure. These tests were performed with the flight spare wind sensor (FM2), with the flight-like PFM electronics module. The Flight Model sensor could not be used for this test because it had already been delivered.

The sensor was put through a series of step changes in wind speed, while the wind direction was held constant. This was done in order to check the performance of the sensor in a situation more akin to real Martian conditions than the calibration runs, during which wind speeds were kept constant. Wind speeds were calculated from the sensor output data using the data interpretation procedure described above.

Tests were performed in air and carbon dioxide, with incident wind angles of 0° and 180° (at angle 0°, film 1 is facing directly upstream). In Figures 5.21 through 5.24 are shown the real wind speed (shown in blue) and measured wind speed (shown in red) from these tests. Wind speed is presented as a Reynolds number to allow easy comparison between figures; it may be convenient to note that, for CO_2 at 250 K and 7 mbar, $Re \sim 12 \times u$, where u is wind speed in metres per second. Note that the vertical and horizontal scales differ between the different figures.

Unfortunately, the temperature measurement system in the wind tunnel failed just before these tests were performed, and could not be fixed in time for these tests. The temperature in the chamber was calculated, therefore, by using the sensors in TEMP mode. The film temperatures were measured in TEMP mode, then corrected for self-heating using the formula $T_{air} = T_{film} - q_{film}/C(u{=}0)$, using the same $C(u{=}0)$ as was measured in WIND mode. This is a gross simplification, since only 1 mW is dissipated in TEMP mode compared with 35 mW in WIND mode; therefore, although the size of the correction is only ~ 2 K, the uncertainty inherent in this correction is estimated at ± 1 K. The air temperature so calculated was then assumed to be constant during the rest of the experimental run. This last assumption was deemed acceptable given that variations in air temperature observed during other runs had always been less than 1°C. However, some variation in temperature almost certainly resulted from fluctuations in chamber pressure (shown in the lower panels of Figures 5.21 to 5.24). It is difficult, with manual control, to achieve more pressure stability than this when changing the flow rate.

To quantify the effect this temperature error may have had on the calculated wind speed, the wind speed was re-calculated assuming an error in the temperature reading of +1 K, and then again assuming an error of –1 K. The calculated data for theses two cases are included in Figures 5.23 and 5.24. The error incurred is ± 3.5% of measured wind speed, over the whole range of measured wind speeds. That this error is relatively small is due largely to the fact that it represents a small portion of the total overheat ($T_{film} - T_{air}$), which ranges from 70 K at nil wind to ~50 K at Re = 200.

However, this assumption of temperature stability appears to break down in the CO_2 runs at high speed ($Re > 140$). This can be seen by looking at the film temperatures; In Figure 5.25 are shown the film temperatures during the data run shown in Figure 5.23. In most of the step changes, it is observed that the film temperature stabilises within about 45 seconds; but at $Re = 240$ the film temperature starts

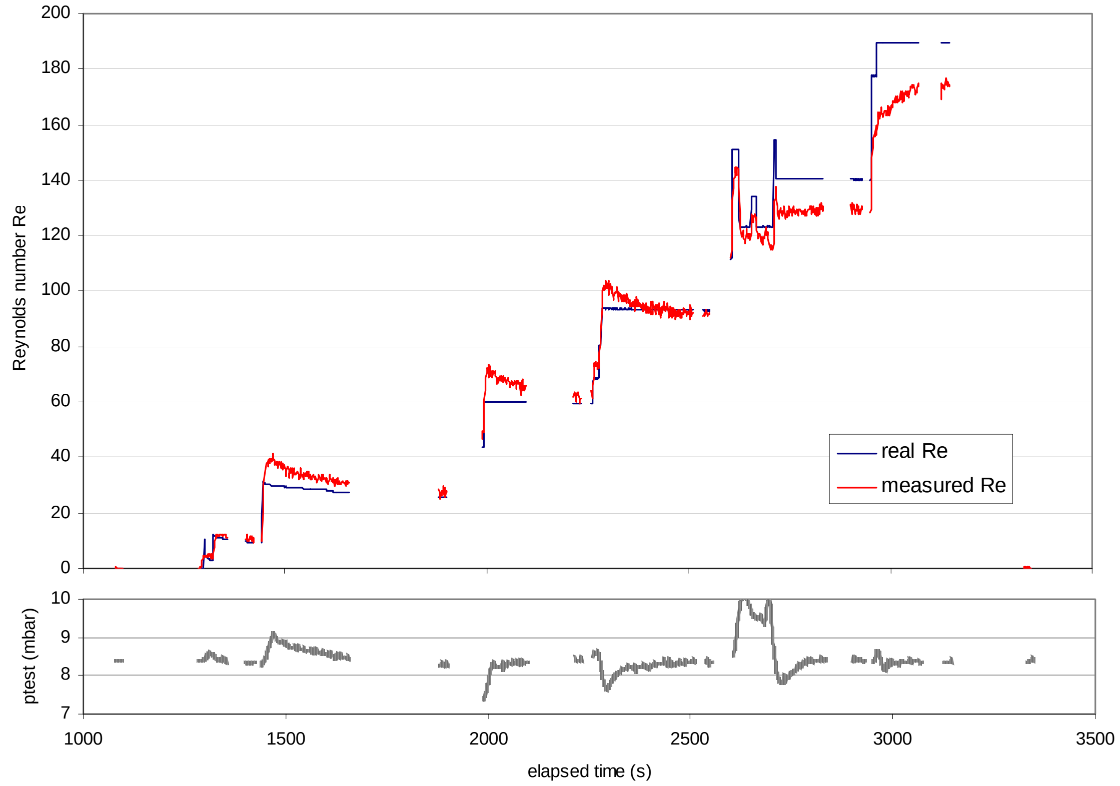

Figure 5.21 – Real (blue) and measured (red) wind speed during a wind tunnel test with sensor FM2. Test gas is air, wind angle is 0º (film 1 is facing upstream).

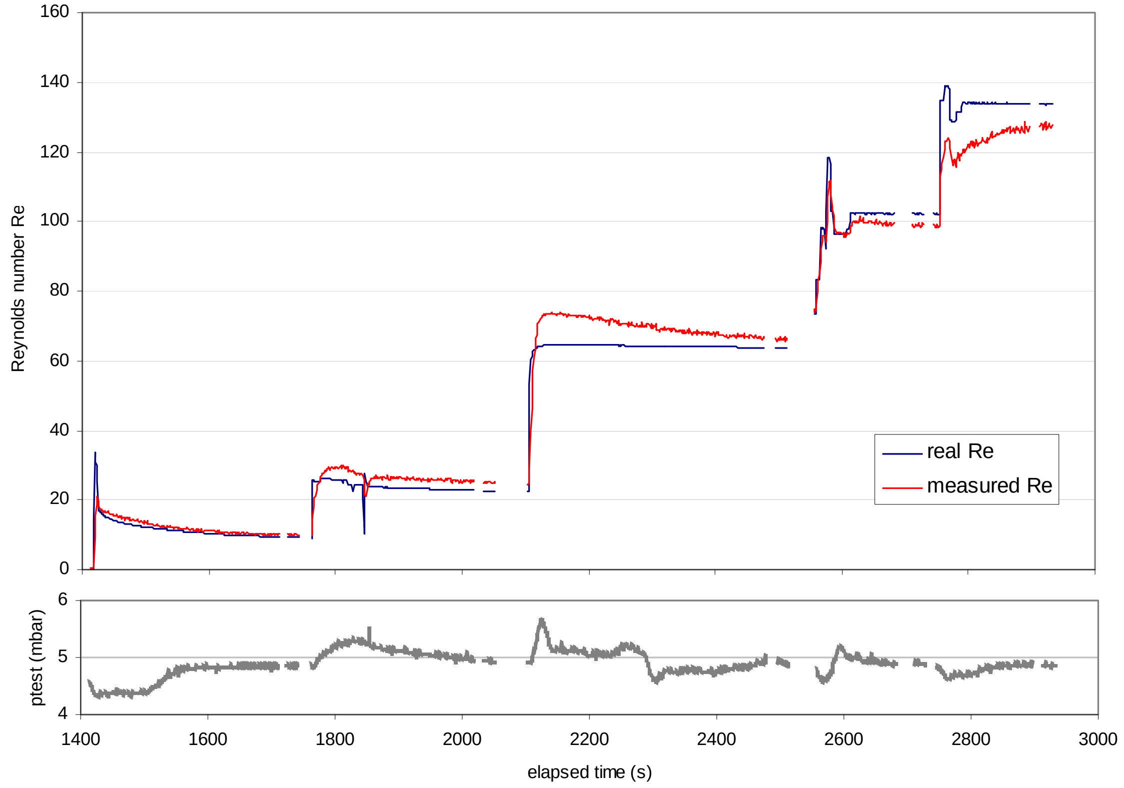

Figure 5.22 – As for Figure 5.22, but with wind angle = 180º (film 1 is facing downstream).

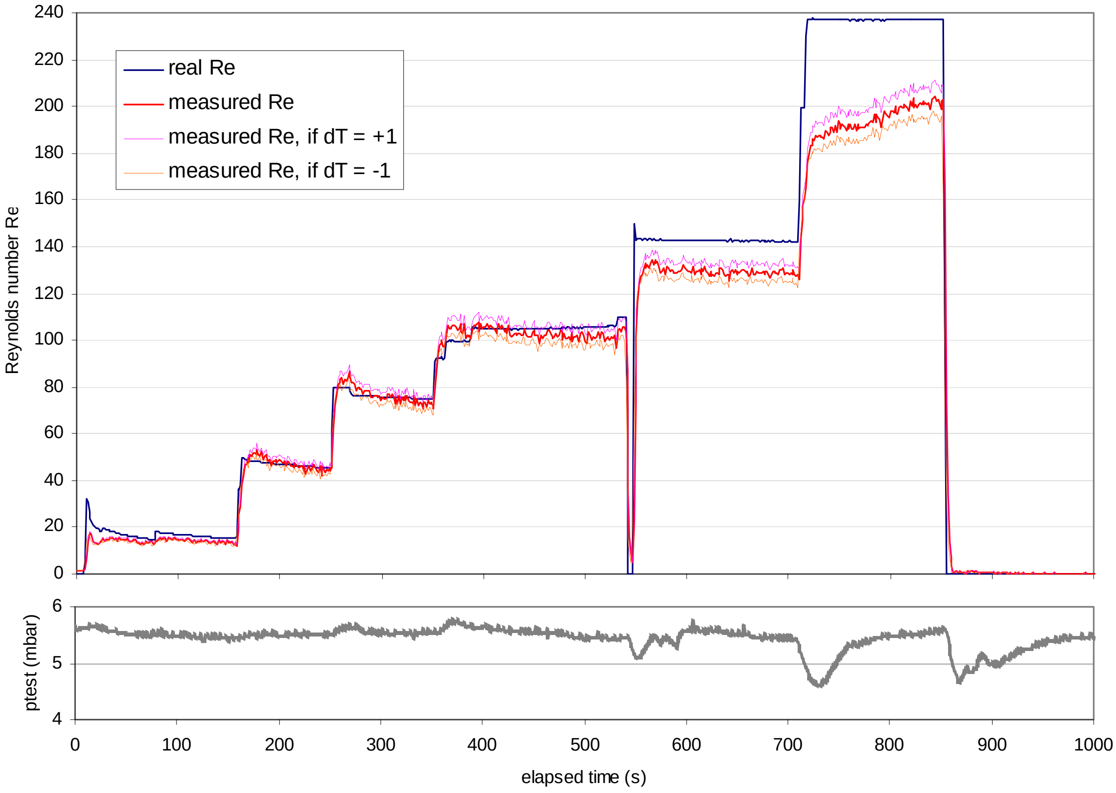

Figure 5.23 – As for Figure 5.21, but using carbon dioxide as the test gas. Wind angle is 0º (film 1 is facing upstream)

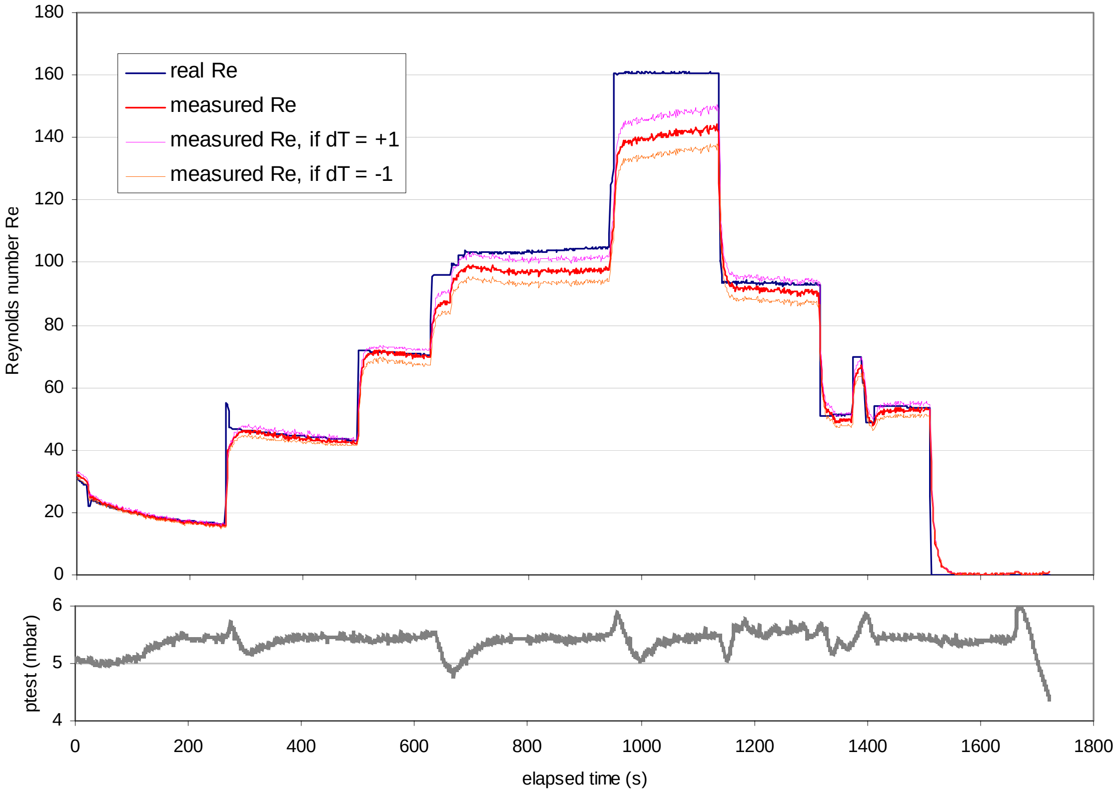

Figure 5.24 – As for Figure 5.23, but with wind angle = 180º (film 1 is facing downstream).

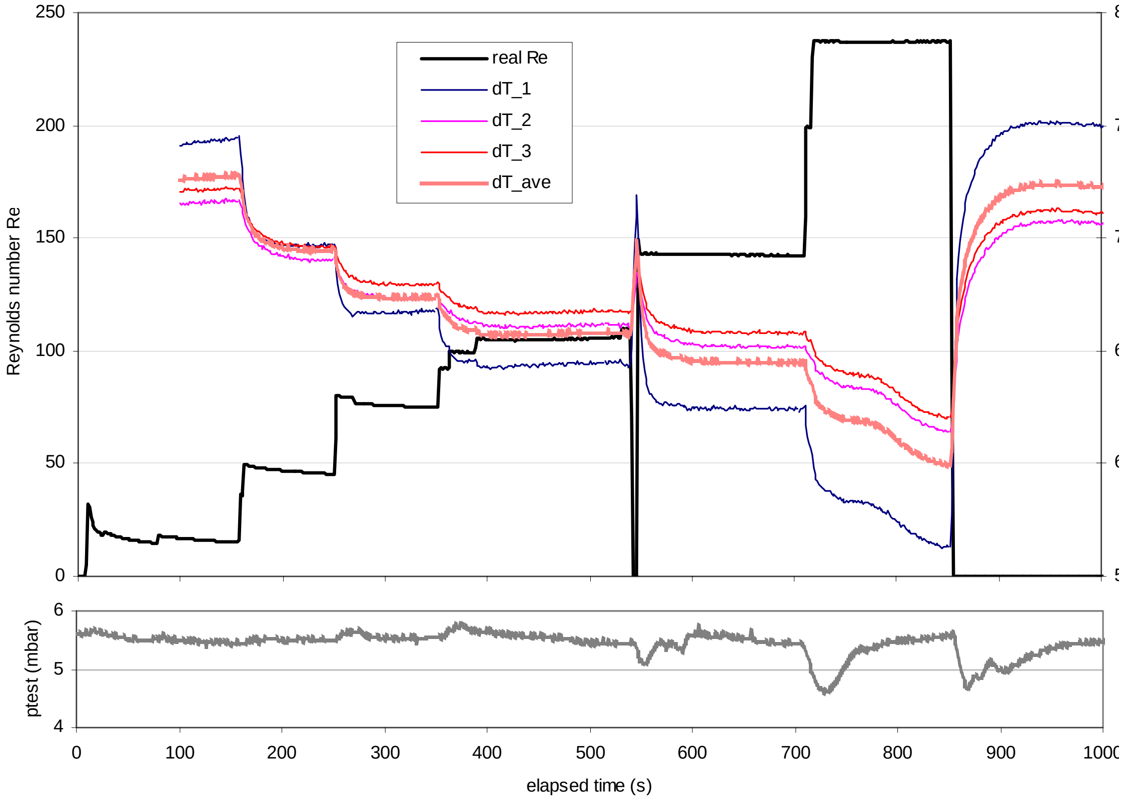

Figure 5.25 – Film temperatures are shown for the run shown in Figure 5.23.

dropping steadily, at a rate of roughly 1 K/minute (modified slightly by the adiabatic temperature changes associated with the chamber pressure fluctuation). One expects sensor response time to be faster at higher wind speeds rather than slower, due to the higher heat transfer rates at high speeds. Therefore it is concluded that the air temperature falls at high speeds due to some thermodynamic cooling effect in the wind tunnel upstream of the nozzle. It is well-known that CO_2 passing at high speed through regulators exhibits very strong cooling – the same effect probably happens to a lesser extent as the CO_2 passes into the nozzle’s settling chamber. This is due to real gas effects specific to CO_2 – it is noted that the same problems to not appear to occur in the runs performed with air (Figures 5.21 and 5.22). This effect was not observed another time because these were the only two runs performed with CO_2 at such high speeds.

The measured wind speed also appears to ‘overshoot’ the real step changes in wind speed, especially at wind angle = 0°; this is due to variation with angle of the thermal response times of the films, a phenomenon which will be discussed further below.

Except for these two problems – the overshoot effect, and the discrepancy at high speeds – the agreement between real and measured wind speeds in Figures 5.21 to 5.24 is generally good, to within 10% for most wind speeds up to Re = 140. This applies both for runs in air and in carbon dioxide. The good agreement in the CO_2 runs in particular is particularly encouraging, because the calibration runs were carried out using air as the test gas; the good agreement between the measured and the real wind speeds shown in the wind tunnel results is broadly interpreted as validation of the technique used of coping with different gas densities.

Another point which can be made here is that the agreement is good despite the fact that the data are not corrected for uncertainties in chamber temperature. This is due to the use of differences between the film temperatures, rather than their average, to calculate the wind speed. As an illustration of this point, Figure 5.26 shows the average of the three Nusselt numbers, $Nu_{ave} = (Nu_1 + Nu_2 + Nu_3)/3$ during the test sequence shown in Figure 5.23. It can be seen that Nu_{ave} shows a great sensitivity at t ~750 s to the presumed drift in gas temperature occurring at this time. This can be seen in the error in Nu_{ave} at the end of the run, which is due to the cooling of the gas temperature at high speeds. This sensitivity to gas temperature is not evident in the data of Figure 5.23. Furthermore, it is clearly evident that Nu_{ave} responds much more slowly to changes in wind speed than does the wind speed calculated using (Nu_x, Nu_y). This validates the approach used here of using the difference between the Nusselt numbers to calculate wind speed. However, it should also serve as a warning – this means that the wind sensor is taking a long time (over 20 seconds) to approach thermal equilibrium, even though the measured wind speed in Figure 5.23 appears to respond much more quickly. The response time of the sensor will now be examined in more detail.

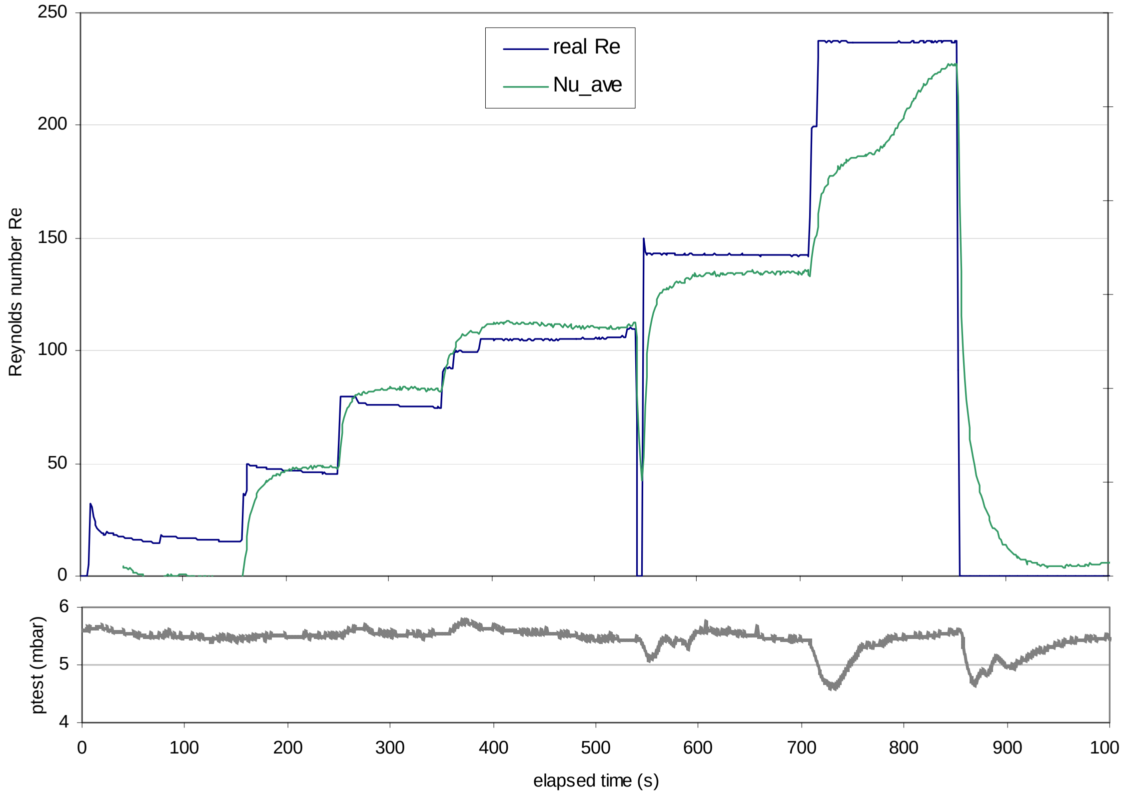

Figure 5.26 – An average Nusselt number (Nu_1+Nu_2+Nu_3)/3 is calculated for the data shown above.

5.5.1 Response time

To fulfil all of its science goals, the sensor needs to be capable of achieving a fast response. The goal set in Section 4.1 was to achieve a response time of 1 second, mainly to improve our knowledge of turbulence spectra. The response time of the final B2WS can be investigated by looking more closely at the data presented in Figures 5.23 and 5.24. For this purpose, 60-second segments of the data from these figures are reproduced in Figures 5.27 and 5.28. Sensor output was sampled at 1.4 second intervals.

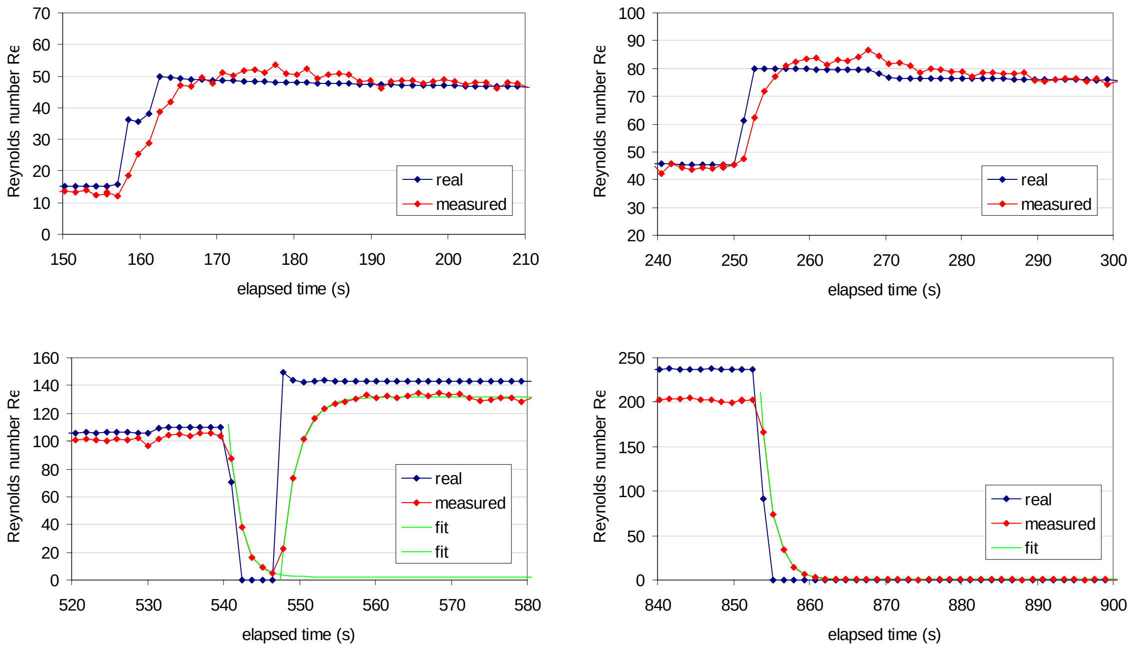

Figure 5.27 – Details from Figure 5.23. The sampling interval is 1.4 seconds. The vertical scales vary between figures. Exponential fits are shown with decay times of (from left to right) τ = 1.6, 2.2, and 1.7 seconds.

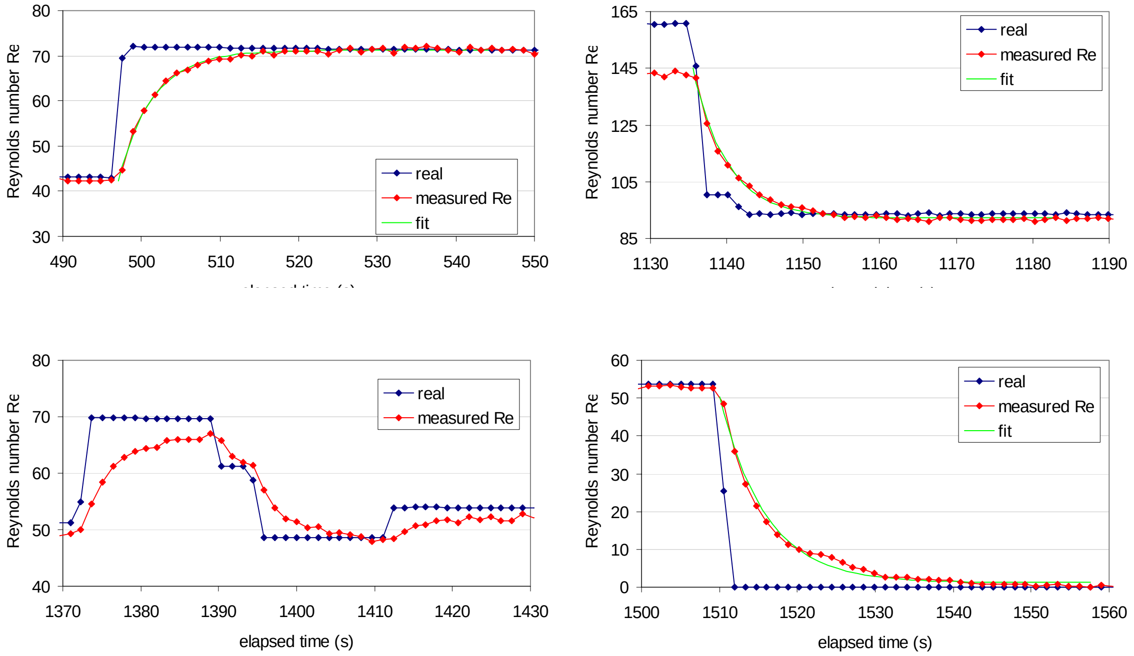

Figure 5.28 – Details from Figure 5.24. As above, but this data is for wind angle = 180°. Exponential fits are shown with decay times of (from left to right) τ = 4.4, 4.5, and 5.8 seconds.

The step change from speed u_1 to u_2 can be modelled as an exponential curve of the form $u(t) = u_2 + (u_1 - u_2)\exp(-t/\tau)$, as shown in selected panels in Figures 5.27 and 5.28. The values of τ obtained are (1.8 ± 0.3) seconds for wind angle = 0°, and (4.8 ± 0.5) seconds for wind angle = 180°. This response time is not significantly correlated with wind speed. Similar curves fitted to film temperature graphs show time constants varying from $\tau = 5$ seconds to $\tau = 10$ seconds, again varying with film angle but not varying much with wind speed.

Why does the response time differ between the two runs? When the wind angle is 180°, film 1 is facing downstream and has only a fairly low heat transfer coefficient, while films 2 and 3 are experiencing near-maximum heat transfer coefficients. Therefore, films 2 and 3 reach a new equilibrium faster than film 1. The final wind measurement is only obtained once all three have reached equilibrium. Therefore, the sensor response is faster when the wind angle is 0°, when the heat transfer coefficients at the three films are more even. Because of the three-fold symmetry, the response time is quicker also for wind angles of 120° and 240° than for wind angles of 60° and 300°. This variation of response time with film angle also explains the slight 'overshoot' of the sensor evident in these figures.

Exponential decay curves were also fitted to film temperature data from the same sequence of step changes. In Fig 5.29, these response times are shown as a function of wind speed, and as a function of the angular position of the film relative to the upwind direction. It can be seen that the response times of the films decrease with increasing wind speed, as one would expect; and that they increase as the film angle is increased from 0 to 180º, which is broadly consistent with heat transfer decreasing as the film moves away from the stagnation point.

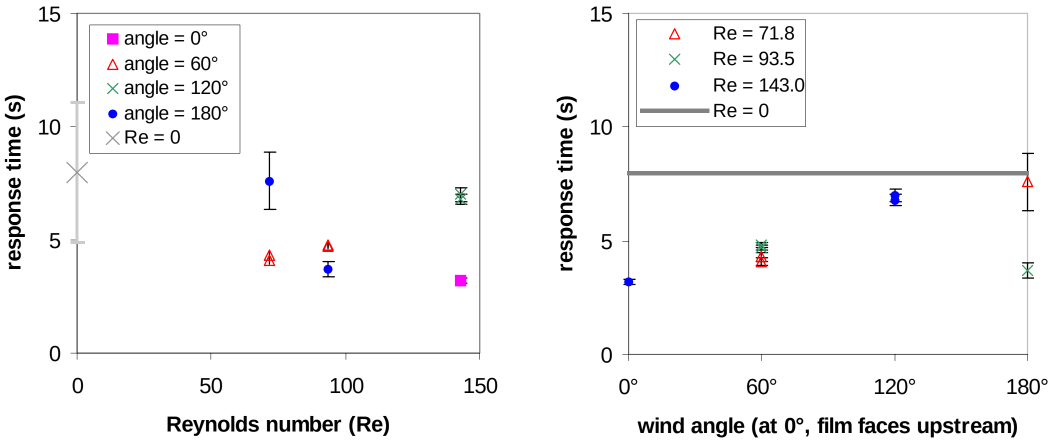

Figure 5.29 – Response times of film temperatures to step changes in wind speed, calculated using the data presented in Figures 5.23 through 5.28. Response times are shown as a function of (left) wind speed and (right) wind angle. Because wind angle is meaningless when wind speed is zero, all points at zero wind speed are represented by a single value marked in grey.

The response times of the calculated wind speed (2-5 s) are faster than those of the individual film temperatures (5-10 s), as was seen in the data presented in the previous section. This longer response time is interpreted as being representative of the time taken for the central core of the sensor to reach a new equilibrium temperature after a step change in wind speed. One can check whether this interpretation is consistent with the observed response times through a simplistic analytical calculation. Consider one-dimensional heat flow through a slab of Rohacell, 5 mm thick. One can use the heat equation $\partial T/\partial t = c^2\Delta^2 T$ to solve this, for a sudden change of temperature on one face of the Rohacell. In this case the temperature on the other face approaches its new equilibrium value exponentially with a characteristic time τ given by $\tau = L^2 / (\kappa\pi^2)$, where κ is the diffusivity of the material, given by $\kappa = k/\rho C_p$ [see Kreyzig (1993) p.648]. Although Rohacell has a very low conductivity, it also has a very low density, so its diffusivity is only about 4 times less than that of glass. The response time τ calculated using this equation using L = 5 mm is 15 seconds, which is of the same order of magnitude as the empirically measured response of the film temperatures. This also confirms the supposition above that the slow drift in temperature of 1 K/minute in Figure 5.23 was too slow to be explained by a slow response time of the sensor.

5.5.2 Noise due to ADC resolution

It can be seen that the measured wind signal shows random fluctuations from one reading to the next. This is due to the resolution of the ADC which is being used to read the B2WS outputs. Each voltage reading was actually the average of 100 individual ADC readings, taken within a second. The ADC had 12-bit resolution, used over a range of 0 – 6.67 V; therefore had an input resolution of ~± 1.7 mV. The flight ADC has a 14-bit resolution, and a range of 0 – 5 V, so noise due to ADC input resolution should be roughly five times less in B2 data than in the data shown here.

It is interesting to note that the noise is roughly twice as great in the two runs where the wind angle is 0°. This is because $d(Re)/d(Nu)$ at wind angle = 0° is roughly twice as large as at wind angle = 180°. Therefore the interpreted wind speed is twice as sensitive to any fluctuations in Nu at 0° than at 180°.

5.6 Predicted B2WS response to VL2 wind data

In this section, the sensor response in a Martian environment is simulated using real Martian wind and temperature data from Viking Lander 2 (VL2). This simulated response will later modified to simulate various errors which could affect the B2WS measurement.

The reference atmospheric data used include data segments with sampling intervals of only 1.2 s. From the wind data, a Reynolds vector is generated and converted into a B2WS Nusselt vector $\underline{Nu}$ using the B2WS calibration map. From this are generated the individual B2WS film temperatures, which represent the ‘ideal’ film temperatures which B2WS would have if it had an instantaneous, perfectly accurate response.

Starting from this set of ideal film temperatures, a number of investigations into the accuracy of the B2WS can be carried out. Three examples will be shown here, using the same VL2 data segment. This data segment, starting at 12:04 on sol 554, is one of the few data segments recorded with a time interval of 1.2 seconds, and occurs in the daytime turbulent convective period.

First, an exponential response of film temperature was simulated. Each film temperature in the time series was calculated by taking a weighted average of the last 20 data points, using the equation

$$T_n = \frac{\sum_{m=0}^{m=20} T_{n-m}\exp(-m\Delta t/\tau)}{\sum_{m=0}^{m=20} \exp(-m\Delta t/\tau)},$$

where Δt is the time step of the data series. The same equation was also used to simulate an exponential response function for the temperature sensor. For initial runs, a response time of $\tau = 4$ s has been used for the B2WS films, and a response time of $\tau = 8$ s has been used for the air temperature sensor (B2TS). This was done to see whether a mismatch in response times between the B2WS films and the B2TS would lead to an error in the measured wind speed. The simulated measurements of wind speed and direction for these conditions is shown in Figure 5.30. It can be seen that some of the high-frequency variability is lost, as would be expected. Nevertheless, the wind sensor manages to capture much of the variability on the time scale of its response time (~4 s), and its accuracy is not compromised by the mismatch of time constants with the B2TS. Another test which should be done in future, though, is to introduce a mismatch in response times between the films as a function of angle; this might affect the results more significantly.

To calculate this sensor response, it was assumed that the B2WS calibration maps are valid not only for different gas types and densities as has been suggested in this chapter, but also for different gas temperatures. To examine the basis of this claim, an analytical model of heat flows in the sensor has been developed; this forms the subject of the next chapter. This simulated B2WS measurement of VL2 data will be revisited using the analytical model, modified by sources of error such as incident sunlight and errors in air temperature measurement.

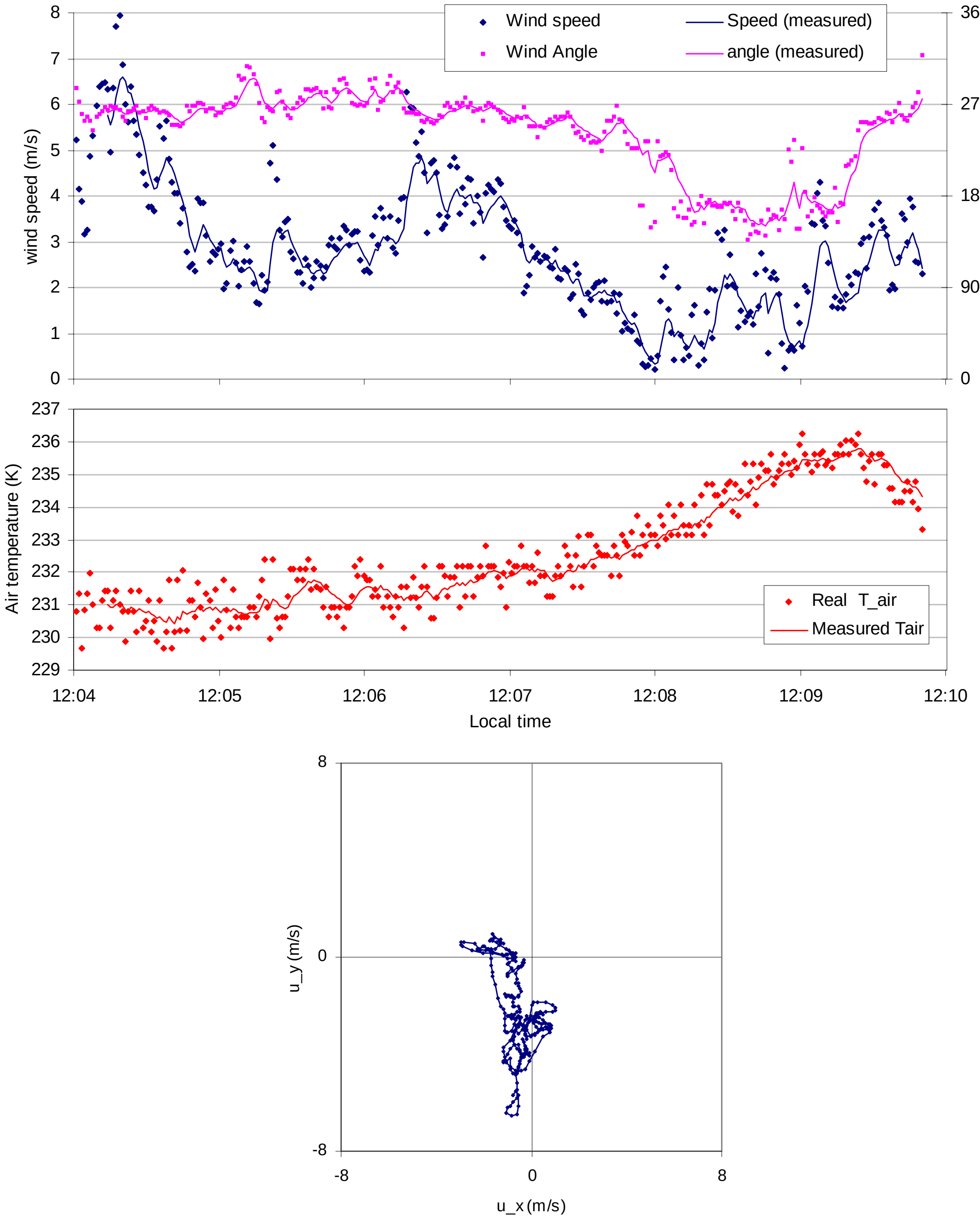

Figure 5.30 – Simulated B2WS measurements in response to real wind and temperature data obtained from the Viking Lander 2. In this simulation, a response time of τ = 4 s has been assumed for the B2WS films, and a response time of 8 s for the Beagle 2 temperature sensor (see text for details). The top panels show wind speed and direction and air temperature. The ‘real’ data from VL2 is marked with points; simulated B2WS measurements are marked with lines. A hodograph of measured wind speeds is shown in the bottom panel.

Chapter 6 - B2WS: Analytical thermal model

In this chapter is presented a simple semi-analytical thermal model of the sensor. This enables analytical calculation of what fraction of the heat dissipated in the sensor is lost to the environment via which pathways. This model has been developed in order to estimate the errors due to conditions which were not simulated during the calibration process. Calculations are presented which predict the effect of sunlight on the sensor, and the effects of variations in thermal IR radiative exchange with the surroundings. Finally, the overall accuracy of the B2WS sensor will be discussed.

The model represents only one third of the sensor, i.e. one film and surrounding Rohacell. Heat flows between the following 'nodes' are considered:

Node	**Subscript**	**Comments**
Film	*film, f*	
Contact pads	*pads*	
Rohacell	*Rohacell, R*	The surface of the Rohacell is assumed to have a single temperature.
Air	*air, a*	
Background	*background, b*	The effective blackbody temperature of the Martian environment.
Lander	*lander*	The support on which the wind sensor is mounted.

The heat flows to be considered are shown in Figure 6.1. The parameterisations for the heat flows will be given below.

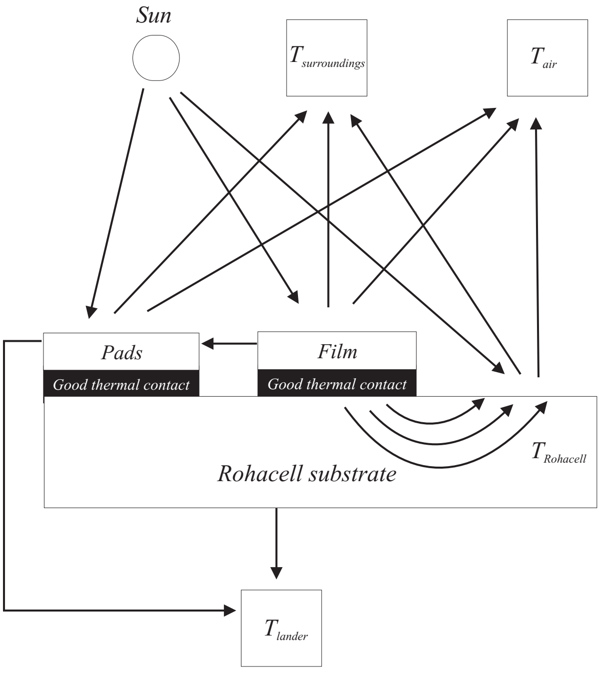

Figure 6.1 – Heat flows considered in the analytical thermal model. This represents only one hot film, i.e. one third of the sensor.

Initially, it is assumed that $T_{lander} = T_{air}$, and that $T_{air} = T_{background}$. This is reasonable for all the wind tunnel tests performed; the validity of these assumptions for use on Mars will be addressed later on. Also, the effects of sunlight will be ignored in this section. This too is valid for wind tunnel tests; the effect of sunlight on Mars will be addressed later on.

The assumption that the surface of the Rohacell is at one temperature is simplistic, but is a common approach in this sort of problem [see e.g. Wilson *et* al., 1999]. This approach is partly validated by an infrared photograph of the wind sensor shown in Figure 6.2. This photo shows a QM wind sensor, in air at 1 atm and T = 20ºC, and the film temperature is T_{film} = 80ºC. This image was obtained using a camera which measures thermal IR integrated over the range 7 µm < λ < 14 µm. From the measured radiance at each pixel the blackbody temperature is calculated using the emissivity of the Rohacell. This photo shows that, beyond about 1 mm from the hot film itself, the temperature of the Rohacell is relatively uniform. There is more information to be gleaned from this picture, and it will be discussed again below in connection with calculation of radiative heat transfer from the sensor.

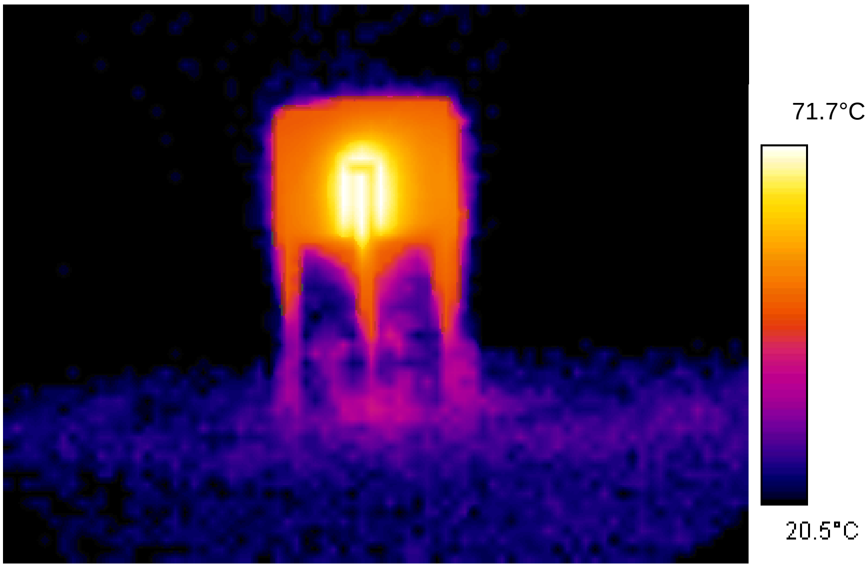

Figure 6.2 – An infrared photograph of a prototype wind sensor (QM3), in air at p = 1 atm. This was obtained by measuring infrared radiation integrated over the range 7 µm < λ < 14 µm. The temperature scale on the right is obtained by assuming an emissivity of 0.67 over this spectral range. The platinum film appears dark because of the low emissivity of platinum (~0.1). Note also that the surface of the Rohacell cylinder is isothermal, unless within 1-2 mm of the hot film.

6.1 Parameterisations

Ohmic heating: The ohmic heating in each circuit is 35 mW. From the geometry of the films, it is calculated that 91% of the resistance in each film circuit is in the hot film itself. A further 7% is dissipated in the broader ‘contact pad’ area, and the remaining 2% is in the 1 m long leads joining the sensor to the electronics.

For parameterisations of **convection**, the dimensionless Reynolds, Nusselt, Prandtl, and Grashof numbers are used. The Reynolds number was introduced in Chapter 3; the other numbers are given by:

$$Nu = \frac{h_{convective} L}{k}$$

$$Gr_L = \frac{g\beta L^3 \Delta T}{\nu^2}.$$

$$Pr = \frac{\nu}{\kappa} = \frac{\mu C_p}{k}$$

In these equations *h* represents the convective heat transfer, *g* is the gravitational acceleration, and *L* represents a characteristic length of the system. The kinematic viscosity ν is equal to the dynamic viscosity µ divided by the gas density *ρ*. The symbols *k* and C_p represent the thermal conductivity and heat capacity at constant pressure of the gas. Finally, *β* represents the thermal expansion coefficient of the gas; at these low pressures CO_2 behaves as an ideal gas, for which $\beta = 1/T$.

The Nusselt number is a dimensionless representation of convective heat transfer, representing the ratio of convective to conductive heat transfer. The Grashof number is the ratio of buoyant to inertial forces, and thus represents the importance of free convective heat transfer. The Prandtl number is the ratio of the kinematic viscosity of a fluid to its thermal diffusivity, and enables scaling of convection problems between different fluid types. The Prandtl number is dependent on temperature but not pressure – it is interesting to note that the Prandtl number of air at $T = 300$ K is the same (to within 1%) as that of carbon dioxide at $T = 250$ K, although the Prandtl numbers of air and CO_2 differ by ~10% when both at $T = 20$ºC.

Free convection has been parameterised using the semi-empirical formulation:

$$\overline{Nu_L} = \frac{\bar{h}L}{k} = \frac{4}{3}\left(\frac{Gr_L}{4}\right)^{1/4} g(\text{Pr}), \qquad \text{[Incropera \& DeWitt, 2002].}$$

where g(Pr) is an empirical function to enable scaling for different fluids:

$$g(\text{Pr}) = \frac{0.75\,\text{Pr}^{1/2}}{(0.609 + 1.221\,\text{Pr}^{1/2} + 1.238\,\text{Pr})^{1/4}}$$

This free convection parameterisation above predicts Nusselt numbers of ~ 0.3 in Martian conditions, both for free convection from the hot film itself and for free convection from the Rohacell surface. The Nusselt number is roughly the ratio of free convective to conductive heat transfer, so this result of less than one signifies that gaseous conduction is important.

Gaseous conduction is important in comparison to free convection, as explained above. The effective conductivity from a circular contact of radius *a* to a semi-infinite medium of conductivity *k* is given simply by $q = 2ka\Delta T$ [Holman, 1989]. For non-circular source areas, the effective radius *a* is defined as the radius of a circle with the same perimeter.

At extremely low pressures ($p << 1$ mbar), thermal conduction is via free-molecular gas conduction; the thermal conductivity k_{mol} associated with this process has been calculated using an equation quoted in [Roth, 1990]:

$$k_{mol.} = \frac{\gamma + 1}{2(\gamma - 1)}\left(\frac{R_o}{2\pi M T}\right)^{1/2} p$$

Though it need not be considered at Mars pressures ($p > 5$ mbar), the parameterisation of molecular conduction is included here in order to evaluate the sensor's performance in the lab at lower pressures. The overlap between the continuum and molecular flow regimes, labelled 'slip flow', has not been fully calculated, since it is not needed to understand B2WS performance on Mars.

The pressure dependence of molecular gas conduction, continuum gas conduction and free convection from the hot film are shown in Figure 6.3. Data shown are for CO_2; air exhibits qualitatively similar behaviour. It can be seen that at Martian pressures (5-10 mbar), the dominant mechanism is continuum gas conduction. Therefore, the variation of performance with atmospheric pressure is quite small over this range.

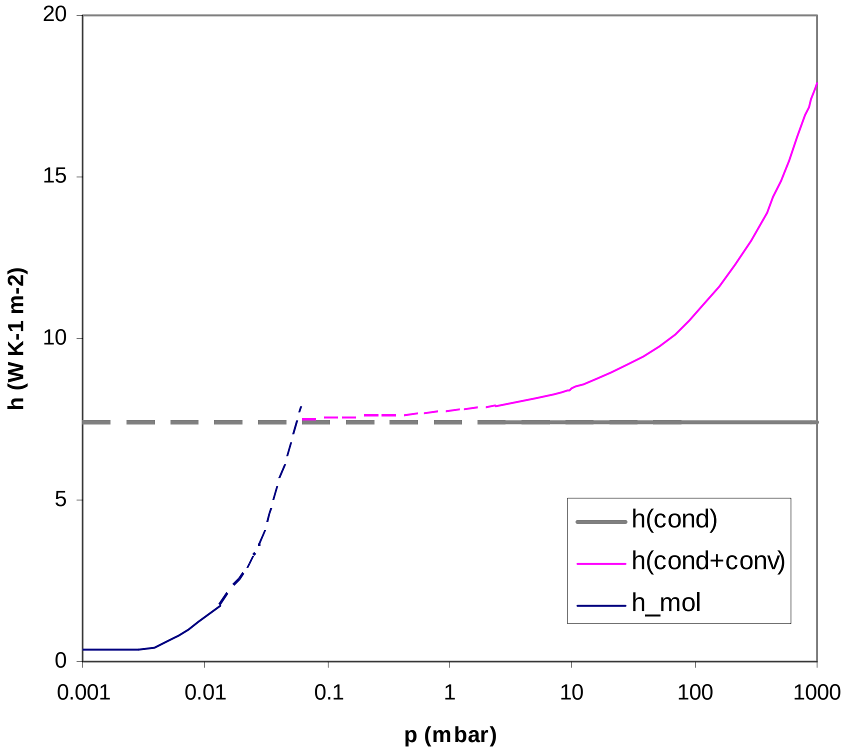

Figure 6.3 – Pressure dependence of direct heat transfer from the hot film to surrounding atmosphere of carbon dioxide. The thick line represents continuum gaseous conduction. The pink line is this plus free convection. The blue line represents free molecular heat conduction. Solid lines are used when the parameterisation is reasonable in the pressure range; dashed lines are used if not. A similar pressure dependence applies for heat transfer from the surface of the Rohacell.

Two forms of **forced convection** are considered: that from the hot film itself, and that from the Rohacell. The hot film forms an isolated hot patch in a cooler surrounding surface; the heat transfer in this case is a function of *skin friction*, i.e. the velocity shear immediately above the surface divided by the free stream dynamic pressure. Figure 6.4 shows an experimental plot of velocity shear locally as a function of position on the cylinder. It can be seen that the maximum occurs not at the stagnation point (i.e. at the point facing directly upwind), but at a point roughly 50°-60° on either side of this point, which is where the maximum wind shear occurs. This can be seen in Figure 6.5, which shows streamlines of flow past a cylinder for low Reynolds numbers of 0.1 to 300 (corresponding to wind speeds of 0.01 to 25 m/s in CO_2 at 250 K and 7 mbar) [Lange *et al.*, 1998]. It can be seen that flow is laminar in all cases, with vortex shedding starting to occur at $Re > 50$. No *a priori* equation for heat

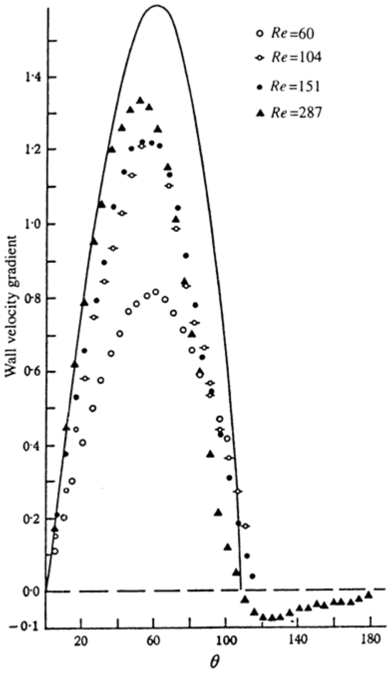

Figure 6.4 – Empirical measurement of the angular dependence of skin friction [Zdravkovich, 1997]. The forced convective heat transfer from an isolated hot patch is proportional to skin friction. Note that this function peaks when the film is at 50° to 60° from the upwind direction; this is consistent with the B2WS film response.

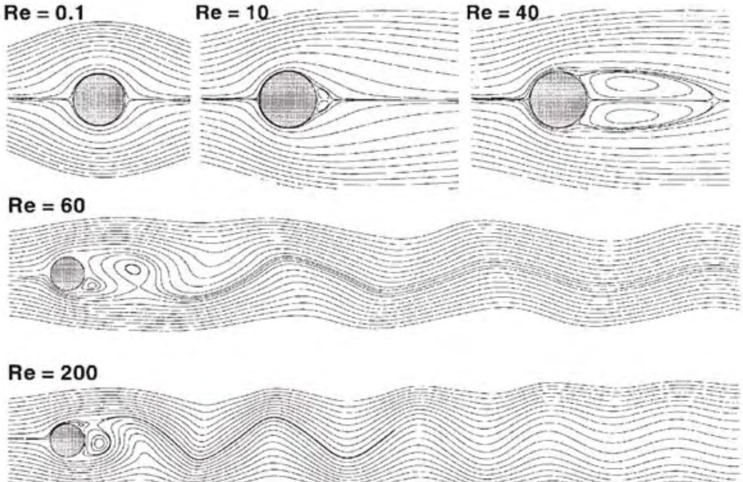

Figure 6.5 – Representation of the different laminar flow regimes around a cylinder at low Reynolds number, calculated by FEM [Lange *et al.*, 1998].

transfer in this case was found; therefore the dependence was assumed to be of the form $Nu = 0.023 \times (Re)^{0.8}$. The constants in this equation were picked to match wind tunnel test results. The dependence of *Nu* on wind direction was also chosen to match wind tunnel results. It is based on a quadratic curve, centred on a wind angle of 51°; this is based on the skin friction dependence shown in Figure 6.4. To match the empirical results, this quadratic curve was then widened to account for heat flow spreading beyond the immediate area of the hot film itself. That this had to be done to match empirical results is a reflection not only of the non-zero width of the hot film but also of the fact that in reality some of the angular variation in heat transfer is not due to heat loss from the hot film itself, but from the surrounding Rohacell. The angular dependence used, normalized to a maximum of 1, is shown in Figure 6.6.

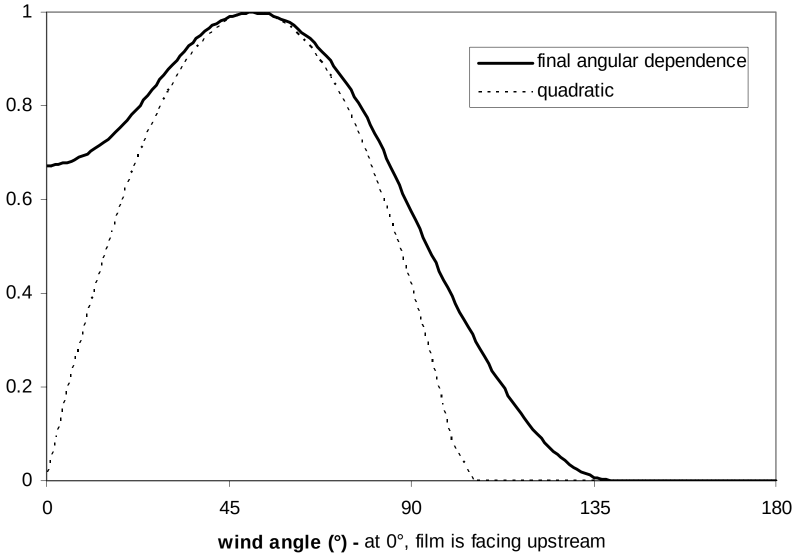

Figure 6.6 – Angular dependence $f(\theta)$ assumed for the convective heat transfer coefficient from the hot film $q_{f\text{->}a}$, based on empirical results in Chapter 5. The function is scaled such that the maximum value is 1.

Heat transfer from the exposed surface of the Rohacell is different from that from the hot films, because the Rohacell cylinder is, approximately, a cylinder of uniform temperature, as seen in Figure 6.2. The heat transfer coefficient, averaged over the circumference of the cylinder, can be approximated by an empirical formula:

$$\overline{Nu} = 0.3 + \frac{0.62 Re^{1/2} Pr^{1/3}}{\left[1+\left(0.4/Pr\right)^{2/3}\right]^{1/4}} \left[1+\left(\frac{Re}{282{,}000}\right)^{5/8}\right]^{4/5} \qquad \text{[Incropera \& deWitt, 2002].}$$

It is noted that $Re \ll 282{,}000$ in this experiment, so this equation provides a relationship of $Nu \sim Re^{1/2}$. Also, the 0.3 which is the first term in the equation matches the Nusselt number calculated earlier for free convection. Therefore this equation effectively states that forced convection = free convection + constant × Re^2.

We will ignore any variation in local heat transfer coefficient around the circumference of the cylinder. This is in keeping with the approach used in the data interpretation scheme presented in the last chapter, namely to scale the data as if all angular variation in heat transfer can be scaled as if it was all from the hot film itself rather than from the Rohacell. However, it is recognized that local heat transfer coefficient may vary by up to a factor of two around the circumference of the cylinder at these Reynolds numbers [Zdravkovich, 1997].

Two forms of **radiative** heat transfer are considered: firstly, thermal exchange with the surroundings (both the Martian surface and the Martian sky); and secondly, absorption of incoming sunlight. The emissivity of platinum is taken as 0.3 in the visible [http://www.matweb.com] and 0.1 in the infrared [http://www.newportuk.com /Pdf/OS101.pdf]. The same quantities for Rohacell are taken to be 0.05

and 0.67 ± 0.13 [Caps *et al*., 1997 - note that these data were obtained for a different polyimide foam]. Radiative transfer with the environment is calculated using:

$$q_{rad} = \sigma \varepsilon A\left(T^4 - T_{background}^4\right),$$

where σ is Stefan-Boltzmann's constant (5.67×10^{-8} W m^{-2} K^{-4}), and A and ε represent respectively the area and emissivity of the emitting material.

Because of Rohacell's greater IR emissivity and its greater area, most thermal IR emitted by the wind sensor comes from the Rohacell instead of from the hot film itself, despite the film's higher temperature. This can be seen clearly in the IR photograph of the sensor shown in Figure 6.2.

Heat conduction across the hot pads and films is very small due to the extremely small thickness of the platinum films (effectively ~10 nm, based on the resistivity of the films – see Section 4.2.5). Heat conduction through the Kapton film is similarly small.

Conduction down the wires can be easily calculated using the equation $q = C\Delta T$. The conductance C is given by $C = kA/L$ where k, A and L represent respectively the conductivity, cross-sectional area and conductivity of the wire. For the stainless steel wires connecting the solder pads to the contact board, $C_{wires} = q/\Delta T \sim 0.05$ mW/K; for the copper wires beyond connecting this to the PAW electrical harness, $C_{wires} \sim 0.1$ mW/K. Though these values may seem large, they are only relevant for heat losses from the pads, because very little heat is conducted down the pads from the films.

Finally, we have conduction of heat from the hot films through the Rohacell to the exposed surface of the Rohacell. This is not easily calculated. However, it can be deduced from sensor performance data at very low pressures (at which convective and gaseous conduction losses can be assumed to be zero), as will be seen below. This calculation suggests that $C_{conduction} \sim 0.7 \pm 0.1$ mW/K.

6.2 Results

Using these parameterisations, one can calculate the heat flows in the wind sensor. Figures 6.7 a) and b) show the major heat flows for a sensor for wind speeds of $u = 0$ and 9.7 m/s respectively, in an atmosphere of CO_2 at $p = 7$ mbar and $T = 250$ K (this corresponds to Reynolds numbers of 0 and 116). Each arrow represents a heat flow, and the width of the arrow is proportional to the magnitude of that heat.

Several points can be noted here:

1- Very little heat is lost directly from the film – only 10% in still wind conditions, about 25% in moderate winds ($Re = 116$). This is due mainly to the relatively small area of the film.

2- In still air, the dominant heat loss mechanism is conduction through the Rohacell, followed by radiative loss to the surroundings.

3- In strong winds, the dominant heat loss mechanism is conduction through the Rohacell, followed by convective heat loss to the surroundings.

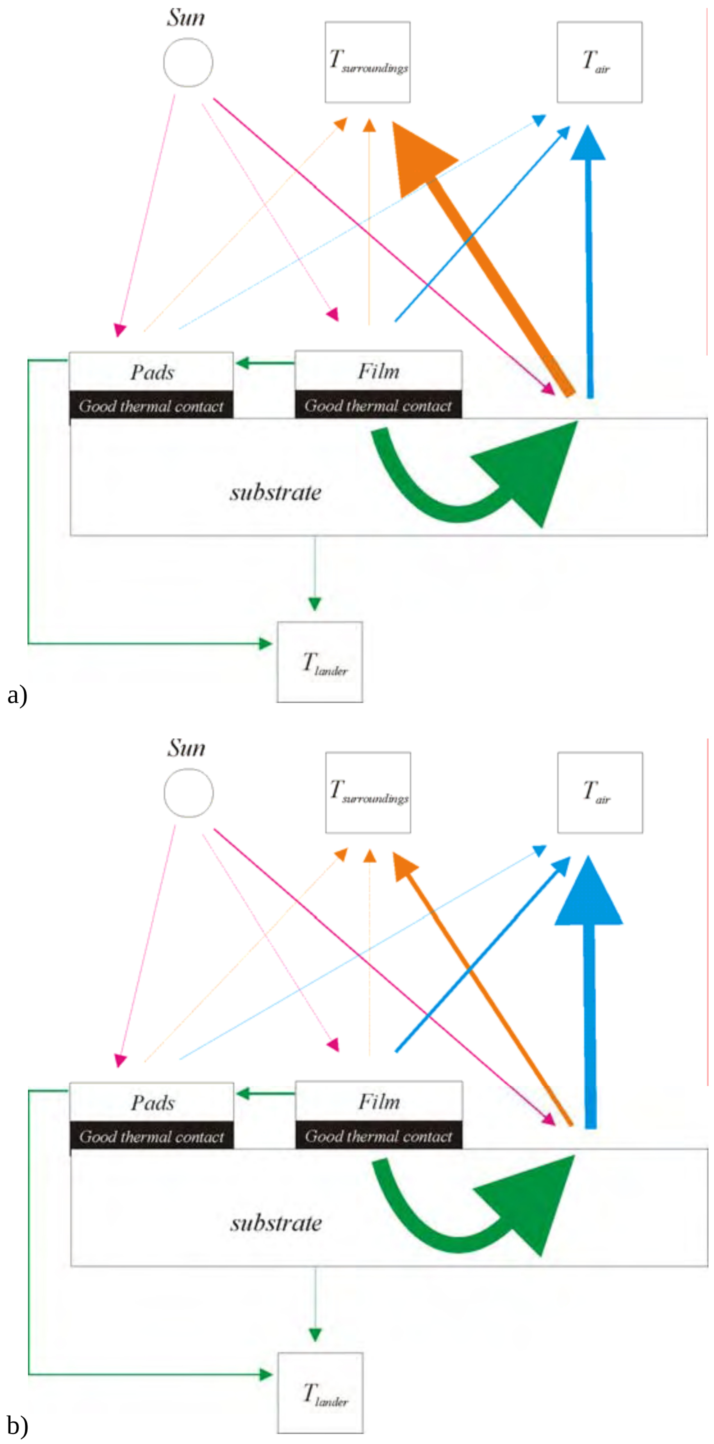

Figure 6.7 – A schematic diagram showing heat flow in B2WS, showing solid conduction, convection and gaseous conduction, radiative loss to surroundings, and sunlight, with wind speeds of *Re* = 0 (top) and *Re* = 116 (below). The width of the arrows is proportional to the magnitude of the heat flow. Heat is generated in the films (~32 mW) and in the pads (~2 mW). Most of the heat dissipated in the pads is conducted to the surface of the Rohacell, from whence it is lost to the atmosphere both by radiation and convection.

At this point, the model will be further simplified to leave just its essential elements. It can be seen in Figure 6.7 that the heat flows through the contact pads are fairly small (only 3 mW are dissipated here). Therefore they will be ignored henceforth. The simplified thermal model can cut down to just the heat flows shown in Figure 6.8.

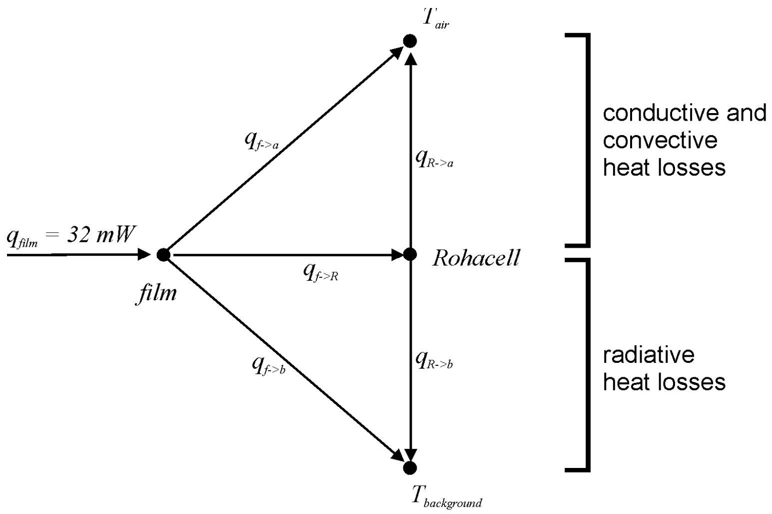

$$q_{f\text{->}R} = (T_f - T_R)\left(0.7\ \text{mW/K}\right)$$

$$q_{f\text{->}a} = C_{f\text{->}a}(T_f - T_{air})\left(2ka_f + f(\theta)\frac{kA_f}{L_f}\left(0.023\times Re^{0.8}\right)\right)$$

$$q_{R\text{->}a} = C_{R\text{->}a}(T_R - T_{air})\left(2ka_R + \frac{kA_R}{D_{sensor}}(0.3 + 0.48\sqrt{Re})\right)$$

$$q_{f\text{->}b} = \sigma\varepsilon_f A_f (T_f^{\ 4} - T_{background}^4)$$

$$q_{R\text{->}b} = \sigma\varepsilon_R A_R (T_R^{\ 4} - T_{background}^4)$$

Figure 6.8 – Analytical thermal model used to calculate heat flows. See text for details.

The equations corresponding to the arrows in the diagram are:

$$q_{f\text{->}R} = (T_f - T_R)\left(0.7\ \text{mW/K}\right)$$

$$q_{f\text{->}a} = C_{f\text{->}a}(T_f - T_{air})\left(2ka_f + f(\theta)\frac{kA_f}{L_f}\left(0.023\times Re^{0.8}\right)\right)$$

$$q_{R\text{->}a} = C_{R\text{->}a}(T_R - T_{air})\left(2ka_R + \frac{kA_R}{D_{sensor}}(0.3 + 0.48\sqrt{Re})\right)$$

$$q_{f\text{->}b} = \sigma\varepsilon_f A_f (T_f^{\ 4} - T_{background}^4)$$

$$q_{R\text{->}b} = \sigma\varepsilon_R A_R (T_R^{\ 4} - T_{background}^4)$$

The symbols $q_{f\text{->}b}$ and $q_{R\text{->}b}$ represent radiative heat losses from the film and the Rohacell respectively. The symbols $q_{f\text{->}a}$ and $q_{R\text{->}a}$ represent respectively heat losses from the film and the Rohacell surface due to combined gaseous conduction and convection. It may be noted that the equation for $q_{f\text{->}a}$ is the only one which includes any angular dependence; the shape of this function $f(\theta)$, as well as its magnitude and velocity dependence, were obtained from the wind sensor calibration data.

This model has been used to calculate heat flows for wind speeds of Re = 0, 116, and 300 on Mars (CO_2 at 250 K) and on Earth (air at 300 K). These Reynolds numbers correspond to wind speeds of roughly 0, 10 and 25 m/s on Mars (CO_2 at 250 K and 7 mbar). It is assumed for these calculations that $T_{background} = T_{air}$. These results are shown in Table 6.1. Heat flows via convection and gaseous conduction have been listed separately for convenience.

	MARS			EARTH			
	CO2, $T_{air} = T_{background}$ = 250K			air, $T_{air} = T_{background}$ = 293 K			
	Re = 0	Re = 116	Re = 300	Re = 0	Re = 116	Re = 300	
ΔT_{film}	82.0	54.2	46.6	63.6	43.0	36.4	K
$\Delta T_{rohacell}$	41.6	16.8	12.0	24.9	8.9	6.1	K
$q_{conv\_f\text{->}a}$	0.3	3.6	5.9	0.4	5.1	8.2	mW
$q_{cond\_f\_\text{>}a}$	3.0	2.0	1.7	4.2	2.8	2.4	mW
$q_{rad\_f\text{->}b}$	0.3	0.2	0.2	0.2	0.2	0.1	mW
$q_{conv\_R\text{->}a}$	2.3	16.8	17.6	2.4	15.8	15.8	mW
$q_{cond\_R\text{->}a}$	9.9	4.0	2.9	10.6	3.8	2.6	mW
$q_{rad\_R\text{->}b}$	16.2	5.4	3.7	14.2	4.4	3.0	mW

Table 6.1 – Heat flows, and film and Rohacell temperatures, calculated using the thermal model shown above for gas and CO_2 at different wind speeds. All figures here assume that the film is at an angle of 55° to the wind (such that it experiences the maximum heat transfer).

These figures show a marked increase in the sensor overheat on Mars, of roughly 80 K in still air compared with 60 K in air at room temperature. The reasons for this are twofold. Firstly, carbon dioxide has a lower thermal conductivity than air, especially at low temperature. Secondly, when the sensor is operating at Martian temperatures it experiences less radiative heat transfer, due to the strong T^4 dependence of radiative heat transfer. However, the actual overheat to be expected on Mars is likely to be closer to 70 K, due to strong radiative cooling to the cold Martian sky.

The analytical model, using the full form of free convection parameterisation presented earlier in this chapter, was also used to calculate the dependence of the sensor on ambient pressure p, and on dissipated power q_{film}. Calculations are shown both for the case of ‘Earth’ (air, p = 5.9 mbar, $T_{air} = T_{background}$ = 293 K) and for ‘Mars’ (CO_2, p = 7 mbar, $T_{air} = T_{background}$ = 250 K). The ‘Earth’ conditions were selected to allow comparison with experimental data, which were presented in Figures 5.4 and 5.5. These experimental data, together with analytical calculations, are shown in Figures 6.9 and 6.10. The weak dependence of $C(u{=}0)$ on pressure shown in Figure 6.10 confirms that free convection is not an important path of heat flow away from the sensor, as explained above. It is interesting to note that the predicted C on Mars is lower than on Earth even at $p = 10^{-3}$ mbar, despite the fact that there is effectively no gas at this pressure; this is due to lower radiative heat loss caused by the lower temperature of the sensor in this case.

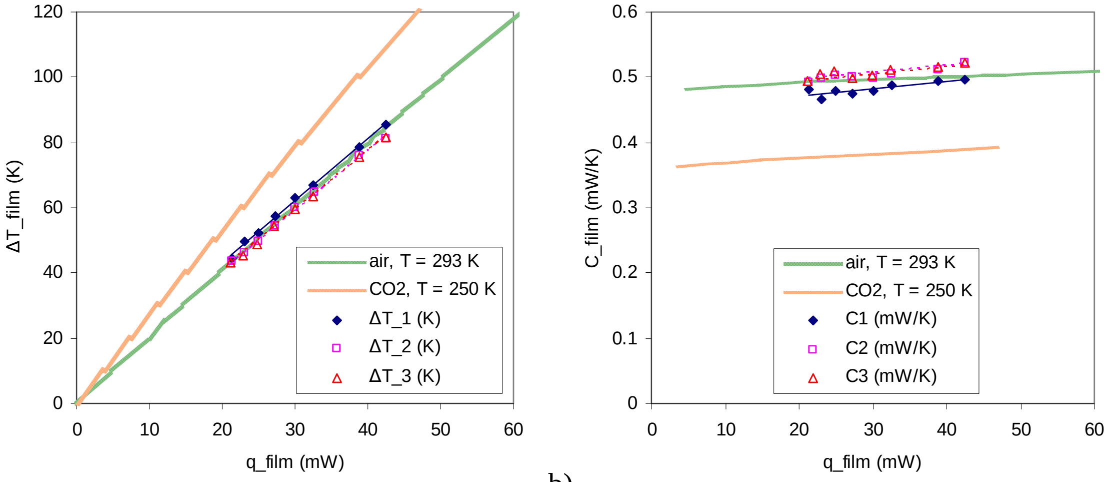

a) b)

Figure 6.9a shows the overheat $\Delta T_{film} = (T_{fllm} - T_{air})$ achieved as a function of power dissipated in the film, for the three films of sensor FM2. Figure 6.9b shows the same information, plotted as $C_{film} = q_{film}/\Delta T_{film}$. Experimental results shown are reproduced from Figure 5.4; the thick lines show results calculated using the analytical model, for the conditions shown. See text for notes.

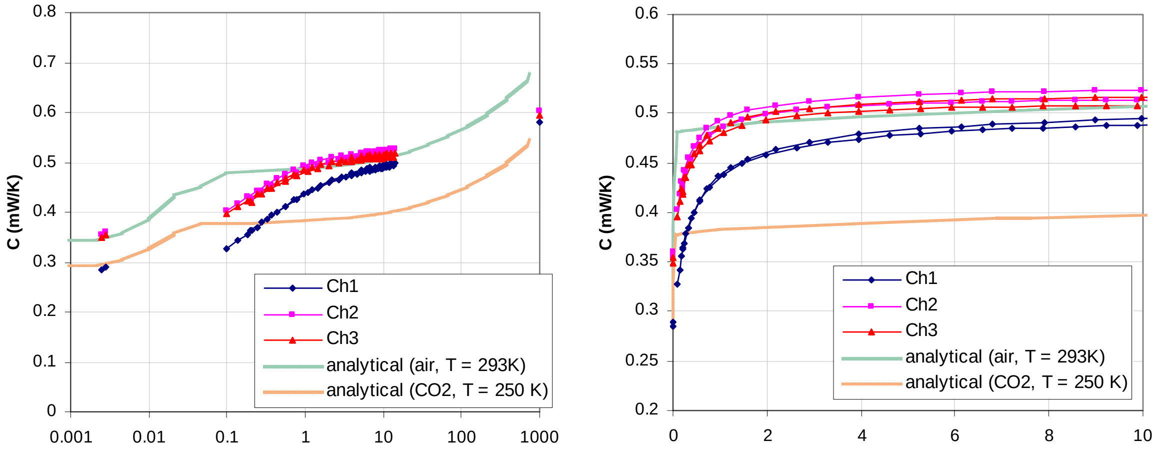

a) b)

Figure 6.10 – Pressure dependence of the sensor output C_{film}, shown as a function of pressure. Note that the left panel shows a logarithmic pressure scale, while the right panel shows a linear plot of $p < 10$ mbar. Experimental data shown are reproduced from Fig 5.5; the thick lines show results calculated using the analytical model, for the conditions shown. See text for notes.

The analytical model can be used to predict the sensor output as a function of wind speed and direction for any conditions, using the angular dependence function. This is illustrated in Figure 6.11; sensor performance has been predicted for atmospheres of air at 293 K and CO_2 at 250 K, for various wind speeds. For both it has been assumed that the effective blackbody temperature of the surroundings $T_{background} = T_{air}$. The conditions for the first of these plots were selected to enable comparison with the B2WS calibration data, shown in Figure 5.7. It can be seen that the analytical model does not manage to accurately reproduce the magnitude or velocity dependence of heat transfer on the downwind side of the sensor.

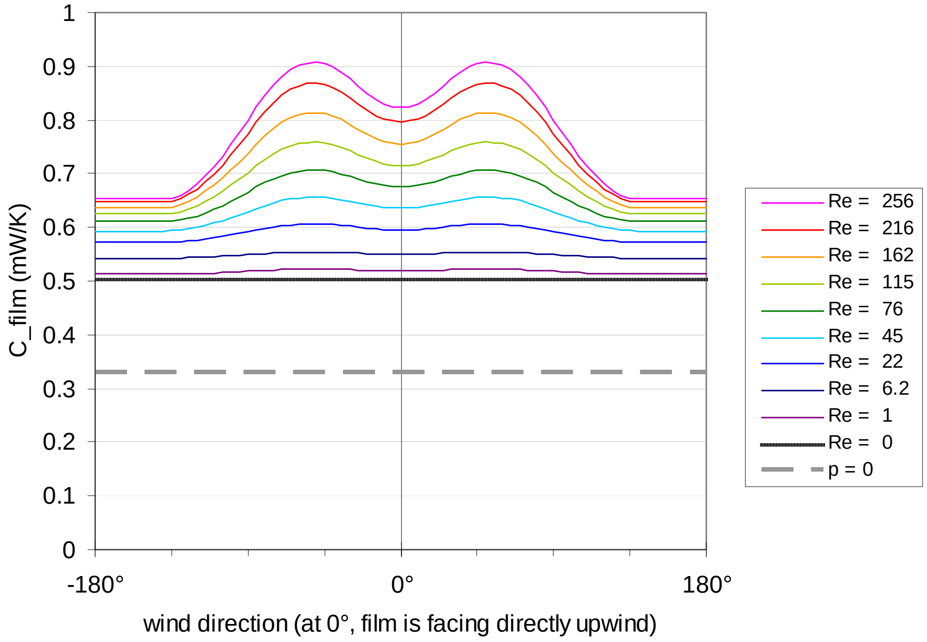

a)

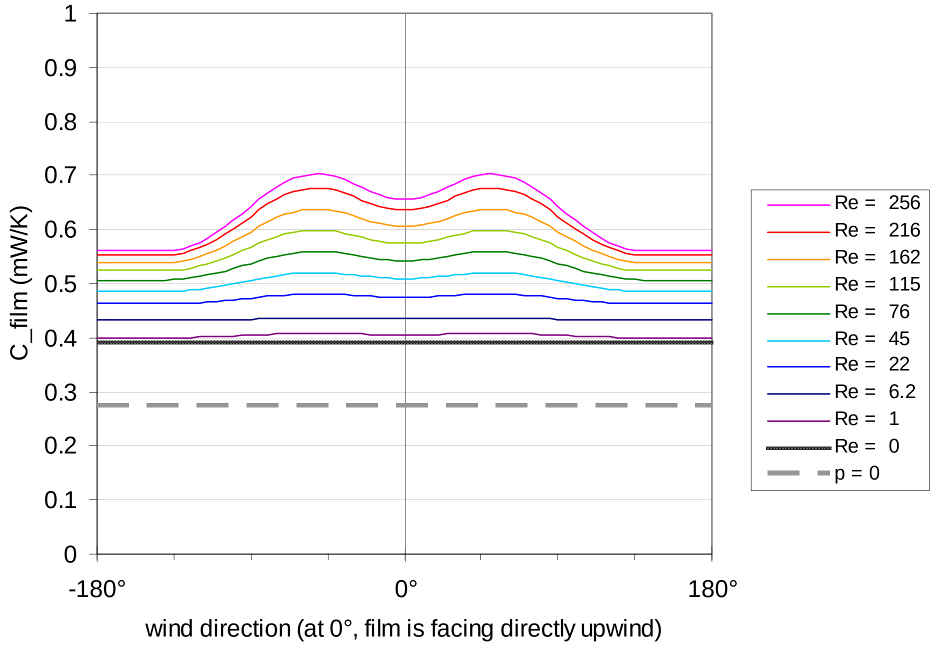

b)

Figure 6.11 – Predictions of sensor performance using the analytical thermal model. These graphs show the sensor performance expressed as $C_{film} = q_{film} / (T_{film} - T_{air})$, in a) air at 293 K and 7 mbar, and b) CO_2 at 250 K and 7 mbar. The Reynolds numbers have been selected to be compared with experimental data in Figure 5.7.

This is a further sign that one of the fundamental assumptions of this model, i.e. that the variation of $q_{r\text{->}a}$ with angle is negligible, is not physically accurate; for a cylinder of uniform surface temperature, it varies with angle by up to a factor of 2 [Zdravkovich, 1997]. This should be of increased concern now that we know that q_{conv_r} turns out to be significantly greater than q_{conv_f}. If time permits, the model may be altered to introduce angular variation of q_{conv_r} based on results from engineering publications such as [Eckert & Soehngen, 1952]. For now, though, we shall continue to use the analytical model to predict the effects of solar radiation and background temperatures on sensor performance, because the analytical model still provides a useful first approximation to sensor performance.

6.3 Sensitivity to air temperature

In Chapter 5 it was shown that the dimensionless calibration maps shown in Figure 5.13 – 5.15 can be used to scale the B2WS calibration in air to be used for different gas types and densities. According to the assumptions underlying the data interpretation scheme and the analytical model, this method should also be valid for different gas temperatures. Two potential sources for error include the scaling of the 'error vector' due to differences in $C(u=0)$ for use in different gas temperatures; however, this is expected to cause an error of less than 1 m/s in the measured wind speed, as was discussed in Section 5.4. Also, the accuracy of the scaling laws may be slightly modified by the fact that some of the angular heat variation is due to heat transfer from the Rohacell rather than from the film. However, any such errors should be small (a few percent), because the scaling of convective heat transfer from the Rohacell $q_{R->a}$ has the same temperature dependence as does convective heat transfer from the film $q_{f->a}$ (both scale with gas conductivity k to calculate Nusselt numbers). If an error is caused by the incomplete parameterization of $q_{R->a}$ in this model, it would change the effective gain of the sensor, but probably only by a couple of percent.

This discussion on whether or not the calibration maps can be validly applied across a range of air temperatures requires that the air temperature is accurately known – this is of course not necessarily the case. The sensitivity of calculated wind speeds to an error in the value assumed for T_{air} was shown in Figures 5.23 and 5.24 for CO_2 winds at 293 K. In this section this analysis is extended to predict sensitivity to errors in T_{air} at Martian temperatures.

This is most effectively done by looking at the same segment of meteorological data from Viking Lander 2 as was shown in Figure 5.29. The B2WS measurement of this data sequence was simulated again in exactly the same way as before, but it was assumed that the air temperature sensor was in fact reading $T_{air} + 2$ K, an error which is greater than the nominal ± 1 K accuracy of the B2TS. The simulated measurement is shown in Figure 6.12. The average over this period of the measured wind speed (2.84 m/s) is only 7% higher than that of the real wind speed (2.67 m/s). This weak sensitivity to errors in air temperature measurement is a result of the data interpretation method based on the differences between film temperatures.

6.4 Sensitivity to sunlight

The average solar constant of Mars, that is the solar radiance reaching the outside of the Martian atmosphere, varies from 500 to 700 W m^{-2} (the variation is due to the eccentricity of the Martian orbit). Any sunlight absorbed on the top circular surface of the Rohacell will affect all three films equally and can therefore be ignored in the first instance. The axis of the sensor will be vertical in most operations. The maximum solar heat fluxes into the hot film and the Rohacell surface are 0.5 and 1.7 mW respectively. For these calculations, an atmospheric optical depth of 0.2 has been assumed, which represents a fairly low dust content in the atmosphere. At this optical depth, the maximum solar heat flux on the vertical sides of the sensor occurs when the sun is at ~ 60° to the vertical.

The effect of this solar flux onto the platinum film is quite easy to calculate. Instead of operating with just the dissipated power input q_{film}, the actual power input is actually $q_{film} + q_{solar->film}$. The mechanisms of heat loss from the film remain unchanged, though, so effectively the sensor output C will be underestimated by a factor $q_{film} / (q_{film} + q_{solar->film})$. Therefore:

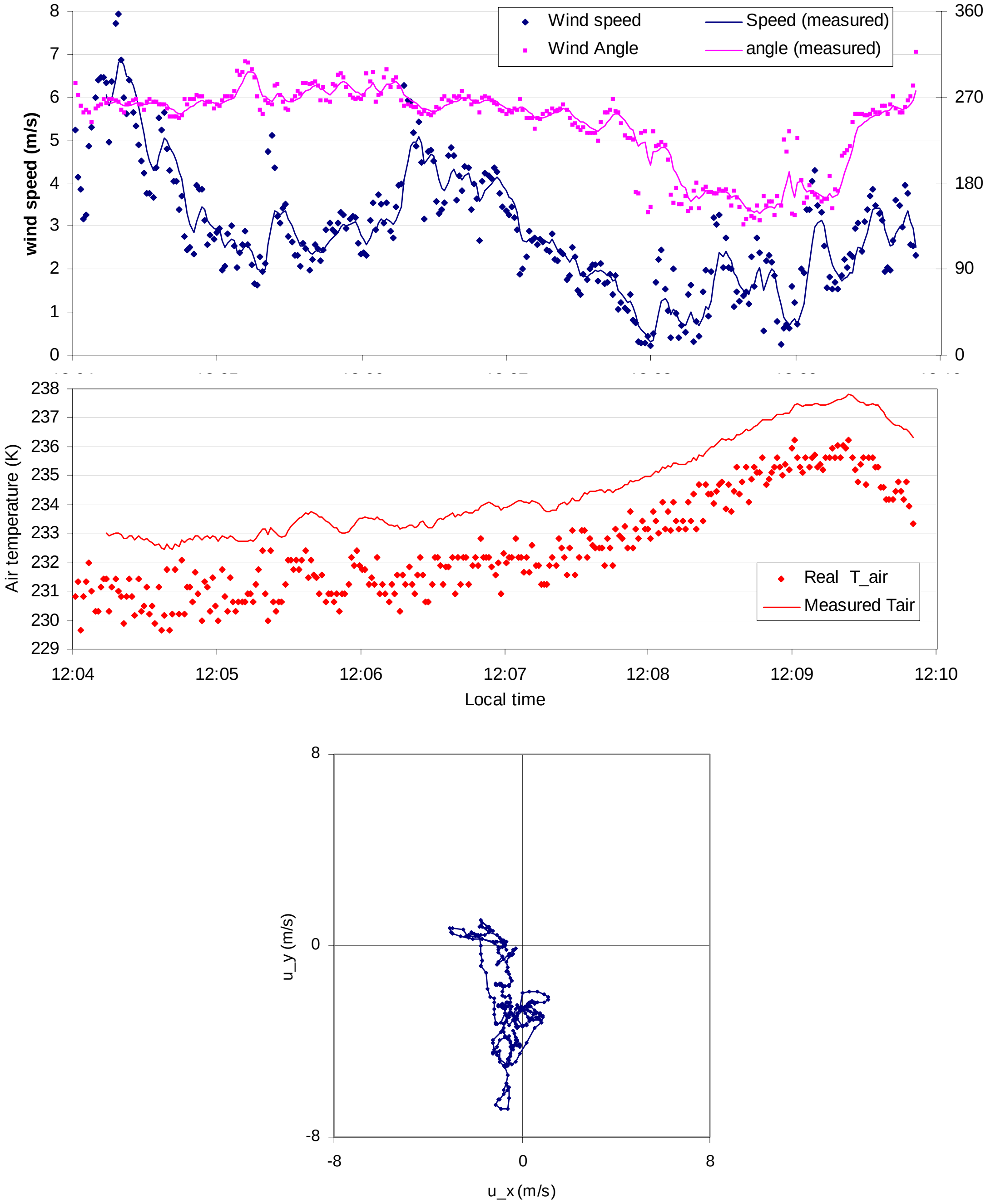

Figure 6.12 – Simulated B2WS measurements in response to real wind and temperature data obtained from the Viking Lander 2. The original data and simulation conditions are as for Figure 5.30, but in this simulation it is assumed that the Beagle 2 temperature sensor is reading $T_{measured} = T_{air} + 2$ K.

$$C_{actual} = \frac{q_{film} + q_{solar->film}}{\Delta T_{film}}$$

$$C_{measured} = \frac{q_{film}}{\Delta T_{film}}$$

$$\frac{C_{actual}}{C_{measured}} = 1 + \frac{q_{solar->film}}{q_{film}} \sim 1.014 \text{ max.}$$

The effect of the solar flux onto the Rohacell is a bit more complicated to calculate, but it can be readily worked out using the analytical model shown in Figure 6.8. This calculation shows that solar flux onto the Rohacell contributes another ~+1.5% to the measured sensor output C_{film} in maximum sunlight (varying with conditions). Although the Rohacell has a much larger absorbing area than the hot film, its absorptivity is lower in the visible and it has a less direct effect on the sensor output C_{film}.

This total change of up to 3% in sensor output due to sunlight may sound small. However, it falls asymmetrically on the sensor, falling on only or two films. Measured wind speeds are computed from the differences between the sensor outputs of different films; therefore, an effective radiative input of 1 mW on one side of the sensor film is important.

To get an idea of how this will affect wind measurements on Mars, its effect was simulated on the same segment of VL2 data as was used earlier. The B2WS measurement of wind speed was repeated with an error of – 0.017 mW/K in the output C_3 of film 3, which is equivalent to full sunlight shining on film 3 in an atmosphere with low dust (optical depth = 0.2) at an angle of 60^o to the vertical. The 'measured' wind speed and direction are shown in Figure 6.13.

The effect is slightly more complex than the last example, and can be seen most clearly by looking at the hodograph shown in the bottom panel of the figure. The orientations of the three films are marked on the figure to aid understanding. Simply put, when sunlight falls on film 3, its temperature will increase; therefore it seems as if it is experiencing less wind cooling; therefore, it seems as if less wind is blowing from that side of the sensor. The shift in the hodograph is a linear translation in (Nu_x, Nu_y) space – the same axes as used in the calibration maps – but non-linear in (u_x, u_y) space. This is illustrated in Figure 6.14, in which the 'hodograph' of $\underline{Nu}$ vectors is superimposed on a calibration map, with and without this linear shift applied. For this data series, the average magnitude of the shift in (u_x, u_y) due to this error is ~1.7 m/s.

This kind of error – a shift of the effective zero of the sensor – is a disadvantage of this technique of using the differences between the film temperatures, rather than their average, to measure the wind vector. Use of the average film data in the data interpretation code may help reduce the zero error of the sensor; this is a subject which will be investigated further before the Beagle 2 landing.

The error in C_{film} due to sunlight is almost independent of atmospheric pressure, temperature and wind speed, since it is largely dependent on solar flux, radiative loading, and conductivity through the Rohacell, all of which are independent of ambient gas properties. Therefore this error δC_{solar} can be calculated in advance for each film, as a function of local time and film orientation.

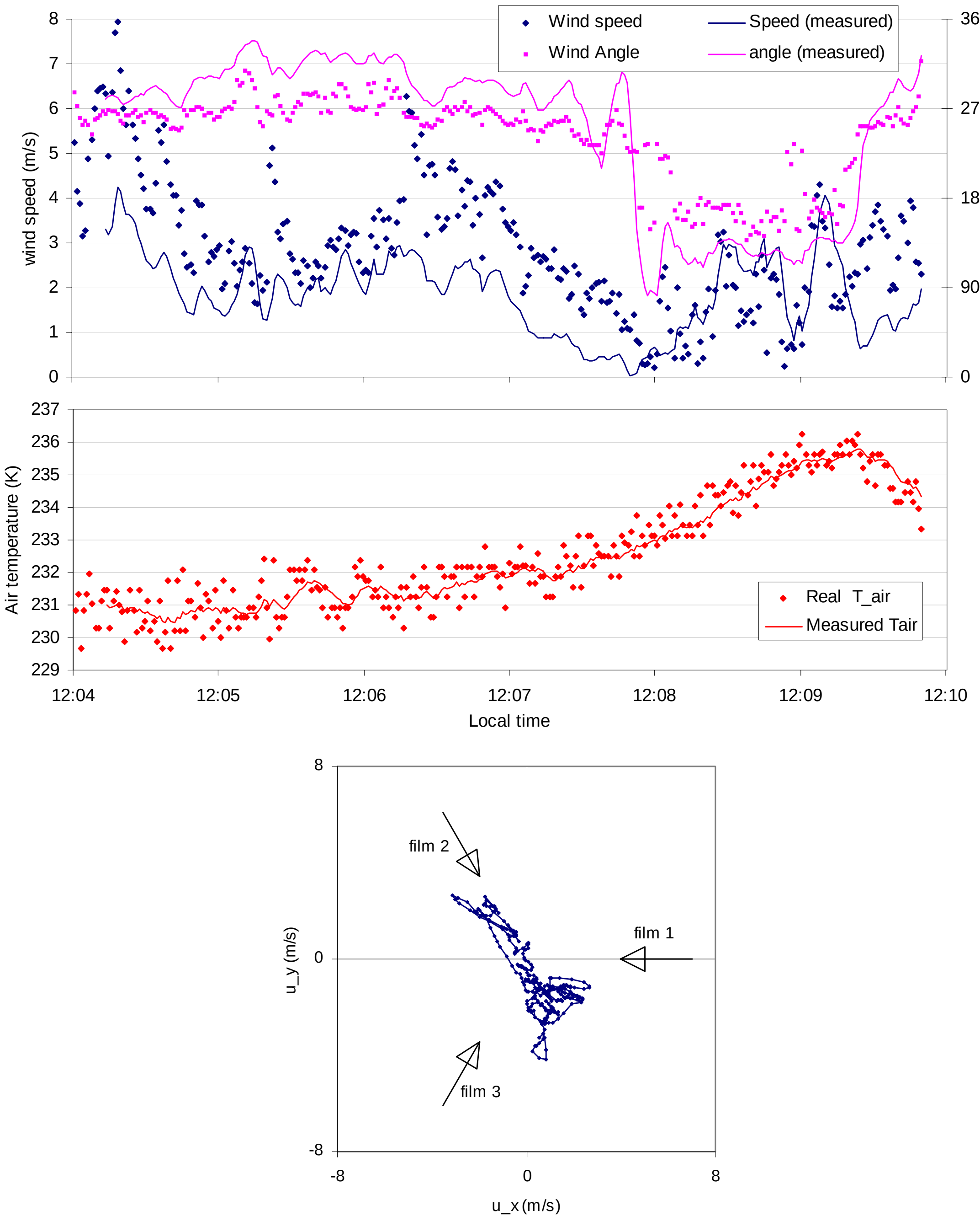

Figure 6.13 – as for Figure 5.30, but in this simulation an error of – 0.017 mW is assumed in the output, C_3, of film 3. This is equivalent to the error caused by bright sunlight shining onto film 3, if no correction is applied. The orientations of the films are indicated on the hodograph for clarity.

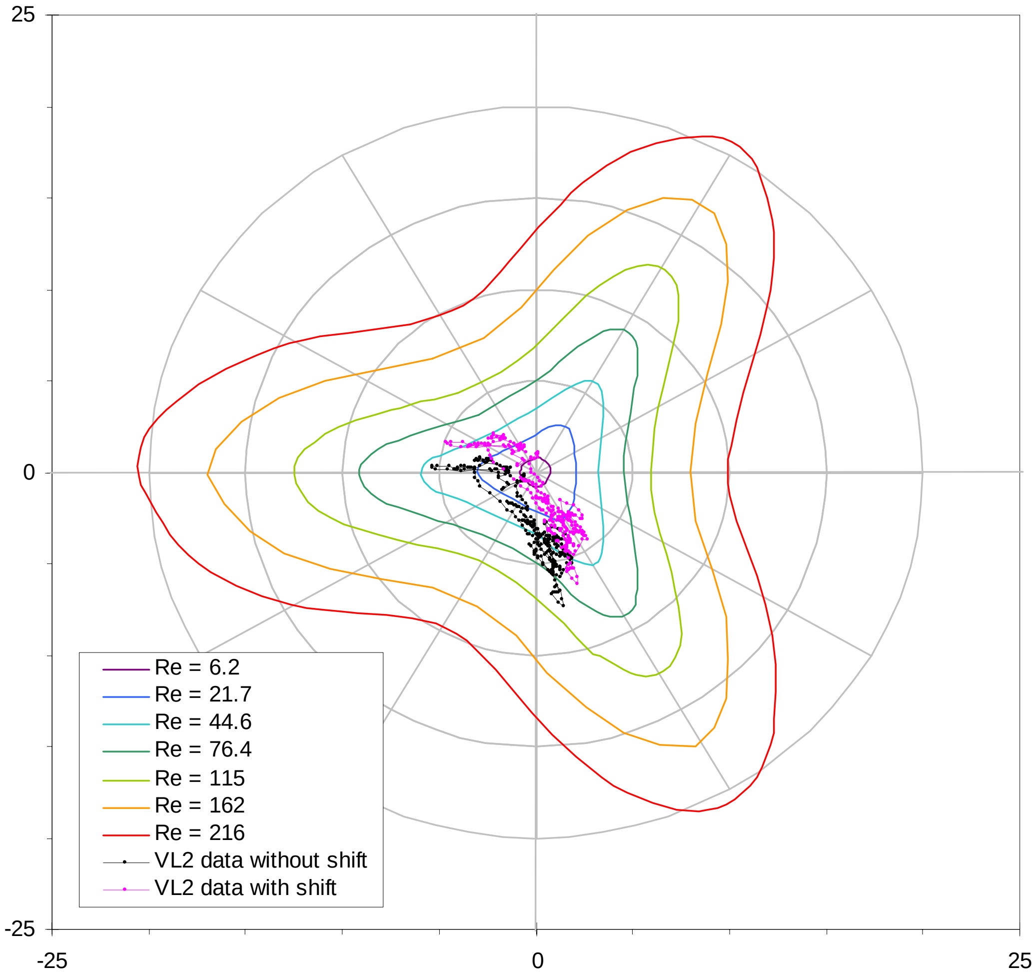

Figure 6.14 – Illustration of the 'zero shift' effect of the data shown in Figure 6.13. The data marked with black points is a hodograph of the *Nu* vector from Figure 6.13 as it would be if correctly measured. The data marked with pink points shows the *Nu* hodograph as it would be if measured in the conditions as described in Figure 6.13. Superimposed on these points is a calibration map for this sensor (FM4).

6.5 Effect of error in background temperature

The analytical model has shown that the dominant heat loss mechanism in low wind conditions is thermal IR from the surface of the Rohacell. The magnitude of thermal heat loss is dependent on the effective blackbody temperature 'visible' to the sensor, which is referred to in this document as the background temperature $T_{background}$. The background temperature 'seen' by each film will be a combination of the sky temperature and the ground temperature. The effective sky temperature can vary from 120 K on a clear night (low dust, optical depth = 0.4) to 190 K at midday in a high dust case (optical depth = 4.5). The effective ground temperature is typically about 10 K warmer than the air temperature at 1 m height in the daytime, and ~ 10 K colder than the air temperature at night [Peskett, 2001].

As a sample case, let us suppose that T_{ground}, T_{air} and T_{sky} are respectively 250 K, 250 K and 150 K – such temperatures might be encountered in late afternoon in a scenario of relatively low dust [Peskett, 2001]. If the sensor is perfectly vertical, the horizon will be halfway across the 'field of view' of all three films, so the effective temperature of all three will be $T_{background} = (T_{sky} + T_{ground})/2 = 200$ K. In these conditions, the films are expected to reach an overheat of 72 K. This is less than the predicted overheat of 82 K at $T_{air} = T_{background} = 250$ K; this lower overheat is due to greater radiative heat losses. The analytical model predicts that, as long as $T_{background}$ is the same for the three films, the data interpretation scheme should calculate the correct wind speed and temperature, using the dimensionless calibration maps. This is a similar argument as was used above for scaling with respect to air temperature.

However, the Beagle 2 is not going to land on a perfectly horizontal plane, and will have some degree of tilt. Though it will be possible to adjust the angle of the sensor once the lander's orientation is known, this will not occur immediately after landing. Therefore, it is important to estimate the effect that wind sensor tilt will have on the readings. If the sensor is tilted by 10° to the vertical, $T_{background}$ will range from 191 to 209 K for different sides of the sensor (assuming T_{sky} and T_{ground} as above). This error of 9 K in $T_{background}$ would in turn cause an error in C_{film} of 0.010 mW/K, which will cause a 'zero shift error' in the measured wind speeds very similar to that simulated in Figures 6.13 and 6.14, although the magnitude of this shift would only be 60% as great as that simulated in those figures. The average magnitude of the error in the wind speed vector is ~1 m/s.

Another case worth considering is when the sensor is rotated by 90° such that its axis is horizontal, as might be done to measure vertical wind speeds. In this case the upward-facing side of the sensor will experience much greater radiative heat loss than the down-facing side. This would be interpreted as meaning that it was windier on the up-facing side, and might lead to a conclusion that there was a strong downdraft! Using the sky, ground and background temperatures given in the paragraph above, the analytical model predicts an error of about 0.11 mW/K in C_{film}, which in turn would lead to an error of in wind speed of $\delta u > 10$ m/s.

This is clearly a very important error in comparison to expected wind speeds, especially in comparison with vertical wind speeds which are likely to be less than 1 m/s! However, the sky and ground temperatures will be relatively constant with respect to time, whereas any vertical air currents would transitory, associated with turbulence or convective vortices. For example, a convective vortex passing over the lander might produce a measurable updraft; a simultaneous drop in pressure would confirm the observation. The validity of the wind sensor's calibration is very doubtful under these extremely imbalanced radiative loads. For this reason it would be impossible to obtain quantitative measurements of vertical wind speed unless a calibration for such radiatively imbalanced situations can be arranged.

However, a far more persuasive argument against measurement of vertical wind speeds is that the shape of the wind sensor, and its position on the spacecraft, are unsuitable for such measurements. The flat disc-shaped base would give rise to severe turbulence around the wind sensor films if there is any component of horizontal wind in the direction of the axis of the wind sensor; this turbulence would probably have stronger vertical components than that associated to 'real' PBL vertical wind speeds. Operations on Mars will be discussed further in the next chapter.

6.6 Conclusions & discussion of overall accuracy

In this chapter an analytical thermal model of the sensor has been presented. This model has revealed that most of the heat dissipated in the hot films is not lost directly from the hot film, but passes through the Rohacell. This has made thermal analysis of the B2WS more complex than that of a single hot wire anemometer, so the model presented here has necessarily included some gross simplifications. However, it is useful because it a) provides insight in the heat flows in the sensor, and b) allows predictions about how sensor performance will change in environmental conditions for which testing was not possible. Ways have been suggested in which the analytical model could be improved at a later date; in particular, angular variation of convective heat transfer from the Rohacell should be introduced. Furthermore, the analytical model's predictions for the sensor's response to different air and background temperatures are in need of validation.

A rigorous error analysis has not been undertaken because it would be unable to resolve two large uncertainties:

1 – The analytical predictions of sensor performance at low temperature have not been validated empirically. The same applies for sensor behavior when radiating to a cold background, as will be the case on Mars.

2 – There are significant uncertainties concerning the interaction of B2WS with the Beagle 2 spacecraft electronics. Specifically, no tests have been performed with the flight ADC, with the flight power supplies, or with the flight cables linking the sensor head to the electronics board. The B2WS outputs are low-gain analogue voltage signals, so these uncertainties are important.

In this section are assembled the different sources of uncertainty which have been flagged in this thesis, in an attempt to quantify the overall accuracy of the wind speed measurements. Sources of error can be divided into two categories: those affecting all films equally (such as an error in air temperature measurement), and those affecting the differences between the films (such as sunlight shining on one side of the sensor). It is hoped that the differences between these has been clearly demonstrated in Figures 6.12 through 6.14. It is difficult to set out the errors in a clear, user-friendly form; this is because the relative importance of different heat flows varies over the range of temperatures of the model. As a baseline, the magnitude of all errors listed here are for incremental changes from the baseline condition of CO_2 at p = 7 mbar at $T_{background} = T_{air} =$ 250 K.

	Source Uncertainty	Resulting gain error	resulting zero error	
Wind Tunnel speed	± 3%	3%		
Uncertainty in air temperature:	± 1 K	3.5%		
Uncertainty in lead resistance:	± 0.5 Ω	3%		
Electronics temperature	220 - 290 K	Not calculated		
Uncertainty in V_{supply}	± 10 mV	1.5%		
		5.7%	if added in quadrature	
Direct radiation (Solar heating)	up to 2 mW		± 1.7	m/s
Tilt -> uncertainty in background temp	± 10°		± 1.0	m/s
Uncertainty in BEE resistances	up to ±0.1%		± 1.5	m/s
Repeatability (from Figures 6.21-6.24)		~ 10%		
Overall steady-state accuracy		16%	± 4.2	m/s

The last entry in this table, ‘repeatability’, has been added in response to the wind tunnel tests described in Section 5.5. In these tests it was found that the agreement between real and measured wind speeds could not be demonstrated to be significantly better than 10%.

The large zero shift error of ± 4.2 m/s may seem a greater cause for concern, because this is in fact greater than many of the wind speeds one would expect to measure on Mars. However, this can be significantly reduced through one of two methods.

The first is by measuring the average wind vector during a 360º rotation of the wind sensor around a vertical axis while on Mars. It is assumed during this process that the average of the wind vector measured relative to the wind sensor is close or equal to zero. Validation of this statement, and descriptions of planned operations on Mars, will be presented in the next chapter. It is estimated that this process allows re-zeroing of the sensor to an accuracy of ±1 m/s[*]. However, this *in situ* sensor rotation requires spacecraft resources, and is only likely to be performed once per week. Therefore, it will be performed only in a very small subset of the environmental conditions in which the sensor will be operating, so there will still be some uncertainty as to which effective zero vector should be used in the data interpretation process, especially because it will not be known what mechanism led to the need for a zero shift, so it will be difficult to correct the zero shift correction for different temperature conditions.

The second process of correcting the zero shift error relies on using the *common-mode* variation of the three wind sensor outputs. Effectively, the common-mode variation (say Nu_{ave}) provides a second, almost independent measurement of wind speed. This was demonstrated in Figure 5.26. If Nu_{ave} is plotted in two-dimensional (Nu_x, Nu_y) space, the minimum Nu should occur at (0, 0). If the minimum does not occur at (0, 0), the effective zero vector (δNu_x, δNu_y) should be changed accordingly. This correction process has not yet been developed, but looks like a promising technique and so will be investigated further before the ground phase of Beagle 2 operations.

Two more potential error sources are long-term drift in sensor performance, and changes in the film resistances. The first of these is an unknown quantity, as B2WS performance data were only taken over an 8-month period, during which the sensors were stored in conditions quite unlike either the cruise phase or the landed phase. Changes in film resistances can be detected and compensated for by use of the sensor in TEMP mode. However, the accuracy of the resistance measurement possible in TEMP mode is only expected to be 0.3 Ω, which could lead to a zero shift error of ~1.7 m/s. Again, though, such an error might be corrected for using one or both of the zero shift correction techniques mentioned above.

The uncertainty in wind direction has not been discussed independently; this is because the retrieval of wind direction is intimately linked with the retrieval of wind speed. Any error in the gain of the wind

---

[*] Accuracy of the assumption that the average Re vector during a whole rotation sequence is = 0 is estimated to be <0.5 m/s, based on a simulation presented in Chapter 7. Also, analysis of the calibration maps shows that the average of the Nu vector during a rotation is < 0.5 for all wind speeds. This error is equivalent to an error in wind speed of 0.6 m/s. The sum of these two errors is ~ ± 1 m/s.

speed measurement should not affect the accuracy of the wind direction measurement. Therefore, the error in the wind speed measurement is expected to be entirely due to the ‘zero-shift’ type errors. To a first approximation, the error in wind angle measurement is therefore given by

$$\text{error in wind angle} = \arctan^{-1}\left(\frac{|\delta u|}{|u|}\right),$$

where |δu| and |*u*| represent respectively the wind speed and the magnitude of the zero-shift error in wind vector. If the wind speed zero error can be reduced to ±1 m/s through *in situ* recalibration, as discussed above, the error in measured wind direction will be ± 10º for wind speeds above 5 m/s.

Chapter 7 - B2WS: Operations on Mars

With any spacecraft, it is necessary to plan observations in advance. Beagle 2, with its stringent limitations on available power and data bandwidth, is no exception. In the case of Beagle 2, meteorological observation planning is complicated by the fact that the wind and temperature sensors are on a moving arm. This offers new measurement opportunities, but also reduces the time available for meteorology because the arm is needed also by other instruments.

In this chapter I will first describe the general meteorological sampling modes. I will then explain implementation of the two diagnostic procedures available for the B2WS on Mars, namely TEMP mode and *in situ* rotation of the wind sensor. I will then go on to describe further ‘activity sequences’ – measurement sequences which require movement of the arm.

7.1 Meteorological sampling

Three modes of meteorological sampling are planned: *high-rate*, *low-rate*, and *listening*. The default arm position for all this meteorological sampling, shown in Figure 7.1, is called WIND_HIGH. The wind sensor can be seen projecting vertically above the PAW. The arm has been set at 20° to the vertical, so that the wind sensor is not above the lander base; this was done in order to minimize the effects of lander interference (as was done for Viking). The wind sensor is 93 cm above the plane of the base of the lander, which is less than the Viking and Pathfinder wind sensors but as high as the NetLander wind sensor. The wind sensor will be 77 cm above the plane of the rim of the lander, so should be less affected by mechanically-induced turbulence when the wind is blowing from the direction of the lander than was the Viking wind sensor. If the lander is more than 10º from the horizontal, this position will be modified using the ‘wrist’ joints of the ARM so that the axis of the wind sensor is vertical.

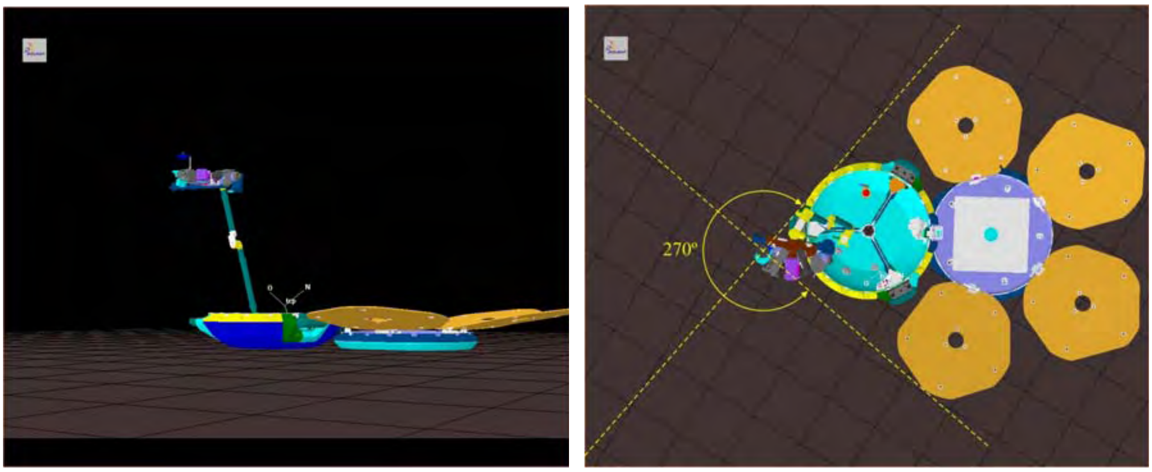

Figure 7.1 – Computer-generated view of WIND_HIGH, the main wind sensing position, shown in (left) side view and (right) top view. In the right panel, a 270º arc has been included to show the range of wind directions for which no portion of the lander is upwind of the wind sensor. For scale, the wind sensor is 93 cm above the ground plane.

7.1.1 High-rate Mode

The high-rate mode will normally involve returning data from the temperature, wind and pressure sensors at a nominal sampling rate of 2 Hz. This sampling rate, faster than that used in previous missions, has been specified in order to allow better study of convective vortices and of PBL turbulence. This fast sampling rate will be used in the daytime, when the PBL is unstably stratified and thus experiencing maximum turbulence. This sampling rate is fast compared with the response times expected of the wind and temperature sensors; however it remains in the baseline operations strategy to help diagnose problems with noise in the data.

It is noted that many of the meteorological papers based on Pathfinder meteorological data have been based on data taken on one of the four 'presidential MET-sessions', i.e. one of those four occasions on which meteorological data were taken continuously for a full Martian sol. It is hoped that it will be possible, at least once, to turn on the meteorological sensors continuously for an entire Martian sol. It is hoped that a sampling rate of 1 Hz can be used during the daytime (0800-1600 local time), reduced to 0.25 Hz at night. Further reduction of sampling rate may be necessary in order to provide a manageable amount of data.

7.1.2 Listening Mode

'Listening' mode has been designed specifically to study convective vortices and dust devils. In this mode, the sensors are turned on and record data at 4 Hz. At the end of each 300-second period, the data are examined onboard Beagle 2, to see whether a dust devil 'event' is likely to have occurred. This is done by setting certain trigger criteria. If the trigger criteria are met, this 300-second segment of meteorological data is saved and eventually transmitted to Earth; if the trigger criteria are not met, the data are discarded. This mode will hopefully result in some meteorological signatures of dust devils, recorded at a high sampling rate (4 Hz), without prohibitively large data downlink requirements.

The format of the criteria is quite flexible: a trigger criterion is defined by comparing an average or a standard deviation of the last n readings, to another value, which may be either a constant or another average or another standard deviation. This can be applied to any of the 16 voltage output lines of the environmental suite, which include sensors for pressure, temperature, and dust momentum as well as wind. The software to perform this task has been written, and is already onboard Beagle 2. The trigger criteria can be uploaded to Beagle 2 when it is in place – therefore, it will be possible to examine preliminary data obtained from Beagle 2 in high-rate mode before deciding what threshold criteria to upload.

The selection of trigger criteria is informed by studies of previous Mars *in situ* meteorological data sets. Murphy & Nelli (2002) found that the single most salient signature of a convective vortex was an abrupt pressure drop of $> 5\ \mu$bar, when compared with a 15-minute average. Ringrose *et al.* (2003) identified dust devils in Viking Lander 2 data by comparing a short term average (STA) of the last n wind speed and direction readings, to a long term average (LTA) over the last m readings (typically $n = 3$, $m = 50$). The trigger criteria used were $|\mathrm{STA} - \mathrm{LTA}| > 6$ m/s for wind speed, or 40° for wind direction.

Other signatures may include an abnormally high rate of dust deposition on Beagle 2's dust momentum sensor, or sudden rise in temperature associated with the warm core of the vortex. This last signature would be very difficult to spot, though, because the temperature fluctuations in the daytime PBL are considerable anyway.

Triggering from the wind sensor output voltages is difficult, because they vary strongly with temperature as well as with wind speed. As discussed in Section 4.5.2, a sudden rise of 100 mV in one of the wind sensor output channels might signal a change of wind speed from 14 m/s to 7 m/s; but it might also signal a rise in air temperature of 8°C, a commonplace occurrence in the daytime PBL. The wind direction, too, is not easy to obtain onboard Beagle 2 from the output voltages. Therefore, the wind sensor outputs will probably not be used as a trigger criterion in listening mode. The most promising trigger criterion *a priori* for use on Beagle 2 is a sudden pressure drop, as used by Murphy & Nelli (2002).

The default position for the listening mode will be WIND_HIGH. The possibility of putting the wind sensor with its axis horizontal, as shown in Figure 7.2, has been considered. The goal of this would be to obtain the first ever measurements of vertical wind speed in the core of a Martian convective vortex. A sudden upward wind might even be used as a trigger criterion. If using this position, though, the wind sensor will no longer be able to measure the circular swing in horizontal wind direction which is the clearest sign of a convective vortex. Therefore, it would be impossible to put the measurement of an updraft into its proper meteorological context. Furthermore, the data are near-meaningless if the wind direction is from behind the PAW, as this would lead to turbulence around the wind sensor. Since the passage of a convective vortex necessarily involves a swing in wind direction, the wind direction is almost sure to come from behind the PAW at some point, causing turbulence which would lead to erroneous results. Therefore sensing of vertical wind has been removed from the operations plan.

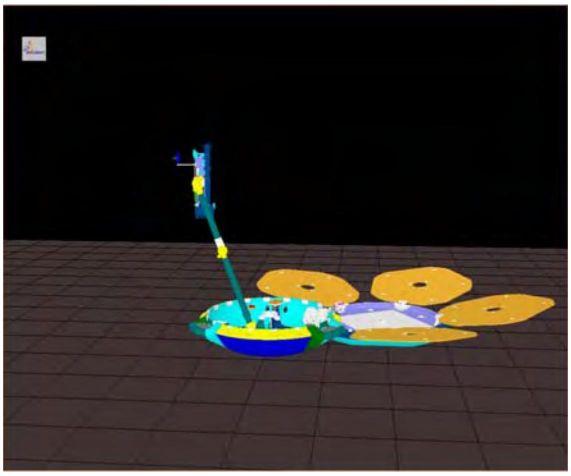

Figure 7.2 – Computer-generated view of WIND_VERTSENSING_0. Note that the axis of the wind sensor is horizontal, and points away from the lander. This position was designed to be used for vertical wind sensing.

7.1.3 Low-rate Mode

Finally, the ‘low-rate’ meteorology mode specifies the minimum data rate. This will apply, for example, when the ARM is being used to examine rocks, so that the wind and air temperature sensors are not in a useful position for meteorology. In this mode, the meteorological sensors will be turned on once every half hour and will take five readings at 1 Hz. The average and standard deviation of these readings will then be returned to Earth. This averaging of five points will not capture the fluctuations of air temperature, or of wind; it is used to reduce instrument noise and ADC errors. Whether or not these readings prove to be of any use for the wind air temperature sensors is highly doubtful, but it will provide a continuous half-hourly record of atmospheric pressure, as well as data from the other environmental sensors.

7.2 TEMP mode

As discussed in Chapters 4 and 6, there are two diagnostic checks on Mars which can be used to perform a limited *in situ* recalibration of the wind sensor. The first is using the TEMP mode of the wind sensor electronics.

Every time the wind sensor electronics board is powered up, it starts in TEMP mode, which measures the resistance of the wind sensor films. This will be monitored often at the beginning of the mission, and once a day for the rest of the mission (otherwise, the TEMP mode data will not be returned to Earth to save bandwidth).

The TEMP mode resistance measurement can be used to signal whether there has been any gross change in the film resistance during the interplanetary cruise phase, or as the result of dust erosion. An anomalous reading in TEMP mode might also signal a failure in the wind sensor electronics. However, the accuracy of the TEMP mode resistance measurement is much less than that of the cryostat calibration (described in Section 5.1), so the *in situ* resistance measurement will not be used for wind vector calculation unless it is clear that there has been a gross change in the film resistances. This is tentatively defined as an error of 1 ohm when looking at TEMP mode measurements averaged over a diurnal cycle. However, agreement between the different films will be taken in to account, as will the performance of the air temperature sensor.

7.3 Wind sensor rotation

The second diagnostic resource for the wind sensor is the *in situ* rotation of the wind sensor on Mars. All wind tunnel calibration data were obtained by rotating the wind sensor around a vertical axis, first by 360° in one direction, then in the reverse direction. It is possible to perform exactly the same sequence on Mars, by rotating the shoulder and wrist joints of Beagle 2’s arm, while the arm is vertically upwards. The Beagle 2 arm motors can be rotated at a maximum speed of 1°/second, so the whole rotation sequence, in both directions, will take 12 minutes. During this period the wind sensor output will be recorded at a sampling rate of 0.5 Hz.

The most obvious difference between this procedure on Mars and the wind tunnel test on Earth is that the wind speed and direction will not be stable on Mars, as they were in the wind tunnel. However, any steady component of drift in temperature, wind speed or direction over the 12-minute period will be cancelled out by averaging data from the two rotation directions. The use of two rotations will provide some indication of how repeatable these data are for re-calibration.

How will this information be used? The easiest way to use it is to simply average the output vector $\underline{Nu}$ obtained for all points during the rotation. The result, in a stable wind, would be equal to zero. Therefore this provides an opportunity to 're-zero' the sensor. If this 'zero $\underline{Nu}$' vector is obtained separately for the two rotations, the repeatability of this measurement will be evident. If the wind field is reasonably steady, it may be possible to determine further performance information about the wind sensor performance, for example to see if the effective gain on one of the channels has changed (this might occur as a result of failure of the electronics board).

In order to minimize fluctuations in wind and temperature while performing this sequence, it must be performed outside the hours of unstable stratification (~ 0800 – 1600). However, the arm cannot be moved at night because of power limitations. Therefore the recalibration sequence has been scheduled to occur at 1800 local time, which is roughly the time in the evening when the vertical temperature gradient is closest to zero (as seen in the Pathfinder air temperature measurements, shown in Figure 1.7). It has been requested that this sequence be performed twice early on in the mission (in the first week), then once every two weeks thereafter. If possible the sensor rotation will also be performed at dawn, before the period of convective turbulence. This would be useful as the ground and air temperatures will be quite different to the dusk case, and it may be possible to see if this affects the calibration.

The lander will, of course, not be perfectly horizontal. Therefore, the wind sensor will not, in this sequence, be perfectly vertical. This is unavoidable. Furthermore, the ARM geometry makes it virtually impossible to rotate the sensor about a vertical axis if the lander is anything but horizontal. This test will still provide useful diagnostic information, whatever the angle of the lander.

7.3.1 Simulation with Viking Lander 2 wind data

Can this technique really be used in the turbulent environment of Mars to re-zero the sensor? To find out, B2WS response to real Mars wind data was simulated. In Figure 7.3, wind hodographs are shown for two twelve-minute data segments of wind data as measured by Viking Lander 2. The data segments start at 1800 local time on sols 030 and 554, and have sampling rates of 8 and 16 seconds respectively. The average air temperature during these data segments was 239.7 K and 237.1 K respectively, with fluctuations of no more than ±1.2 K during these sequences, due to the stable stratification of the atmosphere at dusk. Wind speeds ranged from 0 to 2.5 m/s during the first segment and from 1 to 4 m/s during the second. These two sols were chosen because they were the only ones for which data were obtainable at dusk with a sampling time of less than 30 seconds.

The wind speed data which would be measured by the B2WS during the *in situ* rotation sequence in this wind field are shown in the right panels of Figure 7.3. Red circles are used to indicate the average wind vector *Re* calculated for each individual rotation (each sequence consists of two 360°, in opposite directions). It can be seen that, for all four rotations, the average *Re* vector is less than 3, which corresponds to a wind speed error of about 0.2 m/s.

The effect of temperature fluctuations on this process is not expected to be significant; during these data sequences the maximum temperature fluctuation was only deviant by ±1.2 K from the average.

Also, the temperature fluctuations during these segments were mostly of short time scale (~10 seconds) and so would have been averaged out over the 12-minute duration of the rotation sequence.

The effect of sensor response time, too, was not simulated for this particular data run; it was assumed that the sensor response was complete and instantaneous. If a non-zero sensor response time is assumed, the fluctuations are smoothed out. For the 12-minute time scale of the *in situ* rotation sequences, this does not reduce the accuracy of the procedure.

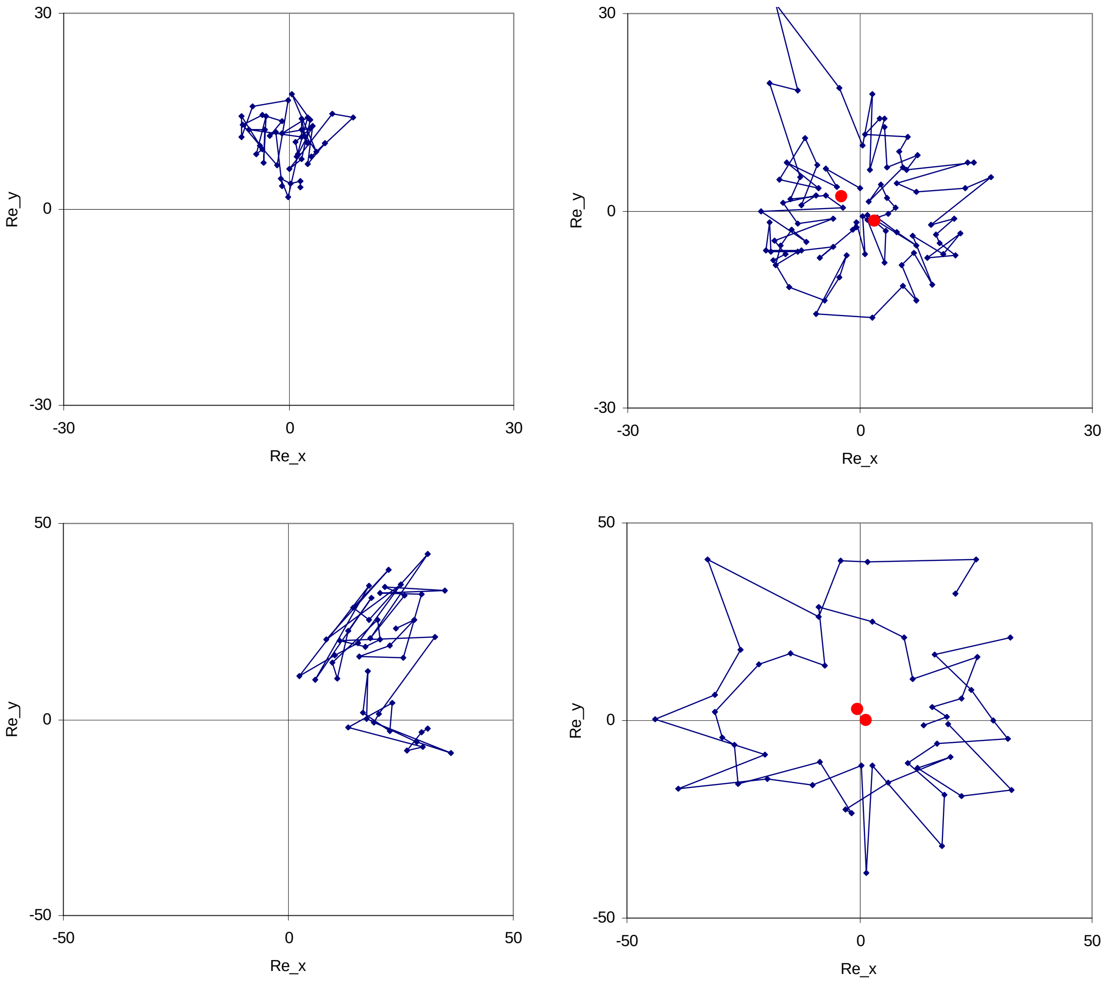

Figure 7.3 – The left panes show wind hodographs measured from Viking Lander, for a twelve-minute period starting at 1800 local time, for (top) sol 030, and (bottom panel) sol 554. The sampling time for these data is (top) 8 seconds and (bottom) 16 seconds. The right panels show simulated hodographs of the wind vector as it would be measured by the B2WS if performing an *in situ* rotation sequence as described in Section 7.3. It has been assumed for this prediction that the sensor measurement is perfectly accurate. The red dots indicate the average wind vector when averaged over an entire rotation.

7.4 Vertical scan

To characterise turbulence in the planetary boundary layer, following on from the work of [Tillman, Landberg & Larsen, 1994], it would be very useful to obtain wind and temperature data at various heights above the surface. This will be done using by moving the Beagle 2 arm to the positions shown in Figure 7.4. The arm is positioned as far away as possible from the hot lander body and the solar panels. The heights of these positions are respectively 96, 79, 61, 39, 28, and 19 cm above the base plane of the lander. In the lowest position, the PAW is brought to rest on the surface. This position will be modified once it is known where exactly the Martian surface is relative to the lander.

Ideally, one would like to obtain data at different heights simultaneously. In practice, we can only obtain data at one height at a time. There are two conflicting ideals: on the one hand, if the dwell time at each height is relatively short – say 5 minutes – then it would take about half an hour to perform this whole sequence. During this time, the average air temperature at any one height may have changed by 4°C between the start time and the finish time of the profile.

On the other hand, a five-minute data segment would not be enough to obtain useful turbulence spectra. This would require a longer measurement time at each height, say an hour (this was the time interval used by [Tillman, Landerg & Larsen, 1994]). It clearly becomes impossible, then, to obtain even a near-simultaneous reading at different heights. We will attempt to get such one-hour measurement sequences at different heights, using the high-rate sampling mode at 1 Hz.

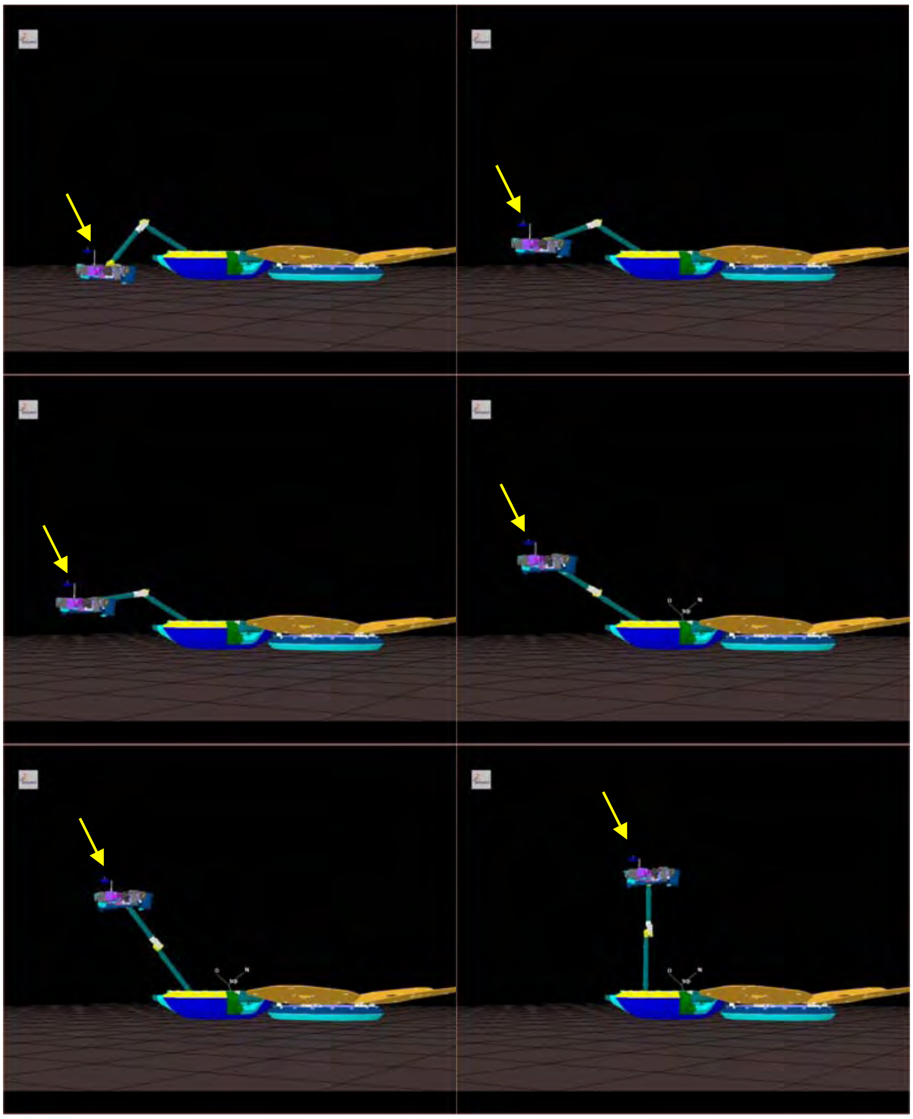

Figure 7.4 – This set of pictures show the six WIND_RADIALSCAN positions. These will be used to obtain vertical profiles of temperature and wind speed. The measurement heights are 19, 28, 39, 61, 79, and 96 cm above the ground.

7.5 Lander interference

The lander is heated, to allow the electronics to survive the cold Martian nights. The main heating technique is passive solar absorption: the lander’s batteries and electronics are housed in an insulated compartment underneath a solar absorber panel, which absorbs sunlight while re-emitting very little in the infra-red. This heats the lander, and means it can get up to 100°C hotter than the surrounding air [Peskett, 2001]. In this situation one would expect convective updrafts to form above the lander, which might significantly affect any meteorological measurements made above the lander. This is of concern not only for Beagle 2 and NetLander. Convective updrafts above the Pathfinder lander may have contributed to the largest temperature fluctuations of +20 K which were observed in the air temperature data from that mission – the magnitude of these variations appears to be larger than would be expected given the PBL parameters deduced for Pathfinder’s meteorological data. However, the effects of such updrafts on meteorological measurements have not yet been studied to my knowledge.

It is unclear what form the convection above a hot lander on Mars is likely to take. Some unpublished Finite Element Modelling (FEM) work done for Beagle 2 suggests that the convection is unsteady with respect to time [Barber *et al.*, 2002], and thus is more likely to take the form of thermals, or ‘puffs’ of hot air, breaking away intermittently from the lander.

The form of these thermals can be studied by moving the wind and air temperature sensors to different positions above the hot lander. This takes the form of two horizontal scans at different heights and one vertical scan above the centre of the lander. These positions are shown in Figures 7.5 through 7.7. Measurements will be taken probably for 240 s at 1 Hz in each of these positions before moving on to the next position. This is done, rather than taking single measurements at many more positions, because it is important to remove the temporal fluctuations from the data set. The disadvantage of this approach is that the whole sequence of twelve positions will take an hour to complete. In this time the atmospheric conditions will have changed appreciably. In Figure 7.7 it can be seen that the centre positions of the horizontal scans are very similar to some of the VERTSCAN positions. This use of repeated positions may allow the data user to quantify the drift in air temperature during the scan.

What should one expect to see in these data? The average air temperature will probably be slightly higher when above the centre of the lander, perhaps by a few °C. It is suspected that this will probably not take the form of a consistently higher temperature, but rather of a greater fluctuation in temperature, caused by ‘puffs’ of hot air breaking away from the lander base.

It is very difficult to get a sensible wind measurement during this scan sequence. If the axis of the wind sensor is horizontal it may be possible to detect a small vertical wind signal when an updraft passes by. However, this would probably be swamped by vertical air currents caused by turbulence around the PAW and the lander itself. If the axis of the wind sensor is vertical as for conventional measurements, thermal updrafts will have an unpredictable and thus undetectable effect. Therefore wind measurements will be ignored during these readings.

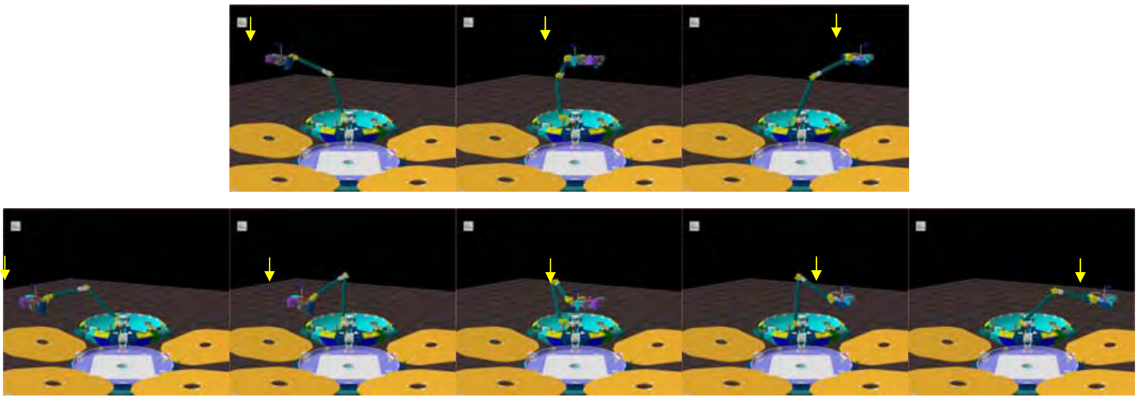

Figure 7.5 – The MEDSCAN (top three pictures) and LOWSCAN (bottom three pictures) will be used to obtain temperature measurements at various points around the lander.

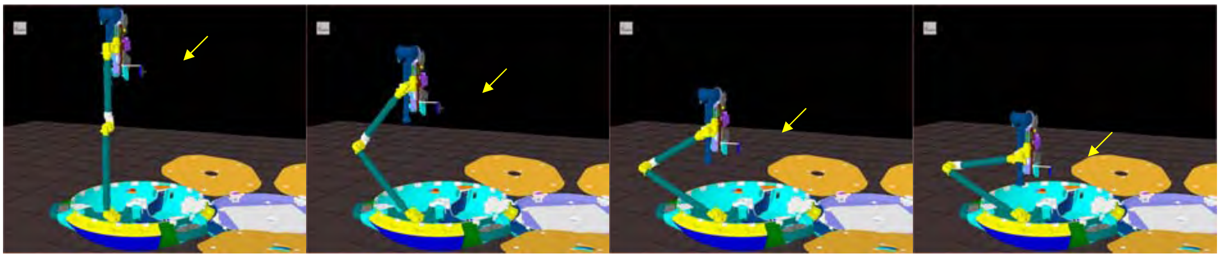

Figure 7.6 – The VERTSCAN positions, like the MEDSCAN and LOWSCAN positions, are intended primarily to make air temperature measurements in the vicinity of the lander. The axis of the wind sensor in these positions is vertical, which may provide observations of updrafts above the hot lander.

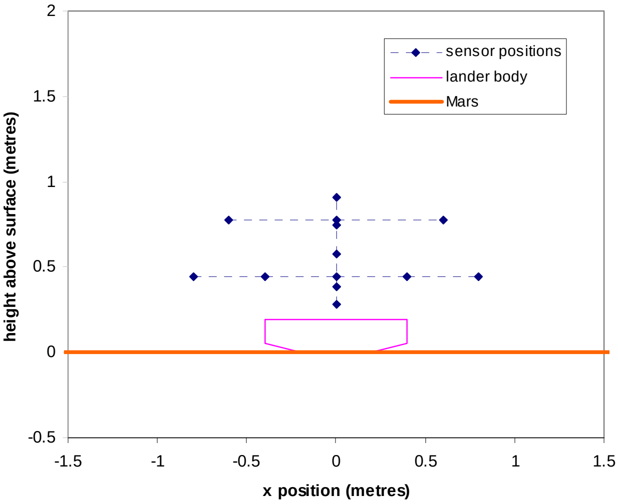

Figure 7.7 – Diagram showing the positions of Figures 7.5 and 7.6 in relation to the lander body. Heights are exact; horizontal positions are approximate.

Chapter 8 - Conclusions & Future Work

8.1 Summary

A wind tunnel has been developed for testing and calibration of anemometers in low-density, low-speed winds. The facility has been used to simulate flow speeds of 0.5 – 30 m/s with air and CO_2 at pressures of 5-10 mbar. The absolute accuracy of the flow speed measurement is 3% for all speeds above 1 m/s. A feature of this wind tunnel which is unique among current Mars wind tunnels is the ability to simulate step changes of wind speed in ~ 1 second. The velocity profile in the test section has been calculated analytically and using finite element techniques, and validated experimentally using a pitot probe. Stability with respect to time of the flow speed appears to be better than 0.3%, which is a great improvement on previous facilities. A gas cooling system must be implemented in future, though, if the facility is to be used to simulate the full range of Martian conditions; a design is suggested in Appendix A.

A wind sensor has been designed, calibrated, and delivered to the Beagle 2 Mars lander. The sensor had to fit in with very tight constraints dictated by the Beagle 2 project. The wind sensor development was completed in only 12 months from start of the feasibility study to delivery of flight hardware. This wind sensor is smaller and lighter than previous Martian wind sensors, weighing only 15 grams including electronics. The sensor consists of three platinum films deposited on a Kapton film, equally distributed around the sides of a vertical cylinder. The cylinder is 18 mm high x 10 mm diameter, and is made of Rohacell, a closed-cell polyimide foam with an extremely low thermal conductivity. A simple analogue circuit is used to dissipate ~32 mW in each film, heating them up to 40 – 80 K above the ambient gas temperature. The circuit outputs three voltages, representative of the resistances of the three films; these voltages are read by an ADC onboard the spacecraft. The resistances of the films are temperature dependent, allowing calculation of the film temperatures. The temperature of the films is dependent on various environmental properties, including air temperature as well as wind speed and direction.

The sensor’s dependence on wind speed and direction, and on gas type and density, has been investigated using the wind tunnel described above. A novel scheme has been proposed in order to calculate a wind vector from the outputs of the sensor. Rather than obtain a wind speed from the *average* of the three film temperatures, as was done for the wind sensor on NASA’s Mars Pathfinder, a wind vector is calculated from *differences* between the film temperatures. This makes the measured wind vector less prone to common-mode errors such as uncertainties in air temperature or effective sky temperature. However, it does make the measured wind vector more sensitive to errors which affect the different films asymmetrically; examples include sunlight falling on one side of the sensor, or a change in the resistance of one of the films due to erosion. Use of the difference technique also leads to an improvement in response time, apparently from ~ 10 seconds to ~ 4 seconds. This response time of the sensor is more than the 1 second response time which was specified in the original science goals. The response time could have been improved by using a smaller sensor but this would have had to be manufactured externally and would have required vibration testing. Neither of these were possible within the Beagle 2 schedule and budget constraints.

Several deficiencies in the design have been pointed out in this thesis. In particular, the substrate (Rohacell) has a high emissivity of 0.67 in the thermal infrared, so loses more heat to the environment via thermal infrared radiation than would be desired. Despite this, however, the films will still be typically 60 – 80 K hotter than air temperature. This large overheat further reduces the sensitivity of the measured wind speed to uncertainties in air temperature to only ~± 3.5 % K^{-1}.

A simple analytical model of heat flows in the wind sensor has been developed to predict performance in different air temperatures and in different radiative environments. The data interpretation scheme, based on the *differences* between heat transfer of the different films and using Nusselt and Reynolds numbers to scale between different gas temperatures and densities, is predicted to be relatively insensitive to common-mode errors in gas and background temperatures. However, the validity of these predictions has not been verified experimentally, which leads to a great uncertainty in the accuracy in the measured wind speed. The data interpretation scheme will require some environment-dependent corrections to be applied to account for any non-isotropic effects such as differences between thermal heat contact beneath the different films. The details of this scheme are yet to be worked out.

Uncertainties in sensor performance, though, are compensated for by two techniques which may be used *in situ* to diagnose and partially correct for errors in sensor performance. The first is use of the electronics in a secondary mode to measure the film resistances. This will permit diagnosis of any change in film resistance, and enables a backup air temperature measurement. The second *in situ* recalibration technique is made possible by the wind sensor’s position on the end of a motorized arm; the wind sensor can be rotated through 360° around a vertical axis and back again, while recording wind data. This will allow diagnosis and correction for any shift in the effective zero of the wind vector measurement, caused by uncertainties which affect the three films unequally.

Finally, planned operations for the wind sensor on Mars have been outlined. The wind sensor will be able to measure horizontal wind vectors at a variety of heights from 0.2 to 0.95 metres above the ground. Sampling modes include high-rate and low-rate sampling modes, as well as a ‘listening’ mode which is designed to return high-rate meteorological data only in the event of a suspected convective vortex or dust devil observation. The most promising trigger criterion to be used will be a sudden pressure drop of 10 μbar. The position of a temperature sensor next to the wind sensor on the end of Beagle 2’s motorized arm allows measurements of air temperature within 1 m of the lander. The air temperature sensor will be scanned horizontally and vertically in an attempt to characterize the thermal convection which occurs above the lander. The wind sensor may be rotated such that its axis is horizontal, in which case it would be sensitive to vertical winds. However, vertical wind speeds are likely to be smaller than airflows due to mechanical turbulence around the sensor. Therefore it is concluded that measurements of vertical wind speed are unlikely to be obtained successfully.

8.2 Future work on wind tunnel

The wind tunnel described in Chapter 3 represents a valuable facility, well suited for testing and calibration of Martian anemometers in fluctuating conditions. However, the wind tunnel cannot be said to be representative of Martian conditions unless it allows operation at Martian temperatures. This is especially important for thermal anemometers. A gas cooling system for the wind tunnel was designed and built (described in Appendix A). However, it did not have enough cooling power to chill the pipes and the nozzle assembly, and suffered from water icing problems. If a budget is available in future, a refrigerant loop could be installed both to cool the gas (downstream of the flow control valve) and to pre-cool the nozzle assembly.

A number of improvements to the Mars wind tunnel could be implemented. It will be easy to fix the pressure measurement error, by placing the pressure sensors nearer the test section. It will also be easy to install a turntable or other mount to allow motorized adjustment of sensor tilt. The operation of the wind tunnel would be facilitated by automating some of the controls. Automation of the pressure control would be easy, relatively cheap (<£2000), and would free the wind tunnel operator to perform other tasks. Also, it should improve the pressure stability of the wind tunnel, and would certainly improve pressure control during step changes in wind speed. Automation of the flow control valve (also <£2000) would allow repeatable step changes in wind speed, as well as allowing precise, automatic regulation of flow speed.

Once temperature control of the incoming gas has been implemented, further temperature controls can be envisaged. For example, a separate cooling loop could cool the instrument or a radiative shroud to be at a different temperature to the gas flow; this would be useful for many potential Mars wind sensors. Another possibility is to create step changes of temperature; this could be achieved by passing a high current through a wire mesh placed across the nozzle. This is a technique already in use at the wind tunnel labs, so the equipment is readily available.

In the long-term, the most promising anemometry technique for Martian use may be Laser Doppler anemometry (LDA), as discussed in Chapter 2. The wind tunnel could be used to evaluate LDA sensors in Martian conditions, or LDA probes could be used to calibrate wind speed measurements in the wind tunnel. In order to allow this, though, particles need to be introduced into the air stream; although dust particles cannot be used for fear of damaging the vacuum pumps, a fine spray of liquid droplets could be used.

8.3 Future work for B2WS

The main future work for the Beagle 2 wind sensor is of course implementation of the operations plans described in Chapter 7, during the surface phase of operations. Before then however, there are some further projects to be undertaken.

More simulations of B2WS response to VL2 data, such as those presented in Sections 6.6 and 7.3.1 are being carried out. These simulations have two goals. Firstly, they are providing a better understanding of how the instrument and the data interpretation technique work in practice; simulations of measurement and calibration errors such as those shown in Figure 7.31 are invaluable. Secondly, these simulations allow us to gain practice in using the B2WS data to achieve its science goals; for example, simulations are being run using wind and temperature signatures of dust devils from VL2 data.

The analytical thermal model could be improved. In particular, variation of the local heat transfer coefficient from the Rohacell should be introduced. The accuracy of the analytical model would be better if the emissivity of Rohacell were measured in the visible and in the thermal infrared – I have been using measurements of the emissivity of a different polyimide foam. This improved analytical model should then be used to re-examine the validity of the data interpretation technique given the low air and sky temperatures likely to be encountered on Mars. More investigations need to be performed into the optimization of the error correction and *in situ* recalibration techniques. If the B2WS returns a lot of data, the calibration of the B2WS could be repeated at low temperatures, which would lend validity to the B2WS measurements.

Bibliography

Anderson, J. D. (1990), *Modern compressible flow*, McGraw-Hill, New York.

Arya, S. P. (1988), *Introduction to Micrometeorology*, Academic Press, London.

Balme, M. R., Whelley, P. L., & Greeley, R. (2003), Mars: Dust devil track survey in Argyre Planitia and Hellas Basin', *Journal of Geophysical Research* **108**(E8), 5086.

Bandfield, J.L., Glotch, T. D. & Christensen, P. R. (2003), 'Spectrocopic identification of carbonate minerals in the Martian dust', *Science* **301**, 1084-1087.

R. W. Barber, X. J. Gu, D. R. Emerson & B. M. Shaughnessy (2002), 'Numerical simulation of convective losses from the Martian Beagle 2 lander'. CCLRC Daresbury Lab, UK, web page: http://www.cse.clrc.ac.uk/ceg/misc/beagle/beagle2.shtml

Barlow, J. B. (1999), *Low-speed wind tunnel testing*, Wiley, New York.

Bown, N.W.; Cain, T.M.; Jones, T.V.; Shipley, P.P.; Barry, B. (1994), 'In flight heat transfer measurements on an aero-engine nacelle', *Proceedings of the International Gas Turbine and Aeroengine Congress and Exposition*, The Hague, 13-16 June 1994. published by ASME, New York.

Boynton, W.V., Feldman, W.C., Squyres, S. W., Prettyman, T., Brückner, J., Evans, L. G., Reedy, R. C., Starr, R., Arnold, J. R., Drake, D. M., Englert, P. A. J., Metzger, A. E., Mitrofanov, Igor, Trombka, J. I., d'Uston, C., Wänke, H., Gasnault, O., Hamara, D. K., Janes, D. M., Marcialis, R. L., Maurice, Mikheeva, I., Taylor, G. J., Tokar, R., Shinohara, C. (July 5 2002) 'Distribution of Hydrogen in the Near Surface of Mars: Evidence for Subsurface Ice Deposits', *Science* **297**, 81-85.

British Standard 1042, *Measurement of fluid flow in closed conduits*, Sections 1.1 (1981) and 1.4(1992). Also BS ISO TR 15377 (1998), BSI, London.

Bruun, H. H. (1995), *Hot-wire anemometry: principles and signal analysis*, OUP, Oxford.

Catling, D. C. (1995), Meteorological Measurements on the Surface of Mars, DPhil thesis, Oxford University.

Chamberlain, T. E., Cole, H. L., Dutton, R. G., Greene, G. C. & Tillman, J. E. (1976), 'Atmospheric measurements on Mars: the Viking meteorology experiment', *Bulletin of the American Meteorological Society* **57**, 1094-1104.

Chicarro, A.., Martin, P. & Trautner, R. (2004), 'The Mars Express Mission: an Overview'. In SP-1240, European Space Agency.

Christensen, P. (6 March 2003), 'Formation of recent martian gullies through melting of extensive water-rich snow deposits', *Nature* **422** (6927), 45-48.

Clancy, R. T., Muhlemann, D. O. & Berge, G. L. (1990), ‘Global changes in the 0-70 km thermal structure of the Mars atmosphere derived from 1975 to 1989 microwave CO spectra’, *Journal of Geophysical Research* **95**, 14543-14554.

Clifford, S. M., Crisp, D., Fisher, D.A., Herkenhoff, K.E., Smrekar, S.E., Thomas, P.C., Wynn-Williams, D.D., Zurek, R.W., Barnes, J.R. & Bills, B.G. (2000), ‘The state and future of Mars polar science and exploration’, *Icarus* **144**, 210-242.

Crisp, D. (1998), ‘Wind sensors for the Mars Express NetLanders’, draft, NetLander project internal report (unpublished).

Eckert, E.R.G. & Soehngen, E. (1952) ‘Distribution of heat-transfer coefficients around circular cylinders in crossflow at Reynolds numbers of 20-500’, *Transactions of the American Society of Mechanical Engineers* **74**, 343-7.

Edwards High Vacuum Ltd. (1963), Specifications for Rootes-type Booster pump Model 1R80. Manor Royal, Crawley, Sussex.

Evlanov, E.N., Zubkov, B.V., Nenarokov, D.F., Linkin, V.N., Zavjalov, M.A. & Tyuryukanov, P.M. (2001), ‘Gas-Discharge Anemometer for the Investigation of Flow Dynamics in Rarefied Gas Media’, *Cosmic Research* **39** (5), 484-490.

Farrelly, F.A., Flamini, E., Petri, A., Pitolli, L. & Pontuale, G. (2001), ‘Environmental Acoustic Reconnaissance and Sounding (EARS) Instrument for Mars Exploration’, *Proceedings of 17th International Congress on Acoustics*, Rome, 2-7 September 2001, ISBN 88-88387-03-X .

Farmer, C. B., Davies, D. W. & LaPorte, D. D. (1976), ‘Mars: Northern summer ice cap – water vapor observations from Viking 2’, *Science* **194**, 1339-1340.

Fay, J.A. and Sonwalkar, N. (1991) *Fluid Mechanics*, MIT, Boston. Available on-line at http://www.mas.ncl.ac.uk/~sbrooks/book/nish.mit.edu/2006/Textbook/

Ferri, F. (2000), *Scientific Rationale for Beagle 2 environmental sensors*, ESA ESTEC internal document, unpublished.

Forget, F., Hourdin, F., Fournier, R., Hourdin, C., Talagrand, O., Collins, M., Lewis, S. R., Read, P. L. & Huot, J.-P. (1999), ‘Improved general circulation models of the Martian atmosphere from the surface to above 80 km’, *Journal of Geophysical Research* **104**(E10), 24,155-24,175.

FT Technologies Ltd (1999), ‘FT702 Ultrasonic Anemometer Specification’, Data sheet published by FT Technologies Ltd, Church Lane, Middlesex, UK.

Greeley, R., Lancaster, N., Lee, S. & Thomas, P. (1992), ‘Martian Aeolian processes, sediments, and features’, in *Mars*, University of Arizona Press, chapter 22, pp 730-766.

Greeley, R., Balme, M.R., Iversen, J.D., Metzger, S., Mickelson, R., Phoreman, J., White, B. (2003), ‘Martian dust devils: Laboratory simulations of particle threshold’, *Journal of Geophysical Research* **108** (E5), art. no. 5041.

Haapanala, S., Kyhäräinenen, S., Lehto, A., Harri, A.-M., Polkko, J. & Siili, T. (2001), *Barobit – Pressure Transducer for Beagle 2 lander*, Poster presented at Beagle 2 Environmental Sensors Science Meeting, Leicester University, 24th April 2001.

Haberle, R. M., Houben, H. C., Hertenstein, R. & Herdtle, T. (1993), ‘A boundary-layer model for Mars: Comparison with Viking Lander and entry data’, *Journal of the Atmospheric Sciences* **50**(11), 1544-1559.

Haberle, R. M & Catling, D. C. (1996), ‘A micro-meteorological mission for global network science on Mars: rationale and mission requirements’, *Planetary and Space Sciences* **44**(11), 1361-1383.

Haberle, R. M., Joshi, M. M., Murphy, J. R., Barnes, J. R., Schofield, J. T., Wilson, G., Lopez-Valverde, M., Hollingsworth, J. L., Bridger, A. F. C. & Schaeffer, J. (1999), ‘General circulation model simulations of the Mars Pathfinder atmospheric structure investigation/meteorology data’, *Journal of Geophysical Research* **104**(E4), 8957-8974.

Harri, A.-M., Siili, T., Pirjola, R. & Pellinen, R. (1995), ‘Aspects of atmospheric science and instrumentation for Martian missions’, *Advances in Space Research* **16**(6), 15-22.

Harri, A.-M., Marsal, O., Lognonne, P., Leppelmeier, G. W., Spohn, T., Glassmeier, K.-H., Angrilli, F., Banerdt, W. B., Barriot, J. P., Bertaux, J.-L., Berthelier, J. J., Calcutt, S., Cerisier, J. C., Crisp, D., Dehant, V., Giardini, D., Jaumann, R., Langevin, Y., Menvielle, M., Musmann, G., Pommerau, J. P., Di Pippo, S., Guerrier, D., Kumpulainen, K., Larsen, S., Mocquet, A., Polkko, J., Runavot, J., Schumacher, W., Siili, T., Simola, J., Tillman, J. E. & the NetLander team (1999), ‘Network science landers for Mars’, *Advances in Space Research* **23**(11), 1915-1924.

Henry, R. M. & Greene, G. C. (1974), ‘Anemometers for Mars’, in *Flow, its measurement and control in science and industry* (R. B. Dowdell, editor). Instrument Society of America, Pittsburgh.

Hess, S. L., Henry, R. M., Leovy, C. B., Ryan, J. A. & Tillman, J. E. (1977), ‘Meteorological results from the surface of Mars: Viking 1 and 2’, *Journal of Geophysical Research* **82**(28), 4559-4574.

Hickey, G. S. (1997), *Thermal Insulation for Mars Surface Exploration*, JPL Technical Report, http://techreports.jpl.nasa.gov/ .

Hinson, D. P., Simpson, R. A., Twicken, J. D., Tyler, G. L. & Flasar F. M. (1999), ‘Initial results from radio occultation measurements with Mars Global Surveyor’, *Journal of Geophysical Research* **104**(E11), 26997-27012

Holman, J. P. (1989), *Heat Transfer* (SI Metric edition), McGraw-Hill Book Company, Singapore.

Houben, H. (2000), ‘Martian Meteorology from the Mars Global Surveyor’, Abstract from *Meteorology at the Millenium* conference, Royal Meteorological Society, Cambridge, UK.

Incropera, F. P. & DeWitt, D. P. (2002), *Fundamentals of Heat and Mass Transfer* (5th ed.), Wiley, New York.

Kahn, R. (1983), ‘Some observational constraints on the global-scale wind systems of Mars’, *Journal of Geophysical Research* **89**, 6671-6688.

Kahn, R. (1984), ‘The spatial and seasonal distribution of Martian clouds, and some meteorological implications’, *Journal of Geophysical Research* **89**, 6671-6688.

Kapartis, S. & Strachan R. (1999), ‘Wind speed and direction measurement using Acoustic Resonance airflow sensing’, information sheet published by FT Technologies, Church Lane, Middlesex, U.K.

Kargel, J. S. & Strom, R. G. (1996), ‘Global climatic change on Mars’, *Scientific American* **275**(5). 80-83.

Kreyzig, E. (1993), *Advanced Engineering Mathematics*, 7th edition. John Wiley & Sons, New York.

Jørgensen, F. E. (1982), ‘Characteristics and calibration of a triple-split probe for reversing flows’, *DISA Information* **27**, 15-22. Published by Dantec Measurement and Technology, Denmark.

Lange, C.F., Durst F. & Breuer M. (1998), Momentum and heat transfer from cylinders in laminar crossflow at $10^{-4} \leq \mathrm{Re} \leq 200$, *International Journal of Heat and Mass Transfer* **41** 3409-3430.

Lekakis, I. (1996), ‘Calibration and signal interpretation for single and multiple hot-wire/hot-film probes’, *Measurement Science and Technology* **7**, 1313-1333.

Leovy, C. B. & Zurek, R. W. (1979), ‘Thermal tides and Martian dust storms: direct evidence for coupling’ *Journal of Geophysical Research* **84**, 2956-2968.

Lewis, S.R., Read, P. L. & Collins, M. (1996), ‘Martian atmospheric data assimilation with a simplified general circulation model: orbiter and lander networks’, *Planetary and Space Sciences* **44**(11), 1395-1409.

Lewis, S. R. (1998), ‘Validation of a Mars general circulation model against recent observations from Mars Pathfinder and Mars Global Surveyor’, *Annals of Geophysics* **16**, C1000.

Lindal, G. F., Hotz, H. B., Sweetnam, D. N., Shippony, Z., Brenkle, J. P., Hartsell, G. V., Spear, R. T. & Michael, W. H. Jr. (1979), ‘Viking radio occultation measurements of the atmosphere and topography of Mars: Data acquired during 1 Martian year of tracking’, *Journal of Geophysical Research* **84,** 8443-8456**.**

Main, A.J., Day, C.R.B., Lock, G.D., Oldfield, M.L.G. (1996), “Calibration of a four-hole pyramid probe and area traverse measurements in a short-duration transonic turbine cascade tunnel”, Experiments in Fluids, Vol.21, p.302-311

Martin, L. J. & Zurek, R. W. (1993), ‘An analysis of the history of dust activity on Mars’, *Journal of Geophysical Research* **98**(E2), 3221-3246.

McCleese, D. J., Haskins R. D., Schofield, J. T., Zurek, R. W., Leovy, C. B., Paige, D. A. & Taylor, F. W. (1992), ‘Atmosphere and climate studies of Mars using the Mars Observer Pressure-Modulator Infrared Radiometer’, *Journal of Geophysical Research* **97**(E5), 7735-7757.

Merrison J.P., Field D., Finster K., Lomstein, B.Aa., Nørberg, P., Ramsing, N.B. & Uggerhøj, E. (2001) ‘The Mars simulation laboratory, University of Aarhus’ 1st European Workshop of the European-Exo/Astrobiology-Network, MAY 21-23, 2001, Frascati, Italy.

Merrison, J.P., Bertelsen, P., Frandsen, C., Gunnlaugsson, H.P., Knudsen, J.M., Lunt, S., Madsen, M.B., Mossin, L.A., Nielsen, J., Nørnberg, P., Rasmussen, K.R. and Uggerhøj, E. (2002) ‘Simulation of the Martian Dust Aerosol at Low Wind Speeds’ *Journal of Geophysical Research* **107** (E12), pages 16-1 to16-8.

Metzger, S. M., Carr, J. R., Johnson, J. R., Parker, T. J. & Lemmon, M. T. (1999) ‘Dust devil vortices seen by the Mars Pathfinder camera**’,** *Geophysical Research Letters* **26** (18) 2781-2784.

Mischna, M. A., Bell, J. F., James, P. I. & Crisp, D. (1998), ‘Synoptic measurements of Martian winds using the Hubble Space Telescope’, *Geophysical Research Letters* **25**(5), 611-614.

Modaress, D., Fourguette, D., Taugwalder, F., Gharib, M., Forouhar, S., Wilson, D., and Scalf, J. (2002), "Miniature and Micro-Doppler Sensors". Published on the website of Viosense corporation, Pasadena; http://www.viosense.com

Murphy, J. R., Leovy, C. B. & Tillman, J. E. (1990), ‘Observations of Martian Surface Winds at the Viking Lander 1 Site’, *Journal of Geophysical Research* **95**(B9), 14,555-14,576.

Murphy, J. R. & Nelli, S. (2002), ‘Mars Pathfinder convective vortices: Frequency of occurrence’, *Geophysical Research Letters* **29** (23): art. no. 2103.

NASA EPIMS Materials outgassing database. http://epims.gsfc.nasa.gov/og/

NASA PDS (Planetary Data System). Data from all NASA planetary missions, including Viking and Pathfinder landers. Available at http://pds.jpl.nasa.gov

Nguyen, N. T. (1997), ‘Micromachined flow sensors – a review’, *Flow Measurement and Instrumentation* **8**(1), 7-16.

Owen, T. (1992), ‘The composition and early history of the atmosphere of Mars’, in *Mars*, University of Arizona Press, chapter 25, pp 818-834.

Peskett, Simon (2000), speaking at Beagle 2 Consortium meeting, Leicester University, 29 March 2000, unpublished.

Peters, Dan (2004), Radiometric Calibration of the High Resolution Dynamics Limb Sounder. DPhil thesis, Oxford University.

Piccini, E., Guo, S. M. & Jones, T.V. (2000), ‘The development of a new direct-heat-flux gauge for heat transfer facilities’, *Measurement Science and Technology* **11**(4), 342-349.

Pullan, D., Sims, M.R., Wright, I.P., Pillinger, C.T. & Trautner, R. (2004), ‘Beagle 2: the Exobiological Lander of Mars Express’. In SP-1240, European Space Agency.

Renno, N. O. & Nash, A. N. (2000), ‘Martian and terrestrial dust devils: Test of a scaling theory using Pathfinder data’ *Journal of Geophysical Research* **105**(E1), 1859-1865.

Ringrose, T. J., Towner, M. C. & Zarnecki, J. C. (2003), ‘Convective vortices on Mars: a reanalysis of Viking Lander 2 meteorological data, sols 1-60’, *Icarus* **163**, 78-87.

Röhm (2000), Rohacell data sheet. Röhm GmbH, Chemische Fabrik, D-64275 Darmstadt, Germany.

Ryan, J. A., Henry, R. M., Hess, S. L., Leovy, C. B., Tillman, J. E. & Walcek, C. (1978), ‘Mars Meteorology: three seasons at the surface’, *Geophysical Research Letters* **5**(8), 715-718.

Ryan, J. A. (1985), ‘Mars Atmospheric Circulation: Aspects From Viking Landers’, *Journal of Geophysical Research* **90**(A7), 6319-6325.

Ryan J. A. & Lucich, R. D. (1983), ‘Possible dust devils, vortices on Mars’, *Journal of Geophysical Research* **88** (NC15), 1005-1011.

Salby, M. L. (1996), *Fundamentals of Atmospheric Physics*, Academic Press, London.

Savijärvi, H. & Siili, T. (1993), ‘The Martian slope winds and the nocturnal PBL jet’, *Journal of the Atmospheric Sciences* **50**(1), 77-88.

Schofield, J. T., Barnes, J. R., Crisp, D., Haberle, R. M., Larsen, S., Magalhães, J. A., Murphy, J. R., Seiff, A. & Wilson, G. (1997), ‘The Mars Pathfinder Atmospheric Structure Investigation/Meteorology (ASI/MET) Experiment, *Science* **278**, 1752-1757.

Seiff, A, Tillman, J.E., Murphy, J.R., Schofield, J.T., Crisp, D., Barnes, J.R., LaBaw, C., Mahoney, C., Mihalov, J.D., Wilson, G.R., and Haberle, R.M. (1997), The atmosphere structure and meteorology instrument on the Mars Pathfinder lander, *Journal of Geophysical Research* **102** (E2), 4045-4056.

Siili, T. (1996), ‘Modelling of albedo and thermal inertia induced mesoscale circulations in the midlatitude summertime Martian atmosphere’, *Journal of Geophysical Research* **101**(E6), 14,957-14,968.

Siili, T., Haberle, R. M., Murphy, J. R. & Savijärvi, H. (1999), ‘Modelling of the combined late-winter ice cap edge and slope winds in Mars’ Hellas and Argyre regions’, *Planetary and Space Science* **47**, 951-970**.**

Sims, M. R., Pillinger, C. T., Wright, I. P., Dowson, J., Whitehead, S., Wells, A., Spragg, J. E., Fraser, G., Richter, L., Hamacher, H., Johnstone, A., Meredith, N. P., de la Nougerede, C., Hancock, B., Turner, R., Peskett, S., Brack, A., Hobbs, J., Newns, M., Senior, A., Humphries, M., Keller, H. U., Thomas, N., Lingard, J. S., Underwood, J. C., Sale, N. M., Neal, M. F., Klingelhofer, G. & Ng, T. C. (1999), ‘Beagle 2: A proposed exobiology lander for ESA’s 2003 Mars Express Mission’, *Advances in Space Research* **23**(11), 1925-1928.

Sims, M. R. (2000), speaking at Beagle 2 Consortium meeting, Leicester University, 28 March 2000, unpublished.

Smith, M.D., Conrath, B. J., Pearl, J. C. & Ustinov, E. A. (1996), ‘Retrieval of atmospheric temperatures in the Martian planetary boundary layer using upward-looking infrared spectra’, *Icarus* **124**, 586-597.

Smith, P., Bell, J., Bridges, N., Britt, D., Gaddis L., Greeley, R., Keller, H.U., Herkenhoff, K.E., Jaumann, R., Johnson, J.R., Kirk, R.L., Lemmon, M., Maki, J.N., Malin, M.C., Murchie, S.L., Oberst, J., Parker, T.J., Reid, R.J., Sablotny, R., Soderblom, L.A., Stoker, C., Sullivan, R., Thomas, N., Tomasko, M.G. & Wegryn, E. (1997), ‘Results from the Mars Pathfinder camera’, *Science* **278**, 1758-1765.

Strom, R. G., Croft, S. K. & Barlow, N. G. (1992), ‘The Martian impact cratering record’, in *Mars*, University of Arizona Press, chapter 12, pp 383-423.

Sullivan, R., Greeley, R., Kraft, M., Wilson, G., Golombek, M, Herkenhoff, K, Murphy, J. & Smith, P. (2000), ‘Results of the Imager for Mars Pathfinder windsock experiment’, *Journal of Geophysical Research* **105** (E10), p 24547-24562.

Sutton, J. L., Leovy, C. B., and Tillman, J. E. (1978), ‘Diurnal variation of the Martian surface layer meteorological parameters during the first 45 sols at the two Viking Lander sites’, *Journal of the atmospheric sciences* **35**, 2346-2355.

Thomas, P., Veverka, J., Gineris, D., Wong, L. (1984), ‘Dust streaks on Mars’, *Icarus* **60** (1), 161-179.

Thomas, P. & Gierasch, P. J. (1985), ‘Dust Devils on Mars’, *Science* **230** (4722), 175-177.

Tillman, J. E. (1972), ‘The indirect determination of stability, heat and momentum fluxes in the atmospheric boundary layer from simple scalar variables during dry unstable conditions’, *Journal of Applied Meteorology* **11**, 783-792.

Tillman, J. E. (1988), ‘Mars global atmospheric oscillations: Annually synchronized, transient normal mode oscillations and the triggering of global dust storms’, *Journal of Geophysical Research* **93**, 9433-9451.

Tillman, J. E. (2001), personal communication, 13 June 2001.

Towner, M., Department of Space Sciences, University of Kent at Canterbury, personal communication, 14 June 2000.

Towner, M.C., Patel, M. R., Ringrose, T. J., Zarnecki, J. C., Pullan, D., Sims, M. R., Haapanala, S., Harri, A.-M., Polkko, J. & Wilson, C. (in press), ‘The Beagle 2 environmental sensors: Science goals and instrument description’. *Planetary and Space Sciences*, submitted Nov 2002.

Tyler, D., Barnes, J. R. & Haberle, R. M. (2002) ‘Simulation of surface meteorology at the Pathfinder and VL1 sites using a Mars mesoscale model’, *Journal of Geophysical Research* **107**(E4), pages 2-1 – 2-17.

White, B. R., Lacchia, B. M., Greeley, R. & Leach, R. N. (1997), ‘Aeolian behaviour of dust in a simulated Martian environment’, *Journal of Geophysical Research* **102** (E11), 25629-25640.

Wilson, C. F., Simko, T. M. & Collins, R. E. (1998), ‘Heat conduction through the support pillars in vaccum glazing’, *Solar Energy* **63**(6), 393-406.

Young, A. D. (1989), Boundary Layers 1st edition. BSP Professional Books.

Zdravkovich, M. M. (1997), Flow around Circular Cylinders: Volume 1,OUP, Oxford.

Zurek, R. W., Barnes, J. R., Haberle, R. M., Pollack, J. B., Tillman, J. E. & Leovy, C. B. (1992), ‘Dynamics of the atmosphere of Mars’, in *Mars*, University of Arizona Press, chapter 26, pp 835-933.

Zurek, R. W. & Martin, L. J. (1993), ‘Interannual variability of planet-encircling dust storms on Mars’, *Journal of Geophysical Research* **98**(E2), 3247-3259.

Appendix A – Wind tunnel temperature control system

For thermal anemometry in particular, it is desirable to vary the temperature of the gas over the range of Martian temperatures (160 K < T < 300 K). A low-cost cooling system was designed which allows the gas to be cooled to any temperature in the range 200-300 K. Incoming CO_2 is cooled by passing it through a bed of granulated CO_2 ice (see Figure below). Every gram of CO_2 ice vaporized from its solid form at 197 K provides enough cooling power to cool 9 grams of gaseous CO_2 from 293 K to 197 K. Bypass valves allow control of what proportion of the gas flow passes through the cooling chamber, allowing temperature control of the gas flow.

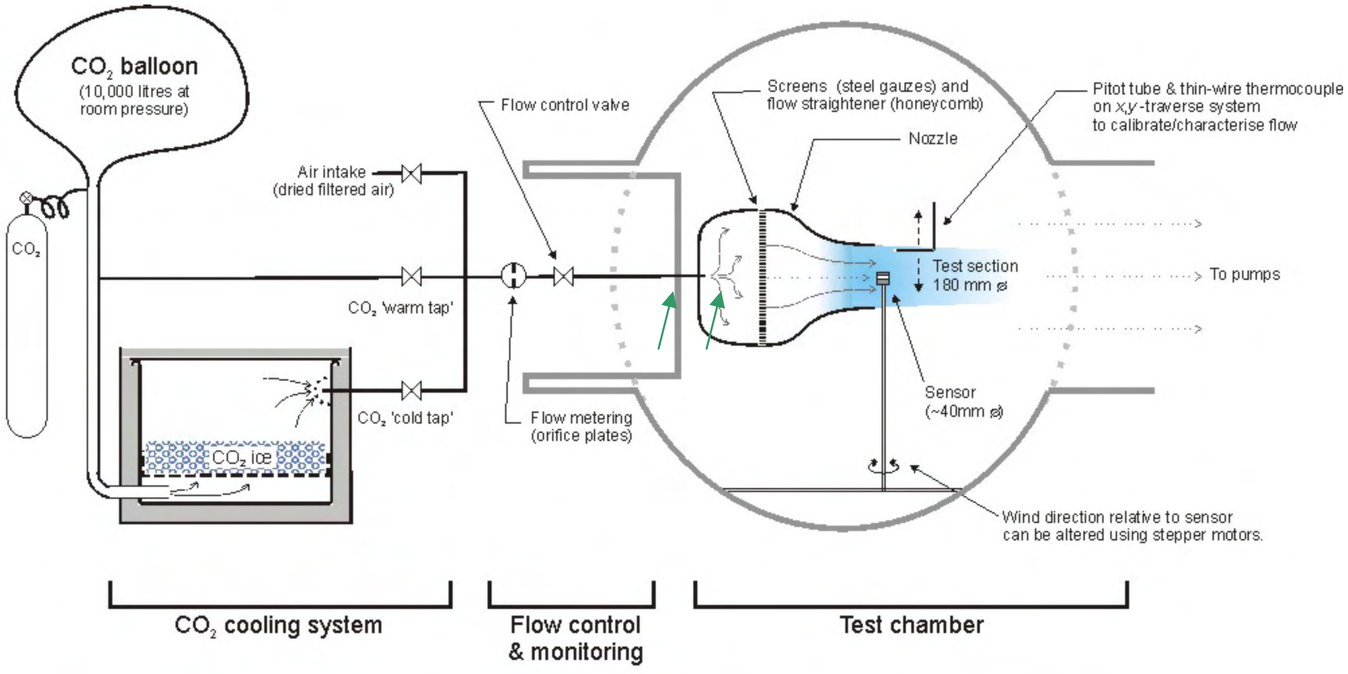

This system was chosen largely because it was inexpensive; dry ice is available very cheaply, and the chamber and pipework were assembled for under £1000 (this compares favourably with estimates of £20,000 for assembly of a refrigerant-cooled system). Initial tests on the system showed that gas cooling down to 210 K was achieved. However, two problems were encountered. Firstly, it is difficult to keep water ice out of the system; dry ice is typically delivered covered in a thin film of water ice, which caused icing problems in downstream flow control valves. Secondly, the cold gas must pass through ~7 metres of pipes between the cooling chamber and the test section, as well as the porous plate and flow straightener in the nozzle. These elements represent a large thermal mass which must be cooled by the cold gas before thermal equilibrium can be achieved; this requires quite a lot of CO_2 usage (an entire gas bottle). It is proposed that both these problems would be alleviated by using the section of pipe downstream of the flow control valve as a heat exchanger (denoted by green arrows in the above figure). As an initial trial, one could try surrounding it in dry ice, and see if sufficient heat transfer were achieved this way. A disadvantage of this system is that temperature control becomes more difficult. Some improvements might also be achieved by pre-cooling the settling chamber section of the nozzle by surrounding it with dry ice (this will also pre-cool the flow-straightener). If these do not work a closed-cycle refrigeration system could be installed.

Because of these two problems, wind tunnel testing at cold temperatures was never successfully achieved. The problems listed are soluble; however, they were not achieved during this DPhil research.

Epilogue: concerning Beagle 2…

At the time when this thesis was submitted, in September 2003, the Mars Express spacecraft was travelling towards Mars at speeds approaching 20 km/s. Bolted to its side was the Beagle 2 lander; and somewhere in that package, buried in layers of structure and multi-layer insulation, was the wind sensor – all 15 grams of it – which is the subject of this thesis.

At 02:54 GMT on Christmas day, Beagle 2 was due to land on Mars. However, all attempts to receive its radio communications were unsuccessful. Furthermore, we have no way of knowing what the cause of failure was, because Beagle 2 did not include a telecommunications system capable of transmitting during descent.

Therefore, the last we saw of Beagle 2 was this black-and-white picture taken by Mars Express on the 19 December 2003, at 08:33 GMT, when the two spaceship parted company:

Image © ESA 2003

Colin Wilson
Oxford, August 2004